



UNIVERSITY
OF TRENTO - Italy

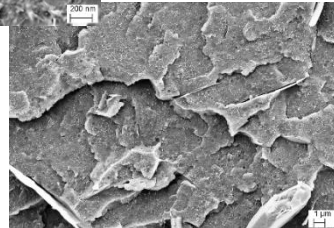
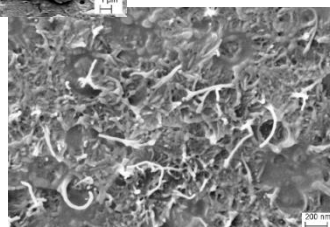
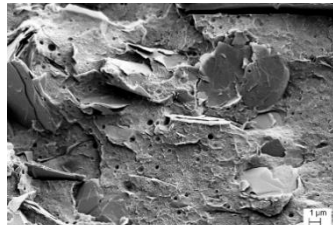
DEPARTMENT OF INDUSTRIAL ENGINEERING

XXX cycle

Doctoral School in Materials, Mechatronics
and Systems Engineering

Carbon-based polymer nanocomposites for 3D-printing

Sithiprumnea Dul



July 2018

CARBON-BASED POLYMER NANOCOMPOSITES FOR 3D-PRINTING

Sithiprumnea Dul

E-mail: sithiprumnea_dul@ yahoo.com

Approved by:

Prof. Alessandro Pegoretti, Advisor
Department of Industrial Engineering
University of Trento, Italy.

Prof. Luca Fambri, Advisor
Department of Industrial Engineering
University of Trento, Italy.

Ph.D. Commission:

Prof. Jose-Marie Lopez-Cuesta,
Centre des Matériaux des Mines d'Alés
(C2MA)
Ecole des Mines d'Alés, France.

Prof. Claudia Marano,
Department of Chemistry, Materials
and Chemical Engineering
Polytechnic University of Milano, Italy.

Dr. Andrea Dorigato,
Department of Industrial Engineering
University of Trento, Italy.

University of Trento, Italy
Department of Industrial Engineering

July 2018

University of Trento - Department of Industrial Engineering

Doctoral Thesis

Sithiprumnea Dul - 2018

Published in Trento (Italy) – by University of Trento

ISBN: -----

To my beloved family

Abstract

In this PhD project, novel polymer nanocomposites are developed with the aim to increase the performances of 3D-printed parts obtained by fused deposition modeling (FDM). The attention is focused on carbon-based nanomaterials incorporated into an acrylonitrile–butadiene–styrene (ABS) polymer by a solvent-free process. ABS-based nanocomposites were prepared by incorporating different kinds and amounts of graphene nanoplatelets (GNP), carbon nanotubes (CNT) and hybrid (GNP/CNT) systems. In order to understand the effect of the manufacturing process on the material's properties, the samples were produced into two different processing routes: (i) melt compounding and compression molding, and (ii) melt compounding, following by filament extrusion, and fused deposition modelling (FDM). Several characterization techniques were employed in order to evaluate the flowability, morphology, mechanical and functional properties of the materials.

In the first part of work, ABS-graphene nanocomposites are described. Two ABS matrices having different viscosity were compared with the addition of various types of commercial graphene nanoplatelets (xGnP® M5, C300, C500, and C750 by XG Sciences) in the range 2–8 wt%. The better processability and higher stiffening effect on compression molded plates were achieved by utilizing the low viscosity ABS. The effects of GNPs on the thermal, electromagnetic shielding (EMI SE), electrical and mechanical behaviour of an ABS matrix were investigated. Melt flow index (MFI) values almost linearly decreased with all the type of GNP, especially with the highest surface area nanofiller (GNP-C750). Due to large size of graphene, nanocomposites filled with GNP-M5 showed the better properties of in electromagnetic interference shielding efficiency (EMI SE) and stiffness. Consequently, GNP-M5 were selected and incorporated at 4 wt% in ABS filaments used to feed a FDM machine to obtain specimens with various build orientations. The elastic modulus and dynamic storage moduli of 3D printed parts along three different build orientations were increased by the presence of GNP-M5 in the ABS matrix. At the same time, a decrease in both strength and strain at break was observed when GNP-M5 is added to ABS. Moreover, higher thermal stability was induced on 3D printed parts by GNP, as indicated by a reduction in both coefficient of linear thermal expansion and creep compliance. A comparison between 3D printed and compression molded parts highlighted the importance of the orientation effects induced by the FDM process.

In the second part of work, the results of the investigation on ABS-carbon nanotubes nanocomposites are reported. ABS-CNT nanocomposites plate production by compression molding and their characterization was a preliminary step. Nanocomposite ABS/CNT filaments at 1–8 wt % were obtained by using direct melt compounding and extrusion. The optimal CNT content in the filaments for FDM was found to be 6 wt %; for this composite, a detailed investigation of the thermal, mechanical and electrical properties was performed. The presence of CNT in ABS

filaments and 3D-printed parts resulted in a significant enhancement of the tensile modulus and strength, accompanied by a reduction of the elongation at break. As documented by dynamic mechanical thermal analysis, the stiffening effect of CNT in ABS is particularly pronounced at high temperatures. Besides, the presence of CNT in 3D-printed parts accounts for better creep and thermal dimensional stabilities of 3D-printed parts, accompanied by a reduction of the coefficient of thermal expansion. 3D-printed nanocomposite samples with 6 wt% of CNT exhibited a good electrical conductivity, even if lower than pristine composite filaments. In addition, the strain sensing capabilities of the conducting 3D-printed samples with 6 wt% of CNT with two different infill patterns (HC, and H45) were studied. Upon the strain applied, the resistance change and damage in the conductive FDM parts were detectable. Fatigue and creep loading on FDM products were also carried out.

In last part of work, ABS-GNP-CNT hybrid nanocomposites are described. ABS nanocomposites plates with addition GNP-M5 and CNT at 2-8 wt% were compared. A significant higher reduction in MFI value by the addition of CNT compared to GNP was observed. The ABS/GNP nanocomposites showed the slightly higher stiffness and the creep stability compared to the ABS/CNT nanocomposites, but showed the lower tensile strength. Also, the ABS/CNT samples showed significant higher electrical properties in comparison to ABS/GNP. The total nanofiller content of CNT/GNP hybrid plates was fixed at 6 wt%. The hybrid nanocomposites showed a linear increase in modulus and strength as a function to CNT/M5 ratio. Moreover, conductive hybrid nanocomposite plates were obtained by the addition of CNT. The composition of 50:50 of CNT/GNP at 6 wt% was selected for FDM process due to the good compromise between processability and properties (e.g. mechanical and electrical). In agreement with electrical resistivity, EMI SE of 6 wt% ABS/CNT and 50:50 hybrid ABS nanocomposites resulted to be -46 dB and -31.7 dB for plate samples. EMI SE of FDM parts is about for -14 dB HC and H45 build orientation and -25 dB for PC build orientation printing from ABS/CNT nanocomposites, while parts had EMI SE about -12 dB for HC and H45 and -16 dB for PC from hybrid nanocomposites.

Table of contents

Abstract	V
Table of contents.....	VII
List of Figures.....	XII
List of Tables	XXI
List of abbreviation and acronyms.....	XXV
Chapter I	1
Introduction.....	1
Chapter II	3
Background.....	3
2.1 Additive manufacturing (AM).....	3
2.1.1 Main phases of an AM process.....	3
2.1.2 Types of AM processes.....	4
2.2 Fused deposition modelling	7
2.2.1 Filament production by extrusion	8
2.2.2 FDM materials.....	9
2.2.3 FDM processing parameters	10
2.2.4 Limitations and processing problems of FDM	12
2.3 Polymer nanocomposites	13
2.3.1 Graphene-based nanocomposites	16
2.3.1.1 Graphene nanoplatelets	16
2.3.1.2 Properties of graphene-based polymer nanocomposites	17
2.3.2 Carbon nanotubes based nanocomposites	18
2.3.2.1 Carbon nanotubes	18
2.3.2.2 Properties of CNT-based polymer nanocomposites	20
2.4 Development of composites for FDM	23
2.4.1 FDM composites with enhanced mechanical properties	23
2.4.2 FDM composites with enhanced functional properties	25
Chapter III	28
Experimental.....	28
3.1 Materials.....	28
3.1.1 Acrylonitrile-butadiene-styrene (ABS).....	28
3.1.2 Graphene nanoplatelets (GNP).....	29
3.1.3 Carbon nanotubes (CNTs)	31

3.2 Processing and composite preparation	32
3.2.1 Samples designation	32
3.2.2 Compounding	36
3.2.3 Compression moulding (CM)	37
3.2.4 Filament extrusion (E)	38
3.2.5 Fused deposition modelling (FDM)	39
3.3 Testing techniques	45
3.3.1 Microstructural characterizations	45
3.3.1.1 Density measurements	45
3.3.1.2 Melt flow index (MFI)	45
3.3.1.3 Rheological analysis	46
3.3.1.4 Scanning electron microscopy (SEM)	46
3.3.1.5 Transmission Electron Microscopy (TEM).....	46
3.3.1.6 Fourier transform infrared spectroscopy (FTIR)	46
3.3.1.7 X-ray photoelectron spectroscopy (XPS)	46
3.3.1.8 Thermogravimetric analysis (TGA)	47
3.3.1.9 Differential scanning calorimetry (DSC)	47
3.3.2 Mechanical testing	47
3.3.2.1 Quasi-static tensile test.....	47
3.3.2.2 Flexural test	48
3.3.2.3 Dynamic mechanical thermal analysis	48
3.3.2.4 Creep test	49
3.3.2.5 Modelling of tensile modulus	49
3.3.3 Testing of electrical properties	50
3.3.3.1 Electrical resistivity test.....	50
3.3.3.2 Surface temperature evaluation upon voltage application	51
3.3.3.3 Strain monitoring tests	51
3.3.4 Electromagnetic interference shielding effectiveness (EMI SE) test	53
Results and discussions	54
Chapter IV.....	54
ABS-graphene nanoplatelets nanocomposites.....	54
4.1 Characterization of GNP	54
4.2 Selection of ABS matrix	60
4.2.1 Melt flow index	60
4.2.2 FTIR and differential scanning calorimetry	61
4.2.3 Fractography	63

4.2.4 Quasi-tensile tests	64
4.3 ABS-graphene nanocomposites plates	67
4.3.1 Melt flow index	67
4.3.2 Thermal analysis (TGA and DSC).....	68
4.3.3 Electromagnetic interference shielding effectiveness (EMI SE)	74
4.3.4 Quasi-static tensile tests	81
4.3.5 Modelling of tensile modulus.....	84
4.3.6 Fractography	87
4.4 Fused deposition modelling with ABS-graphene nanocomposites	91
4.4.1 Selection of GNP content.....	91
4.4.2 Filament extrusion.....	92
4.4.3 Preliminary study on FDM process (flexural test)	93
4.4.4 Scanning electron microscopy	97
4.4.5 Differential scanning calorimetry	99
4.4.6 Quasi-static tensile tests	101
4.4.7 Dynamic mechanical response and coefficient of thermal expansion ...	103
4.4.8 Creep stability	109
4.5 Summary on ABS-graphene nanocomposites	111
Chapter V.....	113
ABS-carbon nanotubes nanocomposites	113
5.1 Characterization of carbon nanotubes	114
5.2 ABS-carbon nanotubes nanocomposites plates	116
5.2.1 Compounding and morphology	116
5.2.2 Differential scanning calorimetry	118
5.2.3 Quasi-static tensile test	119
5.3 ABS-carbon nanotubes nanocomposites filaments	120
5.3.1 Filament extrusion and melt flow index	120
5.3.2 Bulk density	123
5.3.3 Morphological analyses.....	124
5.3.4 Thermal degradation behaviour	125
5.3.5 Differential scanning calorimetry	128
5.3.6 Quasi-static tensile test	129
5.3.7 Dynamic mechanical response and coefficient of thermal expansion ...	130
5.3.8 Creep stability	134
5.4 Fused deposition modelling with ABS-carbon nanotubes nanocomposites.....	136

5.4.1 Morphological analyses.....	136
5.4.2 Thermal degradation behaviour	137
5.4.3 Differential scanning calorimetry	139
5.4.4 Mechanical behaviour	140
5.4.4.1 Quasi-static tensile test.....	140
5.4.4.2 Fracture mechanism	141
5.4.5 Dynamic mechanical response and coefficient of thermal expansion ...	144
5.4.6 Creep stability	149
5.5 Electrical properties of ABS-carbon nanotubes nanocomposites	150
5.5.1 Electrical resistivity.....	150
5.5.2 Surface temperature under applied voltage.....	157
5.5.3 Strain monitoring	164
5.5.3.1 Tensile fracture	164
5.5.3.2 Ramp strain	166
5.5.3.3 Cyclic strain	167
5.5.3.4 Creep mode	173
5.6 Summary ABS-carbon nanotubes nanocomposites.....	174
Chapter VI.....	176
Comparative study of graphene and carbon nanotube filled ABS nanocomposites plates.....	176
6.1 Morphology.....	176
6.2 Melt flow index	178
6.3 Quasi-static tensile test.....	180
6.4 Creep stability	184
6.5 Electrical resistivity	190
6.6 Summary of a comparative study of graphene and carbon nanotube nanocomposites compression molded plates.....	195
Chapter VII.....	196
ABS-graphene-carbon nanotubes hybrid nanocomposites	196
7.1 ABS-graphene-carbon nanotubes hybrid nanocomposites compression molded plates	196
7.1.1 Compounding and morphology	196
7.1.2 Quasi-static tensile test	198
7.1.3 Electrical resistivity.....	200
7.1.4 Electromagnetic interference shielding effectiveness (EMI SE)	201

List of Figures

Figure 2.1-1. Additive manufacturing (AM) process flow [24].....	3
Figure 2.1-2. The evolution of 3D printing techniques: resolutions and compatible materials [25].	5
Figure 2.2-1. The scheme of FDM process includes a movable platform (1); a feedstock filament (2); feeding rolls (3) that press the yarn through a heated die (4) with a supportive structure (5) [26].	7
Figure 2.2-2. The basic component of an extrusion process [27].	8
Figure 2.2-3. Cross-section of single-screw and twin-screws extruder barrel.....	8
Figure 2.2-4. Scheme of types of extrusion screw.	9
Figure 2.2-5. Cause and effect diagram of FDM process parameters [40].	11
Figure 2.2-6. FDM parameters: (a) Build orientations, (b) layer thickness, and (c) FDM tool path parameters [40].	12
Figure 2.2-7. Failure during FDM process [41].	13
Figure 2.3-1. Three categories of nanofillers based on particle geometry [42].	14
Figure 2.3-2. Schematic representation of the degree of dispersion and distribution of particles in a polymer matrix: (a) good dispersion, poor distribution, (b) poor dispersion, good distribution, (c) poor dispersion, poor distribution, (d) good dispersion, good distribution [43].	14
Figure 2.3-3. Collision behaviour of (a) charged particles and (b) uncharged particles [88].	15
Figure 2.3-4. The proposed interaction scheme of coupling between carbon fibre and LDPE matrix [47].	16
Figure 2.3-5. Graphene nanomaterials based on physical structure: (A) Single layer graphene, (B) double-layer graphene, (C) few-layer graphene and (D) graphene platelets [48].	16
Figure 2.3-6. Graphene and carbon nanotubes: (A) single wall carbon nanotube (SWCNT) and (B) multi-wall carbon nanotube (MWCNT) structures [72]......	18
Figure 2.3-7. The conductivity of polymer composites as a function of filler concentration [87].	21
Figure 2.3-8. A conductive path in a composite with filamentary additives [88].	22
Figure 2.3-9. EMI shielding concepts for a slab of conductive nanocomposite (a) wave propagation and reflection (b) definition of incoming, reflected and transmitted power for shielding effectiveness SE (c) configuration for the definition of reflectivity (R) [93].	23
Figure 2.4-1. Effect of fiber content and preparation process on (a) tensile strength, and (b) modulus, of ABS/CF composites[11].	24
Figure 2.4-2. SEM image of (a, b) pure ABS FDM printed, (c) 10 wt% carbon fiber (CF) loaded FDM parted, (d) 10 wt% CF load compression-moulded ABS/CF composites [11].	24
Figure 2.4-3. Mechanical properties of the (1) ABS(injection moulding), (2) ABS, (3) ABS/SiO ₂ , (4) ABS/MMT, (5) ABS/MWCNTs, and (6) ABS/CaCO ₃ nanocomposites fabricated by FDM [110].	25
Figure 2.4-4. Thermal conductivity and tensile modulus of CF/PA12 in two different directions [30].	26

Figure 2.4-5. Various examples of 3D nanocomposite macro- and microstructures manufactured using different 3D printing technologies for a wide range of domains such as MEMS, microfluidics, engineered materials and composites, microelectronics and telecommunications [25].....	27
Figure 3.1-1. Chemical representation of acrylonitrile–butadiene–styrene (ABS) polymer macromolecule.	28
Figure 3.1-2. SEM image of graphene nanoplatelets: (a) M5, (b) C300, (c) C500 and (d) C750.....	30
Figure 3.1-3. TEM image of NC7000™ carbon nanotubes.	32
Figure 3.2-1. Examples of notation for compression moulding (CM) materials.	32
Figure 3.2-2. Examples of notation for filament (a), and 3D-printed materials (b) ..	33
Figure 3.2-3. Photographs of (a) Haake® internal mixer, (b) its mixing chamber, and (c) Piovan grinder Model RN 166.	36
Figure 3.2-4. Torque recorded during compounding for neat ABS (F), graphene nanocomposites (F-M5-6) and carbon nanotubes composite (F-CNT-6).	37
Figure 3.2-5. Carver® hot plates press.	37
Figure 3.2-6. Photographs of (a) twin screw extruder Thermo Haake PTW16, (b) view inside of the extruder, (c) take-off unit Thermo Electron Type 002-5341, and (d) extrusion process with cooling fans.	38
Figure 3.2-7. Photographs of 3D printer Next Generation sharebot (a) standard commercial and (b) prototype high-temperature 3D-printer.	40
Figure 3.2-8. Schematic of 3D-printed dumbbell and parallelepiped specimens at different orientations: (a) and (d) horizontal (H); (b) and (e) vertical (V); (c) and (f) perpendicular (P).	41
Figure 3.2-9. 3D samples along horizontal build orientation with different raster angle and infill density of ABS-graphene nanocomposites (L-M5-4) for the flexural test.	42
Figure 3.3-1. Experimental setup for the strain monitoring: (a) Specimens after conductive paint; (b) Schematic of experimental setup; (c) Actual setup for testing.	52
Figure 4.1-1. FESEM images of graphene nanoplatelets: (a) M5, (b) C300, (c) C500 and (d) C750.	55
Figure 4.1-2. XPS spectra of GNP-M5 (1), C300 (2), C500 (3) and C750 (4): a) XPS survey, b) the oxygen core level, and c) the sulfur core level.	57
Figure 4.1-3. Oxygen content associated with the ether/alcohol groups as a function to the surface area of graphene nanoplatelets.	58
Figure 4.1-4. TGA curve of different types of graphene nanoplatelets performed in air atmosphere: (a) mass loss and (b) derivative of mass loss.	60
Figure 4.2-1. Melt flow index of two different types of neat ABS (L and F) and its relative nanocomposites as a function of graphene M5.	61
Figure 4.2-2. FTIR spectra of two types of neat ABS and ABS graphene M5 composites with 8 wt%.	62
Figure 4.2-3. The heating-cooling-heating cycle of DSC thermograms of two neat ABS with (L) and without (F) mold lubricant.	63
Figure 4.2-4. FESEM image of the fracture surface of (a) L-M5-8 and (b) F-M5-8.	64

Figure 4.2-5. Tensile mechanical properties of GNP-M5 nanocomposite with two different kind of ABS resins (L and F): (a) elastic modulus, (b) tensile strength, and (c) strain at break (c)	65
Figure 4.2-6. Improvement of normalized modulus of ABS composites according to Eq. (4.2-1) after incorporation of GNP-M5 into different ABS matrix.	66
Figure 4.3-1. Melt flow index (220°C /10kg) of ABS nanocomposites as a function of GNPs.....	68
Figure 4.3-2. Selected TGA data obtained on neat and nanofilled ABS-graphene performed under a nitrogen atmosphere: (a) mass loss curves, (b) derivative of mass loss curves, and (c) relative residual values at 600°C.....	70
Figure 4.3-3. DSC thermograms (first heating scan) of neat ABS and nanocomposites at different content of M5 (a), C300 (b), C500 (c) and C750 (d) graphene nanoplatelets.	72
Figure 4.3-4. Normalized melting heat (from second DSC heating) of mould lubricant as a function of surface area and content of GNP nanoplatelets in ABS nanocomposites.	73
Figure 4.3-5. Representative curves of EMI SE of nanocomposites containing different types of graphene nanoplatelets: (a) L-M5, (b) L-C300, (c) L-C500 and (d) L-C750.	76
Figure 4.3-6. Influence of absorption and reflection mechanisms on the EMI SE of nanocomposites containing different graphene nanoplatelets: (a) L-M5, (b) L-C300, (c) L-C500 and (d) L-C750, with various fillers contents.	79
Figure 4.3-7. Absorption (a) and reflection (b) of ABS nanocomposites as a function of surface area and content of GNP nanoplatelets.	80
Figure 4.3-8. Relative electromagnetic shield vs relative resistivity of GNP-ABS composite at 8 wt% of M5 and Series C.	81
Figure 4.3-9. Improvement of normalized modulus of ABS composites according to Eq. (4.2-1) after incorporation of different carbonaceous fillers, such as carbon black (CB [154]), MWCNTs [77], graphite flakes (GFs) [62], reduced graphene oxide (rGO [153]), graphene [155], and the GNP nanoplatelets M5, C300, C500, and C750 of the present study. ABS composites reinforced with carbon fiber (CF) and produced by injection molding [152], compression molding [11], and additive manufacturing [10, 151] are also reported.	84
Figure 4.3-10. Elastic modulus of nanocomposites with different type of graphene, i.e., a) L-M5, b) L-C300, c) L-C500 and d) L-C750. Continuous and dot lines represent prediction according to Halpin-Tsai models with in-plane and 3D random orientations, respectively.	87
Figure 4.3-11. SEM micrographs of L-M5 (a), L-C300 (b), L-C500 (c), and L-C750 (d) nanocomposites at graphene loading of 8 wt% obtained at increasing magnifications: 1000x (1), 10000x (2) and 50000x (3).	90
Figure 4.4-1. Tensile modulus, tensile strength and melt flow index values for compression moulded neat ABS (L) and ABS-graphene (L-M5) nanocomposites	92
Figure 4.4-2. Flexural stress-strain curve as measured on 3D-printed specimens: (a) neat ABS Sharebot, (b) ABS with mould lubricant (L) and graphene nanocomposites (L-M5-4).....	94

Figure 4.4-3. Flexural test of neat ABS Sharebot, ABS with mould lubricant (L) and its graphene nanocomposites (L-M5-4) as measured on 3D-printed specimens (a) Specific elastic modulus, and (b) specific maximum stress.	97
Figure 4.4-4. Schematic of 3D-printed dumbbell specimens at different orientations: horizontal (HC), vertical (VC) and perpendicular (PC).	98
Figure 4.4-5. SEM micrographs of 3D-printed dumbbell specimens printed from neat ABS, L-HC (a), L-VC (b) and L-PC (c); and from graphene nanocomposites, L-M5-4-HC (d), L-M5-4-VC (e) and L-M5-4-PC (f).	99
Figure 4.4-6. DSC thermograms of neat ABS (L) and nanocomposites. First heating scan (a), cooling scan (b), and second heating scan (c) of CM (compression moulded), E (extruded) and FDM specimens.	100
Figure 4.4-7. Dynamic mechanical thermograms a) storage modulus (E') and b) loss tangent ($\tan\delta$), of neat ABS and nanocomposite samples as measured on compression moulded (CM), filaments (E) and 3D-printed specimens along horizontal orientation (HC).	104
Figure 4.4-8. Dynamic mechanical thermograms a) storage modulus (E') and b) loss factor ($\tan\delta$) of neat ABS and nanocomposite as measured on 3D-printed specimens along different orientations (HC, VC, PC).	105
Figure 4.4-9. Thermal strain of neat ABS and nanocomposite samples as measured on a) compression molded (CM), extruded (E) and 3D-printed specimens along horizontal orientation (HC) and b) along different orientations (HC, VC, PC).	107
Figure 4.4-10. Creep compliance, $D(t)$ at 30°C and 3.9 MPa, of neat ABS and nanocomposites as measured on a) compression molded (CM), extruded (E) and 3D-printed specimens along horizontal orientation (HC) and b) along different orientations (HC, VC, PC).	110
Figure 5.1-1. TEM micrographs of carbon nanotubes particles (CNT).	114
Figure 5.1-2. Density of carbon nanotube measured through a Micromeritics® Accupyc 1330 helium pycnometry (23.0°C) with 10 cm ³ chamber.	115
Figure 5.1-3. TGA curve of carbon nanotubes performed in air atmosphere: mass loss (continuous line) and derivative of mass loss (dot line).	115
Figure 5.2-1. SEM micrographs of ABS/CNT nanocomposite plates with 2 wt% (a, e), 4wt% (b, f), 6 wt% (c, g) and 8 wt% (d, h) of CNT at magnification of 10,000× (left) and 50,000× (right).	117
Figure 5.2-2. DSC thermogram of neat ABS and ABS/ CNT nanocomposites from compression moulding in the heating-cooling-heating cycle.	118
Figure 5.2-3. Representative of the tensile stress-strain curve of ABS and ABS-CNT compression moulding.	119
Figure 5.3-1. Melt flow index (250°C/10 kg) of ABS nanocomposite as a function of CNT.	123
Figure 5.3-2. Experimental density values of ABS-CNT filaments compared to theoretical density and voids fraction (V_v).	124
Figure 5.3-3. SEM micrographs of F-CNT-6-E (left) and F-CNT-8-E (right) filaments at different magnifications (a, d) ×80, (b, e) ×10000 and (c, f) ×50000.	125
Figure 5.3-4. TGA curves of neat and nanofilled ABS filaments under air atmosphere: (a) Residual mass as a function of temperature; (b) Derivative of the mass loss.	126
Figure 5.3-5. The comparison of experimental and theoretical residues of nanocomposites at 475°C and 575°C.	127

Figure 5.3-6. DSC thermogram of neat ABS and its ABS/CNT nanocomposites filaments in the heating-cooling-heating cycle.....	128
Figure 5.3-7. Representative tensile stress-strain curve of ABS filament with an indication of the tensile energy to break (TEB) and the propagation energy (P) from the yield to break point	129
Figure 5.3-8. Tensile stress-strain curve of ABS and ABS-CNT filaments.....	130
Figure 5.3-9. Dynamic mechanical thermograms a) and c) storage modulus (E') and b) loss modulus (E'') of neat ABS and nanocomposite samples as measured on filaments.	132
Figure 5.3-10. Thermal strain of neat ABS and nanocomposite samples as measured on filaments.	134
Figure 5.3-11. Creep compliance, $D(t)$ at 30°C, of neat ABS and nanocomposites as measured on filaments at 3.9 MPa.....	135
Figure 5.4-1. SEM micrographs of 3D-printed dumbbell specimens printed from carbon nanotubes nanocomposites, F-CNT-6-HC (a, b), F-CNT-6-H45 (c, d) and F-CNT-6-PC (e, f).	137
Figure 5.4-2. TGA curves of neat and 6 wt% nanofilled ABS 3D printed samples (HC and PC) under air atmosphere: (a) Residual mass as a function of temperature; (b) Derivative of the mass loss.	138
Figure 5.4-3. DSC thermogram of neat ABS and its ABS/CNT nanocomposites of 3D-printed samples in the heating-cooling-heating cycle.....	139
Figure 5.4-4. Tensile stress-strain curve of ABS and ABS-CNT of 3D-printed samples.	141
Figure 5.4-5. Frozen fracture of cross-section of 3D-printed dumbbells: (a) F-HC, (b) F-H45, (c) F-PC, (d) F-CNT-6-HC, (e) F-CNT-6-H45 and (f) F-CNT-6-PC.	142
Figure 5.4-6. Tensile fracture of cross-section of 3D-printed dumbbells: (a) F-HC, (b) F-H45, (c) F-PC, (d) F-CNT-6-HC, (e) F-CNT-6-H45 and (f) F-CNT-6-PC.	143
Figure 5.4-7. Dynamic mechanical thermograms a) and c) storage modulus (E') and b) loss modulus (E'') of neat ABS and nanocomposite samples as measured on 3D-printed specimens along different orientation (HC, H45, PC).	145
Figure 5.4-8. Reduction of main transition of storage modulus- R (a) and F -factor (b) as function of CNT nanofiller loading measured on filaments and 3D-printed samples (HC, H45 and PC).	147
Figure 5.4-9. Thermal strain of neat ABS and nanocomposite samples as measured on 3D-printed samples along different orientations (HC, H45, and PC).	148
Figure 5.4-10. Creep compliance, $D(t)$ at 30°C, of neat ABS and nanocomposites as measured on 3D-printed samples along different orientations at 3.0 MPa.	149
Figure 5.5-1. Electrical volume resistivity of ABS nanocomposites: compression moulding (a), filaments (b) and 6 wt% CNT filled nanocomposites with different 3D printing (c).	151
Figure 5.5-2. Electrical volume resistivity of ABS/CNT nanocomposites measured on compression moulding (CM) and filament (E) samples at an applied voltage of 5 V.	152
Figure 5.5-3. Evolution of electrical resistivity in ABS nanocomposite plates with a volume concentration (for ϕ_c detail in section 6.5).	153
Figure 5.5-4. Internal features of FDM samples: (a) HC, (b) H45 and (c) PC.	153
Figure 5.5-5. Electrical resistivity of FDM samples as a volume of voids from Figure 5.4-1.....	154

Figure 5.5-6. Summary of preparation of filament plate with the mould 50×50×1.0 mm starting with filaments at 6 and 8 wt% of CNT: (a) before compression and (b) after compression. (c) Schematic of samples at the different angles (0, 45 and 90°) for measuring electrical resistivity (see Figure 5.5-7)	155
Figure 5.5-7. Electrical volume resistivity of ABS 6 wt% and 8 wt% filled nanocomposites of filament plates at different angles (0, 45 and 90°) as a function of the applied voltage of the applied voltage.	156
Figure 5.5-8. (a) the ratio modulus/resistivity reference at 5 V; (b) the ratio modulus/resistivity and CNT content as a function of CNT % for compression moulding (plates), filament, fiber and 3D samples.	157
Figure 5.5-9. Infrared thermal imaging of F-CNT-6 (left) and F-CNT-8 (right) nanocomposites samples under an applied voltage of 12 V.	158
Figure 5.5-10. Infrared thermal imaging of F-CNT-6 (left) and F-CNT-8 (right) nanocomposites samples under an applied voltage of 24 V.	159
Figure 5.5-11. Increment of surface temperature upon a voltage of 12 V (a) and 24 V (b) for ABS/CNT nanocomposites from compression moulding with different CNT content at room temperature of 23°C.	160
Figure 5.5-12. Results of thermal imaging upon voltage application at 24 V at 120 seconds: F-CNT-6-E (a), F-CNT-6-HC (b), F-CNT-6-H45 (c) and F-CNT-6-PC (d).	161
Figure 5.5-13. Increment of surface temperature upon a voltage of 12 V (a) and 24 V (b) for ABS nanocomposites filaments with different CNT loading at room temperature of 23°C.	162
Figure 5.5-14. Increment of surface temperature upon a voltage of 12 V (a) and 24 V (b) for ABS nanocomposites 3D printed samples with 6 wt% CNT content at room temperature of 23°C.	163
Figure 5.5-15. Electrical resistivity change ($\Delta R/R_0$) and stress of 3D-printed F-CNT-6 nanocomposites under applied strain up to fracture: F-CNT-6-HC (a) and F-CNT-6-H45 (b)....	165
Figure 5.5-16. A representative of electrical ($\Delta R/R_0$) and mechanical response of 3D-printed ABS/CNT nanocomposites during loading (full symbol) and unloading (open symbol) under tensile test: F-CNT-6-HC (a) and F-CNT-6-H45 (b).	167
Figure 5.5-17. Piezoresistivity of the F-CNT-6-HC sample : resistance variation during 50 cycles of controlled strain (0.1-0.5%) under tensile loading.	168
Figure 5.5-18. Piezoresistivity of the F-CNT-6-HC sample as function of stress during 50 cycles (a) under tensile loading and detail of the last 10 cycles (b).	169
Figure 5.5-19. Piezoresistivity of the F-CNT-6-H45 sample: resistance variation as function of controlled strain (0.1-0.5%) during 50 cycles under tensile loading.	169
Figure 5.5-20. Piezoresistivity of the F-CNT-6-H45 samples and (a) 50 strain, (b) 50 stress cycles under tensile loading and (c) detail of the last 10 cycles.	170
Figure 5.5-21. Gauge factor of the 6 wt% CNT 3D-printed nanocomposite samples along number of cycle strain of HC and H45.	171
Figure 5.5-22. F-CNT-6-HC sample: (a) before, and (b) after 50 cycles under tensile loading.	172
Figure 5.5-23. F-CNT-6-H45 sample: (a) before, and (b) after 50 cycles under tensile loading.	173

Figure 5.5-24. Creep compliance at a constant load of 20 MPa and $\Delta R/R_0$ for different infill samples: (a) F-CNT-6-HC and (b) F-CNT-6-H45	174
Figure 6.1-1. TEM micrographs of the selected carbonaceous nanoparticles: (a) GNP-M5 and (b) CNT	177
Figure 6.1-2. SEM micrographs of the samples of F-CNT-6 (a, b), F-M5-6 (c, d) and F-M5-30 (e, f).....	178
Figure 6.2-1. Melt flow index of ABS/graphene (full symbol) and ABS/CNT(open symbols) nanocomposites at different temperatures and nanofiller content ...	178
Figure 6.2-2. Melt flow index of graphene (a) and carbon nanotubes (b) nanocomposites as a function of temperature.	180
Figure 6.3-1. Comparison of tensile properties of nanocomposites with ABS/M5 and ABS/CNT: (a) elastic modulus and (b) strength.	182
Figure 6.3-2. Elastic modulus of nanocomposites with ABS/M5 (a) and ABS/CNT (b). Continuous (—) and dash lines (— —) and dot lines (...) represent prediction according to Halpin-Tsai models with parallel, 2D random and 3D random orientation, respectively.....	184
Figure 6.4-1. Creep compliance of graphene (a) and carbon nanotubes (b) nanocomposites at 30°C at 3.9 MPa.....	185
Figure 6.4-2. Comparison of creep compliance of nanocomposites with ABS/M5 and ABS/CNT: (a) elastic (D_{el}) and (b) total D($t=3600$ s).	186
Figure 6.4-3. Creep compliance of F (a), F-M5-6 (b) and F-CNT-6 (c) nanocomposites under applied load of 3.9 MPa at 30-90°C.	188
Figure 6.4-4. Creep compliance of F, F-M5-6, and F-CNT-6 nanocomposites at 3.9 MPa at different temperature range.....	189
Figure 6.5-1. Electrical volume resistivity of ABS/M5 and ABS/CNT nanocomposites. The applied voltage was 5 V or 100 V for samples having resistivity lower or higher than $10^7 \Omega \cdot \text{cm}$, respectively.....	191
Figure 6.5-2. Percolation theory power law fit of ABS/M5 and ABS/CNT nanocomposites.	192
Figure 6.5-3. The combined effect of elastic modulus, melt flow index and resistivity as a function of nanofiller content.....	193
Figure 6.5-4. Comparison of selected properties of ABS/M5 and ABS/CNT nanocomposites as function of nanofiller content (2-8 wt%).....	193
Figure 7.1-1. Melt flow index (220°C/10kg) of ABS/CNT/M5 hybrid nanocomposites.	197
Figure 7.1-2. SEM micrographs of F-M5-3-CNT-3 nanocomposite plates at different magnification of 3,000 \times (a), 20,000 \times (b) and 50,000 \times (c).	198
Figure 7.1-3. Tensile properties of ABS/M5/CNT hybrid nanocomposites: (a) elastic modulus, (b) maximum stress and (c) strain at break.	199
Figure 7.1-4. Electrical volume resistivity of hybrid nanocomposites with total nanofiller of 6 wt% as a function of CNT/M5 relative amount.....	200
Figure 7.1-5. Representative curves of EMI SE of neat ABS, single and hybrid nanocomposites at 6 wt% from compression moulding.	201
Figure 7.1-6. Influence of absorption and reflection mechanisms on the EMI SE of hybrid nanocomposites from compression moulding.	202
Figure 7.1-7. The combined effect of elastic modulus, melt flow index and resistivity as a function of CNT/M5 relative amount of total 6 wt%.	203

Figure 7.1-8. Processability, resistivity, electromagnetic shielding, tensile properties of graphene, carbon nanotubes and hybrid nanocomposites at 6 wt% from compression moulding.....	203
Figure 7.2-1. Complex viscosity as a function of frequency for F-M5-6, F-CNT-6 and F-M5-3-CNT-3 composite plates at (a) 250°C and (b) 280°C.	205
Figure 7.2-2. SEM micrographs of F-M5-3-CNT-3-E nanocomposite filament at different magnification of 100× (a), 1,000× (b), 5,000× (c) and 20,000× (d). ...	206
Figure 7.2-3. SEM micrographs of 3D-printed dumbbell specimens printed from F-M5-3-CNT-3-HC at different magnification of 100× (a), 1000× (b), 5,000× (c) and 20,000× (d).	206
Figure 7.2-4. Electrical volume resistivity: a). F-M5-3-CNT-3 hybrid nanocomposites as a function applied voltage and b). F-M5-6, F-CNT-6 and F-M5-3-CNT-3 at different processing: compression moulding (CM), the filament (E), FDM samples (HC, H45, and PC).	208
Figure 7.2-5. Representative curves of EMI SE of hybrid nanocomposites from compression moulding and FDM process: (a) HC, (b) H45 and (c) PC.	210
Figure 7.2-6. Influence of absorption and reflection mechanisms on the EMI SE of hybrid nanocomposites from FDM process: (a) HC, (b) H45 and (c) PC.	211
Figure 7.2-7. Electromagnetic shield vs resistivity of neat ABS, ABS-M5, ABS-CNT and hybrid nanocomposite at 6 wt%.	212
Figure 9.1-1. Schematic representation of the specimens built along the three build orientation. For each build orientation from the left to the right: first deposited layer, representation of the second layer and, the resulting solid component with proper dimensions.....	218
Figure 9.1-2. Complex viscosity as a function of frequency for ABS/CNT (a) and ABS/CB (b) composites with various filler contents.	220
Figure 9.1-3. Complex viscosity as a function of frequency of hybrid ABS with 3 wt% total filler amount at different fractions.	221
Figure 9.1-4. Photographs of the FDM components: PC (a), H45 (d) and HC (g). Optical microscopy at 100x magnification, PC (b), H45 (e) and HC (h). Optical microscopy at 50x magnification top view of PC (c), H45 (f) and HC (i).	222
Figure 9.1-5. SEM images of cross-section for respective growing directions: PC (a-c), HC (d-f) and H45 (g-h).	222
Figure 9.1-6. D.C. electrical conductivity of the extruded filaments with 3 wt% of nanofillers.	224
Figure 9.1-7. D.C. volume conductivity of ABS carbon-based solid components produced via FDM in three different layer-by-layer growing directions: perpendicular (left graph), horizontal concentric (center graph) and horizontal alternate (right graph).	225
Figure 9.1-8. Total electromagnetic interference shielding effectiveness of ABS carbon-based composites of 3 wt% of nanofillers in three different layer-by-layer growing directions: perpendicular (upper graph), horizontal concentric (middle graph) and horizontal alternate (bottom graph).	227
Figure 9.1-9. Shielding by absorption (a) and by reflection portion (b) of ABS carbon-based composites of 3 wt% of nanofillers in three different layer-by-layer growing directions: perpendicular (upper graph), horizontal concentric (middle graph) and horizontal alternate (bottom graph).	229
Figure 9.1-10. Stress-strain curve of ABS and nanocomposites filaments.	231

Figure 9.1-11. Stress-strain curve of 3D-printed ABS and nanocomposites. Growing direction: HC	232
Figure 9.1-12. Stress-strain curve of 3D-printed ABS and nanocomposites. Growing direction: H45	232
Figure 9.1-13. Stress-strain curve of 3D-printed ABS and nanocomposites. Growing direction: PC	233

List of Tables

Table 2.1-1. Summary of the 3D printing techniques [25].	5
Table 2.2-1. Variations in properties for the ABS range of FDM materials (compiled from Stratasys data sheets) [24].....	10
Table 2.3-1. Summary of three most common methods for CNT synthesis [74]....	19
Table 2.3-2. Theoretical and experimental properties of carbon nanotubes compared with graphene [75].	20
Table 2.3-3. Electromagnetic interference (EMI) shielding of CNT-polymer nanocomposites.	22
Table 3.1-1. Technical datasheet of the ABS Sinkral®L322 and Sinkral®F322 [114].	29
Table 3.1-2. Dimension and density from the producer of graphene nanoplatelets [51].	30
Table 3.1-3. Data from the technical datasheet of graphene nanoplatelets [51].	30
Table 3.1-4. Technical datasheet of NC7000™ carbon nanotubes [115].	31
Table 3.2-1. Materials and processing techniques investigated in this work.	34
Table 3.2-2. Working parameters of twin screw extruder Thermo Haake PTW16... .	39
Table 3.2-3. Feature of Sharebot Next Generation desktop 3D printer.	39
Table 3.2-4. Summary of 3D samples with details of FDM parameters.	41
Table 3.2-5. Filaments used for 3D-printing and processing temperature to manufacture 3D samples.....	42
Table 3.2-6. Dimensions and processing parameters of FDM specimens.	43
Table 4.1-1. Characteristics of as-received graphene nanoplatelets (GNP). Atomic percentage of surface elemental composition and density, as measured by XPS analysis and helium pycnometry, respectively.	58
Table 4.1-2. Results of TGA analysis of graphene nanoplatelets performed under air atmosphere.....	59
Table 4.2-1. Glass transition temperatures of styrene–acrylonitrile phase (T_g), melting temperature (T_m) and enthalpy of fusion of lubricant (ΔH_m) for both types of neat ABS plate from DSC.....	63
Table 4.2-2. Tensile mechanical properties of two different types of ABS nanocomposites (L and F) as a function of GNP-M5 nanoplatelets.....	66
Table 4.2-3. The mould lubricant (ML)/graphene ratio at different graphene content.	67
Table 4.3-1. Results of TGA analysis of neat and nanofilled ABS-graphene performed under nitrogen atmosphere.	70
Table 4.3-2. Glass transition temperatures (T_g) of styrene–acrylonitrile phase, melting temperature (T_m), melting heat (ΔH_m), and relative crystallinity index (RC) of mould lubricant for ABS and relative nanocomposite as measured in DSC analysis... .	73
Table 4.3-3. Volume resistivity and average EMISE of ABS and nanocomposites with 8% wt of GNP.	80
Table 4.3-4. Tensile properties of nanocomposites as a function of different GNP type and content.	83
Table 4.4-1. Processing properties of L-E and L-M5-4-E nanocomposite during extrusion.	93

Table 4.4-2. Flexural parameters of ABS and its nanocomposite as measured on 3D-printed specimens with different orientations	95
Table 4.4-3. Glass transition temperatures of styrene-acrylonitrile phase (T_g), melting temperature (T_m) and enthalpy of fusion of lubricant (ΔH_m) crystallization temperature (T_c) and crystallization enthalpy (ΔH_c) for ABS and relative nanocomposite as determined from DSC tests.....	101
Table 4.4-4. Quasi-static tensile properties of ABS and its nanocomposite as measured on compression moulded (CM), extruded (E) and 3D-printed specimens with different orientations (HC, VC, PC).....	102
Table 4.4-5. Dynamic mechanical properties of neat ABS and its nanocomposites as measured on compression moulded (CM), extruded (E) and 3D-printed specimens with different orientations (HC, VC, PC).....	103
Table 4.4-6. Coefficients of linear thermal expansion (CLTE) and linear thermal deformation (CLTD) of ABS and its nanocomposites in the glassy state as measured on compression moulded (CM), extruded (E) and 3D-printed specimens with different orientations (HC, VC, PC).....	108
Table 4.4-7. Elastic (D_{el}), viscoelastic $D_{ve}(t=3600s)$ and total $D(t=3600s)$ creep compliance at 3600s, and fitting parameters (Eq. (4.4-7)) of ABS and its nanocomposites as measured on compression moulded (CM), extruded (E) and 3D-printed specimens with different orientations (HC, VC, PC).....	110
Table 5.2-1. Designation and formulation of ABS nanocomposites dependence of melt flow index (250°C/10 Kg)	116
Table 5.2-2. Glass transition temperatures (T_g) of neat ABS and resulting nanocomposite plates from DSC tests	118
Table 5.2-3. Tensile properties of ABS-CNT nanocomposites as function of carbon nanotubes (CNT) content	120
Table 5.3-1. Processing parameters of twin screw extruder for the production of ABS and ABS/CNT nanocomposite filaments	122
Table 5.3-2. Bulk density and linear density of ABS and ABS/CNT nanocomposite during filament extrusion and 3D fiber production. Extrusion and 3D printing draw ratio.....	122
Table 5.3-3. TGA data of pure ABS and its nanocomposites in an air atmosphere.	127
Table 5.3-4. Glass transition temperatures of styrene–acrylonitrile phase (T_g) for ABS and relative nanocomposite of filaments from DSC.....	128
Table 5.3-5. Quasi-static tensile properties of ABS and its nanocomposite of filaments (E) and single fiber (f) produced by twin screw and FDM extrusion, respectively.	131
Table 5.3-6. Storage modulus and stiffness loos from DMTA analysis of neat ABS and its nanocomposites as measured on filaments and FDM samples	133
Table 5.3-7. Damping peaks and loss modulus from DMTA analysis of neat ABS and its nanocomposites as measured on filaments and FDM samples	133
Table 5.3-8. Coefficients of linear thermal expansion (CLTE) and linear thermal deformation (CLTD) of ABS and its nanocomposites as measured on filament samples.	134
Table 5.3-9. Creep test of neat ABS and its nanocomposites as measured on filaments and FDM samples.	136

Table 5.4-1. TGA data of pure ABS and its nanocomposites in an air atmosphere.....	139
Table 5.4-2. Glass transition temperatures of styrene–acrylonitrile phase (T_g) for ABS and relative nanocomposite of FDM samples from DSC.....	140
Table 5.4-3. Quasi-static tensile properties of ABS and its nanocomposite of FDM samples.....	141
Table 5.4-4. Storage modulus and stiffness loss from DMTA analysis of neat ABS and its nanocomposites as measured on filaments and FDM samples.....	146
Table 5.4-5. Damping peaks and loss modulus from DMTA analysis of neat ABS and its nanocomposites as measured on filaments and FDM samples.....	146
Table 5.4-6. Coefficients of linear thermal expansion (CLTE) and linear thermal deformation (CLTD) of ABS and its nanocomposites as measured on filament and FDM samples.....	148
Table 5.4-7. Creep test of neat ABS and its nanocomposites as measured on filaments and FDM samples.....	150
Table 5.5-1. Electrical volume resistivity of different kinds of ABS-CNT samples at an applied voltage of 5 V.....	155
Table 5.5-2. Initial resistance values (R_0) of the 3D-printed samples before the application of the stain.....	164
Table 5.5-3. Gauge factor of ABS/CNT 3D-printed samples at different infill pattern.....	165
Table 5.5-4. Gauge factor of ABS/CNT 3D-printed samples at different infill pattern.....	166
Table 5.5-5. Selected values of gauge factor of ABS/CNT 3D-printed samples ..	171
Table 6.2-1. Melt flow index and activation energy for neat ABS and carbon nanotubes and graphene nanocomposites.....	179
Table 6.3-1. Comparison of the tensile properties of ABS/CNT and ABS/M5 nanocomposites.....	181
Table 6.4-1. Creep compliance data of ABS-graphene and ABS-CNT nanocomposites according E.q (5.3-8)	187
Table 6.4-2. Creep compliance data of ABS-graphene and ABS-CNT nanocomposites according E.q (5.3-8)	189
Table 6.4-3. The activation energy for the creep process	190
Table 6.5-1. Summary of the main properties of ABS matrix and its composites with GNP-M5 and CNT nanofillers. The values at 2 wt% and 8 wt% are reported..	194
Table 7.1-1. Designation and formulation of ABS/CNT/M5 hybrid nanocomposites dependence of melt flow index (220°C/10 Kg).....	196
Table 7.1-2. Tensile properties of ABS/M5/CNT hybrid nanocomposites	198
Table 7.1-3. Electrical volume resistivity of ABS /M5/CNT hybrid nanocomposites with 6 wt% of nanofillers at an applied voltage of 5 V	200
Table 7.1-4. The summary of properties graphene-CNT hybrid nanocomposites..	202
Table 7.2-1. Quasi-static tensile properties of ABS and its nanocomposite of filaments (E) and FDM samples (HC, H45, and PC)	207
Table 7.2-2. Comparison of selected properties of ABS nanocomposites studied in this research with respect to other carbon-based engineering polymers.....	213
Table 9.1-1. Nanocomposites formulations used in the preparation of FDM specimens.....	217

Table 9.1-2. Density of the carbonaceous fillers, polymer nanocomposites volume fraction, density and voids fraction	219
Table 9.1-3. Electrical conductivity (σ) of extruded filaments and the specimens obtained via FDM with 3 wt% of nanofillers.....	226
Table 9.1-4. Total EMI SE, shielding effectiveness by reflection (SE_R) and shielding effectiveness by absorption (SE_A) at the frequency range of 8 to 12 GHz of neat ABS and carbon-based nanocomposites	230
Table 9.1-5. Quasi-static tensile properties of ABS and its nanocomposite of filaments.	231
Table 9.1-6. Quasi-static tensile properties of ABS and its nanocomposite of 3D samples	233

List of abbreviation and acronyms

ADR	Apparent draw ratio
AM	Additive manufacturing
CAD	Computer-aided design
CaCO₃	Calcium carbonate
CB	Carbon black
CF	Carbon fibres
DR	Effective draw ratio
ESD	Electrostatic discharge
GO	Graphene oxide
K	Potassium
ABS	Acrylonitrile-butadiene-styrene
CAD	Computer-aided design
CM	Compression molding
CNT	Carbon nanotubes
CVD	Chemical vapour deposition
DMA	Dynamic mechanical thermal analysis
DS	Die-swelling
DSC	Differential scanning calorimetry analysis
E	Elastic modulus
E'	Storage modulus
E''	Loss modulus
EMI SE	Electromagnetic interference shielding effectiveness EMI SE
FDM	Fused deposition modelling
FESEM	Field emission scanning electron microscope
FTIR	Fourier transform infrared spectroscopy
GIC	Nature graphite
GNP	Graphene nanoplatelets
HNO₃	Nitric acid
MEMS	Microelectromechanical systems
MFI	Melt flow index
MMLR	Maximum mass loss rate
MMT	Montmorillonite
MVR	Melt volume-flow rate
MWCNT	Multi-walled carbon nanotubes
OF_T	Total orientation factor in fiber
P	Propagation energy
PC	Polycarbonate
PCL	Polycaprolactone
PEEK	Polyether ether ketone
PEI	Polyetherimideand
PLA	Polylactic acid
PMMA	Polymethyl methacrylate
PNCs	Polymer nanocomposites
PP	Polypropylene
PS	Polystyrene

PU	Polyurethane
r-GO	Reduced graphene oxide
SAN	Styrene-acrylonitrile
SC-3D printing	Solvent-cast 3D printing
S_D	Cross sectional area of the extrusion die
S_{DE}	Cross-sectional area of the extruder die hole
S_F	Cross-sectional area of the filament
SiO₂	Silica
SLA	Stereolithography
SLS	Selective laser sintering
SWCNT	Single-walled carbon nanotubes
T_c	Crystallization Temperature
TEB	Tensile energy to break
TEM	Transmission electron microscopy
T_g	Glass transition temperature
TGA	Thermogravimetric analysis
T_m	Melting temperature
UV-3D printing	Ultraviolet-assisted 3D printing
V_v	Volume fraction
XPS	X-ray photoelectron spectroscopy
ΔH_c	Crystallization enthalpy
ΔH_m	Enthalpy of fusion of lubricant

Chapter I

Introduction

Additive manufacturing (AM) is a technology of building objects layer-by-layer based on computer-aided design (CAD) [1]. This technology attracts strong interest from both industry and academic for the challenging possibility to build objects with complex shapes and minimal use of harmful chemicals at a reasonable speed [2-5]. Among AM methods, fused deposition modelling (FDM) is one of the most common techniques. In this process, a filament of a thermoplastic polymer is extruded at a temperature above its glass transition or melting temperature through a nozzle and deposited layer-by-layer on a platform to build a tridimensional (3D) object. In fact, the term 3D printing is frequently used to refer to this technology. The most frequently used thermoplastic polymers in FDM are acrylonitrile-butadiene-styrene (ABS), and polylactic acid (PLA) [6-9]. One of the current limitations of this AM technique is related to the limited mechanical properties of the 3D-printed parts [10-12].

Development of composite materials could be a way to improve the mechanical properties of components produced by FDM. In recent years, polymer nanocomposites have attracted attention due to the possibility of improving the properties of host matrices with a small amount of filler. Adding nanomaterials such as carbon nanotubes, nanowires, and nanoparticles to matrices such as polymers, metals, and ceramics via AM has the potential to improve the performance of the resulting components [3, 13]. A quite limited amount of information is available in the open scientific literature on the development of ABS-based micro or nanocomposites for FDM application. In particular, reinforcing materials have been considered in form of spherical particles (such as titanium dioxide [12] or fumed silica [14] or carbon black [15, 16]), microfibers (such as jute fibres [12], short glass fibres [17] and carbon fibres [10, 11]) nanofibers (such as vapour-grown carbon fibres [18]), carbon nanotubes [19-22] and nanoclays [23]. According to the ISI Web of Knowledge database, about 116 papers published in the scientific journal in the period 1980-2018 contain the keywords “nanocomposite” and “3D printing”.

Starting from these considerations, the aim of work was mainly to produce carbon-based nanocomposites through a solvent-free procedure for fused deposition modelling application. The introduction of carbonaceous nanofillers within polymers for FDM may allow an enhancement of their properties (i.e. mechanical and functional), without impairing their processability. Specifically, ABS nanocomposites based on different nanofillers (graphene and carbon nanotubes) were processed through melt compounding and extrusion. To evaluate the effect of nanofillers, the properties of polymeric matrix and nanocomposites were monitored on the samples obtained by compression molding, extruded filament, and FDM-printed parts. To achieve these purpose, different kinds of nanocomposites were considered:

- **ABS-graphene nanocomposites.** In this case nanocomposites were ABS matrix filled with a low amount (2-8 wt%) of graphene nanoplatelets (GNP). Four different types of GNP with the different specific surface area (from 120 up to 750 m²/g) were used (see Chapter IV).
- **ABS-carbon nanotube nanocomposites.** For this purpose carbon nanotubes with an average length of 1.5 µm and a diameter of 9.5 nm were used in the range of 1-8 wt% (see Chapter V).
- **ABS-graphene-carbon nanotube hybrid nanocomposites.** In this case, ABS was reinforced by various mixtures of graphene and carbon nanotubes at a total nanofiller amount of 6 wt % (see Chapter VI and Chapter VII).
- **ABS-carbon black and/ or carbon nanotube nanocomposites.** In this case, ABS was reinforced by various mixtures of carbon black and carbon nanotubes at 3 wt% and 5 wt% (see Chapter IX).

To understand the microstructure and the mechanical properties of the nanocomposites, several techniques were applied. Scanning electron microscopy (SEM) was employed to evaluate the filler dispersion in the matrix and adhesion level. The processability of materials was evaluated through the melt flow test. Calorimetric analysis was carried out to evaluate the effect of the nanofillers on the glass transition temperature of the neat matrix and the thermal stability. The elastic modulus, fracture behaviour was estimated through quasi-static tensile tests, to assess the effect of fillers on the tensile properties. A more detailed analysis on the viscoelastic behaviour of nanocomposites at different temperature, coefficient of thermal expansion and creep compliance was determined by the dynamic mechanical thermal analysis. The electrical behaviour of materials was analysed by electrical resistivity measurements and by evaluation of the Joule's effect and the electromagnetic interference shielding effectiveness (EMI SE) properties of nanocomposites. Additionally, strain monitoring tests were also conducted in which the piezoresistive behaviour of 3D printed parts was.

The main target was to compare the results obtained by compression molding and FDM processes to understand the influence of processing conditions on the material behaviour and finally to assess the influence of selected FDM parameters on the final nanofilled FDM part properties.

Chapter II

Background

2.1 Additive manufacturing (AM)

Additive manufacturing (AM) is defined as a technology capable of joining materials to make objects from 3D model data, usually layer upon layer, as opposed to subtractive manufacturing methodologies. The AM machine reads in data from a digital model and lays down or adds successive layers of liquid, powder, or sheet material, in a layer-upon-layer fashion to fabricate a 3D object. In fact, the term of “3D printing” or “rapid prototyping” are identified as the synonym of additive manufacturing.

AM processes have been developed in more than 20 years and founded applications in aerospace, automotive, biomedical, digital art, architectural design, etc. This technology can offer numerous benefits such as the challenging possibility to build objects with complex shapes, no assembly required for components, fewer materials waste, and minimal use of harmful chemicals at a reasonable speed [2-5].

2.1.1 Main phases of an AM process

All the AM processes share some common operations that are always required for manufacturing of generic products. AM involves a number of steps that move from the virtual CAD concept to resultant physical parts. The process flow chart of additive manufacture is presented in Figure 2.1-1 [24].

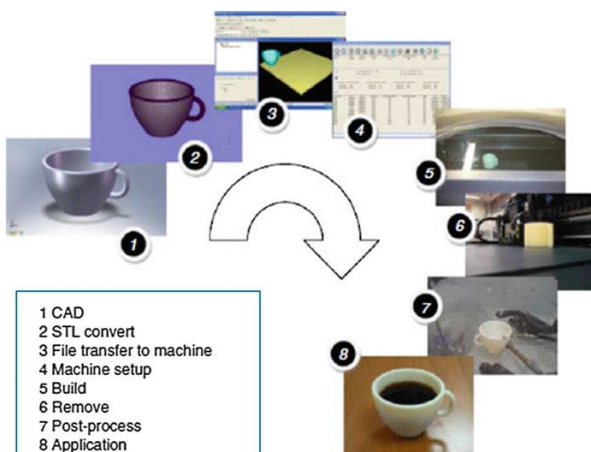


Figure 2.1-1. Additive manufacturing (AM) process flow [24].

- **Step 1-CAD-based 3D model:** For the initial of AM process, a 3D digital model can be obtained by CAD design, available on the internet, or 3D scanning physical objects. CAD-based model is produced in the available software such as Auto-cad or SolidWorks.
- **Step 2-Conversion to STL file:** The 3D model is converted to STL file which describes the external closed surface. Some AM machines accept the STL file format which is export from CAD software.
- **Step 3-Sliced layers and loading to AM machines:** The STL files are used to control the printing process through slicing software (or called CAM software). Some open slicing software are available such as Slic3r, and Cura and non-free CAM software including Kisslicer, Netfabb, and MakerWare. Consequently, from CAM software G-code file is exported and loaded in the AM machine.
- **Step 4-Machine Setup:** Before the build process, the AM machine must be properly set up such as the build parameters like the material constraints, energy source, layer thickness, timings, etc.
- **Step 5-Build:** Following the setting in CAM software, the objects are built layer-by-layer in an automated process. AM machines have different working principals. Depending on the object's size, the machine and the materials used, this process could take hours or even days to complete. Be sure to check the machine periodically to make sure there are no errors.
- **Step 6-Removal:** Remove the printed object (or multiple objects in some cases) from the machine.
- **Step 7-Postprocessing:** Once the 3D-objects are obtained, the post process can be done such as removal of flashes or support structures. Some of AM techniques case the rough surface of parts. Therefore, some surface finishing like mechanical sanding or solvent vapor smoothing operations or painting.
- **Step 8-Application:** After post-processing, printed-parts are ready for use. It should be noted that parts may not behave according to the standard materials specifications from conventional manufacturing approaches (like molding and casting) due to the presence of small voids trapped inside structure parts.

2.1.2 Types of AM processes

There are several AM processes with different capabilities, advantages, and limitations, as summarized in Table 2.1-1. Figure 2.1-2 describes the evolutions of 3D printing techniques concerning the time and resolution and possible materials used.

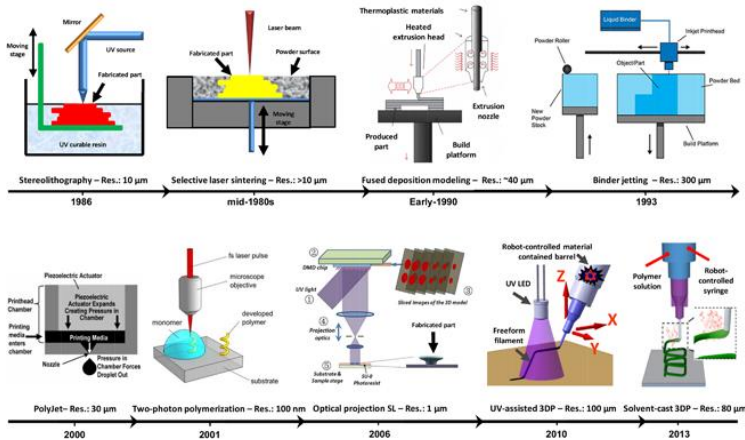


Figure 2.1-2. The evolution of 3D printing techniques: resolutions and compatible materials [25].

Table 2.1-1. Summary of the 3D printing techniques [25].

Technique	Working principle	Compatible materials	Resolution	Printing speed	Some applications
Stereolithography (SLA)	Solidification of photopolymers upon curing under focused UV light	Photopolymers (UV-curable)	≈100 nm	2 mm s ⁻¹	Biomedical applications, tissue engineering
Optical projection SLA	Similar to the SLA, but uses dynamic photomasks (with designed patterns for each layer) which are produced by a digital mirror device	Photopolymers (UV-curable)	Down to 2 μm	Very fast (e.g., 100 layers in ≈10 s)	Detoxification for biomedical applications, flow sensor
Two-photon polymerization (TPP)	Solidification of photopolymers upon curing under focused UV light onto a very small volume	Photopolymers (UV-curable)	< 100 nm	1–10 mm s ⁻¹	Electromagnetic shielding and absorption, biomedical applications
Selective laser sintering (SLS)	Selective fusion of powdered material using a laser	Thermoplastics	< 10 μm	~60 mm s ⁻¹	Tissue engineering, functionally-graded materials
Fused deposition modeling (FDM)	Material extrusion through a heated nozzle	Thermoplastics	≈40 μm	0.1–6 mm s ⁻¹	Customized composites, tissue engineering, electronic sensors
Binder jetting	Selective inkjet printing of a liquid binder over a bed of material powder followed by material solidification	Solutions/Suspensions	Several hundred microns	Typically 2–4 layers per minute	Load bearing bio applications, optics, supercapacitors, water purification
Polyjet	Solidification of an inkjet deposited layer with single or multiple materials using a UV light	Photopolymers (UV-curable)	≈30 μm	10–100 mm s ⁻¹	Strain gauge sensors, flexible electronic devices, supercapacitor, LEDs, sensing, data storage
UV-3D printing	Extrusion and solidification of UV-curable resin upon fast UV curing shortly after exiting the nozzle	Photopolymers (UV-curable)	≈100 μm	0.3–1 mm s ⁻¹	Field effect transistor, sensing applications, MEMS, microelectronics
SC-3D printing	Extrusion through a fine nozzle and solidification of polymer solution upon fast solvent evaporation	Thermoplastic solutions	≈80 μm	0.3–1 mm s ⁻¹	3D sensors for liquid sensing, microelectronics, EMI shielding

- **Stereolithography (SLA):** SLA patented by Chuck Hull in 1986, is a form of 3D-printing technology used a focused UV laser beam to photopolymerize the uncured resin a layer-by-layer. The laser beam is used to solidify the selected thin layer, and then the resin container moves downward or upward to grow another layer. SLA is capable of achieving the high resolution of 100 μm.

- **Selective laser sintering (SLS):** This technique were developed by a team at the University of Texas Austin in mid-1980s. The SLS, which is one of the powder bed 3D printing, uses scanning laser beam (e.g. CO₂ laser) to sinter the powdered materials at the cross-sections. After the first layer is hardened, the powder bed move downward, allowing a new layer of materials apply on the top and the process is repeated until to obtain 3D parts. SLS enable to fabricate with the resolution of around a few tens of microns and the equipment costs a few tens of thousand dollars.
- **Binder jetting:** Binder jetting is also powder bed 3D printing technique, developed by Emanuel Sachs and his team at Massachusetts Institute of Technology in the early 1990s. The binder jetting uses the liquid adhesive to selectively deposit to join powder particles. After the liquid spreading solidification, it is repeated for the next layers until the printing process is complete. This technique has some drawbacks such as the high cost of the powder bed, rough surface finish, and relatively low resolution of the printed parts and post-processing treatment (e.g., thermal sintering or impregnating with another material).
- **Fused deposition modelling (FDM):** The FDM, developed by Scott Crump primarily as a rapid prototyping tool, is the extrusion-based 3D printing technique that utilizes thermoplastics as printing materials. The technique is one of the most popular technologies in the era of 3D printing and is the foundation of most commercial low-cost 3D printers that use thermoplastic spools as feeding materials. The detail of FDM will be described in Section 2.2.
- **PolyJet inkjet printing:** This rapid prototyping process uses ink-jet technology combined with UV curable materials to quickly and economically produce highly detailed and high-precision physical prototypes with a resolution about 30 µm. Similar to an ink-jet printer lays down pigment, the PolyJet print head deposits a small amount of ultraviolet curable materials on build platform to form a single cross-section of the part, while an ultraviolet light attached to the print head simultaneously cures the materials. Once a cross-section is complete, the build platform is lowered to make room for next layer until the end of the printing process.
- **Ultraviolet-assisted 3D printing (UV-3D printing) and solvent-cast 3D printing (SC-3D printing):** These printing processes are among the new-emerging techniques, which deposits the materials directly from continuous filament to build complex 3D features without any support materials. In this UV-3D printing, a dispensing apparatus is capable of moving in three directions (X, Y and Z axe) and a UV laser is employed to solidify an uncured viscous liquid resin in seconds after extrusion. For SC-3D printing, a viscous ink is made by dissolving a polymer in a solvent. The deposited filaments solidify when the

solvent evaporates within a second. The minimum feature size of the structures fabricated by these two techniques is around 100 µm. These techniques enable the fabrication of microstructures with spanning and freeform features.

2.2 Fused deposition modelling

Among AM methods, fused deposition modelling (FDM) is one of the most common techniques. The price of an FDM printer may be as low as a thousand dollars. Due to its low cost and variety of compatible materials, FDM is favourable for research communities, industries, and home users.

This is an extrusion based system, in which a thermoplastic polymer is supplied as a continuous feedstock filament. It is pushed into a heating chamber by a tractor wheel arrangement and it is heated until softening or melting. The extrusion pressure is given by the portion of filament pushed into the chamber that forces the softened material through the nozzle. The extruder head is able to scan on a horizontal plane as well as starting and stopping the flow of material. In addition, the deposition bed can move in the vertical direction. Once a layer is completed, the bed moves the part downwards, so that a further layer can be produced. In order to obtain a flow of material with constant rate and constant cross-section diameter, the extrusion pressure and the travel speed of the nozzle across a depositing surface must remain as constant as possible during all deposition phases.

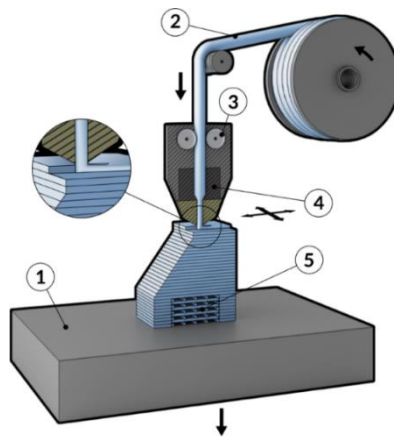


Figure 2.2-1. The scheme of FDM process includes a movable platform (1); a feedstock filament (2); feeding rolls (3) that press the yarn through a heated die (4) with a supportive structure (5) [26].

2.2.1 Filament production by extrusion

The continuous feedstock filaments are usually produced by melt extrusion. Melt extrusion is a manufacturing processing method in which continuous profiles such as sheets, tubes, fibres, and films are formed from a molten plastic mass. During extrusion process, the polymers matrix and additives can be mixed together due to the high shear stress in the extrusion profile. Therefore forces allow the additives to be homogeneously dispersed in the molten polymer. The schematic of extrusion process is presented in Figure 2.2-2 including materials feeder, extruder, die, cooling system (air or/and water).

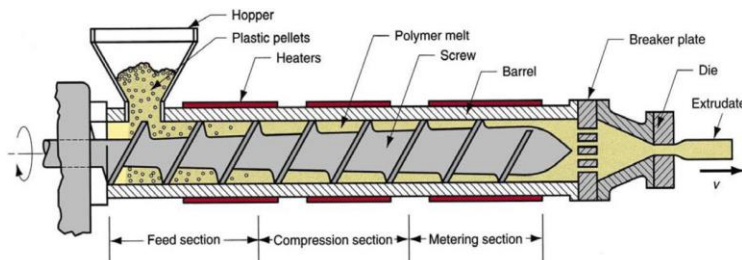


Figure 2.2-2. The basic component of an extrusion process [27].

The melting extrusion process is performed by using an extruder that transports material down the barrel. There are two types of extruders: single-screw and twin-screws as described in Figure 2.2-3. The main regions can be generally identified in extrusion screws: solids conveying, melt and melt pumping.

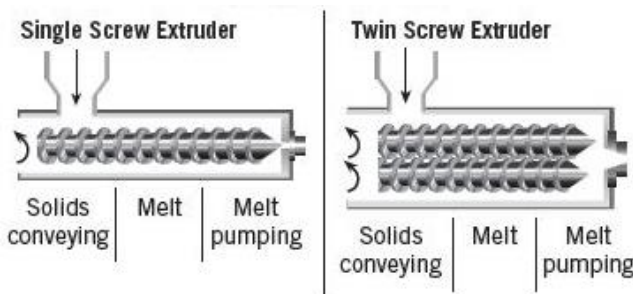


Figure 2.2-3. Cross-section of single-screw and twin-screws extruder barrel.

- **Solids conveying** (feeding zone) - in this zone, materials are filled into hopper and fall by gravity into the heated cylinder when the screw of extruder begins to

- rotate. The height of the threads of the screw is high and constant, and the granules occupy a very high volume due to high voids.
- **Melting zone** (compression zone) - in this zone, the molten polymer is transported and compressed. Due to the heat exchange with the walls, the polymers melt. In order to compress the polymers in this zone, the screw thread is designed to be lower and higher of the core screw. Therefore, internal pressure increases, and cavities and presented gas may be eliminated.
 - **Melt pumping zone** (metering zone) – in this zone the molten polymer through the die is pushed by internal pressure. Similar to the feeding zone, the thread screw is constant throughout this zone.

Single-screw extruders are usually used for the conventional polymer, whereas twin-screws extruders are mostly employed for melt-mixing of polymers and additives such as pigments, reinforcements and fillers. To obtain good materials dispersion, the twin-screws extruder is favoured because of the homogeneous and consistent mixing. In this type of extruder, materials melt in the barrels due to the frictional heating and undergo the shearing introduced between two rotating screws and between screws and the wall of the barrels. In addition, some advantages of twin-screws over single-screw extruders are high capacity, short time residence, facility in cleaning, and the possibility to work with thermally sensible materials [28].

The screws of twin-screws extruder can be counter-rotating (Figure 2.2-4a) or co-rotating (Figure 2.2-4b). The counter-rotating screw is usually used for the profiles extrusion, while the co-rotating screw is usually suitable for the mixing process [29].

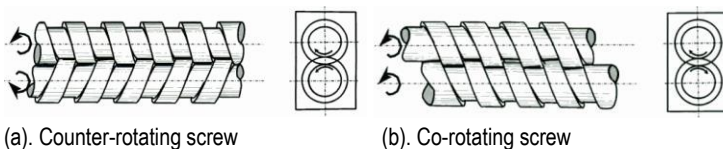


Figure 2.2-4. Scheme of types of extrusion screw.

2.2.2 FDM materials

The most frequently materials used in FDM are thermoplastic polymers such as acrylonitrile-butadiene-styrene (ABS) and polylactic acid (PLA), but also polycarbonate (PC) [6], polyamide (PA) [30], polystyrene (PS) [31], polyurethane (TPU), polypropylene (PP) and polycaprolactone (PCL) [7-9] have been considered [6-9]. Single, double, or even triple-head 3D printing machines have been used with different polymers in order to modulate the properties, as described by Leigh et al. [15] with ABS, PLA and PCL. High-temperature resistance thermoplastics such as

Polyetherimide (PEI) and polyether ether ketone (PEEK) are also being adapted for the FDM printing process [32-34].

Among the materials used in FDM process, ABS is the most popular because it has a good properties profile characterized by high rigidity and strength, easy processing characteristics, chemical resistance, dimensional stability, and good surface finishing. This thermoplastic polymer has been used for various applications in the automotive sector, electronic devices, domestic appliances, etc. [3, 35-39]. The properties of ABS materials and ABS blend, which are widely used by the company Stratasys, the inventor of FDM process, are described in Table 2.2-1.

Table 2.2-1. Variations in properties for the ABS range of FDM materials (compiled from Stratasys data sheets) [24].

Property	ABS	ABSi	ABSplus	ABS/PC
Tensile strength (MPa)	22	37	36	34.8
Tensile modulus (MPa)	1,627	1,915	2,265	1,827
Elongation (%)	6	3.1	4	4.3
Flexural strength (MPa)	41	61	52	50
Flexural modulus (MPa)	1,834	1,820	2,198	1,863
IZOD impact (J/m^2)	106.78	101.4	96	123
Heat deflection at 66 psi ($^{\circ}C$)	90	87	96	110
Heat deflection at 264 psi ($^{\circ}C$)	76	73	82	96
Thermal expansion (in./in./F)	5.60E – 05	6.7E – 6	4.90E – 05	4.10E – 5
Specific gravity	1.05	1.08	1.04	1.2

2.2.3 FDM processing parameters

FDM is a complicated process containing a large number of parameters. These parameters will influence the part quality and materials properties (e.g. mechanical properties). FDM rapid prototyping technology can potentially deliver good part quality, high productivity rate, safety, low manufacturing cost and short lead time. In order to reach such objectives, proper process parameters must be assessed.

The main parameters that can affect the proprieties and quality of FDM products are shown in Figure 2.2-5.

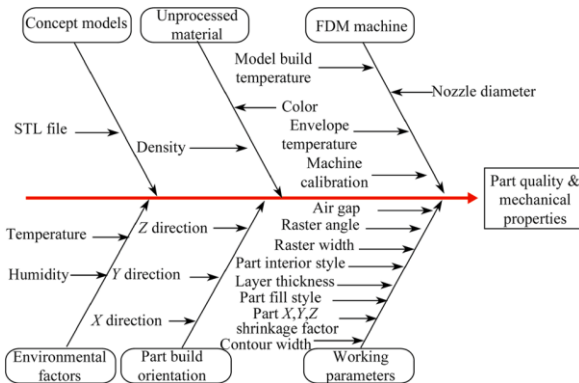


Figure 2.2-5. Cause and effect diagram of FDM process parameters [40].

Specifically, main working parameters in FDM process are shown in Figure 2.2-6, and these parameters are also described as following [40]:

- *Build orientation*: the direction in which the part is grown inside the build platform with respect to X, Y, Z axes, as shown in Figure 2.2-6a.
- *Layer thickness (or height)*: the thickness of the layer deposited through printing nozzle (see Figure 2.2-6b). The value of layer thickness depends on the extruded materials and size of nozzle, usually in the range of 0.1 -0.4 mm.
- *Air gap (or infill density)*: the gap between adjacent raster tool paths at the same layer as presented in Figure 2.2-6c.
- *Raster angle*: the angle of the raster tool paths with respect to the X-axis on the XY part layer. The typical raster angles from 0° to 90° are used.
- *Raster width*: the width of the material deposited raster which depends on nozzle size. Usually, larger of raster width provides a stronger interior, while smaller one consumes less production time and materials.
- *Contour width*: similar to raster width, the width of contour tool path.
- *Number of contours*: number build around inner part curves, as shown in Figure 2.2-6c. The more number of contours may improve perimeter part walls.
- *Contour to contour air gap*: Similar to the air gap, the gap between contours when the multiple contours are used.
- *Perimeter to raster air gap*: the gap between the innermost contour and the edge of the raster fill inside of the contour.

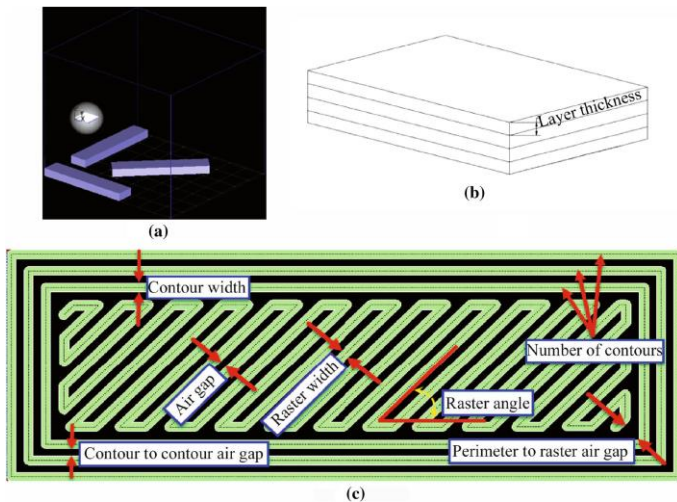


Figure 2.2-6. FDM parameters: (a) Build orientations, (b) layer thickness, and (c) FDM tool path parameters [40].

2.2.4 Limitations and processing problems of FDM

Even if FDM machines meet the demands of many industrial users due to low cost, the disadvantages of this technology include building speed, accuracy, and materials density. For example, the average layer thickness is in the range of 0.1-0.3 mm, and the higher level of resolution (about 0.040 mm) can be only provided by the highly-costing machines at longer build times. Additionally, all nozzles are circular, and therefore it is impossible to draw sharp external corners and a radius equivalent to that of the nozzle will be at any corner or edge. An important design consideration when using FDM is to account for build orientation. The FDM parts usually behave as isotropic in the XY plane, but when deposited microfilaments along with a particular direction preferentially, they behave as anisotropic. Moreover, the strength of FDM parts builds in Z-direction is measurably lower than those in the XY plane. Therefore, it is preferable to grow the parts, which the major stress axes along the XY plane rather than in the Z-direction [12, 40].

During FDM process, several types of undesired processing problems could occur such as not extruding at the start, not sticking to the plate form, under-extrusion, over-extrusion, gaps in top layers, string or oozing, overheating, layer shifting, warping, and cracking. Another critical problem during 3D printing, especially for high viscous materials, is nozzle clogging. All those examples are shown in Figure 2.2-7.

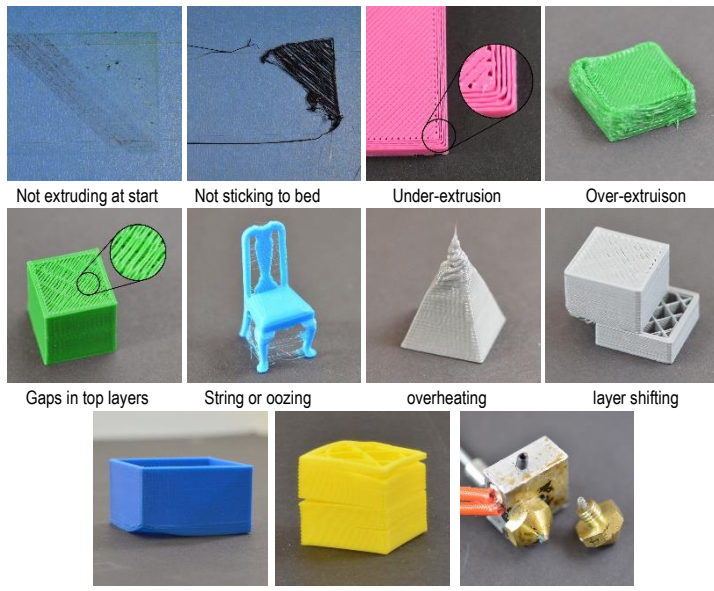


Figure 2.2-7. Failure during FDM process [41].

2.3 Polymer nanocomposites

Polymer nanocomposites (PNCs) have blossomed in both academic and industrial field over the last twenty years due to the remarkable properties of nanostructure materials. Polymer nanocomposites are referred to the polymeric material (i.e. thermoplastic, thermoset, and elastomer) typically consisting one or more nanoscale materials (nanoparticles).

Composites are distinguished by the characteristic size of the inorganic filler particles: (i) traditional composites or micro-composites that contain micrometre-scale fillers and (ii) nanocomposites containing nanometre-scale fillers which having at least a characteristic size less than 100 nm. The nanofillers are generally classified depending on the number of dimensions in the nanometer size (see Figure 2.3-1):

- one nanodimensional filler (1-D) contains layered structural form such as layered silicates, nanoclay, mica, and graphene nanoplatelets.
- two naodimensional filler (2-D) contains rods, tubes and whiskers as, for example, carbon nanotubes, silver nanorods, cellulose nanowhiskers.
- three naodimensional filler (3-D) contains spherical particles like carbon black, silica dioxide and titanium oxide.

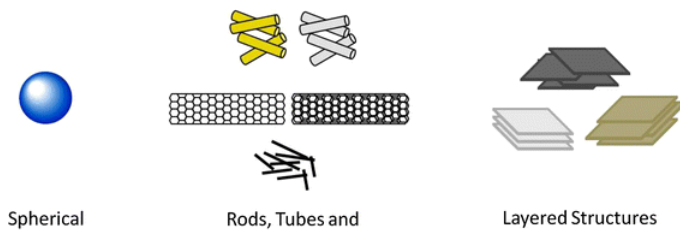


Figure 2.3-1. Three categories of nanofillers based on particle geometry [42].

The nanometric size of the filler provided these nanocomposites with remarkable improvements of mechanical, thermal, optical and physic-chemical properties over the neat polymer. In order to achieve all these positive effects, the dispersion of nanofillers and the filler/matrix adhesion play a dominant role. In fact, the crucial problem in nanocomposite manufacturing is poor dispersion. The possible types of dispersion and distribution of nanofillers in the polymer matrix are shown in Figure 2.3-2.

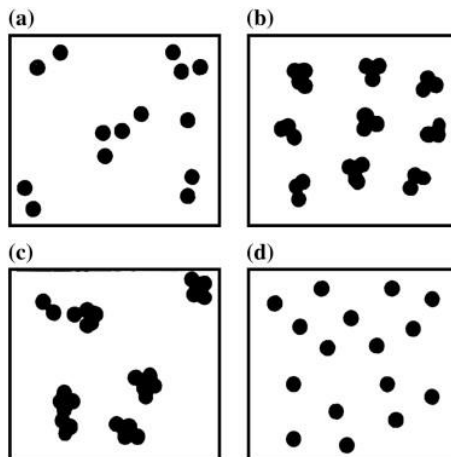


Figure 2.3-2. Schematic representation of the degree of dispersion and distribution of particles in a polymer matrix: (a) good dispersion, poor distribution, (b) poor dispersion, good distribution, (c) poor dispersion, poor distribution, (d) good dispersion, good distribution [43].

In order to obtain a high dispersion degree and good interfacial interaction, the processing techniques were employed such as traditional melt mixing with twin screw

extruder and injection moulding, solution mixing assisted with the aids of sonication and surfactants, in-situ polymerization.

In addition, the dispersion level of nanofillers can be improved by surface treatment of nanofillers to aggregation phenomena within the polymer matrix. Due to very small size of colloid particle, the surface forces at interface of particle are large, resulting in agglomerates. In order to separate and prevent particles from agglomeration, the particles must hold the sample electrical charge (positive or negative) to produce a force of mutual electrostatic repulsion between adjacent particles, as shown in Figure 2.3-3 [44]. In previous research, various surface treatment methods were applied to nanoparticle to increase functional group including O₂ plasma, nitric acid, nitric acid/sulfuric acid, acid/oxidizer, ozone/heat, UV/ozone, and amine grafting treatment [45, 46]. X-Ray Photoelectron Spectroscopy (XPS) is a common technique to quantify the amount and type of functional groups on the particle surface.

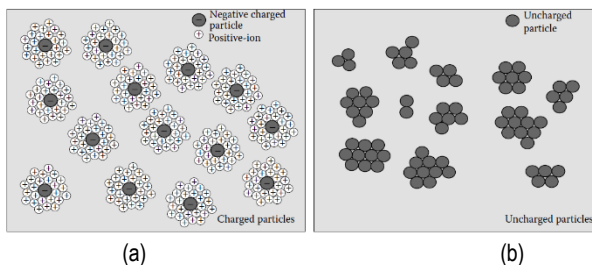


Figure 2.3-3. Collision behaviour of (a) charged particles and (b) uncharged particles [44].

The investigation of the interfacial properties is important for the understanding of the structure/properties relationships governing the mechanical behaviour of polymer nanocomposites [47]. Using a compatibilizer within the polymer matrix and functional nanoparticles could enhance the filler/matrix interface. Organosilane compounds, MA-grafted organic fatty acid derivative, MA grafted petroleum-based polymers (e.g. MA-g-HDPE, MA-g-PP, etc.) are used commonly as coupling agents or compatibilizers. For examples, the possible chemical reactions may include the reactions of the aforementioned -COOH groups of compatibilizers and the -OH groups on surface of oxidized carbon fibre [48]. The interaction scheme of coupling is presented in Figure 2.3-4.

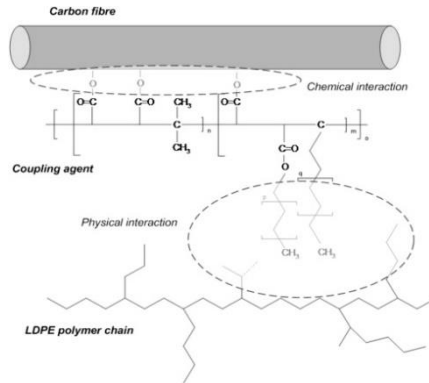


Figure 2.3-4. The proposed interaction scheme of coupling between carbon fibre and LDPE matrix [48].

2.3.1 Graphene-based nanocomposites

2.3.1.1 Graphene nanoplatelets

Graphene nanoplatelets are based on flake-like carbon form ranging from single-layer graphene to a variety of related materials changing by layer number, lateral dimension, and chemical modification. Platelets in the graphene family can be classified based on the physical structure and chemical modification [49]:

- For the physical structure, graphene materials are distinguished by number of layer (see Figure 2.3-5): single-layer graphene, double-layer, called few-layer graphene (few than 10 graphene layers) and multi-layer graphene or graphene nanoplatelets (10-100 graphene layer).
- Depending on the chemical modification, graphene can be either defined as pristine graphene, graphene oxide, reduced graphene oxide or functionalized graphene.

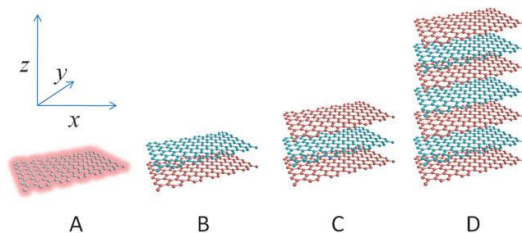


Figure 2.3-5. Graphene nanomaterials based on physical structure: (A) Single layer graphene, (B) double-layer graphene, (C) few-layer graphene and (D) graphene platelets [49].

In this project, graphene nanoplatelets (GNP) have been used. Graphene nanoplatelets can be synthesized through chemical vapor depositions and discharging methods, but the common approaches are mechanical milling and graphite intercalation chemistry [50]. Mechanical milling is a top-down technique by breaking down the Van de Waals of bulk graphite. However, these approaches have the drawback of large particle size and broad particle size distribution.

Graphene nanoplatelets (GNP) are a type of graphitic nanofillers composed of the stacked 2D graphene sheet. The stacked layers are bonded to each other by weak Van der Waals forces with a constant interlayer distance of 0.335 nm [51]. The thickness of graphene nanoplatelets is a range from several to dozen nanometers, as compared to their diameter, usually in the microscale, which leads to the high specific surface area of GNPs (with a theoretical value of 2630–2965 m²/g) and high aspect ratios. In comparison with other classic 2D nanofillers, such as nanoclays, GNPs have lower mass density and are highly electrically and thermally conductive, due to the sp² hybridized carbons in the monolayer graphenes within the GNPs. The single graphene also possesses superior mechanical properties with a reported modulus of 1100 GPa and strength of 125 GPa [49], thermal conductivity of 3000 W/mK (in-plane) and 6 W/mK (z-axis), and electrical conductivity 10⁷ S/m (in-plane) and 10² S/m (Z-axis) [51, 52].

2.3.1.2 Properties of graphene-based polymer nanocomposites

Graphene nanoparticles are under investigation as potential reinforcing fillers for polymer-based nanocomposites. This kind of nanofiller has been used as multifunctional reinforcement resulting in superior mechanical, electrical and thermal properties. Therefore, for thermoplastic nanocomposite filled with graphene dramatic enhancements of mechanical properties and thermal stabilities were reported [42, 50, 53-62].

Specifically, some studies on ABS with graphite/graphene as nanofillers were also reported. Pandey et al. [63] also investigated graphite flake-reinforced ABS up to high loading content (40 vol%). At mentioned loading level of filler, flexural modulus and loss modulus were enhanced by 92% and 250%, respectively. On the other hand, the tensile strength and elongation at break were reduced. They also reported an improvement of thermal conductivity of about 250%. Cheol et al. [64] prepared and characterized octadecylamine-graphene (C18-graphene) incorporated with ABS. Homogeneous dispersion of the hybrid graphene filler, resulting in the improvement of thermal and tensile properties. Sachdev et al. [65] reported graphite/ABS through compression molding within electromagnetic interference shielding and conductivity properties. At 15 wt% of graphene, electromagnetic shielding (EMI SE) and conductivity values of -60 dB and 0.166 S/cm were respectively achieved. Ben Difallah et al. [38] reported ABS polymer matrix filled with graphite powder through melt blending. Graphite powder decreased mechanical properties of neat ABS but

improved the friction and wear resistances especially at a filler loading of 7.5 wt%. Chong et al. [66] reported on ABS filled with graphene nanosheet with a low percolation threshold of 0.13 vol% due to the adopted coagulation method. Fawn et al. [67] reported ABS filled virgin graphite and expanded graphite. However, the mechanical properties were not enhanced. Hong et al. [68] reported on ABS/graphene nanocomposites combined with metal hydroxide nanorods with enhanced mechanical and flame retardant properties. Dahiya et al. [69] also reported on ABS filled with graphite which enhances the electrical and dielectric properties at a loading level of 7.6 vol%. Pour et al. [70] reported polycarbonate/ABS polymer blend with graphene nanoplatelets reinforced. One type of GNP with a length of 15 μm was investigated with improvement by 30% and 54% of tensile and flexural modulus at a content of 3 wt%.

2.3.2 Carbon nanotubes based nanocomposites

2.3.2.1 *Carbon nanotubes*

Carbon nanotubes (CNTs) is 2D nanomaterial which is rolled sheets of a hexagonal array of carbon atoms. CNTs were first observed by Baker et al. [71] in the 1970s but were re-discovered by Iijima et al. in 1991 [72]. CNTs have been widely investigated as nanofillers due to their remarkable physical, mechanical and electrical properties.

Carbon nanotubes are defined by the number of concentric walls: single-walled carbon nanotubes (SWCNT) having only single layer of graphitic carbon atoms, and multi-walled carbon nanotubes (MWCNT) with several layers of coaxial carbon tubes, as shown in Figure 2.3-6.

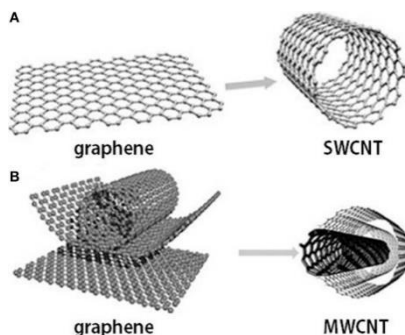


Figure 2.3-6. Graphene and carbon nanotubes: (A) single wall carbon nanotube (SWCNT) and (B) multi-wall carbon nanotube (MWCNT) structures [73].

Several synthesis methods of carbon nanotubes have been used to reach a variety of diameters, aspect ratio, crystallinity, crystalline orientation, purity, and surface chemistry. In particular, CNTs are generally produced by three main techniques: electric arc discharge, laser ablation, and chemical vapor deposition (CVD) [74]. The advantages and disadvantages of each method are summarized in Table 2.3-1.

- *Electric arc discharge*: a vapor is created by an arc discharge between two carbon electrodes. The direct current (~50-120 A) is applied through two high-purity graphite electrodes in a chamber filled with an inert gas (e.g. helium). At the high temperature (approximately 4000 K), graphite fuses, and the matter is torn from one electrode is deposited on another electrode forming nanotubes. By using this method, SWCNT and MWCNT (with the use of metal catalyst) can be produced with an advantage of production of large quantity, but it is difficult to control the alignment of the created nanotubes and impure materials.
- *Laser ablation technique*: a graphite target is vaporized by laser ablation beam in a quartz tube infilled with an inert gas flow in a furnace at temperature 1000-1200°C. This results in soot containing CNTs which are cooled at the walls of a quartz tube. By this method, SWCNT mostly in the form of ropes have been produced. The CNTs formed by this method are higher quality than those produced by the arc discharge method, but the production quantity is low.
- *Chemical vapour deposition (CVD)*: To grow the nanotubes, two gases hydrocarbon and metal catalyst along with inert gas are introduced into the reaction chamber. Carbon atom from vaporous hydrocarbons such as ethylene and acetylene to supply the growth of the nanotubes. The nanotubes grow on the substrate by the decomposition of hydrocarbon while reaction chamber is heated at temperature 700-900°C at the one atmosphere of pressure. CVD is the most promise method due to an economically practical method for large-scale and quite pure CNT production.

Table 2.3-1. Summary of three most common methods for CNT synthesis [75].

Method	Arc discharge	Laser ablation	CVD
Yield rate	>75%	>75%	>75%
SWCNT or MWCNT	Both	Both	Both
Advantages	Simple, inexpensive, high-quality nanotubes	Relative high purity, room-temperature synthesis	Simple, low temperature, high purity, large-scale production, aligned growth possible
Disadvantages	High temperature, purification required, tangle nanotubes	Method limited to the lab scale, crude production	Synthesis CNTs are usually MWCNTs, defects.
		purification required	

Table 2.3-2. Theoretical and experimental properties of carbon nanotubes compared with graphene [76].

Property	CNTs	Graphene
Specific gravity	0.8 g/cm ³ for SWCNT; 1.8 g/cm ³ for MWCNT (theoretical)	2.26 g/cm ³
Elastic modulus	~1 TPa for SWCNT; ~0.3-1 TPa for MWCNT	1 TPa (in-plane)
Strength	50-500 GPa for SWCNT; 10-60 GPa for MWCNT	
Resistivity	5-50 $\mu\Omega\text{cm}$	50 $\mu\Omega\text{cm}$ (in-plane)
Thermal conductivity	3000 W/mK (theoretical)	3000 W/mK (in-plane) 6 W/mK (c-axis)
Magnetic susceptibility	22×10^6 EMU/g (perpendicular with the plane) 0.2×10^6 EMU/g (parallel with plane)	
Thermal expansion	Negligible (theoretical)	-1×10^{-6} (in-plane) 29×10^{-6} (c-axis)
Thermal stability	>700°C (in air); 2800°C (in vacuum)	450-650°C (in air)
Specific surface area	10-20 m ² /g	

CNTs usually have diameters in the range of ~1–50 nm and lengths of many microns [77]. Due to the very small size of CNTs, physical properties of CNTs is relatively more difficult to determine compared to other fillers. However, theoretical and experimental properties of carbon nanotubes have been reported in Table 2.3-2. The CNT also possesses superior mechanical properties with a reported modulus of 1 TPa for SWCNT and 0.3-1 TPa for MWCNT and strength of 50-500 GPa for SWCNT and 10-60 GPa for MWCNT, thermal conductivity 3000 W/mK, and electrical conductivity 5-50 $\mu\Omega\text{.cm}$ [75, 76].

2.3.2.2 Properties of CNT-based polymer nanocomposites

CNT-based polymer nanocomposites have used in real-world applications in different fields including transportation, automotive, aerospace, defence, sporting goods, and energy and infrastructure sectors. In addition, high electrical conductive CNT-based polymer nanocomposites have been used as electrostatic discharge (ESD) and electromagnetic interference (EMI) shielding material, circuits and the conductive coating.

The processing technique determines the dispersion level of CNTs. CNT-based polymer nanocomposites are commonly produced through melt compounding, solution mixing and in-situ polymerization techniques. Among them, the direct melt blending method is more commercially for industrial scale and environmentally friendly.

The addition of particles polymers matrix aim to improve its mechanical properties (i.e. the elastic modulus and tensile strength). By incorporating a small amount of CNT, significant improvement of mechanical properties of the polymer. Jyoti et al. [78] reported that addition of 3 wt% MWCNTs in the ABS by extrusion and

injection molding method, results in 23% and 29% improvements in tensile modulus and tensile strength, respectively. They have also reported an increase of storage modulus (glassy region) by 1.7 times on adding 10 wt% MWCNTs in ABS [79]. Mohammed et al. [80] also found significant improvement in the strength and modulus (72% and 107%) on the addition of 10 wt% MWCNTs in ABS matrix. Homogeneous dispersion and well-embedded of CNTs in polymer matrix had a significant effect on the properties of resulting composites. Lijun et al. [81] reported that anisotropy of PLA/MWCNT nanocomposites by using a twin-screw extrusion, and the strength of nanocomposites at 3 wt% of MWCNTs increased.

Beside good effect of CNT on mechanical properties, electrical properties of CNT-polymer composites were also investigated. Highly conductive electrical properties have been widely reported for CNT-based nanocomposites in the scientific literature [78, 80-84]. The conductivity of CNT-polymer composites depends on properties of CNTs including the type of CNT, aspect ratio, surface functionalization and CNT content. The conductivity of nanocomposites suddenly increases above the critical concentration, transiting the materials from isolated to conductive, as shown in Figure 2.3-7. This critical filler concentration is called electrical percolation threshold concentration. At percolation threshold concentration, filler forms a three-dimensional conductive network within the matrix (see Figure 2.3-8), hence electron can tunnel from one filler to another, and in doing so, and it overcomes the low conductivity caused by the insulating polymer matrix. The intrinsic and aspect ratio of CNT affect the percolation threshold. For example, the higher aspect ratio of CNT, the smaller percolation threshold of CNT in polymer [85]. In addition, Saleh et al. [86] reported carbon nanotube (CNT) dispersed in an ABS matrix was prepared by solution mixing. The good dispersion and selective localization of CNT in the styrene-acrylonitrile (SAN) phase of the ABS matrix allowed to prepare nanocomposites with a percolation threshold of only 0.06 vol%. Brajesh et al. [87] reported that the electric conductivity measurement revealed the electrical percolation threshold at around 0.60 wt % of MWCNT in ABS matrix.

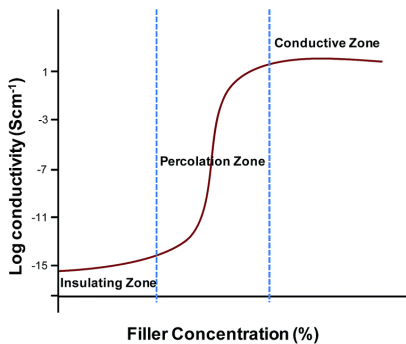


Figure 2.3-7. The conductivity of polymer composites as a function of filler concentration [88].

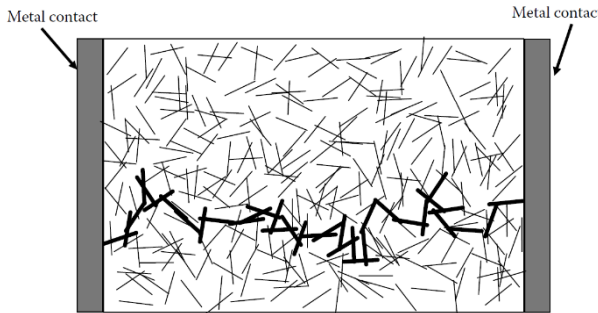


Figure 2.3-8. A conductive path in a composite with filamentary additives [44].

The high electrical conductivity of CNT-based polymer nanocomposites leads to applications in electronics, automotive and aerospace with uses electromagnetic interference (EMI) shielding. Considerable research efforts have been done for the investigation on conducting polymer nanocomposites for EMI shielding materials to substitute the metal-based materials due to light weight, resistance to corrosion and flexibility of processing. By incorporating CNT nanoparticle, remarkable results of EMI SE of nanocomposites have been reported, as shown in Table 2.3-3.

Table 2.3-3. Electromagnetic interference (EMI) shielding of CNT-polymer nanocomposites.

Matrix types	CNT content	EMI SE (-dB)	Reference
Propylene (PP)	7.5 vol%	35	Al-Saleh et al. (2009) [89]
Polystyrene (PS)	7 wt%	20	Yang et al. (2005) [90]
Polyurethane (PU)	20 wt%	17	Lui et al. (2007) [91]
Polymethyl methacrylate (PMMA)	40 wt%	27	Kim et al. (2004) [92]
Acrylonitrile butadiene styrene (ABS)	10 wt%	39	Jyoti et al. (2015) [78]

The EMI SE typically required for commercial application is about -22.0 dB, which corresponds to <1% of the transmitted electromagnetic wave. Three types of EMI shielding mechanisms have been proposed, namely: reflection, absorption and multiple reflections. Some previous studies have shown that in MWCNT/polymer nanocomposites, SE is mainly absorption dominated whereas SWCNT/polymer nanocomposites are mainly reflection dominated material [85]. The application area of EMI shielding materials depends on the dominant shielding mechanism like absorption based EMI shielding materials employed in radar, microwave communication

technology, stealth (self-concealing) technology, microwave darkroom and anti-EMI coating application.

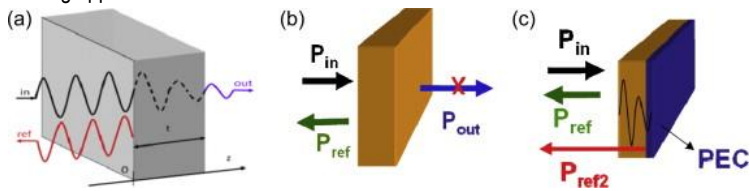


Figure 2.3-9. EMI shielding concepts for a slab of conductive nanocomposite (a) wave propagation and reflection (b) definition of incoming, reflected and transmitted power for shielding effectiveness SE (c) configuration for the definition of reflectivity (R) [93].

2.4 Development of composites for FDM

Development of composites materials for FDM technology has attracted a remarkable interest because incorporated nanoparticles offer the potential to enhance various properties (e.g. mechanical and electrical) of 3D-printed parts. For instance, high-strength products can be applied in aerospace sectors [13, 25, 94]. Moreover, the dispersion of conductive nanoparticles in a polymer matrix makes it possible to produce 3D-printed components for various applications such as electronic sensors [15, 19, 95], cases with good electromagnetic interference (EMI) shielding performances [96], circuits [97] and microbatteries [98].

Over 200 works including few literature review [94, 99, 100] have been done on the composites for FDM. Reinforced materials used are such as titanium dioxide [12], fumed silica [14], jute fibres [12], short glass fibres [17] and carbon fibres [10, 11, 30, 101], vapour-grown carbon fibres [18], carbon nanotubes [19-22, 96, 102, 103] and nanoclays [23], graphene [97, 102, 104, 105], carbon black [15, 16], iron and copper [106].

The incorporation of nanofillers usually increases the viscosity of materials (flowability) that could affect the printability of nanocomposites filament. The viscosity of printing is crucial issue required to choose the mixing strategies in order to obtain the proper dispersion of the nanofillers into the polymer matrix. The most common mixing method is high shear mixing by melt extrusion at the approximate melting point of polymers.

2.4.1 FDM composites with enhanced mechanical properties

The composites in 3D printing process could provide the remarkable mechanical strength and durability that can be used in aerospace, automotive industry, wind energy and similar high material performance demanding industries.

Among reinforcing materials, carbon fibres (CF) lead to the remarkable enhancements of stiffness and strength. For recent examples, Tekinalp et al. [11] reported that 30 wt% CF-ABS composites exhibited significant enhancement 115% and 700% in strength and elastic modulus, respectively, as shown in Figure 2.4-1. They also mentioned the high fiber orientation in the printing direction, and decreased voids between beads (see Figure 2.4-2). Ning et al. [107] incorporated 5 wt% or 7.5 wt% of CF in ABS with enhancements of 22.5% and 30.5% in tensile strength and modulus, respectively. They also indicated that longer CF (150 μm vs 100 μm) provided the better mechanical properties. Guangxin et al. [30] found that the tensile strength and flexural strength of 10 wt% CF/PA12 composites were enhanced by 102% and 251% respectively. Zhong et al. [17] also reported improvement of tensile strength by addition of short glass fibers (10-18 wt%). Continuous carbon fiber reinforced polymers in FDM is also another interesting research area because improvements of mechanical properties are even higher than short fiber. As an example by Li [108], the tensile strength of continuous CF/PLA can reach up to 91 MPa while only 68 MPa for short CF.

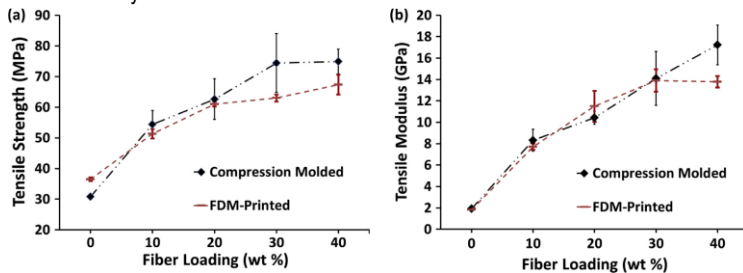


Figure 2.4-1. Effect of fiber content and preparation process on (a) tensile strength, and (b) modulus, of ABS/CF composites[11].

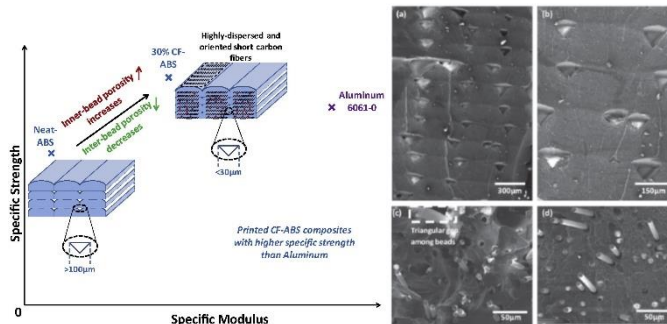


Figure 2.4-2. SEM image of (a, b) pure ABS FDM printed, (c) 10 wt% carbon fiber (CF) loaded FDM printed, (d) 10 wt% CF load compression-moulded ABS/CF composites [11].

Employing nanoparticles in FDM also improves the mechanical properties of 3D-printed parts. For examples, Zhang et al. [97] found the superior mechanical properties of FDM parts by using r-GO/polylactic acid (PLA) of (6wt% r-GO). Wei et al.[104] investigated fully exfoliated GO sheets and ABS were mixed in solution in a solvent (N-methyl-pyrrolidone) up to a concentration of 5.6 wt%. The GO sheets were chemically reduced and the resulting nanocomposites extruded in filaments used to feed an FDM machine. Even if the mechanical properties were not investigated, for the 3D printed samples containing graphene, a very slight decrease of the coefficient of linear thermal expansion (by about 4%) was reported along with a reduction of the loss factor. Angel et al. [12] reported the improved strength and modulus of FDM parts in XYZ (or horizontal build orientation) 13% and 11% by the addition of titanium dioxide in ABS. The inclusion of CNTs increased Young's modulus by 30% at 5% CNT loading in PLA but reduced the tensile strength and overall toughness of the FDM parts by Huseini et al. [109]. Shuna et al. [110] compared the mechanical properties of ABS nanocomposites from injection moulding and FDM. Also, different kinds of incorporated nanoparticles at a fixed 1 wt% of content are used in FDM process including MWCNTs, silica (SiO_2), montmorillonite (MMT) and calcium carbonate (CaCO_3), as shown in Figure 2.4-3.

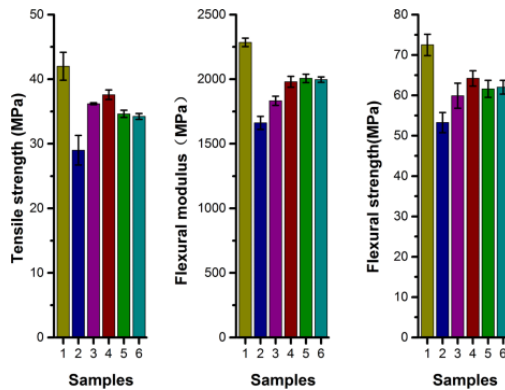


Figure 2.4-3. Mechanical properties of the (1) ABS(injection moulding), (2) ABS, (3) ABS/ SiO_2 , (4) ABS/MMT, (5) ABS/MWCNTs, and (6) ABS/ CaCO_3 nanocomposites fabricated by FDM [110].

2.4.2 FDM composites with enhanced functional properties

Conductive nanoparticles have been used in FDM such as carbon black (CB) [15, 16], graphene oxide (GO) [104, 111], reduced graphene oxide (r-GO) [97], graphene [102, 112] and carbon nanotubes [19, 21, 22, 102, 103]. However, few

studies investigated the production of filament feedstock nanocomposites and FDM products. For example, Zhang et al. [97] reported the resistivity of composites filaments with a diameter of 1.75 mm of r-GO/Polylactic acid (PLA) of $0.21 \Omega \cdot \text{cm}$ (6wt% r-GO). Zhang et al. [16] reported 15 wt% of CB in ABS resistivity of feedstock filaments about $2900 \Omega \cdot \text{cm}$, and they specifically characterized the resistivity of 3D-printed composites by some FDM parameters. Wu et al. dispersed MWCNTs in poly(hydroxyalkanoate to produce feedstock filaments up to 3 wt%, but the resistivity of filaments was not described [103]. Wei et al. [104] were able to 3D-print 5.6 wt% of GO in ABS matrix, but they did not investigate on electrical properties of composites filaments and FDM samples.

Conductive nanocomposites have been intensively used in electromagnetic interference shielding application by adding fillers mostly CNT. The composites for EMI shielding applications have been produced through conventional fabrication method such as solvent cast and melt mixing followed by compression molding. However, there are very few publications about EMI SE from FDM method. For example, only one paper by Chizari et al. [96] reported EMI SE of 20 wt% of CNT/PLA by solution casting 3D printing (SC3D). The specific EMI SE of 3D scaffolds is -37 dB.g⁻¹.cm³ compared -70 dB.g⁻¹.cm³ by hot compression process.

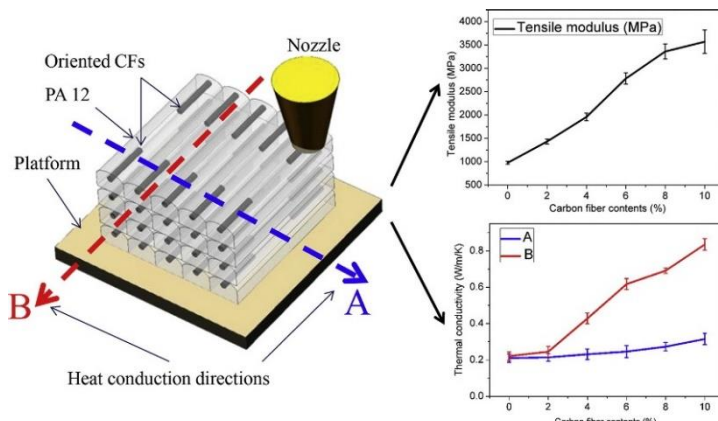


Figure 2.4-4. Thermal conductivity and tensile modulus of CF/PA12 in two different directions [30].

Another interesting property from FDM nanocomposites is thermal conductivity. A remarkable improvement in thermal conductivity of carbon fiber/PA12 composites was shown by Guangxin et al. [30]. Due to the establishment of heat-channel, the thermal conductivity along the printing direction increased from 0.221 W/m/k for pure PA12 to 0.835 W/m/k for CF/PA12 (increase about 277.8%), as shown Figure 2.4-4.

Another study is an investigation of thermal conductivity of metal- particle filled ABS (copper and iron) [106].

3D patterning and complex 3D feather are other benefits offered by 3D printing. The ability to 3D print nanocomposites can be used to optimize the sensors' geometries and to replace the existing 2D sensors with a 3D product showing higher sensing efficiency and more reliable results [19]. In addition, the ability to construct complex 3D features using the new printing nanocomposite materials has been interested by various sectors such as microelectromechanical systems (MEMS), lab-on-a-chip, microfluidics, engineered materials and composites, microelectronics, tissue engineering, and photonics (see Figure 2.4-5) [25].

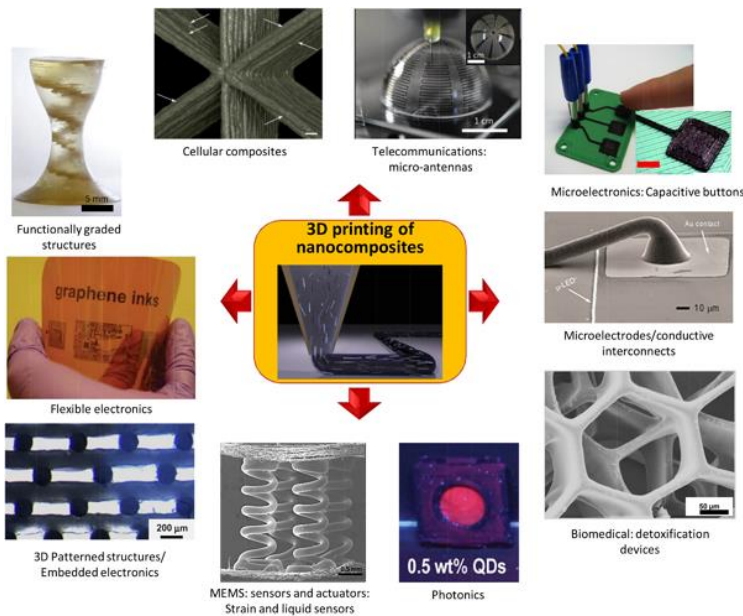


Figure 2.4-5. Various examples of 3D nanocomposite macro- and microstructures manufactured using different 3D printing technologies for a wide range of domains such as MEMS, microfluidics, engineered materials and composites, microelectronics and telecommunications [25].

Chapter III

Experimental

3.1 Materials

This work involved the use of acrylonitrile–butadiene–styrene (ABS) as a matrix and carbon-based particles as nanofillers. Two grades of ABS with different viscosity were used, while two types of carbon-based nanofillers such as graphene nanoplatelets and carbon nanotubes were selected. The following paragraphs are dedicated to present their properties.

3.1.1 Acrylonitrile-butadiene-styrene (ABS)

ABS is produced by a combination of three monomers: acrylonitrile, butadiene, and styrene (see Figure 3.1-1) and its property are controlled by the ratio and distribution of the unique characteristics of each monomer. For instance, acrylonitrile influences the chemical resistance, heat and ageing stability; butadiene promotes toughness, impact resistance and low-temperature properties; styrene contributes in improving the rigidity, glossy surface appearance, and processability. ABS resins contain two phases: a continuous glassy matrix of styrene–acrylonitrile copolymer (SAN), and a rubbery phase (butadiene) within SAN graft. SAN branches are grafted to poly-butadiene backbone thus forming the boundary to continuous glassy SAN matrix. The higher molecular weight of SAN and the higher is its strength. The concentration, size, and distribution of the butadiene particles affect product toughness and impact strength [113].

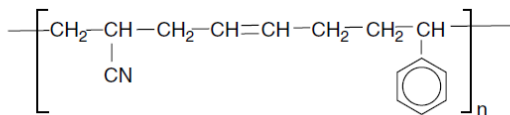


Figure 3.1-1. Chemical representation of acrylonitrile–butadiene–styrene (ABS) polymer macromolecule.

The matrices of the nanocomposites used in this work were two different grades of acrylonitrile–butadiene–styrene (ABS) polymer in the form of white pellets, provided by Versalis S.p.A. (Mantova, Italy) with the tradename Sinkral®L322 and Sinkral®F322. Both ABS are high flow moulding grade for general purpose. According to the producer's technical data sheet, both ABS are characterized by a density of 1.04 g/cm³. The manufacturer reports different viscosity values for the selected ABS

grades. In fact, melt flow index (MFI) values of 26 and 14 cm³/10min (220°C/10 kg) are reported for Sinkral®L322 and Sinkral®F322, respectively. The principal properties of the ABS grades used in this research, according to the producer datasheet, are listed in Table 3.1-1.

Table 3.1-1. Technical datasheet of the ABS Sinkral®L322 and Sinkral®F322 [114].

Properties	Test Standard	ABS®L322	ABS®F322
Melt volume-flow rate, MVR (cm ³ /10min)	ISO 11133 220°C, 10kg	26	14
Density (kg/m ³)	ISO 1183	1040	1040
Mechanical properties			
Tensile Modulus (MPa)	ISO 527-1/-2	2350	2250
Yield stress (MPa)	ISO 527-1/-2	42	44
Yield strain (MPa)	ISO 527-1/-2	3	3
Nominal strain at break (%)	ISO 527-1/-2	12	30
Thermal properties			
Glass transition temperature (°C)	ISO 11357-1/-2	100	107
Temp. of deflection under load,	ISO 75-1/-2 (1.80 MPa)	83	83
Vicat softening temperature,	ISO 306 (50°C/h 50N)	96	102
Coeff. of linear therm. expansion, parallel (E-6/K)	ISO 11359-1/-2	90	90
Electrical properties			
Volume resistivity (ohm.m)	IEC 60093	1E13	1E13
Surface resistivity (ohm)	IEC 60093	1E14	1E14
Rheological calculation properties			
Density of melt (kg/m ³)	ISO Data	960	960
Spec. heat capacity of melt (J/(kg K))	ISO Data	2150	2150
Test specimen production			
Injection Molding, melt temperature (°C)	ISO 294	250	250
Injection Molding, mold temperature (°C)	ISO 10724	60	60
Injection Molding, pressure at hold (MPa)	ISO 294	70	70
Other properties			
Water absorption (%)	Sim. to ISO 62	0.6	0.6
Humidity absorption (%)	Sim. to ISO 62	0.2	0.2

3.1.2 Graphene nanoplatelets (GNP)

Four different grades of graphene nanoplatelets (GNP), namely M5, C300, C500 and C750 with increasing surface area, i.e., 120-150 m²/g, 300 m²/g, 500 m²/g and 750 m²/g, respectively, were purchased from XG Sciences, Lansing, MI, USA.

The data available from the producer on the dimension and density of the nanoplatelets are reported in Table 3.1-2, and the properties are in Table 3.1-3.

Table 3.1-2. Dimension and density from the producer of graphene nanoplatelets [52].

Samples	Surface area (m ² /g)	Lateral dimension (μm)	Thickness (nm)	Density (g/cm ³)
GNP-M5	120-150	~5	6	2.2
GNP-C300	300	1-2	2	2-2.25
GNP-C500	500	1-2	2	2-2.25
GNP-C750	750	1-2	2	2-2.25

Table 3.1-3. Data from the technical datasheet of graphene nanoplatelets [52].

Properties	Parallel surface	Perpendicular surface
Carbon content (%)	>99.5	~5
Thermal Conductivity (W/mK)	3000	6
Thermal Expansion (m/m/K)	4 - 6 × 10 ⁻⁶	0.5-1.0 × 10 ⁻⁶
Tensile Modulus (GPa)	1000	N/A
Tensile Strength (GPa)	5	N/A
Electrical Conductivity (S/m)	10 ⁷	10 ²

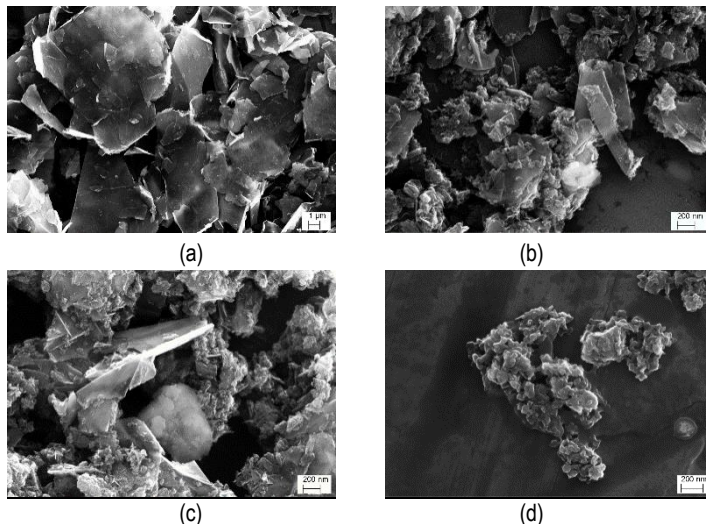


Figure 3.1-2. SEM image of graphene nanoplatelets: (a) M5, (b) C300, (c) C500 and (d) C750.

Graphene nanoplatelets (GNPs) are ultrathin particles with wide aspect ratio which represent a new class of carbon nanoparticles with multifunctional properties. Thanks to the unique size and platelets morphology, GNPs are efficient at providing barrier properties, and their pure graphitic composition makes them excellent electrical and thermal conductors. Potential applications include additive for light weighting composites, barrier material for packaging, conductive additive for battery electrodes, thermally-conductive films and coatings, electrically-conductive inks, etc. [52]. Addition of little amount of GNP can significantly improve the mechanical properties of polymer matrices including stiffness, strength and surface hardness. GNP® graphene nanoplatelets are reported to be compatible with almost all polymers. XG Science has adopted non-oxidizing manufacturing processes which can maintain the pristine graphene surface of sp^2 carbon molecules. Thus, resulting polymer nanocomposites might be suitable for high electrical or thermal conductivity.

3.1.3 Carbon nanotubes (CNTs)

NC7000™ carbon nanotubes are used in various applications, mainly requiring low electrical percolation thresholds such as high-performance electrostatic dissipative plastics or coatings. These nanoparticles can provide high electrical conductivity, good processability, maintaining mechanical properties, the best cost in use ratio, thermal dissipation, etc. [115].

In this work, NC7000™ thin multiwall carbon nanotubes provided by Nanocyl S.A. (Sambreville, Belgium) were used. This carbon nanotube (CNT) are produced via the catalytic chemical vapor deposition (CCVD) process. The technical data sheet reports an average length of 1.5 μm , a diameter of 9.5 nm and a surface area of 250-300 m^2/g . The main features of CNTs used in this work are summarized in Table 3.1-4. Figure 3.1-3 reports a representative TEM image of NC7000™ carbon nanotubes.

Table 3.1-4. Technical datasheet of NC7000™ carbon nanotubes [115].

Properties	Value	Method of measurement
Average diameter (nm)	9.5	Transmission electron microscopy (TEM)
Average length (μm)	1.5	Transmission electron microscopy (TEM)
Carbon purity (%)	90	Thermogravimetric analysis (TGA)
Transition metal oxide	<1%	Inductively coupled plasma mass spectrometry (ICP-MS)
Amorphous carbon	*	High-resolution Transmission Electron Microscopy (HRTEM)
Surface area (m^2/g)	250-300	BET surface area analysis
Volume resistivity ($\Omega \cdot \text{cm}$)	10^{-4}	Internal test method (resistivity on powder)

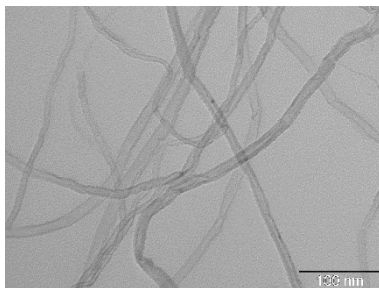


Figure 3.1-3. TEM image of NC7000TM carbon nanotubes.

3.2 Processing and composite preparation

In this work, several types of composites materials were transformed and processed by various techniques. For these reasons, the description of materials composition and composites preparation is described in Samples designation. The samples were produced according to three techniques: (i) melt compounding and compression molding, (ii) melt compounding and filament extrusion, and (iii) fused deposition modelling. A list of notation of materials and processing techniques used in this work is reported in Table 3.2-1.

3.2.1 Samples designation

The sample notation of compression moulding was identified indicating the matrix type, the kind of filler and its amount. For example, a sample L-M5-4 (Figure 3.2-1) indicate the ABS Sinkral@L322 filled 4 wt% of graphene M5 from compression moulding (CM).

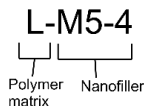
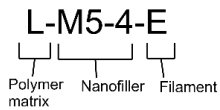
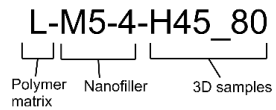


Figure 3.2-1. Examples of notation for compression moulding (CM) materials.

For filaments and FDM products, samples were designated indicating the matrix type, the kind of filler and its amount, and its processing. For example, a sample L-M5-4-E (Figure 3.2-2) indicates the ABS Sinkral@L322 filled 4 wt% of the graphene M5 extruded filament. A sample L-M5-4-H45_80 indicate the same composition of materials by FDM process with horizontal build orientation, raster angle [45°/-45°] and infill of 80%.



(a)



(b)

Figure 3.2-2. Examples of notation for filament (a), and 3D-printed materials (b).

Table 3.2-1. Materials and processing techniques investigated in this work.

Materials	Composition						Processing			
	ABS polymer			GNP			CNT (wt%)	Compression moulding	Filament extrusion (E)	3D-printing (FDM)
	L322 (wt%)	F322 (wt%)	C300 (wt%)	C500 (wt%)	C750 (wt%)	M5 (wt%)				
Low viscosity ABS matrix										
L	100	-	-	-	-	-	-	x	x	x
L-C300-2	98	-	2	-	-	-	-	x	-	-
L-C300-4	96	-	4	-	-	-	-	x	-	-
L-C300-8	92	-	8	-	-	-	-	x	-	-
L-C500-2	98	-	-	2	-	-	-	x	-	-
L-C500-4	96	-	-	4	-	-	-	x	-	-
L-C500-8	92	-	-	8	-	-	-	x	-	-
L-C750-2	98	-	-	-	2	-	-	x	-	-
L-C750-4	96	-	-	-	4	-	-	x	-	-
L-C750-8	92	-	-	-	8	-	-	x	-	-
L-M5-2	98	-	-	-	-	2	-	x	-	-
L-M5-4	96	-	-	-	-	4	-	x	x	x
L-M5-8	92	-	-	-	-	8	-	x	-	-

High viscosity ABS matrix										
F	-	100	-	-	-	-	-	x	-	-
F-M5-2	-	98	-	-	-	2	-	x	-	-
F-M5-4	-	96	-	-	-	4	-	x	-	-
F-M5-6	-	94	-	-	-	6	-	x	x	x
F-M5-8	-	92	-	-	-	8	-	x	-	-
F-M5-12	-	88	-	-	-	12	-	x	-	-
F-M5-16	-	84	-	-	-	16	-	x	-	-
F-M5-30	-	70	-	-	-	30	-	x	-	-
F-CNT-1	-	99	-	-	-	-	1	-	x	-
F-CNT-2	-	98	-	-	-	-	2	x	x	-
F-CNT-4	-	96	-	-	-	-	4	x	x	-
F-CNT-6	-	94	-	-	-	-	6	x	x	x
F-CNT-8	-	92	-	-	-	-	8	x	x	-
Hybrid nanocomposites										
F-CNT-0.6-M5-5.4	-	94	-	-	-	0.6	5.4	x	-	-
F-CNT-1.8-M5-4.2	-	94	-	-	-	1.8	4.2	x	-	-
F-CNT-3-M5-3	-	94	-	-	-	3	3	x	x	x
F-CNT-4.2-M5-1.8	-	94	-	-	-	4.2	1.8	x	-	-
F-CNT-5.4-M5-0.6	-	94	-	-	-	5.4	0.6	x	-	-

3.2.2 Compounding

Various amounts of nanofillers were melt compounded with ABS by a Thermo-Haake Polylab Rheomix counter-rotating internal mixer at 190°C, rotor speed 90 rpm for 15 min until a constant torque was reached. The batches of about 50 g were processed for each composition, and the resulting material was granulated in a mechanical grinder (Piovan Model RN 166). The photographs of internal mixer and grinder are illustrated in Figure 3.2-3. Prior to the melt processing, as received ABS chips were dried at least 2 hours at 80°C under vacuum before processing.

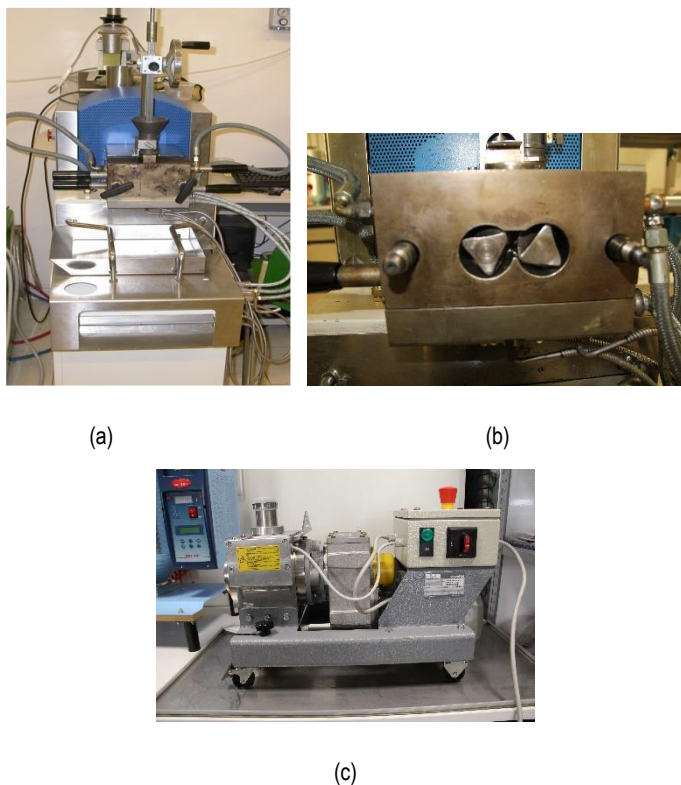


Figure 3.2-3. Photographs of (a) Haake® internal mixer, (b) its mixing chamber, and (c) Piovan grinder Model RN 166.

In order to investigate the effect of the melt mixing on materials, the torque applied by the melt mixer was monitored during the processing time (see Figure 3.2-4). ABS was melted in the first 4 min, and after the addition of nanofillers (at minute 5) a direct increase of torque was observed, followed by a slight decrease in torque. Then

in the last about 10 min of compounding, a plateau constancy in the torque value was reached. Neat ABS was also processed under the same conditions. Moreover, slightly increase in torque can be noticed with the incorporation of nanofiller.

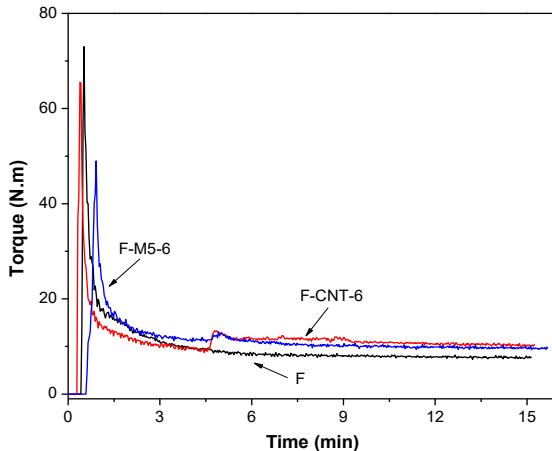


Figure 3.2-4. Torque recorded during compounding for neat ABS (F), graphene nanocomposites (F-M5-6) and carbon nanotubes composite (F-CNT-6).

3.2.3 Compression moulding (CM)

Compounded materials were hot pressed in a Carver Laboratory press at a temperature of 190°C under a pressure of 3.9 MPa applied for 10 min and a cooling rate of 20°C/min to obtain square plaques with dimensions 160×160×1.2 mm or 120×120×2 mm.



Figure 3.2-5. Carver® hot plates press.

3.2.4 Filament extrusion (E)

Compounded materials were also used to feed a Thermo Haake PTW16 intermeshing co-rotating twin screw extruder (screw diameter=16 mm; L/D ratio=25) presented in Figure 3.2-6. The processing temperature gradually increased from 180°C (zone 1) up to 220°C (zone 5 – rod die). The screw rotation speed and collection rate were regulated in order to obtain an extruded filament with a final diameter of 1.75 ± 0.10 mm. A constant collection rate was imposed by using a take-off unit Thermo Electron Type 002-5341. The detailed working parameters corresponding to each material are reported in Table 3.2-2. The code E will be used to identify extruded filament samples.

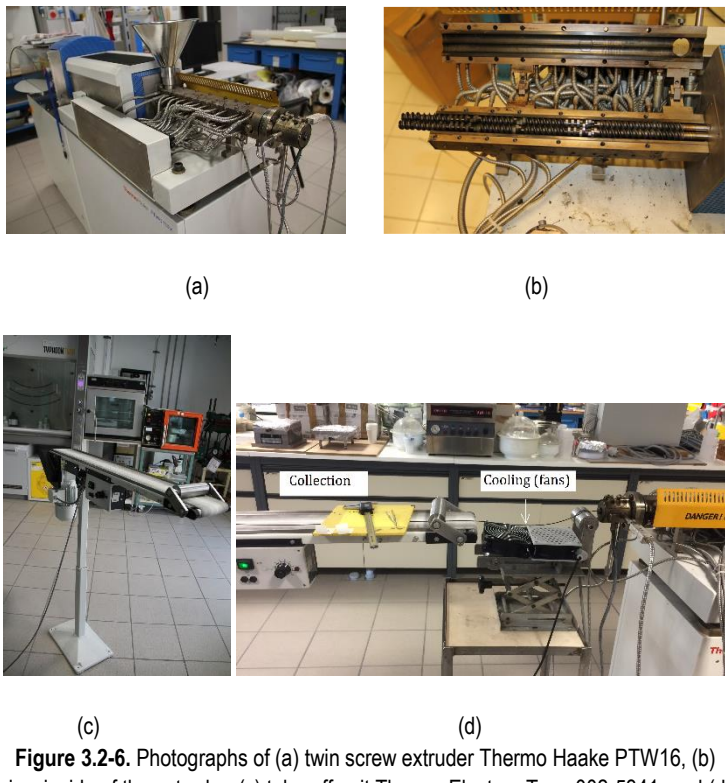


Figure 3.2-6. Photographs of (a) twin screw extruder Thermo Haake PTW16, (b) view inside of the extruder, (c) take-off unit Thermo Electron Type 002-5341, and (d) extrusion process with cooling fans.

Table 3.2-2. Working parameters of twin screw extruder Thermo Haake PTW16.

Twin screw extruder Thermo Haake PTW16			
Parameter	GNP-M5 composites	CNT composites	CNT/M5 hybrid composites
T ₁	180°C	180°C	180°C
T ₂	190°C	205°C	205°C
T ₃	195°C	210°C	210°C
T ₄	195°C	215°C	215°C
T ₅	200°C	220°C	220°C
Screw diameter	16 mm	16 mm	16 mm
Rod die diameter	3.0 mm	1.80 mm	1.80 mm
Screw speed	9 rpm	5 rpm	5 rpm

3.2.5 Fused deposition modelling (FDM)

3D printed specimens were manufactured by fused deposition modelling (FDM) with a Sharebot Next Generation desktop 3D printer (Sharebot NG, Italy) feed with the filaments extruded as described in the previous paragraph. Two different desktop 3D printer (Sharebot NG, Italy) were provided Sharebot NG and used in this work: a commercial standard one and an experimental high-temperature 3D-printer. The main feature of the experimental high-temperature 3D-printer is the capacity to reach higher temperatures in both the extrusion nozzle and deposition bed. The main technical features of each printer are reported in Table 3.2-3.

Table 3.2-3. Feature of Sharebot Next Generation desktop 3D printer.

Features	Standard commercial	Experimental-high temperature
Extrusion type	Dual	Single
Nozzle diameter	0.35 mm	0.40 mm
Max nozzle temperature	260°C	500°C
Max bed temperature	90°C	135°C

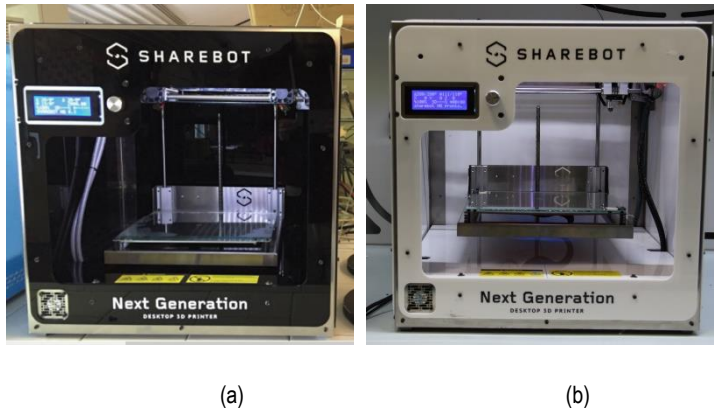


Figure 3.2-7. Photographs of 3D printer Next Generation sharebot (a) standard commercial and (b) prototype high-temperature 3D-printer.

Generally, FDM processing is characterized by a high number of parameters. In particular, three parameters including build orientation, infill pattern and infill density were selected for this work, by using the Slic3r software. The details of 3D-printed samples are summarized in Table 3.2-4.

As schematically represented in Figure 3.2-8, dumbbell shaped and parallelepiped specimens were built-up along three different orientations, i.e., horizontal, vertical and perpendicular, and coded as H, V and P, respectively. X is the direction of filament deposition, and Z is the direction of the overlapping layers.

Printing parameters were used: no raft; layer height 0.20 mm. The deposition rate has been fixed at 40 mm/s for HC, H45 and VC samples, whereas PC specimens were produced at a lower deposition rate (4 mm/s) in order to allow the solidification of deposited beads and provide support for the growing part. For VC specimens it was necessary to generate also a support material deposited at 50 mm/s.

Each filament used to feed 3D-printer in Table 3.2-5 along with information on the temperature of nozzle and bed. The size and the processing parameters of FDM specimens are summarized in Table 3.2-6.

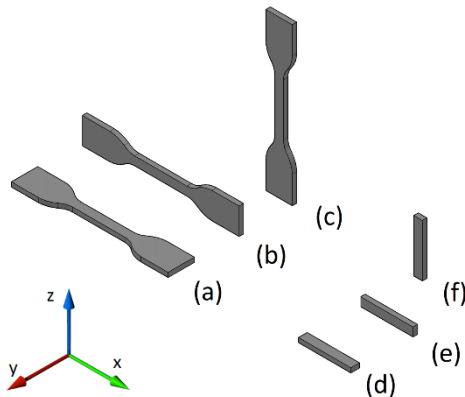


Figure 3.2-8. Schematic of 3D-printed dumbbell and parallelepiped specimens at different orientations: (a) and (d) horizontal (H); (b) and (e) vertical (V); (c) and (f) perpendicular (P).

Table 3.2-4. Summary of 3D samples with details of FDM parameters.

3D Samples	Build orientation	Infill pattern	Raster angle	Infill density
PC	Perpendicular	Concentric	[0°/0°]	100 %
VC	Vertical	Concentric	[0°/0°]	100 %
HC	Horizontal	Concentric	[0°/0°]	100 %
H45	Horizontal	Rectangular	[45°/-45°]	100 %
H45_80	Horizontal	Rectangular	[45°/-45°]	80 %
H45_60	Horizontal	Rectangular	[45°/-45°]	60 %
H45_40	Horizontal	Rectangular	[45°/-45°]	40 %

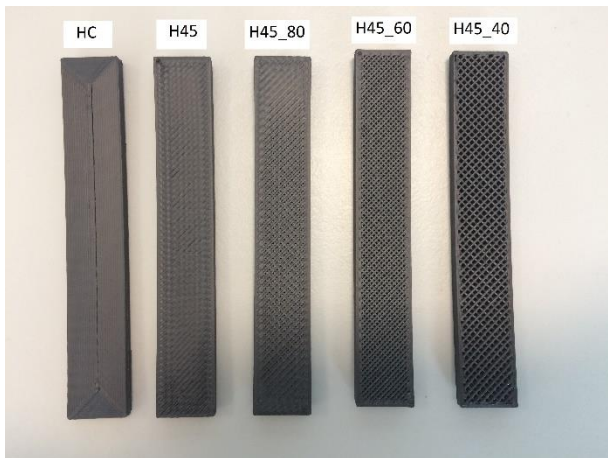


Figure 3.2-9. 3D samples along horizontal build orientation with different raster angle and infill density of ABS-graphene nanocomposites (L-M5-4) for the flexural test.

Table 3.2-5. Filaments used for 3D-printing and processing temperature to manufacture 3D samples.

Filaments	T _{nozzle} (°C)	T _{bed} (°C)	3D-Printer type
L	230	60	Standard
L-M5-4	230	60	commercial
F	250	110	
F-M5-6	250	110	Experimental
F-CNT-6	280	110	high temperature
F-M5-3-CNT-3	250	110	

Table 3.2-6. Dimensions and processing parameters of FDM specimens.

Analysis	X (mm)	Y (mm)	Z (mm)	F ^b filaments in a layer	D deposition time of single layer (sec)	D/F deposition time of single filament (sec)	number of layers	total time ^c (min)	Sample shape
Flexural test									
HC	80	12.7	3.2	31	70	2.3	16	20	
H45	80	12.7	3.2	-	59	-	16	20	
H45_80	80	12.7	3.2	-	51	-	16	15	Parallelepiped
H45_60	80	12.7	3.2	-	42	-	16	13	
H45_40	80	12.7	3.2	-	33	-	16	10	
Tensile test									
PC	4-12.5 ^a	2	75	5	11	2	375	89	
VC	2	75	4-12.5 ^a	5	21	4	20-63	14	Dumbbell
HC	75	4-12.5 ^a	2	11	43	4	10	8	
H45	75	4-12.5 ^a	2	-	33	-	10	6	

Creep test								
HC	25	4	1	11	10	1	5	1.2
H45	25	4	1	-	10	-	5	1.2
VC	25	1	4	3	4	1	20	1.6
PC	1	4	25	3	6	2	125	15
DMA								
HC	25	4	2	11	10	1	10	2
H45	25	4	2	-	10	-	10	2
VC	25	2	4	5	5	1	20	2.1
PC	2	4	25	5	9	2	125	21
Resistivity test								
HC	25	6	2	15	12	0.8	10	4.0
H45	25	6	2	-	11	-	10	4.0
PC	2	6	25	5	11	2.2	125	37.5
Resistive heating								
HC	50	6	2	15	23	1.5	10	7.0
H45	50	6	2	-	16	-	10	5.0
PC	2	6	50	5	11	2.2	250	75.0

^a min and max values of specimen's width are reported

^b number of contiguous filaments in a single layer in the gage length

^c for production of one FDM specimen.

3.3 Testing techniques

3.3.1 Microstructural characterizations

3.3.1.1 Density measurements

Density measurements of nanoparticles were carried out by gas pycnometry technique on a Micromeritics® Accupyc 1330 helium pycnometer (Norcross USA), at a temperature of 23.0°C, using a testing chamber of 10 cm³ and performing at least 99 measurements.

Density measurements on bulk samples were measured by the displacement method weighing the specimens in air and immersed in ethanol-water (a concentration of 96 wt % and density of 0.802 g/cm³) at room temperature on at least three replicated specimens for each sample. The density was calculated through Eq. (3.3-1).

$$\rho_{\text{exp}} = \frac{m_{\text{air}} \times \rho_{\text{ethanol}}}{m_{\text{air}} - m_{\text{ethanol}}} \quad (3.3-1)$$

where m_{air} and m_{ethanol} are the mass of samples in air and ethanol respectively.

In order to compare the experimental results, theoretical density of composites was predicted based on the rule of mixture according to Eq. (3.3-2).

$$\rho_{\text{th}} = \rho_c \times V_m + \rho_f \times V_f \quad (3.3-2)$$

where ρ_c , ρ_m , ρ_f are the densities of the composites, the neat matrix, and the nanoparticles respectively, while V_m and V_f are the volume fraction of the matrix and the nanofiller.

The voids content (V_v) in nanocomposites was evaluated according to the following equation:

$$V_v = \frac{\rho_{\text{th}} - \rho_{\text{exp}}}{\rho_{\text{th}}} \quad (3.3-3)$$

3.3.1.2 Melt flow index (MFI)

The melt flow index (MFI) measurements were carried out according to ASTM D 1238 standard (procedure A), through a Kayeness Co. model 4003DE capillary rheometer, at a temperature of 220°C, 250°C or 280°C under an applied load of 10 kg on samples with a mass of about 5 g (pre-heat and compaction time of about 5 min).

3.3.1.3 Rheological analysis

Rheological properties of neat ABS and the nanocomposites were evaluated using an oscillatory rheometer, model Hybrid Discovery HR1 from TA Instrument Inc., with parallel plate geometry (25 mm). The analysis was performed at temperature of 230°C, 250°C and 280°C and range frequency of 0.01–100 Hz with a 0.5% deformation, in the linear viscoelastic regime.

3.3.1.4 Scanning electron microscopy (SEM)

Morphology of nanoparticles and fracture surface of nanocomposites were studied by using a Carl Zeiss AG Supra 40 field emission scanning electron microscope (FESEM).

Nanoparticles were dispersed in chloroform with a concentration of 0.1 mg/ml and sonicated for 10 min by Ultrasonic Processor UP400S. Finally, nanoparticles dispersion solution was directly dropped and evaporated onto aluminum plates for observation at an acceleration voltage of 10 kV. Nanocomposites were fractured in liquid nitrogen, and the fracture surfaces were observed at an acceleration voltage of 3 kV. Representative micrographs at different level of magnification were selected.

3.3.1.5 Transmission Electron Microscopy (TEM)

The morphology of graphene nanoplatelets and carbon nanotubes nanoparticles was observed by transmission electron microscopy (TEM), using a Philips® EM 400 T (Amsterdam, Netherlands) transmission electronic microscope at an acceleration voltage of 120 kV. Nanoparticles were dispersed in acetone suspension (concentration = 0.5 mg/ml) and sonicated for 5 min, and the nanoparticle suspensions were dropped on a 600-mesh copper grid for TEM observation.

3.3.1.6 Fourier transform infrared spectroscopy (FTIR)

Fourier transform infrared (FTIR) spectra were recorded by a Spectrum One™ spectrometer (Perkin Elmer ATR-FTIR) in a scanning range from 4000 to 400 cm⁻¹.

3.3.1.7 X-ray photoelectron spectroscopy (XPS)

In order to identify the surface chemical compositions of GNP, X-ray photoelectron (XPS) spectroscopy was performed using a Kratos Axis Ultra DLD instrument (Kratos Analytical, Manchester, UK) equipped with a hemispherical analyzer and a monochromatic AlK (1486.6 eV) X-ray source, in spectroscopy mode. The emission angle between the axis of the analyzer and the normal to the surface of samples was 0°. For each sample a survey (for binding energy up to 1300 eV) was collected, to identify the elements on the surface. Afterwards, the core levels C 1s, O

1s and N 1s were also collected, with a higher energy resolution in order to evaluate the chemical differences between the samples. The quantification, reported as relative element percentage, for each sample was performed using the integrated area of the fitted core lines, after Shirley background subtraction, and correcting for the atomic sensitivity factors.

3.3.1.8 Thermogravimetric analysis (TGA)

Thermal degradation was investigated through a Q5000 IR thermogravimetric analyzer (TA Instruments-Waters LLC, New Castle, USA). The samples having a mass of about 10 mg were tested from 30°C up to 800°C at a rate of 10°C /min under a nitrogen flow of 15 ml/min. The onset temperature of degradation (T_{onset}) was defined by the intersection point of the two tangent lines, and the maximum degradation temperature ($T_{d, max}$) was taken in correspondence to the maximum of the first derivative of weight loss. The relative residue was also reported in order to evaluate the content of nanofiller according to the equation:

$$C_{\text{nanofiller}} = R_{\text{comp}} - R_{\text{ABS}} \quad (3.3-4)$$

where R_{comp} and R_{ABS} are the residue of composite and ABS respectively at the same temperature.

3.3.1.9 Differential scanning calorimetry (DSC)

Differential scanning calorimetry (DSC) tests were performed by a Mettler DSC 30 calorimeter under a nitrogen flow of 100 ml/ min on samples with a mass of about 10 mg. The samples were first heated from 30°C to 260°C at a rate of 10°C /min followed by an isothermal stay at 260°C for 5 min. The samples were then cooled down from 260°C to 30°C at a rate of -10°C /min and re-heated at the same rate from 30°C to 260°C. Glass transition temperature (T_g) of SAN phase was measured as an inflection point of the thermograms.

3.3.2 Mechanical testing

3.3.2.1 Quasi-static tensile test

Uniaxial tensile tests were carried out at room temperature by an Instron® 5969 electromechanical testing machine equipped with a 50 kN load cell.

Fracture properties were evaluated at a crosshead speed of 10 mm/min as the average value of at least three replicates. Specimens consisted of i) compression molded (CM) materials ISO 527 type 1BA dumbbell (gauge length 30 mm; thickness 1.2 mm) ; ii) extruded filaments (E) (gauge length 100 mm diameter 1.75 mm); iii) 3D printed materials, ISO 527 type 5A dumbbell (gauge length 25 mm; thickness 2 mm).

Elastic modulus of CM and 3D-printed H, V and P specimens was determined at a cross-head speed of 1 mm/min by an electrical extensometer Instron® model 2620-601 with a gage length of 12.5 mm; whereas the tensile modulus of filament specimens was measured at a cross-head speed of 10 mm/min without extensometer with a gage length of 100 mm taking the system compliance into account. According to ISO 527 standard, the elastic modulus was determined as a secant value between strain levels of 0.05% and 0.25%.

3.3.2.2 Flexural test

Flexural testing (three points bending) was performed according to ASTM D790 on 3D-printed samples (length = 80 mm, width = 12.7 mm and thickness = 3.2 mm). The tests were carried out by using an Instron® 5969 electromechanical testing machine equipped with a 50 kN load cell at a cross-head speed of 1.4 mm/min on specimens with a span length of 51.2 mm. For each sample, at least three specimens were tested with a span length of 51.2 mm. The flexural stress and strain were calculated as shown in Eq. (3.3-5) and (3.3-6) respectively:

$$\sigma_f = \frac{3PL}{2bd^2} \quad (3.3-5)$$

$$\varepsilon_f = \frac{6Dd}{L^2} \quad (3.3-6)$$

where
 P = load
 D = maximum deflection of the center of the beam
 L = support span
 d = depth
 b = width of beam tested

3.3.2.3 Dynamic mechanical thermal analysis

Dynamic mechanical thermal analysis (DMA) tests were performed under tensile mode by a TA Instruments DMA Q800 device. For CM and 3D-printed materials, rectangular specimens were tested with a length of 25 mm, and different cross section (width 5 mm and a thickness 1.2 mm for CM and width 4 mm and a thickness 2 mm for 3D-printed materials). Extruded filaments 25 mm in length and a diameter of 1.75 mm were tested. The gauge length of all samples was fixed at 11.8 mm. Tests were performed from -100°C to 150°C at a heating rate of 3°C/min applying a maximum dynamic strain of 0.05% at a frequency of 1 Hz. Storage modulus (E'), loss modulus (E'') and loss tangent ($\tan \delta$) as a function of the temperature were reported.

From the thermal strain curve, a coefficient of linear thermal expansion (CLTE) below T_g and a coefficient of linear thermal deformation (CLTD) above T_g were determined according to equation (3.3-7):

$$CLTE \text{ or } (CLTD) = \frac{\Delta L / L_0}{\Delta T_0} \quad (3.3-7)$$

where L_0 and ΔL are the initial specimen gauge length and the length variation, and ΔT is the selected temperature interval (i.e., 50/-20°C; 20/50°C; 70/90°C, 108°C/113°C for CLTE and 120/150°C for CLTD).

3.3.2.4 Creep test

Creep tests were performed through a TA Instruments DMA Q800 under a constant stress of about 10% of the yield stress of neat ABS at 30°C up to 3600 s. Rectangular samples with length of 25 mm, width of 5 mm and thickness of 0.9 mm were machined from compression molded plaques. Cylindrical extruded specimen with diameter 1.75 mm with length of 25 mm were used. Rectangular specimens with length of 25 mm, width of 4 mm and thickness of 1 mm were also prepared by 3D printing. The adopted gauge of all samples was about 11.5 mm.

3.3.2.5 Modelling of tensile modulus

The empirical Halpin-Tsai model is a simple approach to predict the modulus of composite materials which takes into account the modulus of matrix E_M and filler E_f , filler aspect ratio ξ , volume fraction of filler V_f , assuming a homogeneous dispersion and perfect interfacial adhesion between polymer/filler, [42, 116-119]. The tensile modulus in both longitudinal E_L and transverse E_T directions can be predicted according to Halpin-Tsai model [120, 121] by the following equations:

$$E_L = \frac{1 + \xi \eta_L V_f}{1 - \eta_L V_f} E_M \quad (3.3-8)$$

$$E_T = \frac{1 + 2 \eta_T V_f}{1 - \eta_T V_f} E_M \quad (3.3-9)$$

where the parameters η_L , η_T and ξ are defined as:

$$\eta_L = \frac{(E_f / E_M) - 1}{(E_f / E_M) + \xi} \quad (3.3-10)$$

$$\eta_T = \frac{(E_f / E_M) - 1}{(E_f / E_M) + 2} \quad (3.3-11)$$

$$\xi = \frac{2}{3} \frac{D_f}{t_f} \quad \text{for plates} \quad (3.3-12)$$

$$\xi = 2 \frac{L_f}{D_f} \quad \text{for fiber} \quad (3.3-13)$$

D_f and t_f are lateral diameter and thickness of platelets and L_f and D_f are length and diameter of fibers, respectively.

The volume fraction V_f is linked to the weight fraction w_f through the following equation:

$$V_f = \frac{w_f \rho_M}{w_f \rho_M + (1-w_f) \rho_f} \quad (3.3-14)$$

where, ρ_M and ρ_f are the density values of ABS matrix and graphene nanoplatelets, respectively.

Subsequently, the modulus of a composite with platelets filler long axis parallel to the loading direction (E_{Parallel}) and randomly oriented platelets/fibers fillers in all two dimensional 2D-direction ($E_{\text{2D,Random}}$) and three dimensional 3D-directions ($E_{\text{3D,Random}}$) can be predicted according to literature [60, 122, 123] as follow

For plates:

$$E_c^{\text{Parallel}} = E_L \quad (3.3-15)$$

$$E_c^{\text{3D,Random}} = 0.49E_L + 0.51E_T \quad (3.3-16)$$

For fiber:

$$E_c^{\text{Parallel}} = E_L \quad (3.3-17)$$

$$E_c^{\text{2D,Random}} = 0.375E_L + 0.625E_T \quad (3.3-18)$$

$$E_c^{\text{3D,Random}} = 0.184E_L + 0.816E_T \quad (3.3-19)$$

3.3.3 Testing of electrical properties

3.3.3.1 Electrical resistivity test

For samples with an electrical resistivity higher than $10^7 \Omega \cdot \text{cm}$, the volume resistivity was measured according to the ASTM D257 by using a Keithley 6517A electrometer/High Resistance Meter and an 8009 Resistivity Test Fixture at the room

temperature. In this test, the constant applied voltage of 100 V was applied to a square specimen of 64×64 mm.

For moderately conductive materials (<10⁷ Ω.cm), electrical resistivity test was carried out following ASTM D4496-04 standard for moderately conductive materials with four-point contact configuration. Each specimen was applied at a voltage from 2 to 24 V by using a DC power supply (IPS303DD produced by ISO-TECH) and the current flow on the samples was measured between external electrodes by using an ISO-TECH IDM 67 Pocket Multimeter electrometer. Compression moulding (CM), filaments (E) and 3D-printed samples were tested with a length of 25 mm and different cross-section (rectangular specimens 6×1.2 mm for CM and 6×2 mm for 3D-printed sample; diameter of 1.75 mm for filament). At least three specimens were replicated for each sample. Due to the surface roughness of 3D-printed samples, a conductive silver paint was applied to the sample surface at the contact electrodes in order to ensure good electrical contact. The electrical volume resistivity of the samples was evaluated by Eq. (3.3-20):

$$\rho = R \times \frac{A}{L} \quad (3.3-20)$$

where R is the electrical resistance, A is the cross-section of the specimen and L is the distance between the internal electrodes (i.e. 3.69 mm).

3.3.3.2 Surface temperature evaluation upon voltage application

The heating of a sample generated by a current flow is known as resistive heating, and it is described by the Joule's law. Surface temperature evolution induced by Joule's effect upon different applied voltages was measured by a Flir E6 thermographic camera. The voltages were applied by a DC power supply (IPS 303DD produced by ISO-TECH), while the samples were fixed with two metal clips with an external distance of 30 mm. In these tests, specimen length was 50 mm with different cross-sections of rectangular 6×1.2 mm for CM, 6×2 mm 3D-printed specimens and diameter of 1.75 mm for cylindrical filaments. The surface temperature values have been recorded for 120 seconds of application of voltage levels of 12 V and 24 V.

3.3.3.3 Strain monitoring tests

The monitoring of the change of resistance upon the application of mechanical strain was performed on the conductive composites specimens. 3D-printed sheets of 100×10×1.4 mm were subjected to tensile, cyclic load and creep test with the distance between the grips of 50 mm by using Instron® 5969 electromechanical testing machine. The fracture test were performed at a cross-head of 0.5 mm/min (strain rate of 1 %/min). For ramp strain, cyclic and creep test, the strain was measured by using extensometer Instron® model 2620-601 with a gauge length of 12.5 mm with a strain

rate of 0.3%/min. Two probes were employed for measurement resistivity at a very low voltage of 0.1 V. To ensure good electrical contact, a silver paint was applied on the surface of the conductive samples at a distance of 30 mm, and the electrical resistivity was measured using a Keithley 6517A high-resistance meter as shown in Figure 3.3-1. The creep tests were performed by using the same equipment on specimens at a constant stress of 20 MPa at the room temperature up to 3600 s.

A gauge factor (k) was calculated by using the following formula:

$$k = \frac{(\Delta R / R_0)}{\varepsilon} \quad (3.3-21)$$

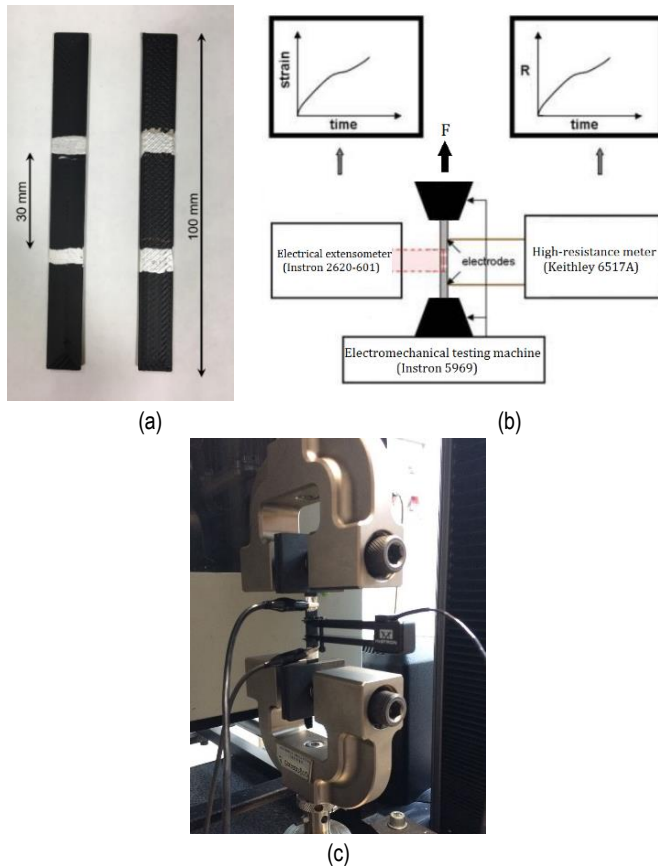


Figure 3.3-1. Experimental setup for the strain monitoring: (a) Specimens after conductive paint; (b) Schematic of experimental setup; (c) Actual setup for testing.

3.3.4 Electromagnetic interference shielding effectiveness (EMI SE) test

The electromagnetic interference properties of ABS and nanocomposites were measured using an Agilent Technology PNA series network analyzer (N5230C Agilent PNA-L, Santa Clara, CA) and a standard rectangular waveguide in the X-band frequency range (8.2 – 12.4 GHz). The analysis was performed on samples with a width of 10 mm, length of 23 mm and thickness of 2 mm, and the S-parameters (S_{11} , S_{22} , S_{12} , S_{21}) were recorded over the X-band frequency range.

The contribution of reflection (SE_R) and absorption (SE_A) to the total EMI SE of the composites were investigated. At the same time, the effect of multiple reflections (SE_M) was neglected, as commonly reported in the literature [124, 125]. For this purpose, the complex scattering parameters that represent the reflection S_{11} (S_{22}) and transmission S_{12} (S_{21}) coefficients were compared with the incident electromagnetic wave, and were used to evaluate reflected power (P_{ref}), transmitted power (P_{trans}) and absorbed power (P_{abs}) according to the equations:

$$P_{ref} = \left| \frac{E_R}{E_I} \right|^2 = |S_{11}|^2 (= |S_{22}|^2) \quad (3.3-22)$$

$$P_{trans} = \left| \frac{E_T}{E_I} \right|^2 = |S_{12}|^2 (= |S_{21}|^2) \quad (3.3-23)$$

$$P_{abs} = 1 - (P_{ref} - P_{trans}) \quad (3.3-24)$$

Subsequently, the contribution of reflection SE_R and absorption SE_A to the total EMI SE was evaluated according to equations (3.3-25), (3.3-26).and (3.3-27).

$$SE_R (dB) = 10 \log \frac{P_{inc}}{P_{inc} - P_{ref}} \quad (3.3-25)$$

$$SE_A (dB) = 10 \log \frac{P_{inc} - P_{ref}}{P_{trans}} \quad (3.3-26)$$

$$SE_{total} (dB) = SE_A + SE_R = 10 \log \frac{P_{inc} - P_{ref}}{P_{trans}} + 10 \log \frac{P_{inc}}{P_{inc} - P_{ref}} = 10 \log \frac{P_{inc}}{P_{trans}} \quad (3.3-27)$$

Results and discussions

Chapter IV

ABS-graphene nanoplatelets nanocomposites

Part of this chapter has been published in:

S. Dul, H. Mahmood, L. Fambri, A. Pegoretti

“Graphene-ABS nanocomposites for fused deposition modelling”

Proceeding of the 17th European Conference on Composite Materials -ECCM 2017 (2016).

S. Dul, L. Fambri, C. Merlini, G.M.O. Barra, M. Bersani, L. Vanzetti, A. Pegoretti

“Effect of graphene nanoplatelets structure on the properties of acrylonitrile-butadiene-styrene-composites”

Polymers Composites. In press.

S. Dul, L. Fambri, A. Pegoretti

“Fused deposition modelling with ABS-graphene nanocomposites”

Composites Part A - Applied Science and Manufacturing. 85. (2016) 181-191.

This chapter is dedicated to ABS-graphene nanocomposites with the aim to produce suitable filaments through a solvent-free procedure based on melt compounding and extrusion for FDM process. In section 4.1, characterizations of graphene nanoplatelets nanofillers were carried out in order to understand the chemical and physical properties. Section 4.2 is about the comparison between two types of ABS (with high and low viscosity used for nanocomposites plates from compression moulding process. In the following section 4.3, four different types of graphene nanoplatelets with different size and surface area were incorporated in low viscosity ABS to produce nanocomposites plates. Section 4.4 describes the ABS-graphene filament were employed in FDM process with a comparison of properties on samples obtained by compression moulding, extruded filament and FDM printed parts. Finally, the summary of the study is provided in section 4.5.

4.1 Characterization of GNP

SEM images of different types of graphene nanoplatelets are shown in Figure 4.1-1. It can be clearly observed that M5 nanoparticles show the largest-size followed by C300, C500 and C750 respectively, in agreement with the corresponding surface area values. Graphene nanoplatelets C300 and C500 resulted to be similar in size as

illustrated in Figure 4.1-1(b-c), whereas C750 appeared as particles rather than platelets. This observation indicates a low aspect ratio for GNP-C750 in good agreement with the observations of other authors [60, 126].

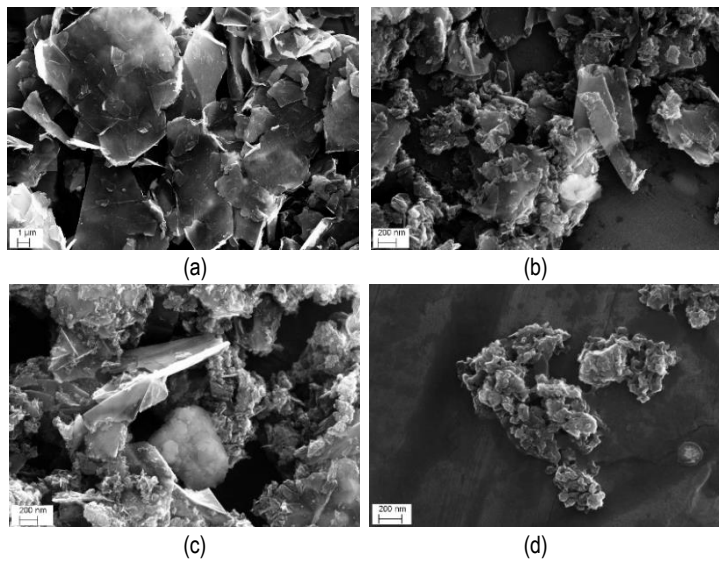


Figure 4.1-1. FESEM images of graphene nanoplatelets: (a) M5, (b) C300, (c) C500 and (d) C750.

Figure 4.1-2a shows the XPS survey spectra of the four different GNPs nanoparticles. As summarized in Table 4.1-1, carbon and oxygen are the main elements detected on the surface from the peaks at 285 and \sim 533 eV, with a very small amount of nitrogen (0.2-0.4%), as evidenced from the peak at about 400 eV for all nanofillers.

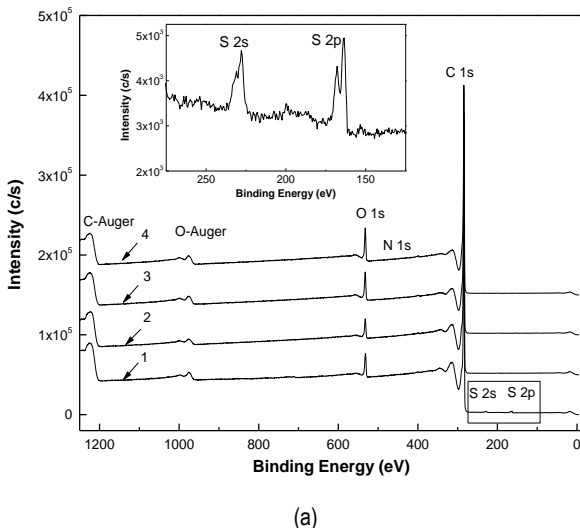
Details of the oxygen core level are shown in Figure 4.1-2b. Samples C750, C500 and C300 exhibit a similar O 1s peak, centred at about 533 eV, that can be attributed to oxydilic and/or ether groups [127]; it is worthwhile to be noted that peak height increased with the surface area, reaching the highest oxygen content of 6.7% for GNP-750, due to smallest particle size resulting in a large proportion of edges, showing an analogous direct relationship with the surface area, as observed for sample C500 and C300.

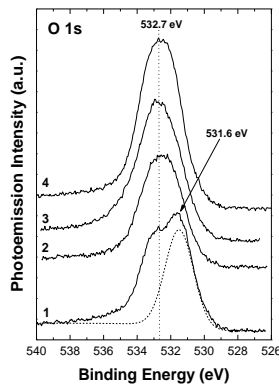
On the other hand, XPS reveals that M5 sample possesses a total oxygen content of 4.2%, which is comparable to literature data [126], but it is higher than expected considering the surface area and the particle dimensions, that are definitively higher than C samples. The explanation could be found by the qualitative difference of O 1s signal observed for sample M5 (double peak) with a significant contribute of

the peak at about 531 eV (see deconvolution in Figure 4.1-2b), that according literature is attributable to the carbonyl group [127]. Following partial integration, the quantitative analysis resulted in an almost equivalent contribute of the carbonyl and the ether/alcohol groups, being 2.2% of $>\text{C}=\text{O}$ and 2.0% of $-\text{O}-$ and $-\text{OH}$ groups. Taking into consideration this latter value, the ether/alcohol content of graphene particles appeared almost directly proportional to the surface area (see Figure 4.1-3).

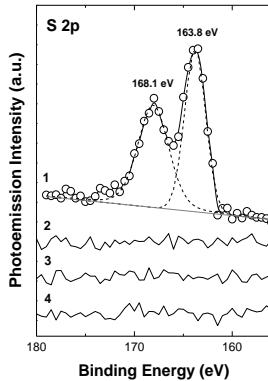
The peculiar aspect of M5 graphene is furtherly evidenced from the surface chemical composition with few traces of sulphur, as documented in Figure 4.1-2a, by the S 2s and S 2p peaks at 225 and about 165 eV respectively.

A comparative enlargement of the S 2p zone (Figure 4.1-2c) confirmed the absence of sulphur in the three graphenes of Series C, whereas sample M5 evidenced two types of sulphur, in particular, the peaks at 163.8 eV and 168.1 eV can be respectively assigned to $2\text{p}_{2/3}$ and to oxidized sulphur groups, according to Quan et al. [128].





(b)



(c)

Figure 4.1-2. XPS spectra of GNP-M5 (1), C300 (2), C500 (3) and C750 (4): a) XPS survey, b) the oxygen core level, and c) the sulfur core level.

The density data of graphene nanoplatelets are also reported in Table 4.1-1. The density of C300 is slightly higher than that of C500 and higher than that of C750, evidencing an almost inverse dependence of their density on the content of ether/alcohol groups and on the surface area. On the other hand, M5 shows lower density (2.06 g/cm^3) with respect to the grade C nanoparticles ($2.21\text{--}2.33 \text{ g/cm}^3$), in conformity to the qualitatively and quantitatively different chemical composition of the

surface of grade M graphene, due to the presence of carbonyl and sulphur containing groups, as revealed by XPS.

Table 4.1-1. Characteristics of as-received graphene nanoplatelets (GNP). Atomic percentage of surface elemental composition and density, as measured by XPS analysis and helium pycnometry, respectively.

Samples	C (%)	O (%)	N (%)	S (%)	Density (g/cm ³)
GNP-M5	95.1	2.2+2.0*	0.3	0.4	2.06 ± 0.03
GNP-C300	96.0	3.8	0.2	0.0	2.33 ± 0.02
GNP-C500	93.8	5.9	0.3	0.0	2.30 ± 0.02
GNP-C750	92.9	6.7	0.4	0.0	2.21 ± 0.03

* contributes to two components (see details in the text).

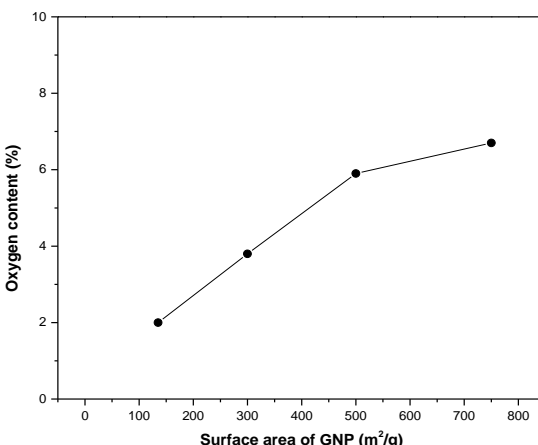


Figure 4.1-3. Oxygen content associated with the ether/alcohol groups as a function to the surface area of graphene nanoplatelets.

The thermal stability of each graphene nanoplatelets was investigated through thermogravimetric analysis (see Figure 4.1-4). One single degradation step can be observed for grade C graphenes (GNP-C300, C500 and C750). Due to the smallest size of graphene nanoplatelets, GNP-C750 showed the lowest degradation temperature, and these results are similar to those reported by the manufacturer [52]. The comparison of thermal stability of graphene are reported in Table 4.1-2 in terms of the selected decomposition temperatures at 10% ($T_{0.1}$), 50% ($T_{0.5}$) and 80% ($T_{0.8}$) of mass loss and maximum degradation rate temperature ($T_{d, \max}$). The maximum mass loss rate (MMLR) of grade C graphenes increases with the surface area.

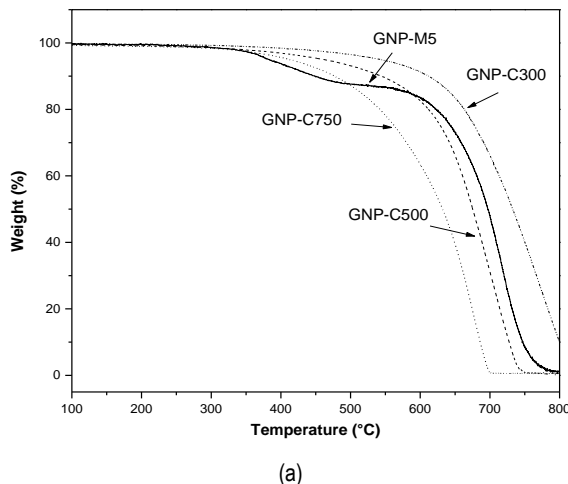
In addition, since all types of graphene began to partially degrade before 500°C, which is the degradation temperature of very small crystalline particles, the presence of some amorphous carbon may be hypothesized. The situation was manifestly more evident in grade M graphene (GNP-M5), which manifest a degradation curve with two clear steps.

Table 4.1-2. Results of TGA analysis of graphene nanoplatelets performed under air atmosphere.

Samples	Temperature of 10% mass loss – $T_{0.1}$ (°C)	Temperature of 50% mass loss – $T_{0.5}$ (°C)	Temperature of 80% mass loss – $T_{0.8}$ (°C)	$T_{d,max}$ (°C)	MMLR (%/°C)
GNP-M5	449	697	732	720	0.95
GNP-C300	611	733	783	762	0.62
GNP-C500	544	675	714	708	0.79
GNP-C750	477	632	675	677	0.87

$T_{d,max}$: maximum degradation rate temperature.

MMLR: Maximum mass loss rate.



(a)

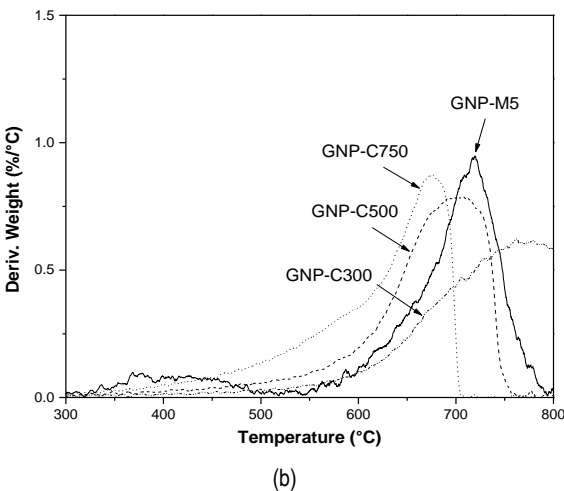


Figure 4.1-4. TGA curve of different types of graphene nanoplatelets performed in air atmosphere: (a) mass loss and (b) derivative of mass loss.

4.2 Selection of ABS matrix

In this section, nanocomposites with two ABS with different viscosity, i.e. Sinkral®L322 (L) and Sinkral®F322 (F) were investigated. Graphene (GNP-M5) nanofiller was selected to be incorporated by melt compounding following by compression moulding. The processability, microstructure and mechanical properties were evaluated on samples prepared by compression moulding.

4.2.1 Melt flow index

The melt flow index (MFI) of two different types of neat ABS (L and F) and its relative nanocomposites as a function of graphene M5 are reported in Figure 4.2-1. The MFI values are 25.4 ± 1.4 g/10min and 14.8 ± 1.0 g/10min for L and F ABS pellets respectively, which are consistent with the reported values in the materials technical data sheet [114]. Melt compounding and hot pressing processes lead to an increase of the melt flow index of neat ABS to 34.8 ± 1.4 g/10min and to 23.6 ± 1.3 g/10min for L and F samples respectively. This lower viscosity can be attributed to the chain scission occurred during the process, after the consumption of antioxidant stabilizers. As reported by Boldizar and Möller [129], melt volume rate of neat ABS significantly increased (up to about two times) after a repetition of seven consecutive extrusion processes and accelerated aging. The melt flow index of both L-M5 and F-M5 nanocomposites showed a nearly linear decrease with the graphene-M5 content.

Moreover, L matrix sample and its nanocomposite show MFI values higher than the corresponding materials based on F matrix. In particular, the MFI ratio of L over F samples is 1.47 for the neat matrix, whereas 1.44, 1.69 and 1.62 for nanocomposite at 2 and 4 and 8 wt% of GNP-M5, respectively. Similarly, the MFI ratio of 1.56 for lubricated ABS over pure ABS was reported, suggesting the similar amount of mould lubricant [130]. This result indicated the better processability for ABS Sinkral®L322 (L) nanocomposites.

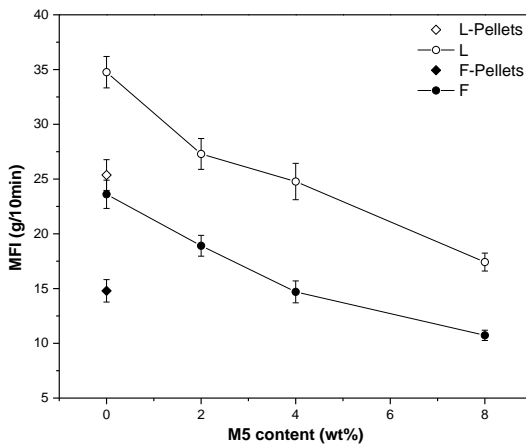


Figure 4.2-1. Melt flow index of two different types of neat ABS (L and F) and its relative nanocomposites as a function of graphene M5.

4.2.2 FTIR and differential scanning calorimetry

FTIR spectra of ABS-graphene nanocomposites and matrices from compression moulding are also shown in Figure 4.2-2. Spectra of L sample clearly show the presence of distinctive peaks at ~ 3296 , 1638 cm^{-1} and 1555 cm^{-1} related to the presence of additives in ABS which correspond to N-H, and C=O stretch of an amide group, respectively.

Figure 4.2-3 shows the typical DSC thermograms in a heating-cooling-heating cycle of the different type of ABS matrices in the form of compression moulded plates. From Table 4.2-1, both ABS have glass transition temperature about 101°C and 108°C for lubricated and non-lubricated ABS indicating styrene-acrylonitrile copolymer (SAN) phase [39, 104, 131]. In addition, lubricated ABS shows the presence of an endothermic peak at a temperature of about 136°C (in Table 4.2-1) associated to the melting of mould lubricant. Differently from the interpretation given by Singh et al. [132] and Rytlewski et al. [133], in our opinion this endothermal peak cannot be attributed to the melting of acrylonitrile (AN) crystallites, but it is mostly related to a mould

lubricant that is generally added for better processing of commercial high viscosity ABS, as described by Reed et al. [134].

Based on FTIR and DSC indications, the mould lubricant additive could be a fatty acid amide (FAA) with a melting point of 150°C, in conformity to the literature [134], or a polyamide [135].

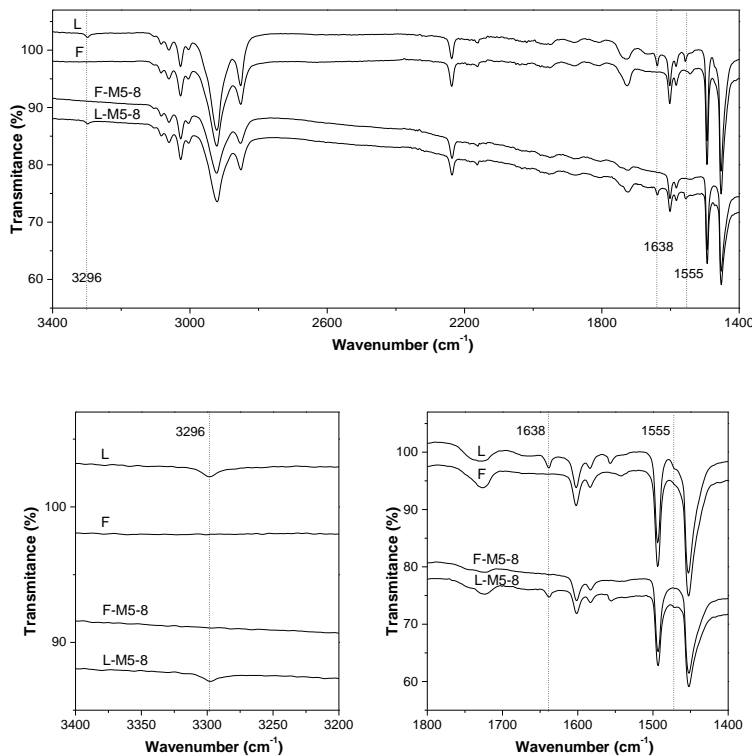


Figure 4.2-2. FTIR spectra of two types of neat ABS and ABS graphene M5 composites with 8 wt%.

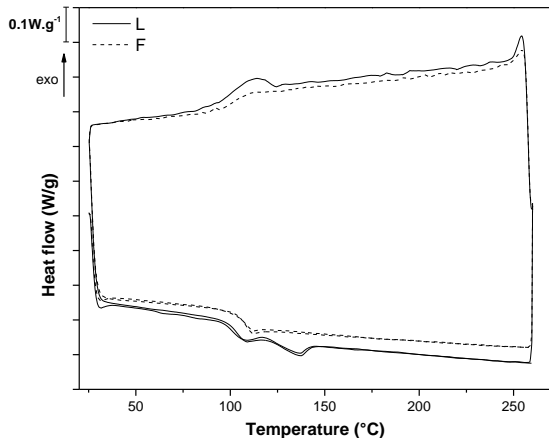


Figure 4.2-3. The heating-cooling-heating cycle of DSC thermograms of two neat ABS with (L) and without (F) mold lubricant.

Table 4.2-1. Glass transition temperatures of styrene–acrylonitrile phase (T_g), melting temperature (T_m) and enthalpy of fusion of lubricant (ΔH_m) for both types of neat ABS plate from DSC.

Samples	First heating			Cooling			Second heating		
	T_g (°C)	T_m (°C)	ΔH_m (J/g)	T_g (°C)	T_c (°C)	ΔH_c (J/g)	T_g (°C)	T_m (°C)	ΔH_m (J/g)
L	100.7	136.4	3.1	100.6	114.1	2.7	103.3	137.1	2.8
F	108.3	-	-	102.4	-	-	108.0	-	-

4.2.3 Fractography

Comparative morphology of both kinds of ABS/GNP-M5 nanocomposites at the highest contraction (8 wt%) is presented in Figure 4.2-4. Larger and more numerous holes were observed in L-M5-8 sample with respect to F-M5-8 sample, most probably depending on the volatilization of the mould lubricant in the high-vacuum SEM chamber.

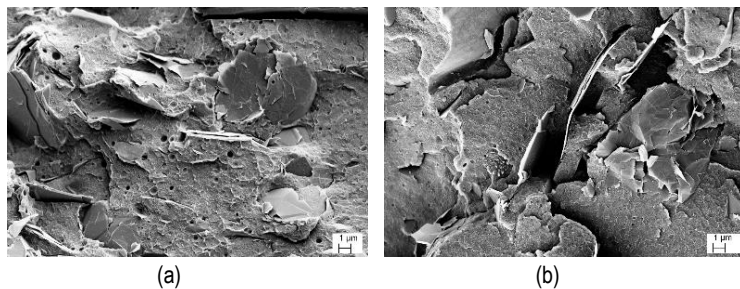
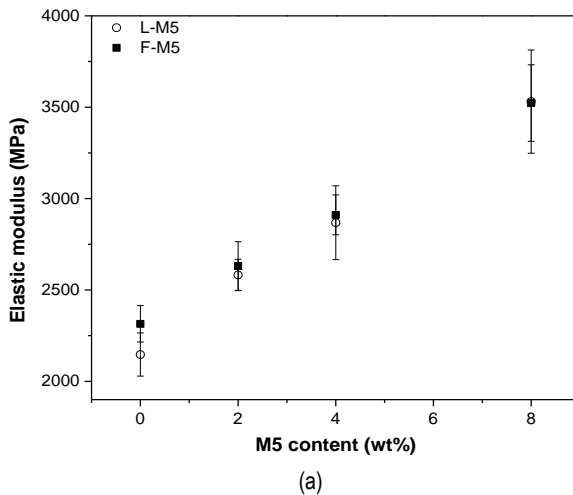


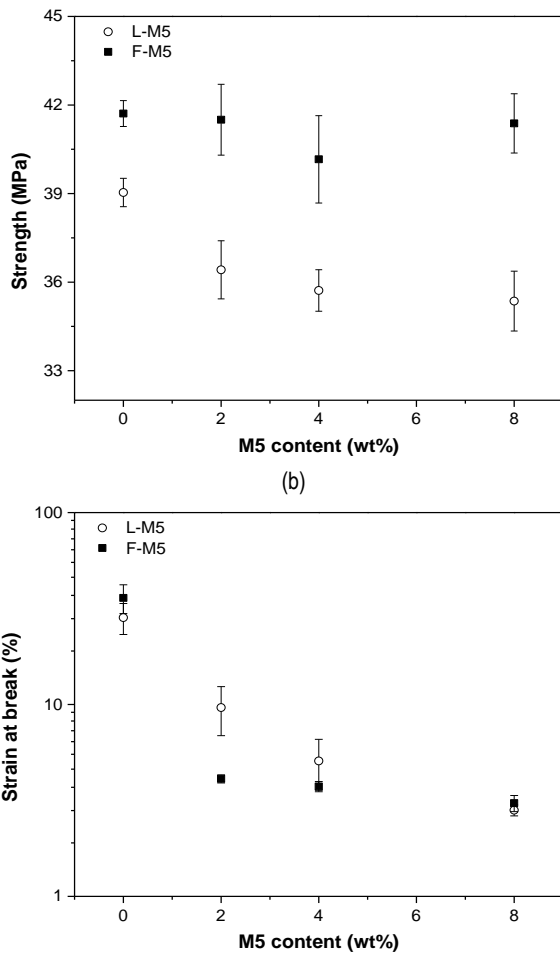
Figure 4.2-4. FESEM image of the fracture surface of (a) L-M5-8 and (b) F-M5-8.

4.2.4 Quasi-tensile tests

The quasi-static tensile properties of both ABS nanocomposites are reported in Table 4.2-2. From Figure 4.2-5, elastic modulus and yield stress of neat ABS (F) matrix are slightly higher than ABS (L) specimen which could be attributed to the presence of the mould lubricant. By adding graphene nanoplatelets, the elastic modulus was improved for both ABS types. On the other hand, the tensile strength (σ_{max}) of F-M5 samples shows relatively constant values with the filler content, but that of L-M5 specimens exhibits a slight reduction (about -9% for L-M5-8). For both nanocomposites, the presence of graphene-M5 led to a significant decrease of strain at break values.



(a)



(c)

Figure 4.2-5. Tensile mechanical properties of GNP-M5 nanocomposite with two different kind of ABS resins (L and F): (a) elastic modulus, (b) tensile strength, and (c) strain at break (c).

Table 4.2-2. Tensile mechanical properties of two different types of ABS nanocomposites (L and F) as a function of GNP-M5 nanoplatelets.

Samples	E (GPa)	σ_y (MPa)	ε_y (%)	σ_b (MPa)	ε_b (%)	E_{norm}^a
L	2147 ± 118	39.0 ± 0.5	4.1 ± 0.2	29.9 ± 0.4	28.4 ± 5.2	nd ^b
L-M5-2	2582 ± 86	36.4 ± 1.0	3.5 ± 0.1	29.1 ± 0.8	9.6 ± 2.8	10.1
L-M5-4	2868 ± 202	35.7 ± 0.7	3.2 ± 0.1	31.5 ± 2.6	5.1 ± 1.5	8.4
L-M5-8	3531 ± 282	35.4 ± 1.0	2.7 ± 0.1	33.3 ± 4.3	2.8 ± 0.2	8.1
F	2315 ± 100	41.7 ± 0.4	4.2 ± 0.1	33.6 ± 0.4	35.9 ± 6.1	nd ²
F-M5-2	2631 ± 133	41.5 ± 1.2	3.7 ± 0.1	39.9 ± 2.3	4.1 ± 0.2	6.8
F-M5-4	2911 ± 109	40.2 ± 1.5	3.6 ± 0.1	39.3 ± 1.2	3.7 ± 0.2	6.4
F-M5-8	3523 ± 209	-	-	41.4 ± 1.0	3.1 ± 0.3	6.5

^a normalised value of the improvement of the modulus following equation (4.2-1).

^b not defined.

To compare the mechanical properties of ABS composites reported in the literature, a normalised modulus (E_{norm}) was evaluated as follows:

$$E_{norm} = \frac{E_c - E_i}{E_i w_f} \quad (4.2-1)$$

where E_c is the modulus of ABS composite; E_i is the modulus of neat ABS, and w_f is the weight fraction of incorporated filler, as proposed by Pandey et al. [63]. E_{norm} formally represents the percentage of modulus variation after addition of 1% of filler.

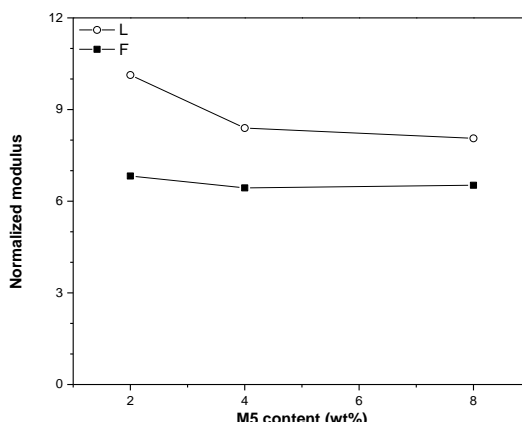


Figure 4.2-6. Improvement of normalized modulus of ABS composites according to Eq. (4.2-1) after incorporation of GNP-M5 into different ABS matrix.

Figure 4.2-6 compares the normalized modulus of ABS nanocomposites according to Eq. (4.2-1) after incorporation of GNP-M5 into two different ABS matrix. The ABS (L) shows the higher normalized modulus than ABS (F), suggesting a relative higher stiffening effect, due to the lower modulus of pure ABS (L) matrix. Moreover, the normalized modulus of ABS (F) matrix appears almost independent on filler content. On the other hand, the highest normalized modulus (E_{norm}) was observed for 2% of graphene in ABS (L) containing about 3.6 % of lubricant (see detail in section 4.3.2) with the highest lubricant/graphene ratio as shown in Table 4.2-3. A possible explanation could be the role of lubricant in the improvement of graphene dispersion. In fact, the higher the graphene content in ABS (L) composites, the lower the lubricant/graphene ratio, and the lower the normalized modulus.

Table 4.2-3. The mould lubricant (ML)/graphene ratio at different graphene content.

Graphene content	2 %	4 %	8 %
ML/GNP	1.8	0.9	0.4

According to the better results regarding MFI and stiffening effect, low viscosity ABS (L) have been selected for further investigation.

4.3 ABS-graphene nanocomposites plates

Following the results of the previous paragraph, this section is aimed at investigating the influence of four commercially available graphene nanoplatelets (M5, C300, C500, and C750) with different size and surface area (120-700 m²/g) on the properties and processability of low viscosity ABS (L) matrix. The specimens were obtained by melt compounding followed by compression moulding (CM). In particular, melt flow index, thermal transitions, electromagnetic shielding (EMI SE) and tensile mechanical properties were investigated as a function of filler content. The Halpin-Tsai model was used to fit the experimental values of tensile modulus. The material properties and modeling of GNP-M5, C300, C500, C750 in ABS matrix have never been previously reported in the open scientific literature.

4.3.1 Melt flow index

The effect of the various types of GNP nanoparticles on MFI of ABS nanocomposites is compared in Figure 4.3-1. The almost linear decrease of MFI with the percentage of nanofillers suggests that a good dispersion of graphene has been reached with the formation of a nanofiller network, determining a significant constrain of the polymer flow, and consequently an increase of viscosity, in agreement with the literature on graphene-based nanocomposites [136-140]. At the highest concentration of graphene (8 wt %), MFI was reduced by about 50% for M5, whereas higher

reduction was observed for grade C nanoparticles, i.e. about 53%, 56%, and 67% for nanofillers with specific surface area of 300, 500 and 750 g/m², respectively. The higher the nanofiller surface area, the higher the rate of reduction of MFI and the higher the viscosity. In prior work, the larger specific surface area of fillers was also reported to increase the viscosity of the unsaturated polyester resin, due to increasing of the interaction between the matrix and the particles [141].

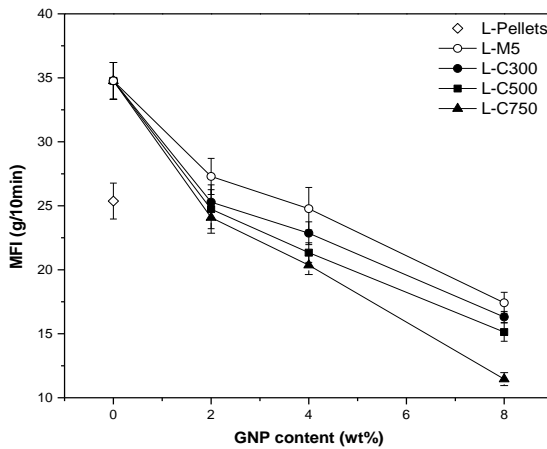
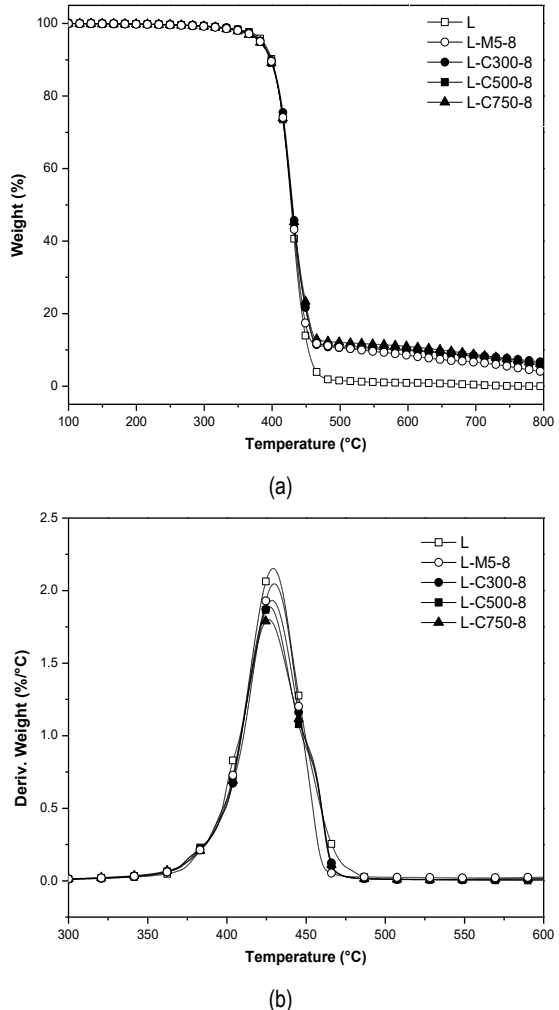


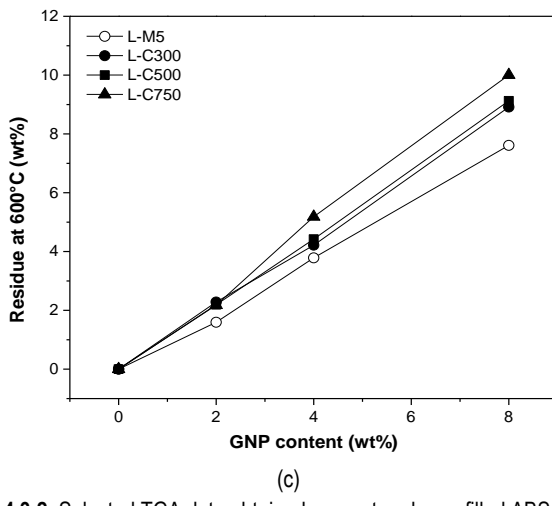
Figure 4.3-1. Melt flow index (220°C /10kg) of ABS nanocomposites as a function of GNPs.

4.3.2 Thermal analysis (TGA and DSC)

The thermal stability of graphene and its graphene-ABS composites has widely been reported in the scientific literature [63, 64, 68, 104]. In Figure 4.3-2 the thermograms of neat ABS and its nanocomposites at the highest content of graphene are plotted. Neat ABS and ABS-graphene composites decompose in one single step of degradation in inert (nitrogen) atmosphere regardless the effect of graphene. This behaviour is probably attributed to the butadiene particle content in ABS structure [80]. In addition, relative chart residue of ABS composite in Figure 4.3-2c linearly increases with the amount of nanofiller up to 7.6-10%. As reported in Table 4.3-1, the maximum degradation temperature ($T_{d,max}$) seems not to be affected by graphene content. In addition, $T_{d,max}$ slightly increases for L-M5 composites but drops for L-C500 and L-C750. This behaviour could be induced by the different size of graphene flakes, as documented in Figure 4.1-1. In general, larger flakes can hinder the diffusion of volatiles products generated by polymer decomposition. In particular, as the concentration of graphene in ABS increases, the maximum mass loss rate (MMLR) is progressively reduced. This behaviour was also observed in ABS-carbon

nanotube[80] and polypropylene-graphene composites [142]. The high surface area of graphene (e.g. C500 and C750) reduces the value of MMLR which is expected as a result of stronger interphase bonding between the matrix and the C-type graphene.





(c)

Figure 4.3-2. Selected TGA data obtained on neat and nanofilled ABS-graphene performed under a nitrogen atmosphere: (a) mass loss curves, (b) derivative of mass loss curves, and (c) relative residual values at 600°C.

Table 4.3-1. Results of TGA analysis of neat and nanofilled ABS-graphene performed under nitrogen atmosphere.

Samples	$T_{d,\max}$ (°C)	Mass loss (wt%)	MMLR (%/°C)	Residual mass at	
				600°C (wt%)	800°C (wt%)
L	429.2	47.5	2.15	0.9	0.0
L-M5-2	428.3	48.5	2.13	2.5	0.9
L-M5-4	430.5	47.3	2.10	4.7	2.0
L-M5-8	430.0	48.2	2.05	8.5	3.9
L-C300-2	428.0	50.4	2.12	3.2	1.1
L-C300-4	429.2	50.2	2.04	5.1	2.9
L-C300-8	428.6	52.9	1.93	9.8	6.6
L-C500-2	428.1	50.2	2.14	3.1	0.7
L-C500-4	426.9	51.6	2.07	5.3	1.9
L-C500-8	426.9	54.3	1.89	10.0	5.8
L-C750-2	426.0	51.2	2.15	3.1	0.2
L-C750-4	427.1	54.4	2.05	6.1	2.2
L-C750-8	426.3	56.1	1.80	10.9	6.1

$T_{d,\max}$: maximum degradation rate temperature.

MMLR: Maximum mass loss rate.

Typical DSC thermograms of ABS and relative nanocomposites are illustrated in Figure 4.3-3. Two transitions can be clearly observed in both first and second heating scan of DSC analysis. At about 101°C ABS displays a glass transition signal of the amorphous styrene-acrylonitrile copolymer (SAN) phase, followed by another signal at about 137°C.

Table 4.3-2 reports thermal data of ABS pellets and compression molded plates. In particular, T_g of SAN phase, and melting temperature (T_m) and melting heat (ΔH_m) of mould lubricant for all the compositions are shown. The mold lubricant content in ABS could be evaluated as 3.6 wt%, according to literature from the ratio of the melting heat of pellets and the reference enthalpy 98.8 J/g of pure lubricant [143]. In both first and second heating scan, the presence of M5 nanoparticles does not significantly affect the T_g of ABS matrix, whereas a slight increase of T_g was observed with other GNP, up to about 2°C in the case of 8% of C750. Moreover, the melting temperature of the mould lubricant (T_m) decreased after addition of graphene, by about 7°C for C750 filled samples. The higher the graphene content and/or the higher the surface area of the filler, the lower the melting temperature. Similarly, a significant decrease of melting heat was found in ABS composites, with values of the endothermal heat lower than that expected from composition, suggesting an interaction between mold lubricant and graphene. This fact is more evident in the second DSC heating, after a controlled cooling scan at -10°C/min, where all the samples exhibited not only an increase of T_g and T_m , and but also a decrease of the melting heat. This latter effect is well evidenced by considering the normalized melting heat of mold lubricant, ΔH_N , referred to the fraction of ABS matrix, according to the equation:

$$\Delta H_N = \frac{\Delta H_m}{1 - w_f} \quad (4.3-1)$$

where w_f is filler fraction in nanocomposite. Figure 4.3-4 shows the reduction of the melting heat of lubricant (ΔH_N) in the second DSC scan with the increase of the surface area and/or of the content of GNP.

Moreover, the relative crystallinity (RC) of mold lubricant in ABS composites could be evaluated according to the equation:

$$RC = 100 \times \frac{\Delta H_N}{3.6} \quad (4.3-2)$$

from the ratio of the normalized melting heat ΔH_N of the composite and the melting heat of pristine ABS pellets (i.e. 3.6 J/g). It is interesting to observe that the percentage of crystallized mold lubricant was found to progressively decrease with the addition of filler, reaching about 36-39% in the case of C500-8 and C750-8, confirming a certain effect of the graphene nanoparticles on the crystallizability of the mold lubricant, both in the first and especially in the second DSC scan (see Table 4.3-2).

These findings not only suggest an interaction between the mould lubricant and graphene but also indirectly indicate a good dispersion of the filler.

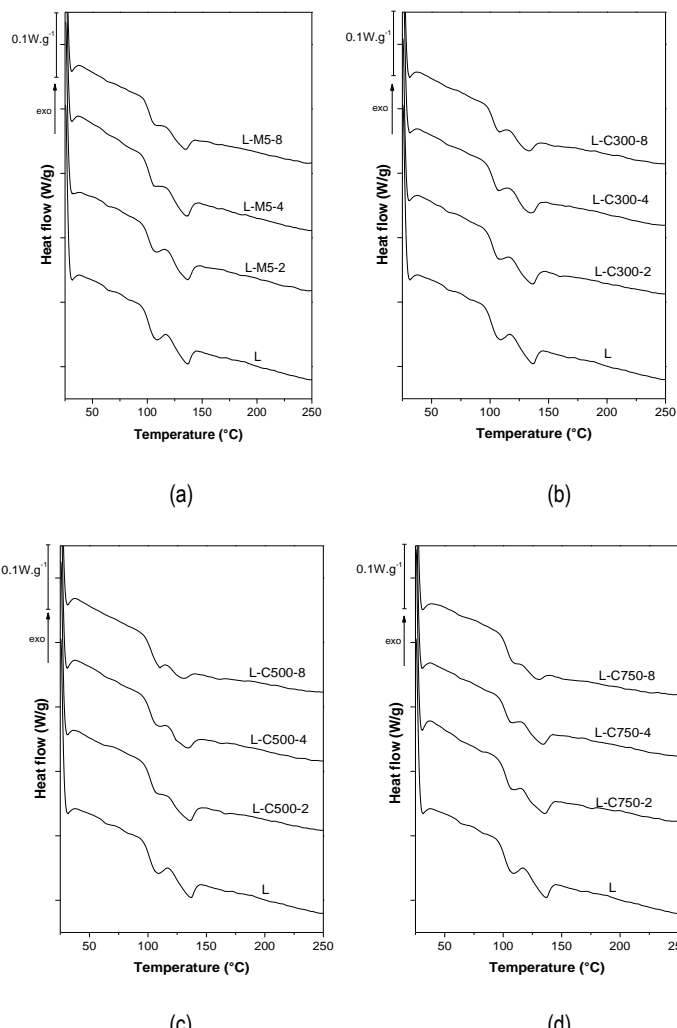


Figure 4.3-3. DSC thermograms (first heating scan) of neat ABS and nanocomposites at different content of M5 (a), C300 (b), C500 (c) and C750 (d) graphene nanoplatelets.

Table 4.3-2. Glass transition temperatures (T_g) of styrene–acrylonitrile phase, melting temperature (T_m), melting heat (ΔH_m), and relative crystallinity index (RC) of mould lubricant for ABS and relative nanocomposite as measured in DSC analysis.

Samples	First heating				Second heating			
	T_g (°C)	T_m (°C)	ΔH_m (J/g)	RC*	T_g (°C)	T_m (°C)	ΔH_m (J/g)	RC*
L-Pellets	101.3	138.9	3.6	100	104.3	138.7	3.0	83
L	100.7	136.4	3.1	86	103.3	137.1	2.8	78
L-M5-2	101.2	136.4	3.1	88	103.8	136.8	2.7	77
L-M5-4	102.0	134.9	2.9	84	103.3	135.7	2.5	72
L-M5-8	102.0	134.1	2.4	72	104.3	135.1	1.8	54
L-C300-2	102.0	135.4	2.6	74	104.3	138.6	2.0	57
L-C300-4	102.5	133.6	2.7	78	104.3	136.6	1.7	49
L-C300-8	102.3	132.3	2.2	66	105.1	134.8	1.1	33
L-C500-2	102.3	135.1	2.7	77	105.3	137.6	2.1	60
L-C500-4	102.0	132.4	2.6	75	104.8	135.5	1.7	49
L-C500-8	102.8	129.1	1.2	36	105.6	132.0	0.8	24
L-C750-2	102.0	134.9	2.7	77	105.2	137.3	2.1	60
L-C750-4	102.1	133.4	2.4	69	105.1	134.4	1.5	43
L-C750-8	103.0	128.9	1.3	39	105.5	129.5	0.7	21

* Relative crystallinity following equation (4.3-2).

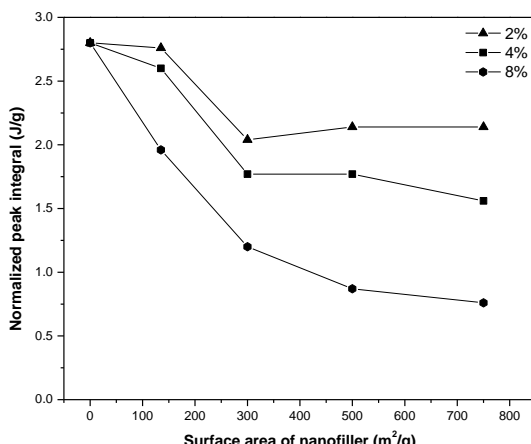
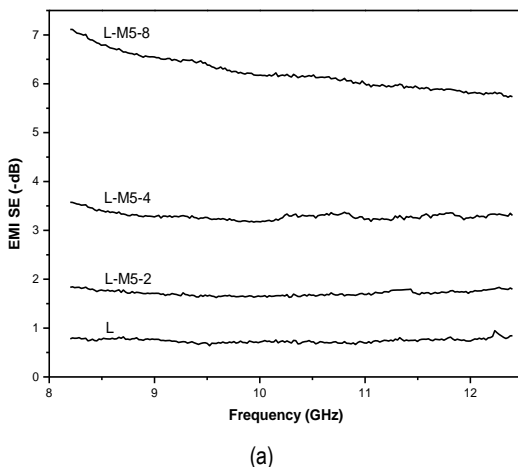


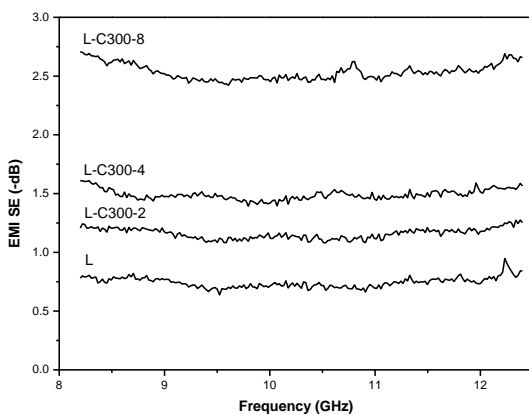
Figure 4.3-4. Normalized melting heat (from second DSC heating) of mould lubricant as a function of surface area and content of GNP nanoplatelets in ABS nanocomposites.

4.3.3 Electromagnetic interference shielding effectiveness (EMI SE)

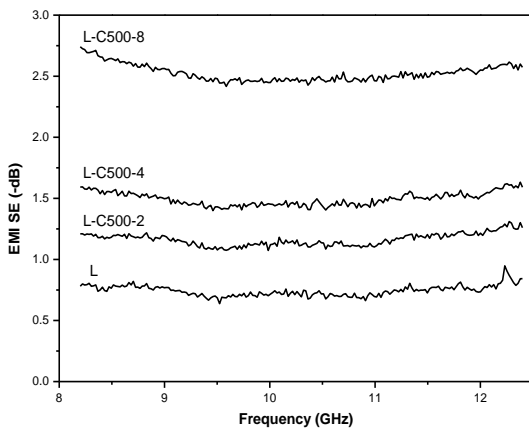
Figure 4.3-5(a-d) shows the representative plots of EMI SE expressed in decibel (dB) of the neat ABS and various GNP-filled nanocomposites in the frequency range from 8 to 12.4 GHz. An average EMI SE value of -0.74 dB for neat ABS was measured, indicating that the polymer is almost transparent to magnetic waves. As expected, the increase in the conductive filler content resulted in an improvement of EMI SE, as reported in literature for various carbon-based ABS composites [65, 78, 125, 144].

Nanocomposites containing C300, C500 and C750 nanoplatelets exhibited similar electromagnetic attenuation, for a given GNP content, almost independently on the surface area of the filler. On the other hand, nanocomposites filled with M5 nanofiller (thickness of 6 nm), showed a higher EMI SE, analogously to ABS composites filled with high structure carbon black [125]. Furthermore, the EMI SE of nanocomposites containing until 4 wt% of GNP is almost independent from the frequency, whereas nanocomposites with 8 wt% of GNP showed a slight influence of the shielding effectiveness on the frequency in the X-band.

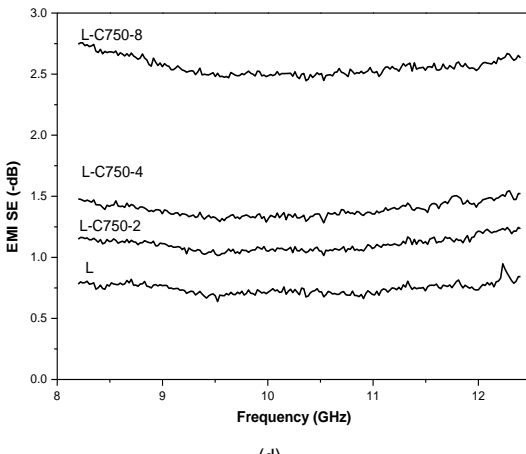




(b)



(c)



(d)

Figure 4.3-5. Representative curves of EMI SE of nanocomposites containing different types of graphene nanoplatelets: (a) L-M5, (b) L-C300, (c) L-C500 and (d) L-C750.

The maximum of shielding effectiveness in ABS composites was obtained with the highest loading of GNP (i.e. 8 wt%). In particular, EMI SE increased 257% after addition of GNP-C (C300, C500, and C750) from -0.7 to -2.5 dB, and 786% with graphene type M5 (from -0.7 to -6.2 dB). However, these results of graphene/ABS composite appeared lower than those of other carbon based ABS composites reported in the literature. For instance, Sachdev et al. obtained a shielding efficiency of -60 dB after addition of 15 wt% of graphite in the X-band [65], whereas by using 10 wt% of multiwall carbon nanotubes (MWCNTs) Jyoti et al. achieved a shielding efficiency of -39 dB in the Ku-band, 12-18 GHz [78]. The EMI SE typically required for commercial application is of about -22.0 dB, which corresponds to <1% of transmitted electromagnetic wave [144]. The results reported in this work indicate that by adding up to 8 wt% of GNP in the ABS matrix, it is not possible to reach the EMI SE levels required for commercial applications.

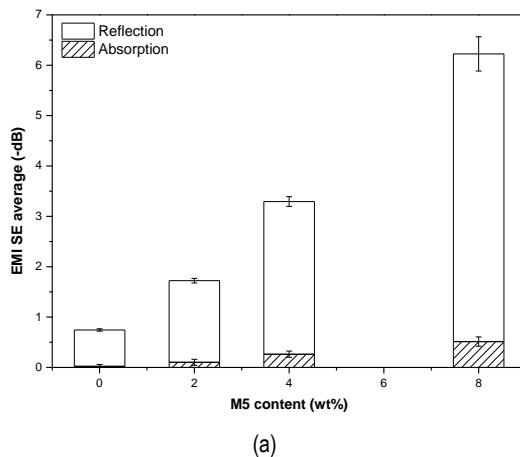
Due to the almost independence on frequency, the average values of reflection and absorption contributes in the range frequency of 8.2–12.4 GHz were reported and compared in Figure 4.3-6 as a function of graphene content. For all compositions, the shielding by either reflection or absorption of composites increases with increasing GNP content, resulting in higher EMI SE. In addition, the effect of the surface of graphene on absorption and reflection of ABS nanocomposites is presented in Figure 4.3-7(a-b), respectively.

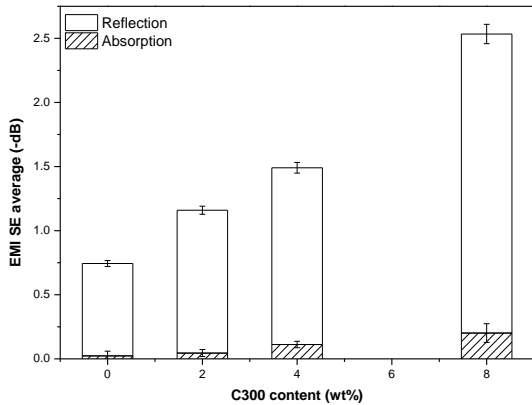
In particular, the dominant shielding mechanism is the reflection for all graphene/ABS composites, due to the platelet-shaped GNP that provide higher

surface area for interaction with the electromagnetic waves, as previously observed in carbon based poly(styrene-b-ethylene-ran-butylene-b-styrene) (SEBS) composite [145]. However, it should be noted that other researchers reported that in different nanocomposites the shielding absorption contribute is higher than that of reflection one, $SE_A > SE_R$ [65, 125, 146, 147].

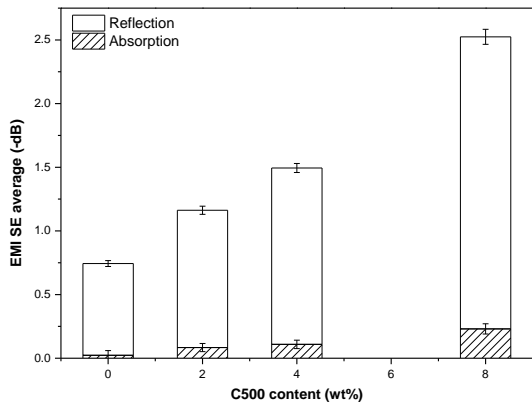
It is interesting to compare the effects of graphene and graphene oxide nanoplatelets that have been recently used to improve the EMI SE of amorphous thermoplastic polymers. It is certainly worthwhile to note that Yan et al. [146] achieved an ultra-efficient EMI shielding of -45.1 dB in the X-band, with 7 wt% of reduced graphene oxide, following a peculiar processing technique of segregation at high pressure starting from micrometric polystyrene powder. On the other hand, following traditional processing conditions, King et al. prepared the various composition of polycarbonate (PC) nanocomposites with GnP type M nanoparticles through twin screw compounding [148]. They reported no effect after addition 4 wt% of GNP-M5 in PC, while nanocomposites filled with 15 wt% showed SE value of -6.3 dB at 0.8 GHz. Similarly, in the present research a lower percentage of GNP-M5, 8 wt%, was shown to obtain -7.1 dB at 8.2 GHz in ABS nanocomposites produced by direct melt compounding. Following these results, it is possible to conclude that M5 nanoparticles appear more effective in EMI SE than C-type graphene nanoplatelets in ABS nanocomposites.

The better performance of ABS nanocomposites containing M5 can also be related to the higher average lateral dimensions of graphene (about 5 microns) with respect to C-type graphene nanoplatelets, and determining an increase of interaction with the radiation, and consequently an improvement of EMI SE.

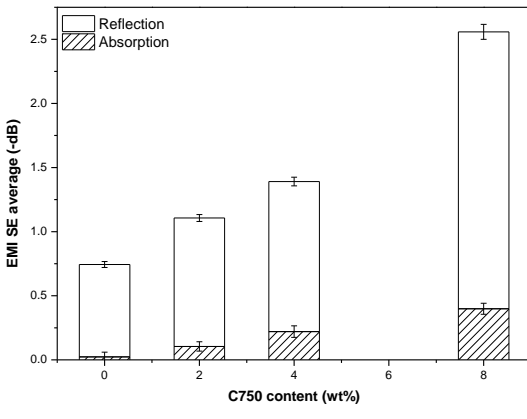




(b)

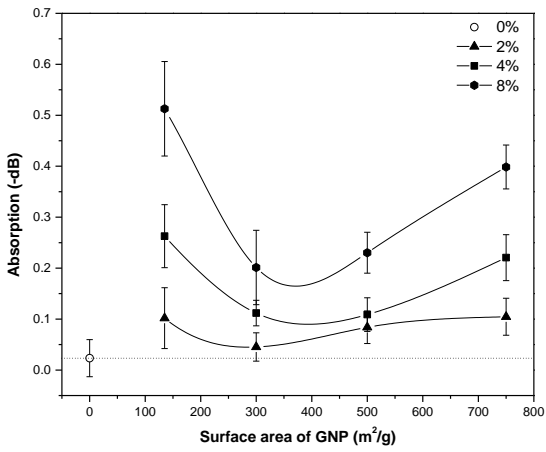


(c)



(d)

Figure 4.3-6. Influence of absorption and reflection mechanisms on the EMI SE of nanocomposites containing different graphene nanoplatelets: (a) L-M5, (b) L-C300, (c) L-C500 and (d) L-C750, with various fillers contents.



(a)

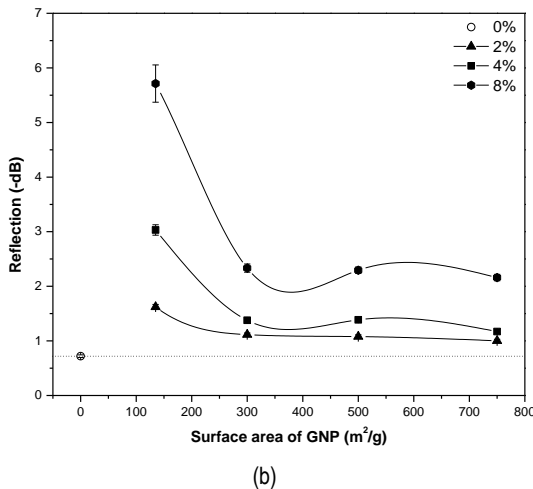


Figure 4.3-7. Absorption (a) and reflection (b) of ABS nanocomposites as a function of surface area and content of GNP nanoplatelets.

In order to shed more light on the EMI SE behaviour, the electrical resistivity of ABS and GNP nanocomposites at highest graphene content (8 wt%, i.e. about 4 vol%), has been compared and reported in Table 4.3-3. Despite the low resistivity of single graphene nanoparticle, about $50 \times 10^{-6} \Omega \cdot \text{cm}$ and $1 \Omega \cdot \text{cm}$ in parallel and in perpendicular direction respectively [149], volume resistivity of ABS ($2.15 \times 10^{15} \Omega \cdot \text{cm}$) was only slightly reduced after addition of GNP of Series C (about $0.9 \times 10^{15} \Omega \cdot \text{cm}$), whereas a better improvement was obtained in composite containing M5 ($1.8 \times 10^{14} \Omega \cdot \text{cm}$). The higher the content of conductive filler, the higher the resistivity reduction, the higher the increase of EMI SE.

Table 4.3-3. Volume resistivity and average EMISE of ABS and nanocomposites with 8% wt of GNP.

Samples	GNP Surface (m^2/g)	Electrical resistivity $\times 10^{-14}$ ($\Omega \cdot \text{cm}$) *	EMI SE (-dB) **
L	-	21.5 ± 3.3	0.74 ± 0.04
L-C750-8	750	9.71 ± 2.57	2.53 ± 0.67
L-C500-8	500	8.03 ± 1.64	2.52 ± 0.66
L-C300-8	300	8.95 ± 3.12	2.56 ± 0.69
L-M5-8	120-150	1.75 ± 0.28	6.23 ± 0.33

*Average of three samples.

**Average between 8.2-12.4 GHz.

The relationship between the decrease of resistivity and the effect of magnetic shield is shown in Figure 4.3-8 that correlates the better performance induced by the addition of M5 nanoparticles with reduced resistivity and the correspondent higher EMI SE. The relative volume resistivity, however, is not reduced enough to reach a conductive behaviour. Therefore, due to the low values of EMI SE achieved by using up to 8 wt% of GNP higher fractions of GNP need to be incorporated in order to reach to higher values. In fact, as reported by Merlini et al. [144], the EMI SE levels required for commercial applications were obtained only after addition of 15 wt% of GNP into a PU matrix.

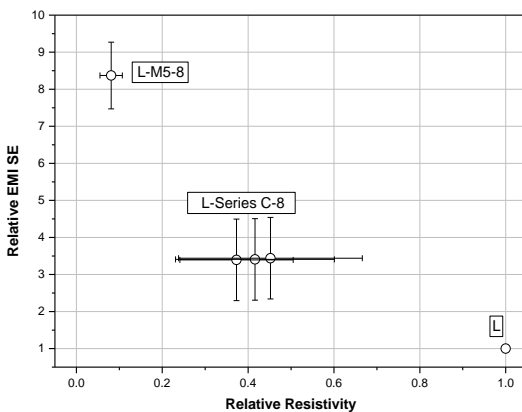


Figure 4.3-8. Relative electromagnetic shield vs relative resistivity of GNP-ABS composite at 8 wt% of M5 and Series C.

It should be noted that King et al. after addition of GNP-M5 at 8 wt% (5 vol %) in polycarbonate matrix reached a percolation threshold with the electrical resistivity of $4.0 \times 10^7 \Omega \cdot \text{cm}$ [150].

Following these results, M5 nanoparticles appear the more promising GNP candidate for the production of ABS nanocomposites for EMI SE applications and a minimum filler content of at least 12 wt% could be suggested.

4.3.4 Quasi-static tensile tests

The tensile properties of nanocomposites with the different types of graphene are summarized in Table 4.3-4. It can be noticed that elastic modulus of ABS increased proportionally to the filler loading. The modulus of composites containing the highest amount (8 wt%) of grade C GNPs is increased from 2147 MPa to 2523 MPa (i.e. 17%), to 2623 MPa (i.e. 22%) and to 2527 MPa (i.e. 17%) for C300, C500 and C750 nanofillers respectively. More effectively, the addition of M5 determined a higher

increase of modulus for all the compositions, reaching 3531 MPa (i.e. 64%) in nanocomposite containing 8 wt% of nanofiller. These better performances of M5 in increasing ABS stiffness are in agreement with other literature data. For instance, King et al. reported an increase of tensile modulus of thermosetting epoxy of about 14% and 23% after addition of 6 wt% of GNP-C300 and GNP-M5 respectively [119]. An analogous and more evident effect was also reported by Wang et al. [126] for epoxy nanocomposites containing 5% of graphene; they showed an increase of tensile modulus of about 22% after addition of C750 and an increase of 48% after addition of M5 nanoparticles. Following their results and other literature data, Wang et al. attributed the superior behaviour of GNP-M5 to their higher aspect ratio [126].

Moreover, the yield stress of ABS nanocomposite is fairly constant at about 39-41 MPa by the addition of grade C GNPs (C300, C750 and C500), whereas the effect of M5 nanofiller is to slightly reduce the yield strength (by about 9%). Concerning the ultimate properties, the strain at break is markedly decreased down to 3-4% after addition of 8% of GNP. Correspondingly, the stress at break reached a maximum of 37-40 MPa in nanocomposites containing graphene of C series, whereas only 33 MPa in the case of M5 nanoplatelets.

The lower yield stress and strength of composites filled with M5 nanoparticles can be attributed to the poor adhesion between ABS matrix and the nanofiller. Similarly, a significant reduction of strength in M5/epoxy nanocomposites [119, 126], and an almost constant strength in C750/epoxy nanocomposites with respect to the pure matrix was also reported [126]. Wang et al. attributed the higher strength and the better adhesion of C750 to the higher content of oxygen functional groups, in comparison to the lower adhesion and the lower oxygen content of M5 [126].

However, in order to understand the ultimate mechanical properties reported in Table 4.3-4, the simple explanation referred to the absolute content of oxygen is not exhaustive/satisfactory. Following a deeper interpretation of XPS analysis (Table 4.1-1, and Figure 4.1-2b and Figure 4.1-2c), the lower ultimate properties of GNP-M5/nanocomposite and the reduced adhesion between matrix and filler, could be attributed not only to the lower content of ether/alcohol groups, but also to the significant content of sulphur and carbonyl groups on the surface of GNP-M5. In general, the higher the content of ether/alcohol groups on the graphene surface, the higher the adhesion to ABS matrix, and the higher the yield stress and strength. The effect of GNP-M5 on mechanical properties with respect to the Series C appeared similar for both thermosetting and thermoplastic matrices [119, 126].

Table 4.3-4. Tensile properties of nanocomposites as a function of different GNP type and content.

Samples	V _f (vol %)	E (GPa)	σ _y (MPa)	ε _y (%)	σ _b (MPa)	ε _b (%)	E _{norm} ^a
L	0	2147 ± 118	39.0 ± 0.5	4.1 ± 0.2	29.9 ± 0.4	28.4 ± 5.2	nd ^b
L-M5-2	1.02	2582 ± 86	36.4 ± 1.0	3.5 ± 0.1	29.1 ± 0.8	9.6 ± 2.8	10.1
L-M5-4	2.06	2868 ± 202	35.7 ± 0.7	3.2 ± 0.1	31.5 ± 2.6	5.1 ± 1.5	8.4
L-M5-8	4.21	3531 ± 282	35.4 ± 1.0	2.7 ± 0.1	33.3 ± 4.3	2.8 ± 0.2	8.1
L-C300-2	0.90	2196 ± 74	38.6 ± 1.0	3.8 ± 0.2	29.3 ± 0.7	11.7 ± 6.0	1.1
L-C300-4	1.83	2340 ± 101	39.8 ± 0.3	3.6 ± 0.1	33.8 ± 2.8	5.1 ± 1.2	2.3
L-C300-8	3.74	2523 ± 224	37.8 ± 0.9	3.3 ± 0.2	37.2 ± 0.8	3.4 ± 0.3	2.2
L-C500-2	0.91	2368 ± 184	41.4 ± 0.7	4.0 ± 0.2	33.2 ± 1.9	6.8 ± 2.5	5.2
L-C500-4	1.85	2434 ± 179	40.7 ± 0.6	3.7 ± 0.2	38.9 ± 1.5	3.9 ± 0.3	3.3
L-C500-8	3.78	2623 ± 101	39.3 ± 2.0	3.5 ± 0.1	38.8 ± 2.2	3.6 ± 0.3	2.8
L-C750-2	0.95	2312 ± 348	41.0 ± 0.9	4.0 ± 0.2	33.1 ± 2.8	12.0 ± 5.3	3.8
L-C750-4	1.93	2271 ± 122	39.8 ± 0.7	3.6 ± 0.1	36.4 ± 1.6	4.0 ± 0.2	1.4
L-C750-8	3.94	2527 ± 177	40.4 ± 2.5	3.4 ± 0.2	40.3 ± 2.4	3.4 ± 0.2	2.2

^a normalised value of the improvement of the modulus following equation (4.2-1).

^b not defined

Figure 4.3-9 compares the normalized modulus at the highest weight fraction from equation (4.2-1) of various carbon based ABS nanocomposites produced from different processes. High normalized modulus between 12-27 were calculated for carbon fiber (CF) composite produced by compression molding [11], or additive manufacturing [10, 151]; and lower values of 3.7 for short CF composite obtained by injection molding [152]. It is also worth noting the case of reduced graphene oxide (rGO) for which a normalized modulus of 11 was obtained, and attributed to the superior dispersion in ABS after chemical modification with respect to the scarce be of graphene oxide [153]. Different the situation of other lower size carbon fillers at micro or nano level, evaluated from recent literature data for ABS composites, for which the normalized modulus was determined in the range 1.5-4.0, i.e. 1.7 after addition of 40 wt% of carbon black (CB) [154], 1.68 with 9 vol% of graphite flakes (GFs) [63], 3.9 with 10 wt% of MWCNTs [78], 3.2 with 7.5 wt% of graphene [155].

It was found that the addition of GNP determines a normalized modulus in the range from 2.2 to 2.8 for C300, C500 and C750, and a remarkable a value of 8.1 for M5 at the highest filler weight fraction of 8 wt %. These results are comparable to those of other nanocomposites with GNP dispersed in different matrices. For instance, in epoxy resin values of 2.3 and 3.9 were obtained for C300 and M5 according to the data presented by King et al. [119]; and higher normalized modulus could be obtained from the results of Wang et al. [126], i.e. 4.4 for C750 and 9.6 for M5. Moreover, in the case of polycarbonate, normalized modulus of 3.6, 4.0 and 11.2 could be determined for carbon black, carbon nanotube and graphene type M5, respectively [150].

It is possible to conclude that between the various examined graphenes, GNP-M5 allows reaching the higher normalized modulus values.

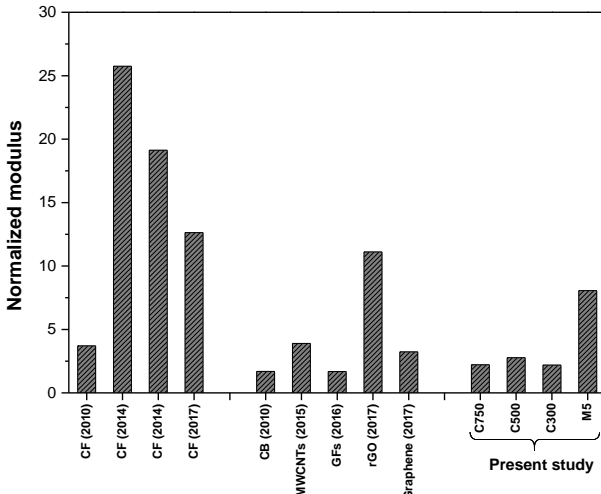


Figure 4.3-9. Improvement of normalized modulus of ABS composites according to Eq. (4.2-1) after incorporation of different carbonaceous fillers, such as carbon black (CB [154]), MWCNTs [78], graphite flakes (GFs) [63], reduced graphene oxide (rGO [153]), graphene [155], and the GNP nanoplatelets M5, C300, C500, and C750 of the present study. ABS composites reinforced with carbon fiber (CF) and produced by injection molding [152], compression molding [11], and additive manufacturing [10, 151] are also reported.

4.3.5 Modelling of tensile modulus

The empirical Halpin-Tsai model is a simple approach to predict the modulus of composite materials which takes into account the modulus of matrix E_M and filler E_f , filler aspect ratio ξ , the volume fraction of filler V_f , assuming a homogeneous dispersion and perfect interfacial adhesion between polymer/filler, [42, 116-119]. The tensile modulus in both longitudinal E_L and transverse E_T directions can be predicted according to Halpin-Tsai model [120, 121] by the following equations:

$$E_L = \frac{1 + \xi \eta_L V_f}{1 - \eta_L V_f} E_M \quad (4.3-3)$$

$$E_T = \frac{1 + 2 \eta_T V_f}{1 - \eta_T V_f} E_M \quad (4.3-4)$$

where the parameters η_L , η_T and ξ are defined as:

$$\eta_L = \frac{(E_f / E_M) - 1}{(E_f / E_M) + \xi} \quad (4.3-5)$$

$$\eta_T = \frac{(E_f / E_M) - 1}{(E_f / E_M) + 2} \quad (4.3-6)$$

$$\xi = \frac{2 D_f}{3 t_f} \quad (4.3-7)$$

D_f and t_f are lateral diameter and thickness of graphene nanoplatelets, respectively. The volume fraction V_f is linked to the weight fraction w_f through the following equation:

$$V_f = \frac{w_f \rho_M}{w_f \rho_M + (1-w_f) \rho_f} \quad (4.3-8)$$

where, ρ_M and ρ_f are the density values of ABS matrix and graphene nanoplatelets, respectively.

Subsequently, the modulus of a composite with platelets filler long axis parallel to the loading direction (E_c^{Parallel}) and randomly oriented platelets fillers in all three dimensional 3D-directions (E_c^{Random}) can be predicted according to the literature [60, 122, 123] as follow:

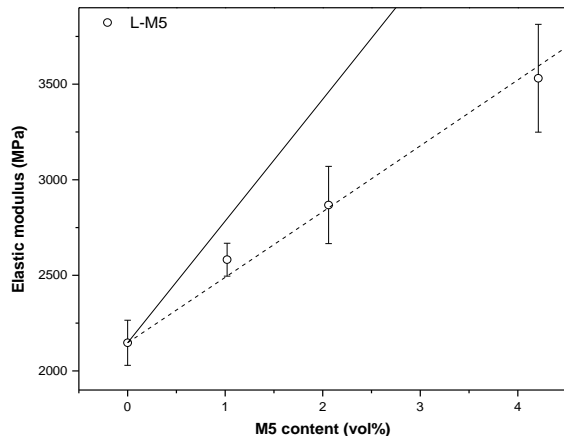
$$E_c^{\text{Parallel}} = E_L \quad (4.3-9)$$

$$E_c^{\text{Random}} = 0.49E_L + 0.51E_T \quad (4.3-10)$$

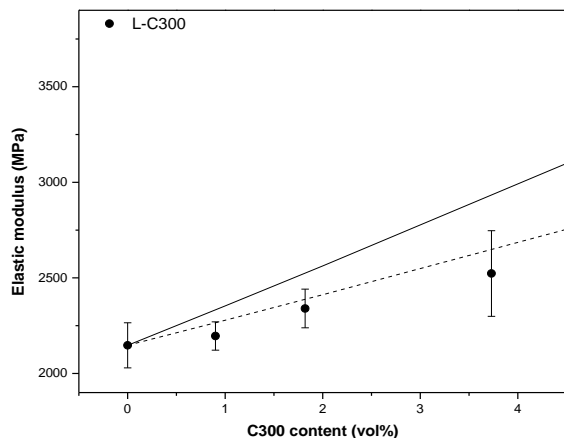
In the Halpin-Tsai model an experimental modulus for neat ABS of 2147 MPa was considered (Table 4.3-4). The aspect ratios are considered equal to 19 for GNP-C (C300, C500 and C750) as reported by Chong et al. [60] and 833 for GNP-M5 ($D_f = 5000$ nm and $t_f = 6$ nm). The outcome of the model largely depends on the value of tensile modulus of the GNP (E_f). The “in the plane” tensile modulus of a single-layer graphene is reported to be as high as 1000 GPa [52, 60, 156]. In prior works, a modulus of 250 GPa was considered for graphene by Gomez-Navarro et al. [157] and Mayoral et al. [158], while Karevan et al. [159] and Pedrazzoli et al. [160] adopted a value of 70 GPa. Since GNPs consists of several layers of graphitic planes bonded by van der Waals dispersive forces, King et al. [119] suggested an elastic modulus of 36.5 GPa. In the present study, an elastic modulus of 70 GPa has been tentatively assumed.

A comparison between the experimental data and the predictions of the two analytical models (in the plane and 3D random orientation) is reported in Figure 4.3-10. It is evident that the experimental modulus of nanocomposites containing GNPs M5, C300, C500 and C750 is adequately well fitted by Halpin-Tsai model assuming a three-dimensional (3D) random orientation of all the fillers. These results are in conformity

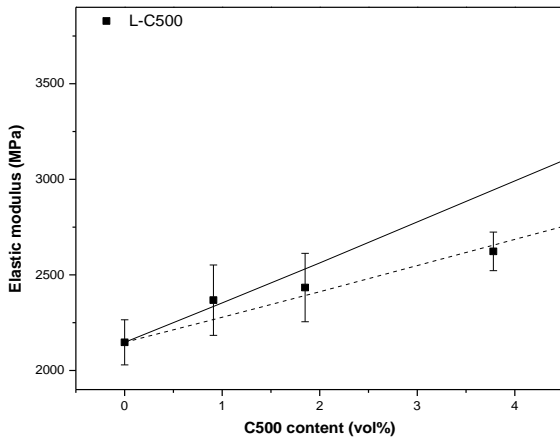
with the processing conditions (compounding and compression molding), where almost no orientation is expected.



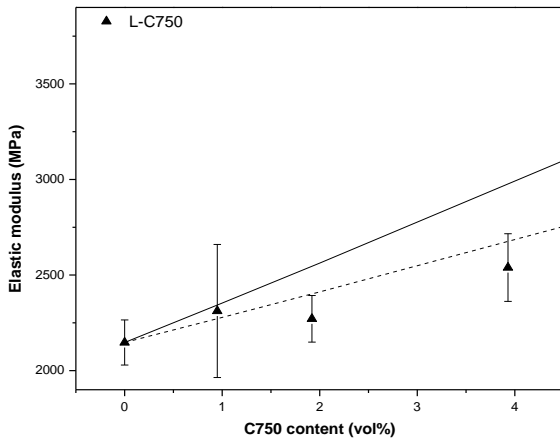
(a)



(b)



(c)



(d)

Figure 4.3-10. Elastic modulus of nanocomposites with different type of graphene, i.e., a) L-M5, b) L-C300, c) L-C500 and d) L-C750. Continuous and dot lines represent prediction according to Halpin-Tsai models with in-plane and 3D random orientations, respectively.

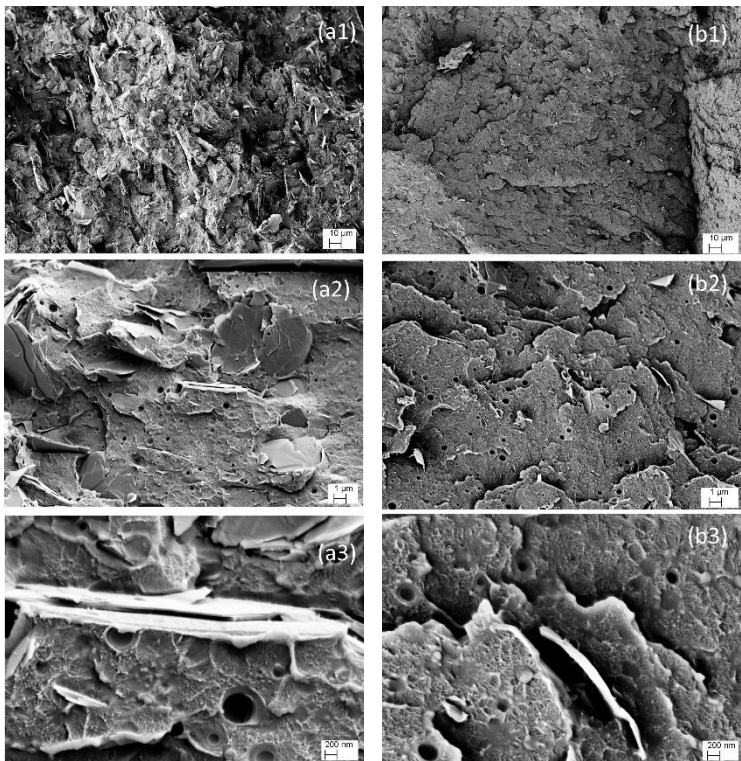
4.3.6 Fractography

Relative good dispersion of graphene in ABS matrix can be observed for all the compositions, as documented in Figure 4.3-11(a1-d1) from the fracture surface of nanocomposites at GNP loading of 8 wt%. For C300, C500, C750 and M5

nano composites, graphene nanoplatelets are likely to be an almost random-like orientation as better shown in Figure 4.3-11(a2, b2, c2 and d2), which confirm the hypothesis of 3D randomly oriented nanoplatelets assumed in the Halpin-Tsai model. For M5 nano composites, wider graphene flakes can be visualized in Figure 4.3-11(a2-a3), composed of single and multilayer platelets, whose thickness appeared to be about 35-40 nm. It is worthwhile to observe that the fracture surface evidences a quite poor filler/matrix adhesion level and wrinkles of graphene flakes were also observed. These features could justify the lower yield stress of M5 nanocomposite (36 MPa) with respect to that of ABS (39 MPa). On the other hand, the higher yield stress of C500 and C750 (40-41 MPa) could be associated to the lower size of the particles and to a better adhesion between ABS matrix and the GNP nanoplatelets at higher oxygen content on the surface.

At the highest magnification, the larger dimension of single graphene can be evaluated with lateral width of about 5.3 micron, 2.7 micron, 580 nm and 410 nm for M5 (Figure 4.3-11a3), C300(Figure 4.3-11b3), C500 (Figure 4.3-11c3) and C750 (Figure 4.3-11d3), respectively. In particular, for C750 samples (Figure 4.3-11d3), the smallest size of the nanoparticle can be confirmed. Moreover, the thickness of about 25-35 nm can be evidenced for all C-type nanoparticles. These geometrical dimensions appeared only partially in agreement with the producer's data sheet (Figure 4.3-11). The larger thickness could be attributed to an overlapping effect of various tightly bonded nanoplatelets.

Some sub-micrometric cavities in the range of about 40-550 nm were also observed in all samples (see Figure 4.3-11 at high magnification), which could be associated with the presence of a mould lubricant additive. In fact, during composite preparation, the mould lubricant could be only partially dispersed in the matrix and/or on the filler surface, and a part of it could be separated in homogeneous spherical microparticles, that could be lost after exposure of the fracture surfaces. Moreover, the observed size of the nanofillers appeared proportional to the melting enthalpy of the mould lubricant, as shown in Table 4.3-2 and Figure 4.3-4.



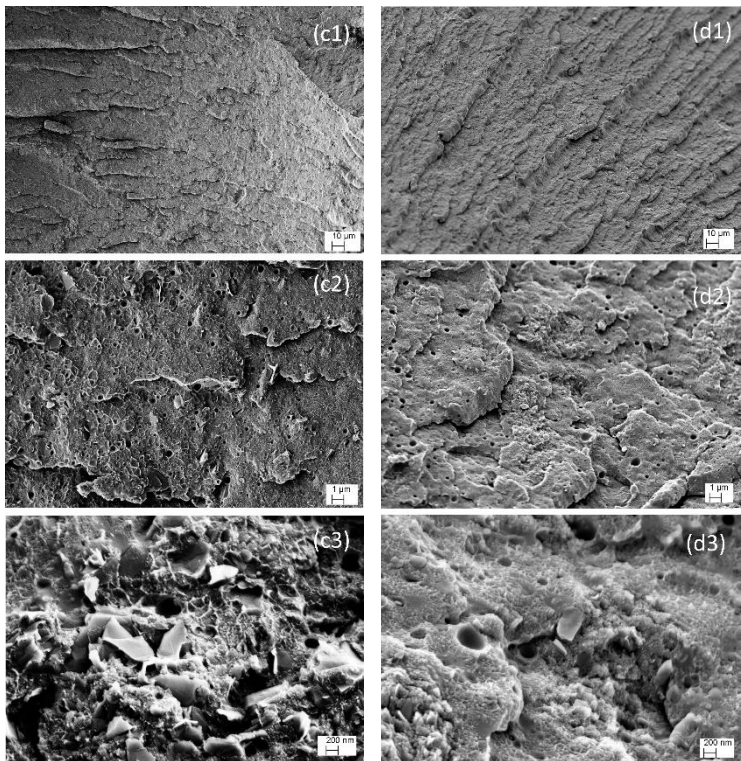


Figure 4.3-11. SEM micrographs of L-M5 (a), L-C300 (b), L-C500 (c), and L-C750 (d) nanocomposites at graphene loading of 8 wt% obtained at increasing magnifications: 1000x (1), 10000x (2) and 50000x (3).

4.4 Fused deposition modelling with ABS-graphene nanocomposites

ABS-graphene-filaments suitable for a fused deposition modeling (FDM) process were produced through melt compounding and extrusion. On the basis of the work presented in the previous sections, ABS (L) with lubricant and graphene nanoplatelets-M5 (GNP-M5) were selected. The material composition was optimized in terms MFI and mechanical properties. The properties of neat ABS and ABS/GNP-M5 nanocomposites were monitored on samples obtained by compression moulding, extruded filament and FDM-printed parts from standard commercial machine. Moreover, the effect of GNP on ABS 3D printed parts was investigated as a function of the most important parameters of the FDM process such as the building (i.e. horizontal, vertical and perpendicular), infill pattern and infill density.

4.4.1 Selection of GNP content

Figure 4.4-1 summarizes the tensile mechanical properties and melt flow index values determined on the compression molded (CM) materials as a function of the GNP-M5 content. The elastic modulus of nanocomposite materials increases with the amount of GNP-M5. On the other hand, the tensile strength of materials slightly decreases when the GNP-M5 concentration increases. At the same time, a remarkable reduction of the deformation at break can be observed when GNP-M5 nanoparticles are added. This experimental evidence could be attributed to a poor adhesion level between the GNP-M5 nanoplatelets and the ABS matrix. It is worthwhile to observe that the MFI values strongly decrease with the GNP-M5 content due to the increasing viscosity in nanocomposites induced by the formation of a nanofiller network, as documented by the torque increase after addition of graphene to ABS in melt-compounding process. Considering the viscosity and elongation at break of extruding filaments for the 3D printing process, a GNP-M5 content of 4 wt% has been considered to be an optimal value. Therefore, all the subsequent investigations have been limited to nanocomposites containing 4 wt% of GNP-M5.

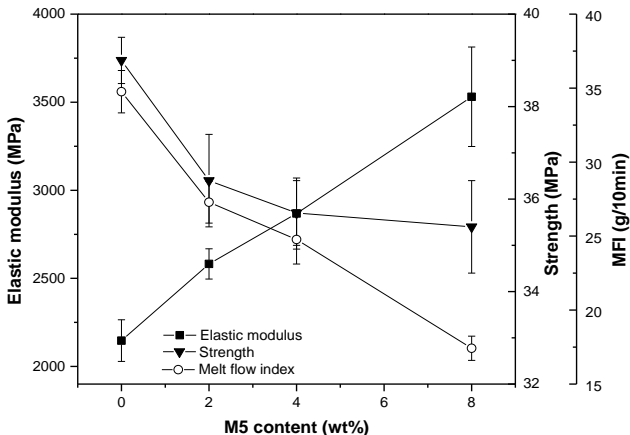


Figure 4.4-1. Tensile modulus, tensile strength and melt flow index values for compression moulded neat ABS (L) and ABS-graphene (L-M5) nanocomposites

4.4.2 Filament extrusion

Filaments of ABS and ABS with 4 wt% of GNP-M5 were extruded with an apparent draw ratio (ADR) of 2.6-3.3 calculated, according to Eq. (4.4-1), as the ratio between the cross sectional area of the extrusion die (S_D) and the cross sectional area of the filament (S_F).

$$ADR = S_D / S_F \quad (4.4-1)$$

The apparent draw ratio includes the effect of die-swelling (DS), i.e. the ratio between the cross sectional area of the extrudate (S_E) and the cross sectional area of the die.

$$DS = S_E / S_D \quad (4.4-2)$$

For nanocomposite filaments, a lower DS value (1.19) was experimentally determined with respect to neat ABS that presented a value of 1.34. This difference could be attributed to the effect of graphene nanoplatelets on the rheological behaviour of the investigated material. Combining Eqs. (4.4-1) and (4.4-2) an effective draw ratio (DR) can be calculated as:

$$DR = ADR \cdot DS = S_E / S_F \quad (4.4-3)$$

DR values of 3.9 and 3.5 were evaluated for ABS (E) and nanocomposite (4-E) filaments, respectively.

ABS (L-E) and nanocomposite (L-M5-4-E) filaments were produced with linear density of 2490 ± 143 tex and 2516 ± 145 tex, respectively [161]. Corresponding bulk

density of $1.036 \pm 0.008 \text{ g/cm}^3$ and $1.049 \pm 0.016 \text{ g/cm}^3$ were also estimated from direct measurement of filament weight and volume.

Table 4.4-1. Processing properties of L-E and L-M5-4-E nanocomposite during extrusion.

Samples	DS ^a	ADR ^b	DR ^c	Linear density (tex)	Density (g/cm ³)
L-E	1.34	2.6-3.3	3.9	2490 ± 143	1.036 ± 0.008
L-M5-4-E	1.19	2.6-3.3	3.5	2516 ± 145	1.049 ± 0.016

^a Die-swellng

^b Apparent draw ratio

^c Draw ratio

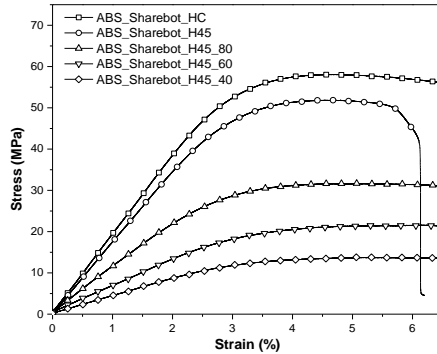
Extruded nanocomposite filaments were less flexible and more brittle than unfilled ABS filaments, and for this reason were wound onto spools with a diameter of 20 cm, instead of spools with 10 cm diameter suitable for standard ABS, in order to avoid fracture of filament during the printing process.

4.4.3 Preliminary study on FDM process (flexural test)

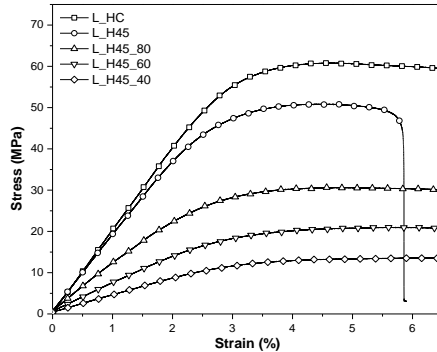
ABS filaments provided by Sharebot, neat ABS (L) and ABS-graphene (L-M5-4) filaments were feed into standard commercial FDM machine to produce the specimens for the flexural test. In Figure 4.4-2, the representative flexural stress-strain curves of ABS from Sharebot, and neat ABS (L), and ABS-graphene (L-M5-4) measured on 3D-printed along horizontal build orientation samples with different infill pattern and density are represented, while in Table 4.4-2, the main flexural parameters are summarized.

From Table 4.4-2, the flexural modulus and maximum stress of neat ABS (L) and commercial ABS from sharebot are similar. It is worthwhile to note that HC samples lead to the highest flexural modulus and maximum stress due to the alignment of deposited filaments. For FDM parts with 45°/-45° infill, the flexural modulus and maximum stress were reduced with the percentage of infill density. On the other hand, the yield strain of FDM horizontal build orientation samples progressively increased with lower infill density. In the literature, only a few scientific articles are about the effect of infill density on mechanical properties [162-164].

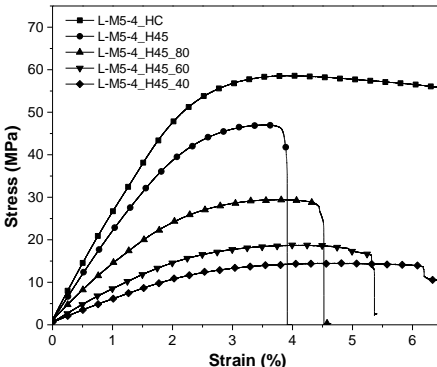
Upon the addition of 4wt% of graphene, it showed the remarkable improvement of flexural modulus for all samples, especially at the high infill density. Similar to tensile properties, the maximum flexural stress were also slightly reduced by the presence of graphene due to poor adhesion between graphene nanofiller and ABS matrix.



(a)



(b)



(c)

Figure 4.4-2. Flexural stress-strain curve as measured on 3D-printed specimens: (a) neat ABS Sharebot, (b) ABS with mould lubricant (L) and graphene nanocomposites (L-M5-4).

Table 4.4-2. Flexural parameters of ABS and its nanocomposite as measured on 3D-printed specimens with different orientations.

Sample	E_f (MPa)	$\sigma_{max,f}$ (MPa)	ϵ_y (%)
	E^* (MPa/(g/cm ³))	$\sigma^{*}_{max,f}$ (MPa/g/cm ³)	
ABS_Sharebot-HC	1900 ± 65	58.3 ± 1.3	4.7 ± 0.1
	2019	61.9	
ABS_Sharebot-H45	1718 ± 36	51.0 ± 1.6	4.7 ± 0.1
	1798	53.4	
ABS_Sharebot-H45_80	1093 ± 59	31.5 ± 1.6	4.8 ± 0.4
	1335	38.5	
ABS_Sharebot-H45_60	631 ± 41	21.0 ± 0.9	5.7 ± 0.6
	952	31.7	
ABS_Sharebot-H45_40	426 ± 9	13.9 ± 0.2	5.6 ± 0.3
	850	27.8	
L-HC	1989 ± 54	60.6 ± 0.9	4.7 ± 0.1
	2030	61.8	
L-H45	1721 ± 62	47.8 ± 2.0	4.6 ± 0.3
	1816	50.4	
L-H45_80	1082 ± 111	30.3 ± 1.6	4.8 ± 0.6
	1348	37.8	
L-H45_60	682 ± 56	21.1 ± 1.8	5.8 ± 0.6
	1014	31.4	
L-H45_40	434 ± 19	13.9 ± 0.8	5.9 ± 0.2
	912	29.1	
L-M5-4-HC	2338 ± 95	58.8 ± 1.5	4.0 ± 0.3
	2480	62.3	
L-M5-4-H45	1998 ± 84	45.4 ± 2.4	3.5 ± 0.1
	2140	48.6	
L-M5-4-H45_80	1283 ± 102	30.0 ± 1.5	3.8 ± 0.2
	1533	35.9	
L-M5-4-H45_60	708 ± 27	18.3 ± 0.7	4.2 ± 0.2
	1122	29.1	
L-M5-4-H45_40	465 ± 54	12.8 ± 1.6	4.2 ± 0.2
	954	26.3	

* the specific properties calculated following the equation (4.4-4) and (4.4-5).

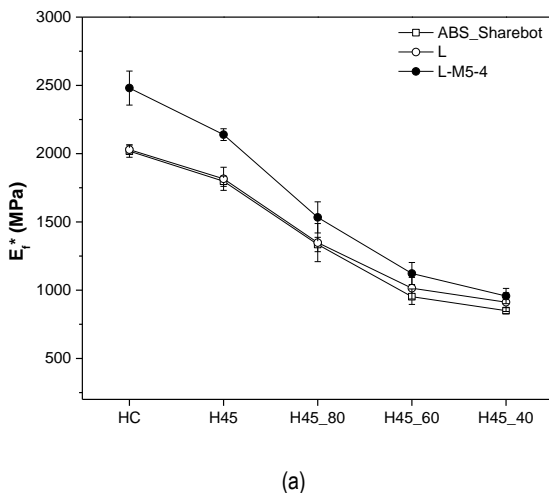
The specific elastic modulus (E_f^*) and specific strength ($\sigma_{\max,f}^*$) were evaluated by the following equations:

$$E_f^* = \frac{E_f}{\rho} \quad (4.4-4)$$

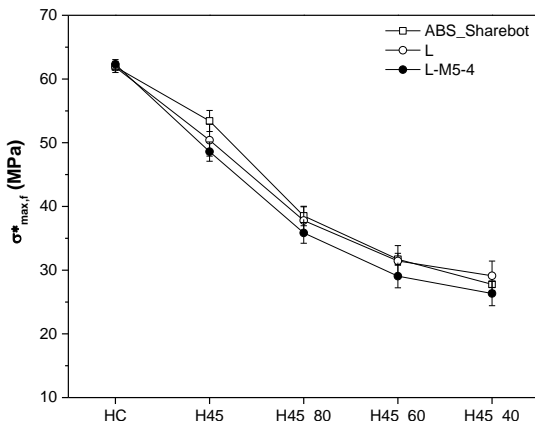
$$\sigma_{\max,f}^* = \frac{\sigma_{\max,f}}{\rho} \quad (4.4-5)$$

where E_f = flexural modulus
 $\sigma_{\max,f}$ = maximum stress
 ρ = density of samples

The specific flexural modulus and the maximum stress of all samples were evaluated by normalizing over the density and presented in Figure 4.4-3. The same tendency of specific properties regarding the type and infill density can be observed. The modulus of composites containing 4 wt% of grade GNP-M5 is enhanced from 2019 MPa to 2480 MPa (i.e. 23%) for HC, from 1789 MPa to 2140 MPa (i.e. 19%) for H45, from 1335 MPa to 1533 MPa (i.e. 15%) for H45_80, from 952 MPa to 1122 MPa (i.e. 18%), and from 850 MPa to 954 MPa (i.e. 12%) for H45_40. The reinforcement effect of graphene was clearly highlighted in specific flexural modulus and strength.



(a)



(b)

Figure 4.4-3. Flexural test of neat ABS Sharebot, ABS with mould lubricant (L) and its graphene nanocomposites (L-M5-4) as measured on 3D-printed specimens (a) Specific elastic modulus, and (b) specific maximum stress.

4.4.4 Scanning electron microscopy

3D-printed dumbbell specimens at different orientations along horizontal (HC), vertical (VC) and perpendicular (PC) were built as shown Figure 4.4-4. In Figure 4.4-5(a-c), low magnification FESEM pictures of the fracture surface of HC, VC and PC dumbbell specimens, are presented. Identification of the FDM process parameters significantly affecting the quality of FDM processed parts is of primary importance [40]. In Figure 4.4-5a and b the cross-sections of single filaments in samples HC and VC can be observed; the trapezoidal shape (final thickness of 0.20 mm and width of about 0.41 mm), indicates not only a shape variation from the initial circular section (nozzle diameter of 0.35 mm) but also a slight reduction of the filament cross-section due to the polymer orientation during FDM process. In particular, a draw ratio of 1.2 could be estimated as the ratio between the original section of the filament at the nozzle and the average section measured from Figure 4.4-5a-b. This drawing is expected to improve the mechanical properties along the correspondent direction (X), as a direct effect of the orientation of polymer chains [165]. Of course, the above considerations do most probably underestimate the drawing of the filament during the FDM process since any filament expansion when it leaves the nozzle is neglected. Moreover, the coalescence of the material showed in the upper level determines an almost flat plane for the next layer deposition; whereas the lack of continuity is evident in triangular cavities at the base of deposition plane. Sample VC has been built-up by layering five

contiguous filaments that have been deposited as follows: first, the external frame (filaments 1 and 5), then the infill process with an inner concentric frame (filaments 2 and 4) and the lastly a third layer is deposited in the middle. Figure 4.4-5b shows some defects between the second and the third layers (see highlighted zone in Figure 4.4-5b), evidencing a non-regular co-contiguity in the middle part; however, these small local imperfections do not impair the mechanical performances of the sample. On the other hand, the fracture surface of sample PC (Figure 4.4-5c) indicates a brittle fracture of an almost homogeneous material, and no traces of the precursor filament are evident. This suggests that deposited filaments completely merge together in quite homogeneous coalesced layers, due to the shorter deposition time of contiguous filaments in the plane X-Y. Moreover, the total deposition time of five filaments of a layer in sample PC is 11 sec (Table 3.2-5), much faster than that of samples HC and VC. Taking into account the number of filaments, about 4 seconds is the average time between the contact deposition in dumbbell specimens HC and VC, whereas for sample PC the average time is about 2 seconds. This processing time is even lower in parallelepiped specimens (about 1-2 seconds). The shorter time, the better the interaction and inter-joining between contiguous filaments, because the filament temperature is higher and closer to the polymer T_g , determining a higher quality of filament bonding [166].

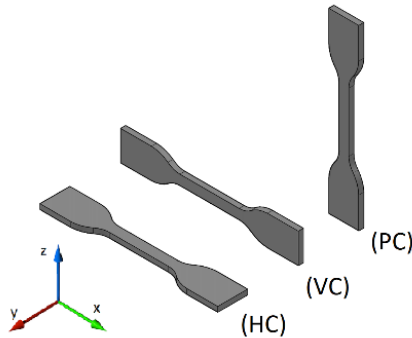


Figure 4.4-4. Schematic of 3D-printed dumbbell specimens at different orientations: horizontal (HC), vertical (VC) and perpendicular (PC).

Higher magnification FESEM pictures of the cross-section of the 3D-printed dumbbell specimens are reported for horizontal, vertical and perpendicular orientation, in Figure 4.4-5d, e and f, respectively. According to Figure 4.4-5d and e, the graphene nanoplatelets for HC and VC parts appear to be oriented mostly perpendicular to the fracture plane and therefore most likely oriented along the loading direction of dumbbell specimens. On the other hand, Figure 4.4-5f clearly proves that in PC specimens, graphene nanoplatelets appear to be distributed parallel to the cross-

section. It can be therefore inferred that, during FDM process, the graphene nanoplatelets are forced to align along the layer plane. A relatively good dispersion of graphene nanoplatelets in ABS matrix can be observed for all building directions.

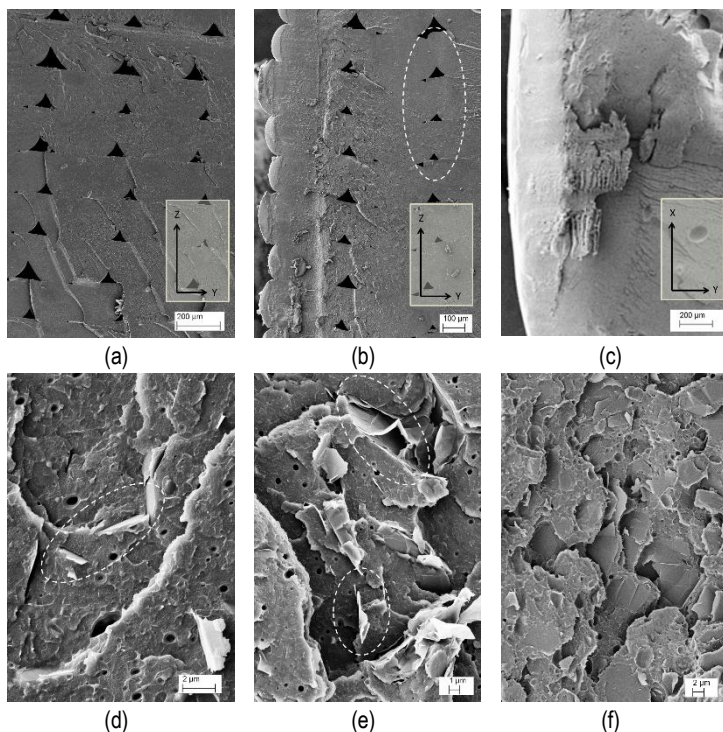


Figure 4.4-5. SEM micrographs of 3D-printed dumbbell specimens printed from neat ABS, L-HC (a), L-VC (b) and L-PC (c); and from graphene nanocomposites, L-M5-4-HC (d), L-M5-4-VC (e) and L-M5-4-PC (f).

4.4.5 Differential scanning calorimetry

Figure 4.4-6 shows the typical DSC thermograms of compression molded specimens, extruded filaments and 3D printed H specimens of neat ABS and nanocomposites Two transitions are clearly visible both in the first (Figure 4.4-6a) and in the second heating scan (Figure 4.4-6c), i.e. the glass transition temperature of styrene-acrylonitrile copolymer phase (SAN) at about 105°C (in conformity to literature indications [104, 131]), followed by an endothermic peak at about 140°C.

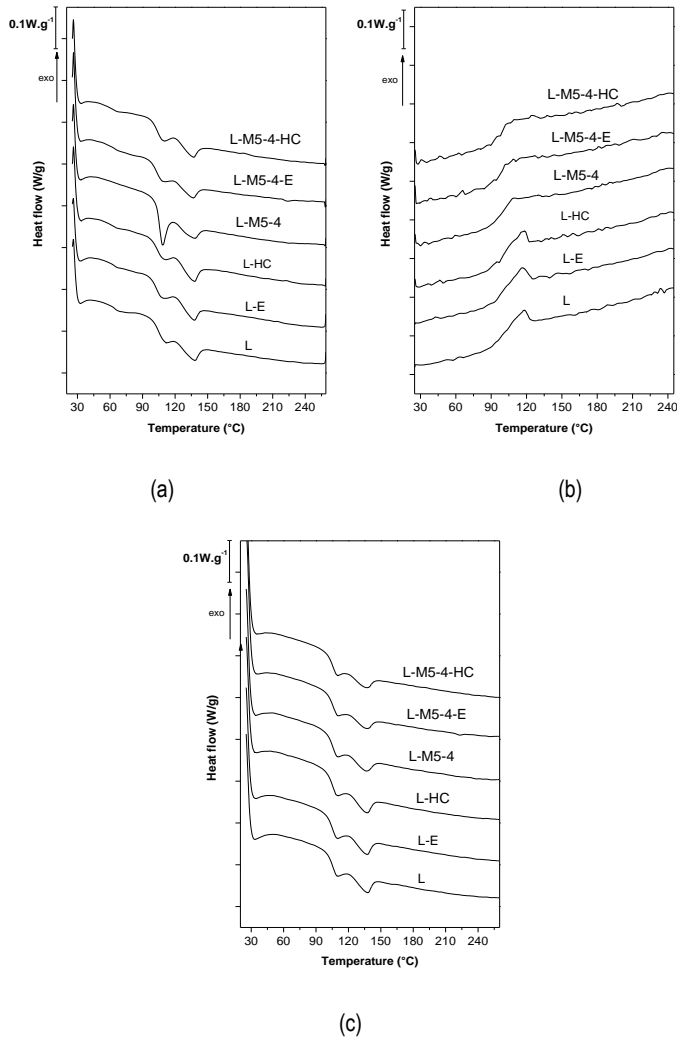


Figure 4.4-6. DSC thermograms of neat ABS (L) and nanocomposites. First heating scan (a), cooling scan (b), and second heating scan (c) of CM (compression moulded), E (extruded) and FDM specimens.

In Table 4.4-3, the T_g of SAN phase and data of melting (T_m , ΔH_m) and crystallization (T_c , ΔH_c) of mold lubricant are summarized. The transition temperatures T_g and T_m for pure ABS were fairly constant at about 105°C and 137°C, respectively, independently from the processing technique. Addition of GNP-M5 did not significantly

affect the glass transition temperature measured by DSC. On the other hand, no crystallization peak was found in the cooling step of nanocomposites (thermograms reported in Figure 4.4-6b and data in Table 4.4-3). However, the increased intensity of the melting peak observed in the second heating scan (Figure 4.4-6c) suggests that graphene could favor the crystallization of the mold lubricant and to play a nucleating effect.

Table 4.4-3. Glass transition temperatures of styrene-acrylonitrile phase (T_g), melting temperature (T_m) and enthalpy of fusion of lubricant (ΔH_m) crystallization temperature (T_c) and crystallization enthalpy (ΔH_c) for ABS and relative nanocomposite as determined from DSC tests.

Sample	First heating			Cooling		Second heating		
	T_g (°C)	T_m (°C)	ΔH_m (J/g)	T_c (°C)	ΔH_c (J/g)	T_g (°C)	T_m (°C)	ΔH_m (J/g)
L	104.8	137.8	3.0	117.8	2.3	105.6	137.6	2.5
L-E	102.2	137.5	3.1	116.2	2.4	105.5	137.3	2.6
L-HC	103.8	137.7	3.4	115.3	2.6	105.7	137.0	2.7
L-M5-4	102.0	134.9	2.9	-	-	103.3	135.1	2.5
L-M5-4-E	103.2	136.8	2.6	-	-	106.0	137.2	2.0
L-M5-4-HC	103.7	136.8	2.7	-	-	105.5	136.9	2.0

4.4.6 Quasi-static tensile tests

The effect of GNP nanoplatelets on the elastic modulus (E), yield stress (σ_y), and stress (σ_b) and strain at break (ϵ_b) of neat ABS and ABS nanocomposite compression moulded, extruded and 3D-printed parts with different orientations are summarized in Table 4.4-4. In general, it can be noted how the presence of graphene nanoplatelets promotes a remarkable increase of the elastic modulus of the ABS matrix, but slightly decreases its strength. Concurrently, a noticeable drop of the strain at break values can be observed when GNP nanoparticles are added. The reduction of ultimate properties could be attributed to a poor adhesion level between the nanofiller and ABS matrix as documented by the FESEM observations of Figure 4.4-5.

As it clearly emerges from Table 4.4-4, for neat ABS the elastic modulus of compression moulded samples is higher than that of 3D-printed samples along the horizontal direction (sample HC). This behaviour could be explained by the fact that a compaction pressure is applied only in the compression moulding process, while both extrusion and FDM processes are characterized by low or no compaction pressure. On the other hand, the almost similar elastic modulus of CM and E parts could be the result of two opposite factors: from one side the underestimation of true strain in tensile test on E samples due to the impossibility of using a contact extensometer, and from the other side the positive effect of orientation during extrusion. Moreover, for 3D-

printed specimens, the presence of voids (about 6 vol% as observed from Figure 4.4-5a) in the microstructure leads to a lower effective cross-section. The strength value of neat ABS compression moulded samples is of about 39 MPa, and it remains almost constant on both extruded filaments and FDM samples along the horizontal direction (sample HC). Tekinalp et al. also reported similar tensile strength values for neat ABS processed by CM or FDM [11].

Upon addition of 4wt% of GNP the elastic modulus improves by about 30% compared to unfilled ABS for all the investigated processing conditions, i.e. CM, extruded and horizontally oriented 3D printed samples. As expected, the build orientation remarkably affects the tensile mechanical properties of 3D printed samples. In fact, as reported in Table 4.4-4, the horizontally built sample exhibits the highest elastic modulus and strength, followed by vertical and then by perpendicular orientations, respectively. Also of HC and VC samples results to be higher than that of PC sample. The behaviour observed for HC and VC samples is certainly related to the direction of the deposited filaments preferentially aligned along the tensile applied load, while the deposited beads in PC specimens are mostly oriented transversally to the tensile load. According to the existing literature information on the effects of build orientation on the elastic modulus and tensile strength of ABS 3D printed parts similar trends were reported [2, 12, 167]. Valentan et al. [168] reported a significant effect of nozzle temperature on tensile elastic modulus and strength. Complementary information on mechanical properties of ABS FDM samples as a function of building directions were also reported by Jami et al. [169].

Table 4.4-4. Quasi-static tensile properties of ABS and its nanocomposite as measured on compression moulded (CM), extruded (E) and 3D-printed specimens with different orientations (HC, VC, PC).

Sample	E (MPa)	σ_y (MPa)	σ_b (MPa)	ϵ_b (%)
L	2147 ± 118	39.0 ± 0.5	29.9 ± 0.4	28.4 ± 5.2
L-M5-4	2868 ± 202	35.7 ± 0.7	31.5 ± 2.6	5.1 ± 1.5
L-E	2080 ± 68	39.3 ± 1.2	30.8 ± 0.8	32.5 ± 9.8
L-M5-4-E	2563 ± 93	37.3 ± 0.7	33.6 ± 2.9	3.2 ± 1.4
L-HC	1866 ± 118	38.8 ± 0.8	33.0 ± 4.3	4.2 ± 0.2
L-M5-4-HC	2463 ± 76	-	35.9 ± 1.0	3.0 ± 0.1
L-VC	1687 ± 104	35.7 ± 2.4	32.0 ± 1.0	4.5 ± 0.2
L-M5-4-VC	2151 ± 78	-	30.5 ± 0.9	3.4 ± 0.5
L-PC	1560 ± 85	23.8 ± 1.3	22.7 ± 2.9	3.3 ± 1.0
L-M5-4-PC	1686 ± 129	-	13.4 ± 1.3	1.8 ± 0.4

4.4.7 Dynamic mechanical response and coefficient of thermal expansion

Dynamic mechanical thermograms of neat ABS and nanocomposites after compression moulding, extrusion and 3D-printing with different orientations are Figure 4.4-7 and Figure 4.4-8, respectively. In Table 4.4-5, selected values of storage modulus (E'), loss modulus (E'') and glass transition temperature from loss tangent ($\tan\delta$) are summarized. Due to the orientation of polymer chains during extrusion, in the entire temperature range, the storage modulus of the extrudate (E) is higher than that of compression molded samples and FDM printed parts (Figure 4.4-7a). In FDM samples the positive effect of filament orientation is counterbalanced by the negative effect of some cavities, as shown in cross section micrographs (Figure 4.4-8 a and b).

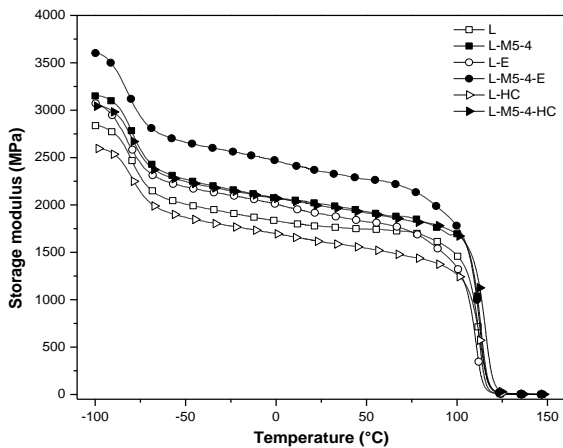
Due to the GNP addition in the ABS matrix, the storage modulus of CM, extrudate and FDM parts increases of about 30-50% with respect to the neat ABS below the T_g . The effect of GNP nanofiller is manifestly more evident above T_g . In fact, as shown in Table 4.4-5, the storage modulus of composite materials at 125°C is more than twice that of neat ABS for all investigated samples, thus revealing a positive stiffening effect of graphene nanoplatelets in the molten state.

Two damping peaks can be clearly observed in Figure 4.4-7b and Figure 4.4-8b as expected in ABS copolymers. In particular, the first peak at about -76°C is related to the glass transition temperature (T_{g1}) of the butadiene rich phase [170], while the second transition (T_{g2}) at about 120°C is associated to the styrene-acrylonitrile (SAN) rich phase.

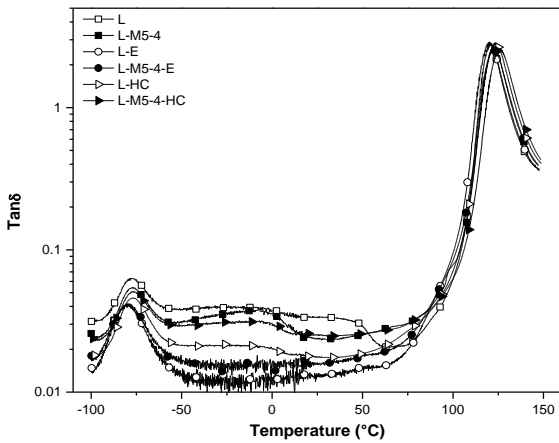
Table 4.4-5. Dynamic mechanical properties of neat ABS and its nanocomposites as measured on compression moulded (CM), extruded (E) and 3D-printed specimens with different orientations (HC, VC, PC).

Sample	Storage modulus			Damping peaks		Loss modulus of SAN peak		
	-50°C (MPa)	30°C (MPa)	125°C (MPa)	B-phase T_{g1} (°C)	SAN-phase T_{g2} (°C)	E''_{peak} (MPa)	T_{peak} (°C)	W_{peak}^* (°C)
L	2009	1769	6.1	-77.6	120.7	333	112.2	10.1
L-M5-4	2271	1995	12.3	-76.7	122.7	402	113.4	11.4
L-E	2191	1889	6.0	-80.1	120.2	316	110.5	12.5
L-M5-4-E	2661	2337	14.0	-79.6	122.4	413	112.6	13.1
L-HC	1871	1598	9.9	-76.9	123.3	286	113.5	12.6
L-M5-4-HC	2248	1975	27.3	-77.4	125.7	372	116.2	12.9
L-VC	1611	1399	6.1	-76.6	120.7	275	112.4	11.2
L-M5-4-VC	2159	1883	15.3	-76.0	123.5	364	114.6	11.9
L-PC	1517	1306	5.8	-76.8	121.7	235	112.8	11.2
L-M5-4-PC	1580	1371	11.4	-75.8	123.9	257	115.3	11.3

*width at half peak

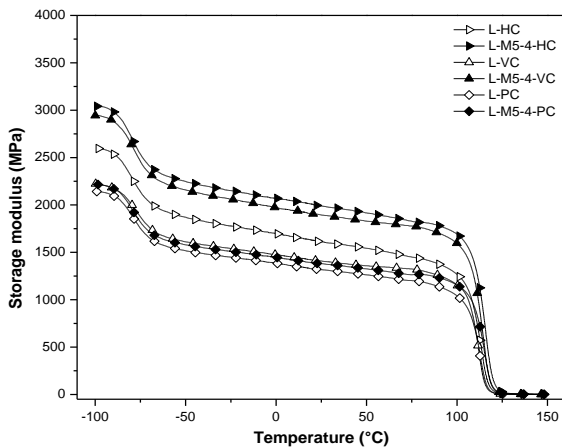


(a)

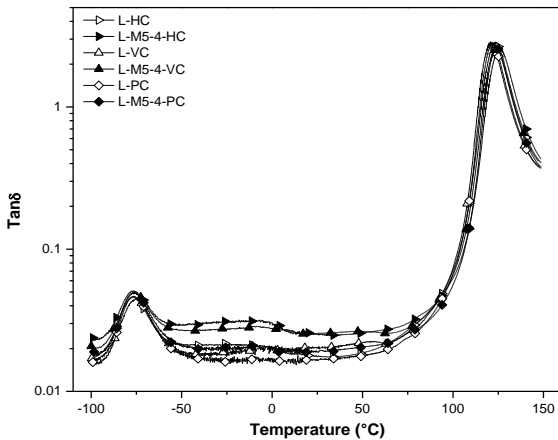


(b)

Figure 4.4-7. Dynamic mechanical thermograms a) storage modulus (E') and b) loss tangent ($\tan\delta$), of neat ABS and nanocomposite samples as measured on compression moulded (CM), filaments (E) and 3D-printed specimens along horizontal orientation (HC).



(a)



(b)

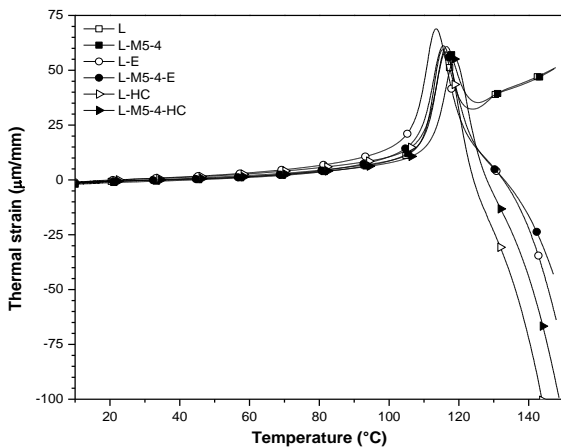
Figure 4.4-8. Dynamic mechanical thermograms a) storage modulus (E') and b) loss factor ($\tan\delta$) of neat ABS and nanocomposite as measured on 3D-printed specimens along different orientations (HC, VC, PC).

For all processing routes, the presence of the GNP causes an increase of T_{g1} values by about 1°C and T_{g2} values by about 2°C due to the restriction of motion of macromolecules. This observation agrees with what reported by Wei et al. [104] on a shift from 105°C to about 106°C for SAN phase transition after addition of 3.5% of graphene in fused deposition modelled ABS.

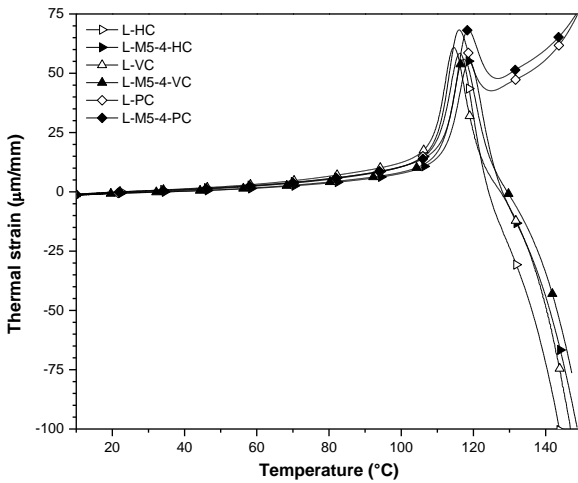
It is worth noting that the position of the glass to rubbery transition damping peak in ABS has been observed in the range 100-124°C [171-173] and it does dependent on various factors, such as copolymer composition, molecular weight and additives.

DMA parameters of FDM samples at various build orientations are also compared in Figure 4.4-8. Horizontally built specimens show the highest storage modulus followed by vertical and perpendicular specimens, respectively. The trend is the same previously observed for the tensile Young's modulus, thus confirming that as recently reported by Arivazhagan and Masood [174], dynamic mechanical properties strongly depend on the deposition orientation in FDM. Addition of GNP causes an increase of the storage modulus in comparison to neat ABS for all build orientation parts: at room temperature the storage modulus increases by 23%, 34% and 5% for HC, VC and PC orientation respectively. Therefore, it is confirmed that graphene nanoplatelets play the best stiffening effect in FDM printed parts when the deposited layers are aligned along the tensile load direction. It is worthwhile to note that the presence of graphene also causes a shift in loss modulus (E'') peak temperature by about two degrees (see Table 4.4-5) for all investigated samples. At the same time, a slight enlargement of the width of loss modulus peak in graphene-ABS composite indicates the coexistence of differently constrained polymer chains, probably due to the restriction of chain motion of ABS matrix in the surrounding of graphene platelets.

Thermal strain of various specimens is compared in Figure 4.4-9. As a common feature, an almost linear increase with temperature is observed up to about 100°C, then in the proximity of T_g a steep increment of thermal strain indicates a transition into the rubbery state with a higher mobility of polymer chains. Eventually, after a relative maximum at about 110-120°C, an abrupt contraction suggests the tendency to recover a random coil conformation. The values of coefficient of linear thermal expansion (CLTE) of ABS and ABS-GNP nanocomposites for different processing routes and along various 3D-printing orientations have been calculated from the thermal strain and summarized in Table 4.4-6. Four temperature ranges have been selected in the glassy zone, i.e. at low temperature ($\Delta T_1=-50/-20^\circ\text{C}$), at room temperature ($\Delta T_2=20/50^\circ\text{C}$) and at high temperature close T_g ($\Delta T_3=70/90^\circ\text{C}$ and $\Delta T_4=108^\circ/113^\circ\text{C}$), respectively. CLTE values of neat ABS up to 50°C are in the range $60-75 \times 10^{-6}/\text{K}$, which are slightly lower than $90 \times 10^{-6}/\text{K}$, the literature value of general purpose ABS [175]. After addition of GNP nanoplatelets, CLTE is remarkably reduced with values in the range $44-66 \times 10^{-6}/\text{K}$, which means a better thermal stability in all the temperature intervals. In particular, GNP causes a reduction of CLTE of about 15% for CM specimen and about 42% for the extruded specimen mostly due to the orientation of graphene along extrusion directions as shown in Figure 4.4-5 (d, e).



(a)



(b)

Figure 4.4-9. Thermal strain of neat ABS and nanocomposite samples as measured on a) compression molded (CM), extruded (E) and 3D-printed specimens along horizontal orientation (HC) and b) along different orientations (HC, VC, PC).

Table 4.4-6. Coefficients of linear thermal expansion (CLTE) and linear thermal deformation (CLTD) of ABS and its nanocomposites in the glassy state as measured on compression moulded (CM), extruded (E) and 3D-printed specimens with different orientations (HC, VC, PC).

Sample	CLTE ($\times 10^{-6}/\text{K}$)				CLTD ($\times 10^{-6}/\text{K}$)
	ΔT_1	ΔT_2	ΔT_3	ΔT_4	
L	62.0 ± 0.2	64.7 ± 0.2	159.7 ± 0.9	5784 ± 281	773 ± 8
L-M5-4	54.2 ± 0.1	54.9 ± 0.2	169.0 ± 1.2	4389 ± 180	678 ± 4
L-E	60.0 ± 0.2	74.7 ± 0.3	232.2 ± 2.1	8266 ± 111	-3292 ± 57
L-M5-4-E	43.8 ± 0.1	43.3 ± 0.2	193.0 ± 1.9	5692 ± 179	-2475 ± 33
L-HC	64.9 ± 0.1	65.5 ± 0.3	174.2 ± 0.9	4081 ± 144	-5722 ± 78
L-M5-4-HC	48.9 ± 0.1	48.3 ± 0.2	141.7 ± 0.9	1907 ± 62	-4466 ± 52
L-VC	65.9 ± 0.1	73.5 ± 0.3	212.6 ± 0.9	6601 ± 209	-4854 ± 83
L-M5-4-VC	49.3 ± 0.1	53.7 ± 0.3	151.0 ± 0.7	2933 ± 112	-3768 ± 55
L-PC	65.6 ± 0.1	66.3 ± 0.3	183.3 ± 1.2	5660 ± 217	1257 ± 24
L-M5-4-PC	60.4 ± 0.1	65.6 ± 0.3	187.4 ± 1.3	2476 ± 90	1169 ± 18

Temperature interval: $\Delta T_1=-50/-20^\circ\text{C}$; $\Delta T_2=20/50^\circ\text{C}$; $\Delta T_3=70/90^\circ\text{C}$; $\Delta T_4=108/113^\circ\text{C}$; and $\Delta T_5=120/150^\circ\text{C}$.

FDM specimens (HC, VC and PC) printed with neat ABS, present room temperature CLTE values of $66-74 \times 10^{-6}/\text{K}$ (Table 4.4-6), comparable to the values of $78-87 \times 10^{-6}/\text{K}$ previously reported for FDM printed ABS [10, 104]. After the dispersion of GNP nanoplatelets, CLTE at room temperature reduces by 26% and 27% for HC and VC specimens, whereas only 1% for PC specimen, respectively. The behaviour of PC specimen indicates that the graphene nanoplatelets have an almost negligible effect on CLTE of ABS matrix because in this case the main role is determined by the adhesion layer (see Figure 4.4-5c). In the proximity of T_g ($\Delta T_4=108/113^\circ\text{C}$) the effect of graphene on ABS matrix indicated a certain reduction of CLTE of CM and E specimens (about 25-30%), and a stronger variation for all FDM printed specimens (about 55% of CLTE reduction).

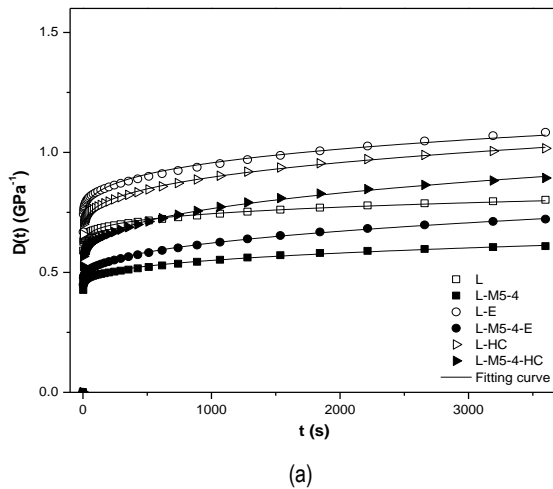
The thermal dilation behaviour above the glass transition temperature of SAN phase (range ($\Delta T_5=125^\circ\text{C}/150^\circ\text{C}$) is described by the CLTD coefficients reported in the last column of Table 4.4-6. Poorly oriented samples, such as CM and P, show a positive thermal strain, corresponding to CLTD values of about 750 and $1250 \times 10^{-6}/\text{K}$ for ABS, respectively, that slightly decrease (-7/12%) after graphene addition. On the other hand, negative CLTD values can be found on extruded filaments and on FDM samples along H and V orientation. In this elevated temperature range, the reinforcing effect of graphene is markedly evident in the more oriented samples (E, HC and VC) with a shrinkage reduced by about 24% with respect to neat ABS. It is worthwhile to observe that nanofiller causes a reduction of both CLTE (below T_g) and CLTD (above T_g), suggesting an effective interaction between graphene and ABS both in the glassy and in the rubbery state.

4.4.8 Creep stability

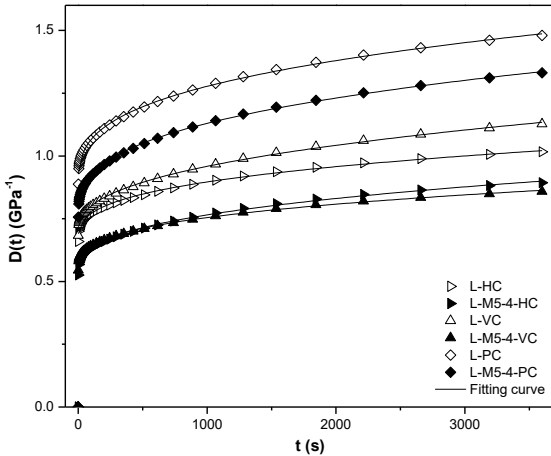
Figure 4.4-10(a-b) show the isothermal creep compliance of neat ABS and relative nanocomposite. If no plastic deformation is produced in the course of creeping, the total creep compliance in isothermal tensile creep in the linear viscoelastic region, $D(t)$, is generally viewed as consisting of two components, i) elastic (instantaneous, reversible), D_{el} and ii) viscoelastic (time-dependent, reversible) $D_{ve}(t)$ [176, 177]:

$$D(t) = D_{el} + D_{ve}(t) \quad (4.4-6)$$

Elastic (D_{el}), viscoelastic $D_{ve}(t=3600s)$ and total $D(t=3600s)$ creep compliance at 3600s have been estimated on creep curves and summarized in Table 4.4-7. It is evident that the addition of graphene nanoplatelets can promote the reduction of creep compliance for each investigated process and build orientation. The role of nanofiller is to restrict the polymeric chain mobility, thus promoting a better creep stability. According to the results, extrudate sample exhibits the highest reduction of creep compliance compared to compression moulded and printed specimens. For FDM printed specimens at various orientation, vertically built specimens show the highest reduction of creep compliance by about 24% owing to the addition of GNP-M5.



(a)



(b)

Figure 4.4-10. Creep compliance, $D(t)$ at 30°C and 3.9 MPa , of neat ABS and nanocomposites as measured on a) compression molded (CM), extruded (E) and 3D-printed specimens along horizontal orientation (HC) and b) along different orientations (HC, VC, PC).

Table 4.4-7. Elastic (D_{el}), viscoelastic $D_{ve}(t=3600\text{s})$ and total $D(t=3600\text{s})$ creep compliance at 3600s , and fitting parameters (Eq. (4.4-7)) of ABS and its nanocomposites as measured on compression moulded (CM), extruded (E) and 3D-printed specimens with different orientations (HC, VC, PC).

Sample	D_{el} (GPa^{-1})	$D_{ve}(t=3600\text{s})$ (GPa^{-1})	$D(t=3600\text{s})$ (GPa^{-1})	D_e (GPa^{-1})	k ($\text{GPa}^{1-\eta} \text{s}^{-\eta}$)	n	R^2
L	0.59	0.21	0.80	0.576	0.037	0.219	0.9853
L-M5-4	0.43	0.18	0.61	0.437	0.010	0.345	0.9877
L-E	0.67	0.42	1.08	0.688	0.039	0.280	0.9786
L-M5-4-E	0.45	0.27	0.72	0.454	0.013	0.371	0.9959
L-HC	0.66	0.36	1.02	0.660	0.024	0.331	0.9950
L-M5-4-HC	0.53	0.37	0.89	0.532	0.020	0.356	0.9947
L-VC	0.68	0.45	1.13	0.696	0.017	0.399	0.9961
L-M5-4-VC	0.55	0.31	0.86	0.543	0.023	0.323	0.9953
L-PC	0.89	0.59	1.48	0.879	0.041	0.329	0.9968
L-M5-4-PC	0.76	0.57	1.33	0.742	0.039	0.333	0.9977

To model the viscoelastic creep response Findley's model (power law) is commonly adopted to fit the experimental data [178]. This model can be obtained by expanding the Kohlrausch–Williams–Watts (KWW) model [179], generally described by a Weibull-like function as a series and ignoring all but the first term [180]:

$$D(t) = D_e + k t^n \quad (4.4-7)$$

where D_e is the elastic instantaneous creep compliance, k is a coefficient related to the magnitude of the underlying retardation process and n is an exponent tuning the time dependency of the creep process. The parameters resulting from the best fitting of experimental creep data are summarized in Table 4.4-7. The elevated R^2 values indicate that the Findley equation can satisfactorily represent the experimental data. The reduction of the creep compliance due to the addition of GNP-M5 seems to be mostly associated with a reduction of the values of parameters D_e , which is comparable to D_{el} and k . In fact, the coefficient n , which represents the kinetics of the flow process of macromolecules during creep time, is only marginally affected by the presence of GNP.

4.5 Summary on ABS-graphene nanocomposites

ABS nanocomposites with graphene nanoplatelets were prepared following different processing routes, i.e. compression molding, twin-screw extrusion and FDM process. Selection of types of ABS matrix and graphene nanoplatelets were carried out, as a preliminary study on compression molding samples. Next, graphene was successfully melt compounded in an ABS matrix then extruded in filaments suitable for fused deposition modelling.

Two different ABS with low (Sinkral®L322) and high (Sinkral®F322) viscosity were used to host GNP-M5 nanofiller in order to produce the nanocomposites from compression molded plates. Microstructure analysis revealed that the low viscosity ABS (L) contains the mould lubricant additive. The strength of ABS with lubricant exhibited slight reductions due to the addition of GNP-M5. On the other hand, ABS with mould lubricant nanocomposites systems confirmed the better processability and stiffening effect.

The influence of different types of graphene nanoplatelets (GNP-C300, C500, C700 and M5) on flow, thermal, electromagnetic shielding, electrical and mechanical properties of low viscosity ABS plates were investigated. XPS analysis revealed an oxygen content of ether/alcohol groups for C300, C500 and C750 nanoparticles progressively increasing with the particle size reduction and the increase of surface area; in the case M5 the total oxygen content is also depending on the contribution of carbonyl groups, and it is associated to traces of sulphur. The melt flow of ABS almost linearly decreased by the presence of graphene up to 8 wt%. For C-type nanoparticles, MFI values decreased proportionally to the filler surface area. Larger M5 nanoplatelets resulted to be the more promising in enhancing the shielding efficiency to electromagnetic interference, while C300, C500 and C750 resulted in a moderate effect on ABS regardless of specific surface area. Correspondingly, M5 determined a higher reduction of electrical resistivity with respect to the almost equivalent effect of

C300, C500 and C750. However, it is necessary to point out that graphene content higher than 8% is required for practical applications in the field of electromagnetic shielding. In addition, GNP-M5 nanoparticles showed the best reinforcement effect on the elastic modulus of the composite in comparison of GNP-C300, C500 and C750. The Halpin-Tsai model was used to fit the tensile modulus of ABS/graphene composite. A 3D randomly oriented Halpin-Tsai model well fitted the experimental values of tensile modulus. Our results suggested that graphene nanoplatelets were 3D randomly oriented in ABS which is in agreement with observation through scanning electron microscopy. It is worth to underline that the improvement of normalised modulus observed for GNP-M5/ABS composite is the highest ever reported in the open scientific literature on carbon-based fillers, except the case of carbon fiber and reduced graphene-oxide ABS composites. Among the various GNP nanoparticles studied in this study, GNP-M5 appears to be the most promising for electrical resistivity reduction and for EMI applications, and the most relevant for improving mechanical properties.

GNP-M5 were successfully incorporated in an ABS matrix to produce the filaments suitable for fused deposition modelling. Due to the processing and materials properties, the filler content was optimized at 4 wt%. The thermo-mechanical properties of neat ABS and its nanocomposites have been compared on samples obtained through various processing routes such as compression moulding, extrusion and fused-deposition modelling. This positive effect was also verified along several different orientations in FDM samples. In all cases, the flexural modulus and maximum stress were reduced regarding type of infill and infill density. In addition, flexural modulus was enhanced by the presence graphene-M5 along the infill density. Also the presence of GNP-M5 improved the tensile modulus of ABS. Concurrently, the presence of GNP causes a slight reduction of tensile strength and strain at break for horizontal and vertical 3D built specimens and a more severe effect along the perpendicular direction. Moreover, GNP was also proven to reduce the coefficient of thermal dilation of 3D printed parts and to improve their stability under long-lasting loads. In fact, the creep compliance significantly reduced by addition of the nanofiller. For FDM-printed parts, the graphene nanoplatelets resulted to play the best reinforcement effect for horizontal and vertical orientation and to be less effective for perpendicularly printed specimens.

Chapter V

ABS-carbon nanotubes nanocomposites

Part of this chapter has been published in:

S. Dul, L. Fambri, A. Pegoretti
“Filaments production and fused deposition modelling of ABS/carbon nanotubes composites”
Nanomaterials. 8. (2018) 49-73.

To date, various conductive nanoparticles have been used in the 3D printing, e.g. carbon black (CB) [15, 16], graphene oxide (GO) [104, 111], reduced graphene oxide (r-GO) [97], graphene [102, 112] and carbon nanotubes [19, 21, 22, 102, 103]. However, very few studies have been focused on the production of nanocomposite filament feedstock for FDM. For example, a resistivity of $0.21 \Omega \cdot \text{cm}$ was reported for composite filaments of GO/polylactic acid (PLA) with 6 wt% of r-GO with a diameter of 1.75 mm along with superior mechanical properties of FDM parts [97]. 15 wt% of CB on the resistivity of composite ABS feedstock filaments (about $2900 \Omega \cdot \text{cm}$) was studied and characterized the resistivity of 3D-printed parts by several FDM parameters [16]. MWCNTs up to 3 wt% was dispersed in polyhydroxyalkanoate to produce feedstock filaments, but the resistivity of filaments have not been reported [103]. 3D-printing with 5.6 wt% of GO in ABS matrix reported, but without information on electrical and mechanical properties of composites filaments and FDM samples [104]. The 3D printing with polymer nanocomposites consisting of CNT- and graphene-based polybutylene terephthalate was reported, finding that 3D-printed objects filled with CNT have better conductive and mechanical properties and better performance than those filled with graphene [102].

In a previous paper of this group, [181] the main effort was focused on the possibility to disperse CNT in ABS by using a commercial masterbatch of ABS/CNT for the production of filaments with a non-standard diameter of 1.4 mm. 6 wt% of CNT was found as an optimal fraction for the production of composite filaments.

This chapter is dedicated to ABS-carbon nanotubes (CNT) nanocomposites with the aim to produce suitable filaments through the possibility to directly disperse CNT in ABS matrix in order to produce the ABS/CNT filaments suitable for the FDM process with a standard diameter of about 1.7 mm. Relatively higher viscosity ABS matrix, and lower processing temperatures with respect to the previous chapter have been properly selected in order to increase the processing shear stresses and to improve/facilitate CNT dispersion.

In the following section 5.1, characterizations of carbon nanotubes nanofillers were carried out in terms of transmission electron microscopy (TEM), density and TGA. Section 5.2 is on the characterization on ABS-CNT nanocomposites in form of compression moulded plates. Section 5.3 describes the filaments production by using common industrial method (internal mixer and twin-screw extruder) with extensive thermal, mechanical, and electrical characterizations of ABS-CNT nanocomposites. Subsequently, the optimization the suitable ABS-CNT filaments for FDM and FDM parts characterizations along various build orientations are presented and discussed in section 5.4. Section 5.5 provides the electrical properties of ABS-CNT composites from different processing routes including compression moulding, filaments, fiber, and FDM samples following by some possible applications (surface temperature under applied voltage and strain monitoring). Finally, a summary of the study is provided in section 5.6.

5.1 Characterization of carbon nanotubes

From transmission electron microscopy (TEM) pictures represented in Figure 5.1-1(a-b), the morphological structure of carbon nanotubes (CNTs) can be observed. In particular, it is possible to note the presence of hollow tubes of CNTs with an outer diameter of about 20-15 nm and a thickness of about 4-6 nm.

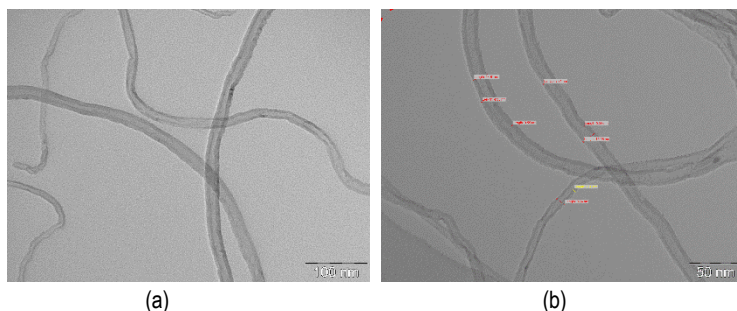


Figure 5.1-1. TEM micrographs of carbon nanotubes particles (CNT).

The helium pycnometer data obtained on carbon nanotubes are reported in Figure 5.1-2. The sample was analysed within 300 measurements in order to reach a plateau. This behaviour can be attributed to the diffused open porosity present on the surface of carbon nanotubes aggregates, among which helium molecules can difficultly penetrate and diffuse. Density of CNT particles was evaluated as $2.151 \pm 0.033 \text{ g/cm}^3$ by the consideration of the last 200 data.

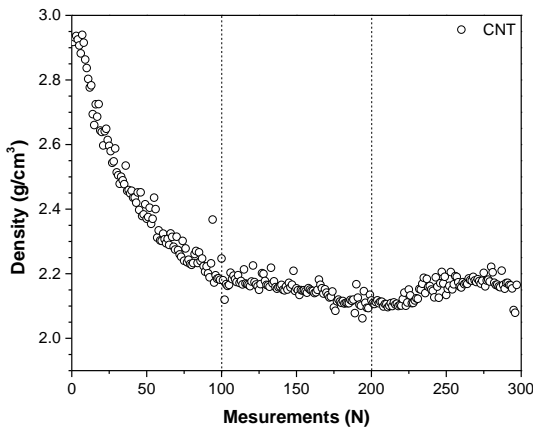


Figure 5.1-2. Density of carbon nanotube measured through a Micromeritics®Accupyc 1330 helium pycnometry (23.0°C) with 10 cm^3 chamber.

The thermal stability of carbon nanotubes was investigated through thermogravimetric analysis (see Figure 5.1-3). One single degradation step can be observed with a maximum degradation temperature ($T_{d,\text{max}}$) of 627.3°C and a maximum mass loss rate (MMLR) of $1.16\text{ \%}/^{\circ}\text{C}$. The residue at 700°C is about 11.3%.

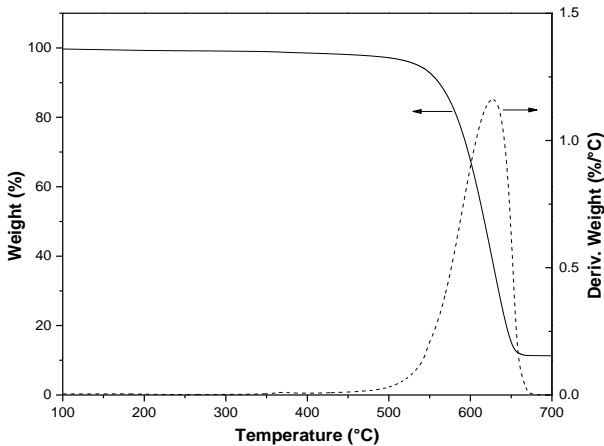


Figure 5.1-3. TGA curve of carbon nanotubes performed in air atmosphere: mass loss (continuous line) and derivative of mass loss (dot line).

5.2 ABS-carbon nanotubes nanocomposites plates

The first step of nanocomposite preparation was performed following previous compounding procedure following compression moulding. At this purpose in order to increase the processing shear stresses during CNT dispersion, an ABS matrix with MFI of $14.8 \pm 1.0 \text{ g/cm}^3$ (220°C and 10Kg) was properly selected, with higher viscosity than ABS with MFI of $25.4 \pm 1.4 \text{ g/cm}^3$ (220°C and 10Kg) previously utilized for the production CNT composite from master-batch [181].

Nanocomposites are designated indicating the type of ABS (F, in this study) and the filler type (CNT) and content. As an example, F-CNT-2 indicates a nanocomposite sample filled with 2 wt% of CNT.

5.2.1 Compounding and morphology

As reported in Table 5.2-1, the investigated formulations are a combination of ABS with carbon nanotubes. It should be noted the MFI value significantly decreased with the percentage of carbon nanotube in the polymer matrix (Table 5.2-1). The density of nanocomposites was increasing with almost linear dependence on the F-CNT composition, suggesting a proper distribution of nanofiller in ABS matrix.

Table 5.2-1. Designation and formulation of ABS nanocomposites dependence of melt flow index (250°C/10 Kg).

Sample	ABS®F322 (wt%)	CNT (wt%)	MFI (g/10min)	Density (g/cm ³)
F	100	0	89.7 ± 2.5	1.042 ± 0.003
F-CNT-2	98	2	39.3 ± 3.2	1.057 ± 0.003
F-CNT-4	96	4	8.4 ± 1.3	1.064 ± 0.003
F-CNT-6	94	6	0.55 ± 0.04	1.074 ± 0.003
F-CNT-8	92	8	0.06 ± 0.01	1.082 ± 0.003

The effect of compounding and the quality of carbon nanotubes dispersion into ABS matrix was evaluated of the fracture surface of ABS/CNT nanocomposites with 2 wt%, 4 wt%, 6 wt% and 8 wt% of CNT by SEM analysis and results are represented Figure 5.2-1(a-d) respectively. From The SEM figures, it is evidenced that carbon nanotubes show an uniform distribution and the excellent dispersion. In addition, at high magnification images (see Figure 5.2-1 (e-h)), adhesion level between CNTs and ABS can be observed which is, expected to enhance the mechanical properties of the composites.

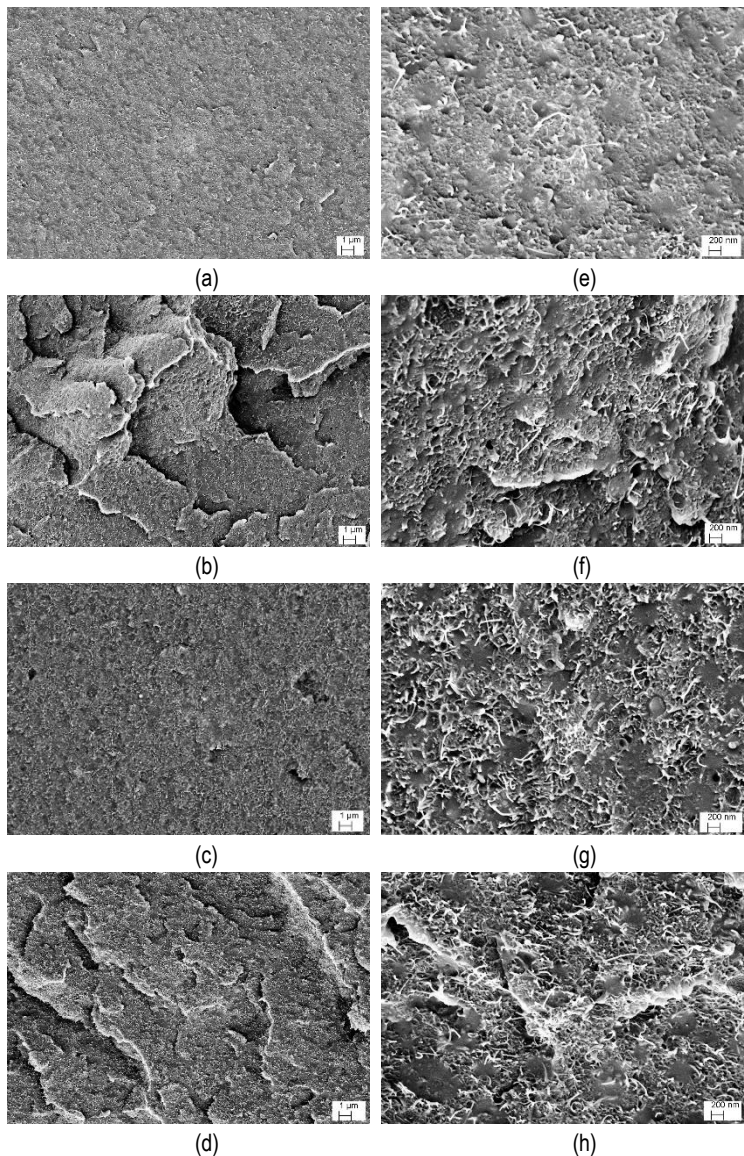


Figure 5.2-1. SEM micrographs of ABS/CNT nanocomposite plates with 2 wt% (a, e), 4wt% (b, f), 6 wt% (c, g) and 8 wt% (d, h) of CNT at magnification of 10,000× (left) and 50,000× (right).

5.2.2 Differential scanning calorimetry

DSC thermogram of ABS and CTN filled nanocomposites are illustrated in Figure 5.2-2, and data are summarized in Table 5.2-2. The glass transition temperatures for unfilled ABS and its nanocomposite of are of about 108°C in both first and second heating stage, which is associated to styrene–acrylonitrile copolymer phase (SAN). According to the data reported in Table 5.2-2, the presence of CNT has no significant effect on the glass transition temperature of composites. Also, Yang et al. reported only a slight increase in T_g promoted by single wall carbon nanotubes (SWCNT) dispersed in ABS [182].

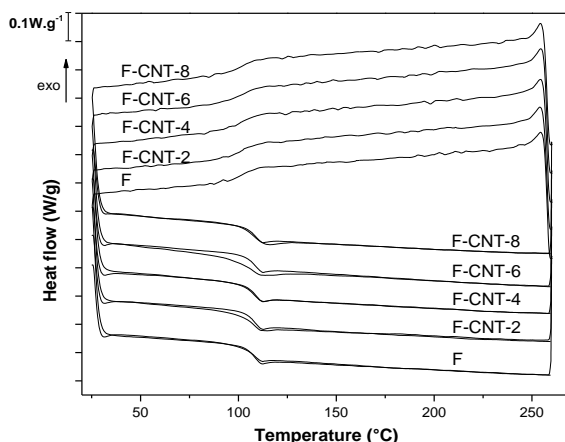


Figure 5.2-2. DSC thermogram of neat ABS and ABS/ CNT nanocomposites from compression moulding in the heating-cooling-heating cycle.

Table 5.2-2. Glass transition temperatures (T_g) of neat ABS and resulting nanocomposite plates from DSC tests.

Samples	T_g (°C)		
	First heating	Cooling	Second heating
F	108.3	102.4	108.0
F-CNT-2	108.0	102.4	107.8
F-CNT-4	108.0	100.5	108.5
F-CNT-6	107.7	104.0	108.5
F-CNT-8	108.2	102.7	108.5

5.2.3 Quasi-static tensile test

Representative stress-strain curves of neat ABS and ABS/CNT nanocomposites obtained by compression moulding are reported in Figure 5.2-3. The tensile properties of neat ABS and nanofilled ABS nanocomposite plates with different amount of carbon nanotubes are summarized in Table 5.2-3. As expected, the introduction of carbon nanotube leads to the improvement of the elastic modulus with respect to the neat ABS [78, 80, 183]. For instance, the modulus of composites containing 8 wt% of CNT is enhanced from 2315 MPa to 3068 MPa (i.e., 32%). At nanofiller higher than 4 wt% of CNT, the samples behave in very brittle manner, and the failure occurs before the yield point (see Table 5.2-3). Moreover, it is important to note that the strength of ABS increased proportionally to carbon nanotubes content. The highest strength was obtained for 6 wt% of CNT in ABS. Tensile strength increased from 41.7 MPa for neat ABS to 46.6 MPa for F-CNT-6 sample (i.e., 12%). Such significant improvement in the tensile modulus and strength is consistent with the scanning electron microscopy analysis that shows a very good dispersion and good adhesion at the CNT/ABS interface. In addition, neat ABS presents a much higher strain at break compared with the filled samples, and nanofiller introduction induces an embrittlement of the samples.

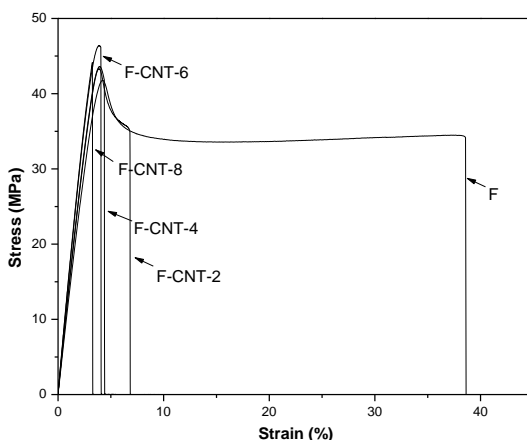


Figure 5.2-3. Representative of the tensile stress-strain curve of ABS and ABS-CNT compression moulding.

Table 5.2-3. Tensile properties of ABS-CNT nanocomposites as function of carbon nanotubes (CNT) content.

Samples	E (MPa)	σ_y (MPa)	ϵ_y (%)	σ_b (MPa)	ϵ_b (%)
F	2315 ± 100	41.7 ± 0.4	4.2 ± 0.1	33.6 ± 0.4	35.9 ± 6.1
F-CNT-2	2513 ± 101	43.3 ± 0.4	3.9 ± 0.1	34.1 ± 1.5	7.5 ± 2.4
F-CNT-4	2622 ± 29	43.5 ± 1.0	3.9 ± 0.1	40.3 ± 1.8	4.5 ± 0.6
F-CNT-6	2849 ± 70	-	-	46.6 ± 0.5	3.9 ± 0.2
F-CNT-8	3068 ± 156	-	-	45.1 ± 2.3	3.2 ± 0.3

5.3 ABS-carbon nanotubes nanocomposites filaments

The first step of composite preparation was performed following compounding procedure with the direct mixing of filler and polymeric matrix as previously reported in [112, 184]. For the purpose to increase the processing shear stresses during CNT dispersion, an ABS matrix with MFI of 14.8 ± 1.0 g/cm³ (220°C and 10 kg) was properly selected, with viscosity higher than ABS with MF of 23 g/cm³ (220°C and 10 kg) previously utilized for the production CNT composite from master-batch [181]. Moreover, in the second step of filament extrusion, lower processing temperatures, 220°C instead of 240°C [181], were set in order to furtherly improve dispersion under high shear stresses.

3D-printed fibers were prepared, starting from extruded filament by using a prototype of a 3D printer for high temperature processing, Sharebot HT Next Generation desktop (Sharebot NG, Nibionno, LC, Italy). through a nozzle with a diameter of 0.40 mm at temperature of 250°C or 280°C for ABS or nanocomposites respectively. Fibers of about 100 cm length with a diameter of 0.50–0.65 mm were also freely extruded at a speed of 40 mm/s for mechanical and electrical testing.

5.3.1 Filament extrusion and melt flow index

The working parameters of extrusion were set for the production of filaments with a standard diameter of about 1.70 mm at constant collection rate, as reported in Table 5.3-1. The torque and internal pressure at the die of extruder significantly increased with CNT content.

The filament of neat ABS and of ABS/CNT composites were extruded with an orientation factor of about 1.0 at 220°C, as evaluated by the ratio between the cross-sectional area of the extruder die hole (S_{DE}) and the cross-sectional area of the obtained filament (S_F) according to Eq. (5.3-1).

$$OF_E = S_{DE}/S_F \quad (5.3-1)$$

Moreover the orientation factor of fiber produced by 3D-printer as the cross-sectional area of the filament (S_f) and the cross-sectional area of the obtained fiber (S_i) according to Eq. (3.3-1).

$$OF_{3D} = S_f/S_i \quad (5.3-2)$$

The orientation factor is higher in the fiber (produced at 250°C for ABS and at 280°C for CNT-6) than filament obtained at 220°C due to the processing conditions. The higher the CNT content, the higher the orientation factor of fibers. Moreover, it is important to observe that linear density of fiber is progressively decreasing with CNT content, as shown in Table 5.3-2.

This result could be explained by considering that the final diameter of fiber is decreasing with the nanofiller content (see detail in Table 5.3-5). Consequently, the free flow of the fibers from die of 3D-printer was used to evaluate the die-swelling (DS), according to Eq. (5.3-3), where S_f is the cross-sectional area of fibers and S_{DP} is nozzle section of 3D-printer (0.40 mm).

$$DS = S_f/S_{DP} \quad (5.3-3)$$

Table 5.3-2 shows that the die-swelling of the investigated composites is significantly reduced as the CNTs fraction increases; in particular, at 6 and 8 wt % of CNTs, die swelling in fiber is almost completely suppressed.

Moreover, a total orientation factor in fiber OF_T could be calculated combining Eqs (5.3-1) and (3.3-1), as shown in Eq. (5.3-4):

$$OF_T = S_{DE}/S_f \quad (5.3-4)$$

The total orientation factor in the fiber increased with CNT content in direct dependence on the first step of filament production at 220°C and the subsequent extrusion from 3D printer at 250°C (for ABS) or 280°C (for nanocomposite), that is the most effective step. This cumulative effect could be a useful parameter for evaluating the processability of the various filaments.

Table 5.3-1. Processing parameters of twin screw extruder for the production of ABS and ABS/CNT nanocomposite filaments.

Samples	Pressure (bar)	Torque (Nm)	Screw speed (rpm)	Collection rate (m/min)	Output (g/h)	Filament diameter (mm)
F-E	16.9	40.4	5	1.00	137.6	1.725 ± 0.049
F-CNT-1-E	17.1	38.4	5	1.00	134.6	1.679 ± 0.007
F-CNT-2-E	21.7	45.9	5	1.00	137.7	1.684 ± 0.025
F-CNT-4-E	28.0	66.8	5	1.00	138.6	1.765 ± 0.026
F-CNT-6-E	44.2	100.1	5	1.15	139.6	1.712 ± 0.035
F-CNT-8-E	45.7	119.6	4.5	0.88	122.1	1.702 ± 0.016

Table 5.3-2. Bulk density and linear density of ABS and ABS/CNT nanocomposite during filament extrusion and 3D fiber production. Extrusion and 3D printing draw ratio.

Samples	CNT content (wt%)	Bulk density (g/cm ³)	Filament Linear density (tex)	Filament Extrusion OF_E^1	Fiber Linear density (tex)	3D-printing OF_{3D}^2	Fiber Swelling DS^3	Fiber OF_T^4
F-E	0	1.042 ± 0.001	2389 ± 139	1.09	349 ± 17	7.1	2.6	7.7
F-CNT-1-E	1	1.046 ± 0.001	2256 ± 18	1.15	290 ± 7	8.1	2.2	9.3
F-CNT-2-E	2	1.051 ± 0.001	2287 ± 71	1.14	267 ± 5	8.8	2.0	10.1
F-CNT-4-E	4	1.059 ± 0.002	2534 ± 83	1.04	231 ± 3	11.2	1.7	11.6
F-CNT-6-E	6	1.071 ± 0.002	2425 ± 64	1.11	224 ± 3	11.1	1.7	12.2
F-CNT-8-E	8	1.081 ± 0.002	2387 ± 64	1.12	219 ± 2	11.3	1.6	12.7

¹ Draw ratio of filament (extrusion) from Eq. (5.3-1). ² Draw ratio in 3D printing from Eq.(5.3-3). ³ Fiber swelling. ⁴ Total Draw ratio of fiber (extrusion and 3d printing) see Eq. (5.3-4).

The effect of CNT on the melt flow index (MFI) of extruded ABS filaments was also investigated. Figure 5.3-1 shows a strong decrease of MFI with the carbon nanotubes content, due to the increasing viscosity induced by the formation of a nanofiller network. This effect is also documented by a significant increase in the torque and internal pressure measured during the extrusion process after addition of CNT to ABS (see Table 5.3-1). Even though the MFI of nanocomposites with CNT content higher than 4 wt % is extremely low, it has been possible to produce feedstock filaments by using twin screw extruder up to 8 wt % of CNT, reaching maximum values of internal pressure of about 46 bar and 120 Nm of torque.

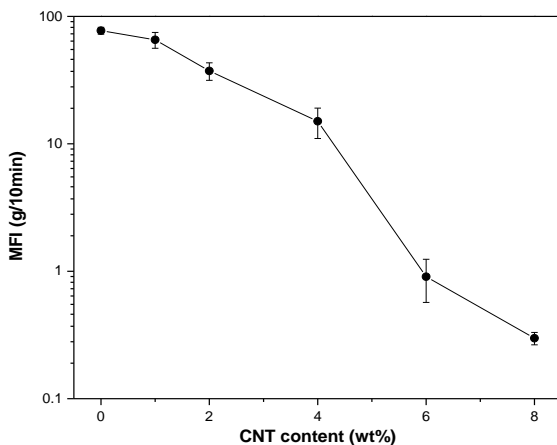


Figure 5.3-1. Melt flow index ($250^{\circ}\text{C}/10\text{ kg}$) of ABS nanocomposit as a function of CNT.

5.3.2 Bulk density

The bulk density of filaments is plotted in Figure 5.3-2 as a function of CNT volume fraction. The density of neat ABS filament is 1.042 g/cm^3 , which is consistent with the reported value in the materials technical data sheet [114]. Density of ABS/CNT composites increases almost linearly with rising fraction of CNT up to 1.081 g/cm^3 at 8 wt % of CNT (corresponding to about 4 vol %). As it can be seen, the experimental density of ABS filled CNT nanocomposites is slightly lower than the theoretical density estimated by using the rule of mixture, which evidences the presence of microvoids, whose volume fraction (V_v) is reported in Figure 5.3-2. Details of voids determination are reported in section 3.3.1.1.

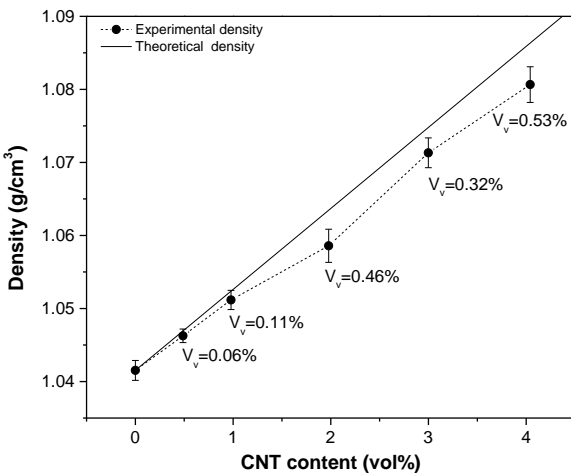
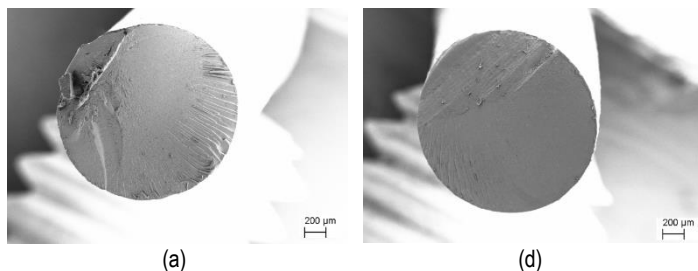


Figure 5.3-2. Experimental density values of ABS-CNT filaments compared to theoretical density and voids fraction (V_v).

5.3.3 Morphological analyses

The fracture surface of cryogenically broken filaments was visualized by SEM microscopy. Figure 5.3-3 illustrates the SEM images of ABS/CNT filaments with a CNTs content of 6 and 8 wt % at increasing magnification. Regarding the CNTs dispersion in both compositions, a homogenous distribution of single nanotubes in ABS matrix can be observed (no aggregates of nanotubes were detected). This means that the adopted two-steps process, consisting of mixing in an internal mixer followed by twin-screw extrusion, was capable to avoid the formation of nanofiller aggregates and to properly disperse CNTs in the ABS matrix. In addition, at high magnifications, a good adhesion level between CNT and ABS can be observed.



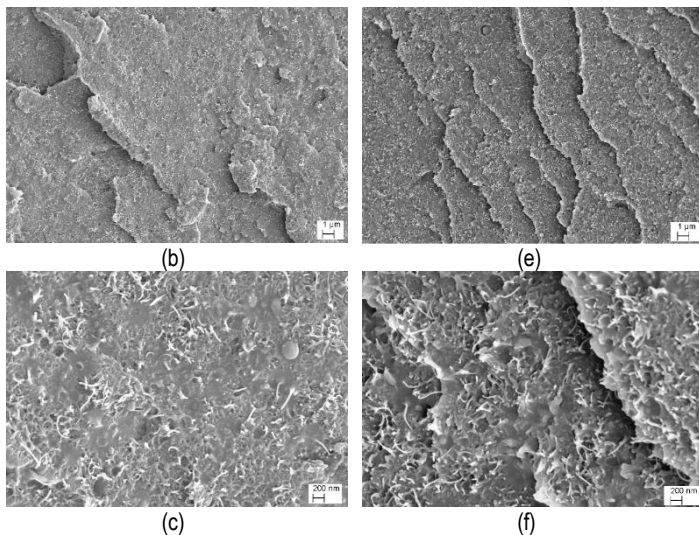


Figure 5.3-3. SEM micrographs of F-CNT-6-E (left) and F-CNT-8-E (right) filaments at different magnifications (a, d) $\times 80$, (b, e) $\times 10000$ and (c, f) $\times 50000$.

5.3.4 Thermal degradation behaviour

Thermal stability of ABS matrix and prepared composites was investigated by using thermal gravimetric analysis (TGA). Figure 5.3-4(a-b) depicts the TGA thermogram of neat ABS and CNT-filled composite filaments, while the most important parameters are summarized in Table 4. For the neat ABS in air environment two main degradation steps can be clearly observed at 416 °C and 514 °C, that could be attributed to the molecular chain scission and the oxidation of residual species, respectively [68, 182]. On the other hand, neat CNTs showed one single decomposition step at around 627°C. The onset temperature (T_{onset}) and the maximum degradation temperature ($T_{\text{d,max}}$) of the composites slightly increase with rising CNTs fraction up to a maximum value for 2 wt % of CNTs; afterwards they decrease. Similar behaviour was also observed for other systems, such as polylactic acid/CNT, where it was attributed to possible aggregation and breakage of CNTs at elevated concentrations [81].

For F-CNT-6-E and F-CNT-8-E samples, it is possible to note that double peaks occurred between 420–430°C. Moreover, an additional peak of nanocomposites with more than 4 wt % of CNT can be observed around 616–618 °C, which might be associated with the presence of CNT. The maximum mass loss rate (MMLR) in Figure 5.3-4b is progressively reduced by the presence of CNT since the nanofiller can hinder the diffusion of volatile products generated by polymer decomposition [80, 81, 182].

As reported in Table 5.3-3, the residue of tested composites at 475°C and 575°C increases with the CNT fraction.

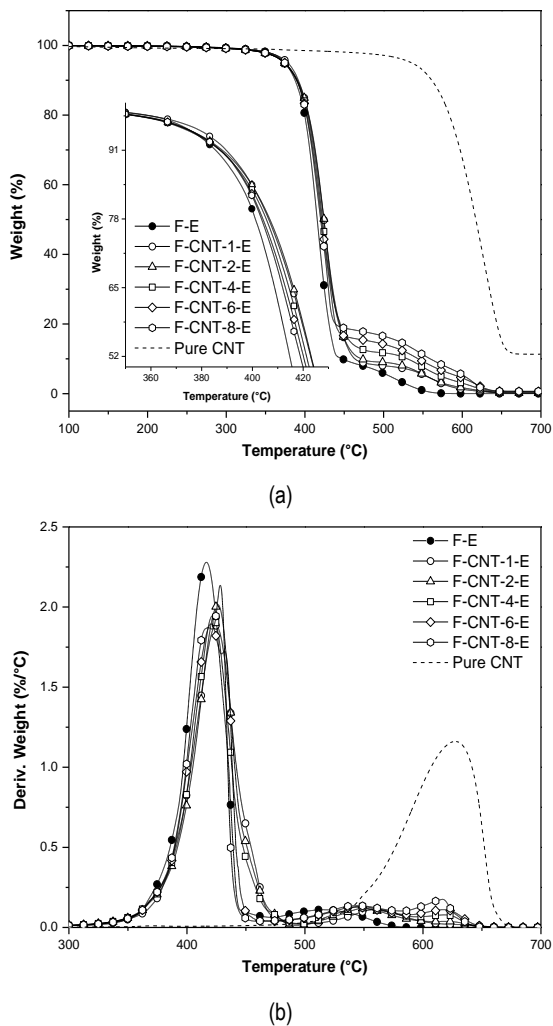


Figure 5.3-4. TGA curves of neat and nanofilled ABS filaments under air atmosphere: (a) Residual mass as a function of temperature; (b) Derivative of the mass loss.

Table 5.3-3. TGA data of pure ABS and its nanocomposites in an air atmosphere.

Samples	T_{onset} (°C)	T_{max1} (°C)	T_{max2} (°C)	T_{CNT} (°C)	Residue at (wt%)			Relative residue at (wt%)*	
					475°C	575°C	700°C	475°C	575°C
F	394.0	416.5	514.4	-	7.9	0.1	0.0	0.0	0.0
F-CNT-1-E	397.5	424.6	560.4	-	8.8	2.8	0.2	0.9	2.7
F-CNT-2-E	399.4	426.2	548.6	-	9.7	3.0	0.2	1.8	2.9
F-CNT-4-E	396.9	421.5	547.1	618.2	12.6	4.8	0.4	4.7	4.7
F-CNT-6-E	394.8	420.6	542.2	617.5	15.4	6.6	0.6	7.5	6.5
F-CNT-8-E	394.6	428.3	544.1	616.6	17.8	8.2	0.7	9.9	8.1
Pure CNT	576.3	-	-	627.3	97.7	84.6	11.3	-	-

*calculated according to the equation (3.3-4).

In Figure 5.3-5, however, the experimental residual mass is slightly higher than theoretical residue from individual components polymer ABS and pure CNT (see equation (5.3-5)). It is suggesting the interaction between ABS and CNT provided a lower degradation in nanocomposites with respect to the behaviour of single constituents.

$$R_{theoretical} = w_f \times R_{CNT} + (1 - w_f) R_{ABS} \quad (5.3-5)$$

where w_f is weight fraction of CNT; R_{CNT} and R_{ABS} are the residue of pure CNT and neat ABS, respectively.

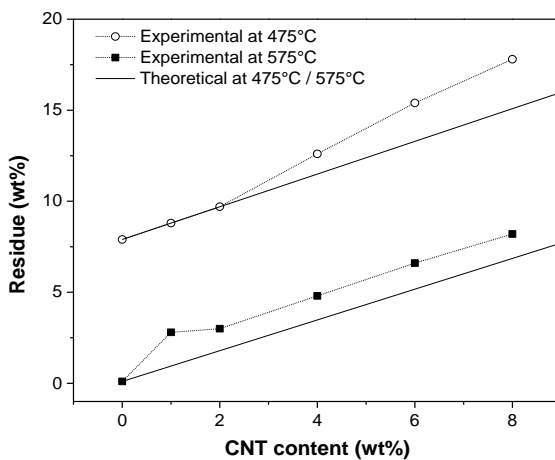


Figure 5.3-5. The comparison of experimental and theoretical residues of nanocomposites at 475°C and 575°C.

5.3.5 Differential scanning calorimetry

All DSC thermograms of neat matrix ABS and of CTN filled composites are depicted in Figure 5.3-6 and were used for the determination of the glass transition temperature T_g (Table 5.3-4). (Table S2). The T_g values found for SAN phase in neat ABS and in CNT-filled ABS filaments are about 106 °C and 108 °C at the first and the second heating run, respectively, which means that the presence of CNT has no significant effects on T_g of ABS/CNT composites. Also, Yang et al. reported only a slight increase in T_g promoted by single wall carbon nanotubes (SWCNT) dispersed in ABS [182].

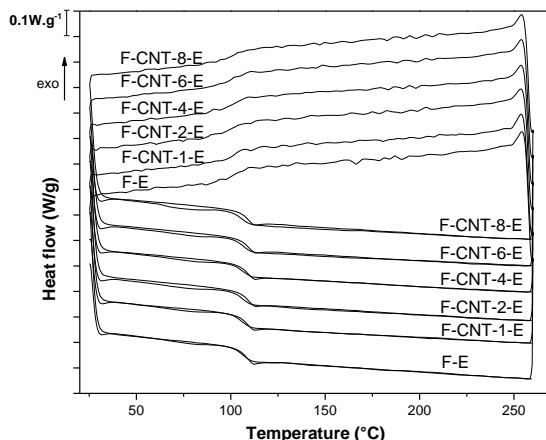


Figure 5.3-6. DSC thermogram of neat ABS and its ABS/CNT nanocomposites filaments in the heating-cooling-heating cycle.

Table 5.3-4. Glass transition temperatures of styrene–acrylonitrile phase (T_g) for ABS and relative nanocomposite of filaments from DSC.

Samples	T_g (°C)		
	First heating	Cooling	Second heating
F-E	106.1	102.1	108.0
F-CNT-1-E	105.8	102.2	108.7
F-CNT-2-E	105.5	102.9	108.8
F-CNT-4-E	105.5	102.7	108.8
F-CNT-6-E	106.7	100.1	109.2
F-CNT-8-E	105.2	102.7	108.8

5.3.6 Quasi-static tensile test

Tensile properties were measured for both filaments and fibers at the various CNT content. Table 5.3-5 shows an almost equivalent mechanical behaviour of the different diameter extrudates (about 1.7 mm and 0.50-0.65 mm) with no direct dependence on the polymer orientation. The representative tensile stress-strain curve of ABS filament with an indication of the tensile energy to break (TEB) and the propagation energy (P) from the yield to break point presents in Figure 5.3-7. Ductility factor is the ratio between the propagation energy (P) from the yield to break point with respect to TEB, calculated according to the equation:

$$\text{Ductility factor} = \frac{P}{\text{TEB}} \quad (5.3-6)$$

In Table 5.3-5, TEB progressively decreases with CNT content, and correspondingly the ductility factor for both filaments and fibers, especially above 4 wt% of nanofiller.

Representative stress-strain curves of filaments of neat ABS and its nanocomposites are reported in Figure 5.3-8. It is worth noting that CNT enhances both tensile modulus (E) and yield strength (σ_y) of the composites (see Table 5.3-5). At the highest concentration of nanotubes (8 wt %) the elastic modulus of ABS/CNT nanocomposites achieved a value 19% higher than that of ABS matrix. The highest σ_y was found for F-CNT-6-E, while F-CNT-8-E shows a slight reduction in σ_y and almost brittle behaviour. Therefore, ABS with 6 wt % of carbon nanotubes was an optimal compromise for FDM application.

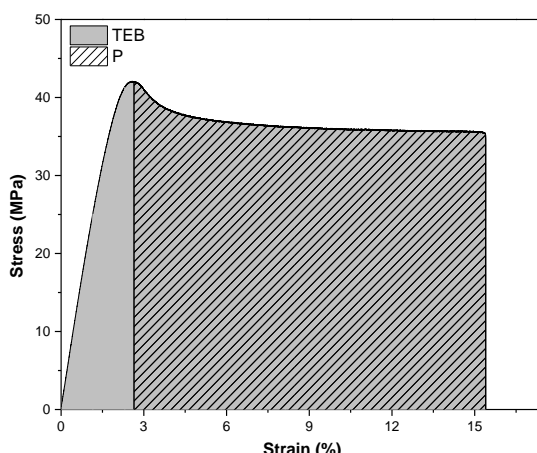


Figure 5.3-7. Representative tensile stress-strain curve of ABS filament with an indication of the tensile energy to break (TEB) and the propagation energy (P) from the yield to break point.

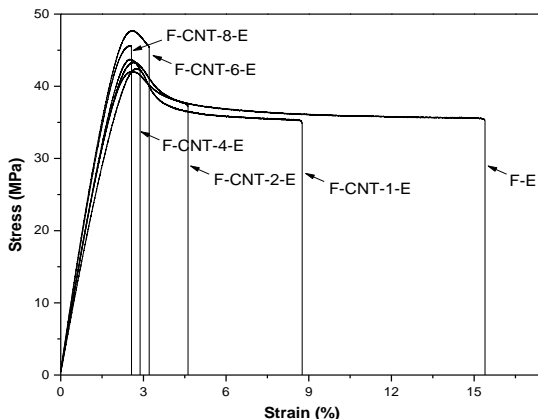


Figure 5.3-8. Tensile stress-strain curve of ABS and ABS-CNT filaments.

5.3.7 Dynamic mechanical response and coefficient of thermal expansion

As reported in Figure 5.3-9, ABS matrix and all composites show two transitions which can be identified with the glass transition of butadiene phase (B-phase; $T_{g1} = -84^\circ\text{C}$) and the glass transition of styrene–acrylonitrile phase (SAN phase; $T_{g2} = 125^\circ\text{C}$). Incorporation of CNT accounts for enhancement of the storage modulus of composites above that of ABS matrix, which becomes more pronounced at higher temperatures. For instance, at the highest concentration of CNT (8 wt %), the storage modulus of composite filament exceeds that of ABS by about 16% at 30°C and by 897% at 130°C .

Incorporated CNT also contributes in enhancing the dissipation of mechanical energy, as represented by the dynamic loss modulus. Moreover, the nanofiller also increases the glass transition temperatures of both butadiene and styrene–acrylonitrile phases by about 3°C due to the hindering of segmental motions at the interface. Similar observations were also reported in prior papers [63, 79].

The stiffness loss (SL_{T_g}) at the glass transition temperature could be evaluated from the reduction of storage modulus before and after the transition ($\Delta E'$), according to Equation (12) as a function of storage modulus at 30°C .

$$SL_{T_g} = (\Delta E') / E'_{30^\circ\text{C}} \quad (5.3-7)$$

Where $\Delta E'$ represents the modulus variation from -100°C to -50°C , or from 90°C to 130°C , in the case of transition of butadiene or SAN phase, respectively (see data in Table 5.3-6).

Table 5.3-5. Quasi-static tensile properties of ABS and its nanocomposite of filaments (E) and single fiber (f) produced by twin screw and FDM extrusion, respectively.

Samples	Filament diameter (mm)	E (MPa)	σ_y (MPa)	σ_b (MPa)	ϵ_b (%)	TEB* (MJ/m ³)	Ductility factor** P/TEB
F-E	1.725 ± 0.049	2207 ± 65	42.8 ± 1.9	35.0 ± 0.4	25.6 ± 15.8	8.94 ± 5.61	0.907 ± 0.040
F-CNT-1-E	1.679 ± 0.007	2132 ± 63	42.9 ± 0.4	35.1 ± 0.3	7.9 ± 2.4	2.59 ± 0.86	0.713 ± 0.104
F-CNT-2-E	1.684 ± 0.025	2226 ± 48	43.3 ± 0.3	37.8 ± 1.8	4.4 ± 1.2	1.36 ± 0.45	0.464 ± 0.153
F-CNT-4-E	1.765 ± 0.026	2320 ± 74	43.4 ± 0.9	41.9 ± 1.7	2.6 ± 0.3	0.65 ± 0.16	0.099 ± 0.083
F-CNT-6-E	1.712 ± 0.035	2625 ± 55	47.1 ± 0.5	44.6 ± 1.0	3.2 ± 0.5	1.04 ± 0.24	0.273 ± 0.158
F-CNT-8-E	1.702 ± 0.016	2650 ± 125	46.8 ± 1.2	46.5 ± 1.1	2.5 ± 0.2	0.73 ± 0.10	0.046 ± 0.065
F-f	0.648 ± 0.021	1918 ± 105	40.4 ± 0.9	33.6 ± 0.8	52.8 ± 27.2	18.5 ± 9.60	0.944 ± 0.023
F-CNT-1-f	0.591 ± 0.012	1801 ± 122	39.3 ± 1.7	35.8 ± 1.5	6.4 ± 3.2	2.00 ± 1.20	0.463 ± 0.259
F-CNT-2-f	0.567 ± 0.007	2033 ± 142	40.4 ± 0.5	33.6 ± 0.8	4.9 ± 1.2	1.53 ± 0.44	0.371 ± 0.168
F-CNT-4-f	0.528 ± 0.001	2035 ± 58	42.9 ± 1.4	40.8 ± 2.4	4.9 ± 1.2	1.59 ± 0.48	0.335 ± 0.220
F-CNT-6-f	0.515 ± 0.003	2099 ± 124	44.9 ± 1.3	44.1 ± 1.6	4.1 ± 0.6	1.29 ± 0.23	0.124 ± 0.098
F-CNT-8-f	0.506 ± 0.005	2147 ± 80	47.1 ± 0.6	46.9 ± 0.9	4.0 ± 0.7	1.31 ± 0.31	0.096 ± 0.075

*Total energy to break. **Ratio between the propagation energy (P) from the yield to break point, with respect to TEB.

In the zone of butadiene transition, the parameter SL was found to progressively decrease from about 0.45 (ABS matrix) up to 0.38 for F-CNT-8-E, in dependence on the content of CNT for all nanocomposite samples. On the other hand, the stiffness loss at the main glass transition (T_g of SAN phase) is almost linearly increasing with CNT content, from 0.80 (ABS filament) to about 0.84 for F-CNT-8-E filaments and it depends on the stiffening of rubbery phase above T_g .

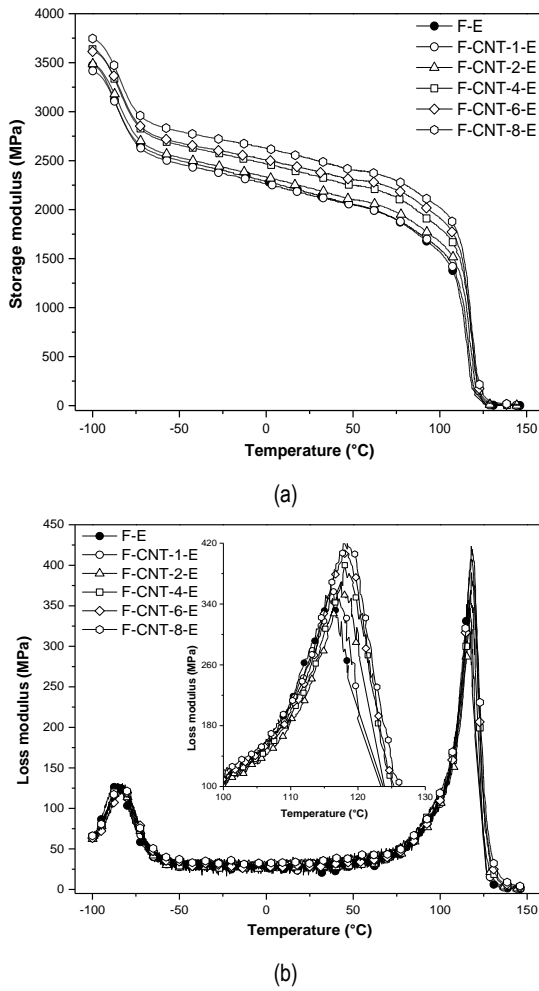


Figure 5.3-9. Dynamic mechanical thermograms a) and c) storage modulus (E') and b) loss modulus (E'') of neat ABS and nanocomposite samples as measured on filaments.

Table 5.3-6. Storage modulus and stiffness loos from DMTA analysis of neat ABS and its nanocomposites as measured on filaments and FDM samples.

Samples	Storage modulus					Stiffness loss* at T _g	
	-100°C (MPa)	-50°C (MPa)	30°C (MPa)	90°C (MPa)	130°C (MPa)	SL T _{g1}	SL T _{g2}
F-E	3474	2503	2145	1711	4.7	0.453	0.795
F-CNT-1-E	3417	2468	2129	1729	6.2	0.446	0.809
F-CNT-2-E	3487	2531	2197	1809	9.7	0.435	0.819
F-CNT-4-E	3636	2662	2342	1952	18.3	0.416	0.826
F-CNT-6-E	3614	2685	2390	2044	28.0	0.389	0.844
F-CNT-8-E	3747	2799	2496	2139	42.2	0.380	0.840

*Stiffness loss calculated following the Eq. (5.3-7).

Table 5.3-7. Damping peaks and loss modulus from DMTA analysis of neat ABS and its nanocomposites as measured on filaments and FDM samples.

Samples	Loss modulus				Damping peaks	
	B peak		SAN peak		B-phase T _{g1}	SAN-phase T _{g2}
	E'' _{peak} (MPa)	T _{peak} (°C)	E'' _{peak} (MPa)	T _{peak} (°C)		
F-E	128	-86.9	347	115.6	-84.9	122.7
F-CNT-1-E	124	-84.5	355	116.3	-83.6	123.2
F-CNT-2-E	122	-85.1	356	117.6	-82.4	125.5
F-CNT-4-E	128	-83.8	380	118.4	-82.9	126.0
F-CNT-6-E	122	-83.3	406	118.0	-81.5	124.6
F-CNT-8-E	128	-83.1	419	118.4	-82.2	125.6

Thermal strain of ABS/CNT filaments is plotted in Figure 5.3-10, and coefficient of thermal expansion of all samples is reported in Table 5.3-8. The thermal strain of composite filaments exhibited the linear trend up to 100°C, i.e. approximately to the glass transition temperature. The steep increment of thermal strain indicates the transition from the glassy state to the rubbery state with the much higher mobility of polymer chains. Above 120°C, the thermal strain showed negative slope concerning the temperature scale due to some shrinkage of the polymer chains orientated during extrusion. Incorporated CNT markedly reduced the coefficient thermal expansion (see Table 5.3-8). As expected, the composite with the highest concentration of CNT shows the largest drop of the coefficient thermal expansion, i.e. 79.6 for ABS to $52.3 \times 10^{-6}/K$ for F-CNT-8-E at the room temperature (20/50°C), and from -891 for ABS to $-51 \times 10^{-6}/K$ for F-CNT-8-E at the temperature (130/150°C).

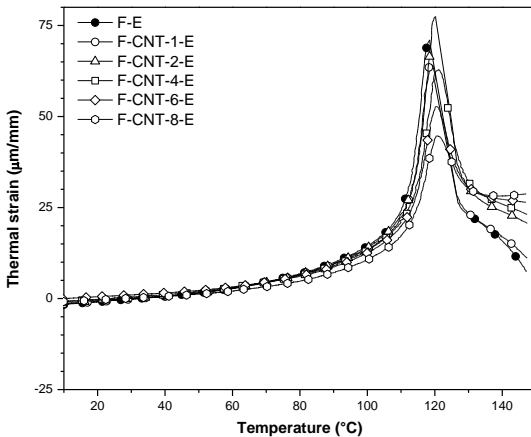


Figure 5.3-10. Thermal strain of neat ABS and nanocomposite samples as measured on filaments.

Table 5.3-8. Coefficients of linear thermal expansion (CLTE) and linear thermal deformation (CLTD) of ABS and its nanocomposites as measured on filament samples.

Sample	CLTE ($\times 10^{-6}/\text{K}$)				CLTD ($\times 10^{-6}/\text{K}$)
	ΔT_1	ΔT_2	ΔT_3	ΔT_4	
F-E	49.7 ± 0.2	79.6 ± 0.4	262.9 ± 2.1	2350 ± 68	-891 ± 11
F-CNT-1-E	51.6 ± 0.3	78.5 ± 0.5	246.1 ± 1.8	1880 ± 55	-678 ± 55
F-CNT-2-E	48.4 ± 0.1	70.3 ± 0.4	250.8 ± 2.0	1770 ± 54	-491 ± 7
F-CNT-4-E	43.2 ± 0.1	67.5 ± 0.5	223.8 ± 2.1	1450 ± 44	-465 ± 7
F-CNT-6-E	38.1 ± 0.1	55.9 ± 0.3	207.0 ± 2.1	1290 ± 26	-206 ± 7
F-CNT-8-E	33.7 ± 0.1	52.3 ± 0.2	191.3 ± 1.9	1150 ± 21	-51 ± 7

Temperature interval: $\Delta T_1 = -50/-20^\circ\text{C}$; $\Delta T_2 = 20/50^\circ\text{C}$; $\Delta T_3 = 70/90^\circ\text{C}$; $\Delta T_4 = 108/113^\circ\text{C}$; $\Delta T_5 = 130/150^\circ\text{C}$.

5.3.8 Creep stability

Figure 5.3-11 shows the creep compliance at 30°C of neat ABS and composites found for filament samples. If no plastic deformation occurs, compliance of isothermal tensile creep, $D_{\text{tot}}(t)$, consists two components: elastic (instantaneous) D_{el} and viscoelastic (time-dependent) D_{ve} , as defined in Eq. (5.3-8).

$$D(t) = D_{\text{el}} + D_{\text{ve}}(t) \quad (5.3-8)$$

Incorporation of CNT in ABS accounts for a pronounced reduction of both compliance components, as reported in Table 5.3-9. D_{el} is characterized by an almost

linear decrease with CNT fraction, which is in conformity with the inverse trend of tensile modulus (Table 5.3-5 and Table 5.3-6). For example, the composite with 8 wt% of the nanofiller showed D_{el} or $D_{tot,3600s}$ by 21% or 26% lower than the neat matrix.

The empirical Findley's model (power law), summarized in Eq. (5.3-9) was used to describe the viscoelastic creep response [178-180]:

$$D(t) = D_e + k t^n \quad (5.3-9)$$

where D_e is the elastic (instantaneous) creep compliance, k is a coefficient related to the magnitude of the underlying retardation process and n is an exponent related to the time dependence of the creep process. The fitting parameters for experimental creep data are summarized in Table 5.3-9. The fitting model was satisfactory, as R^2 around 0.99 was found for all samples value. The addition of CNT reduced the creep compliance of composites; in particular, the value of parameter D_e , for filaments are in good agreement with the values of D_{el} from Eq. (5.3-8). The coefficient n reflects the kinetics of displacements of the segments of macromolecules in the viscous medium in the course of the creep and it was found to slightly decrease with the presence of CNT in ABS filaments.

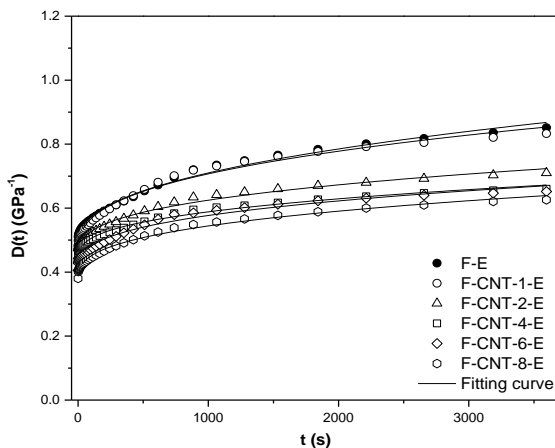


Figure 5.3-11. Creep compliance, $D(t)$ at 30°C, of neat ABS and nanocomposites as measured on filaments at 3.9 MPa.

Table 5.3-9. Creep test of neat ABS and its nanocomposites as measured on filaments and FDM samples.

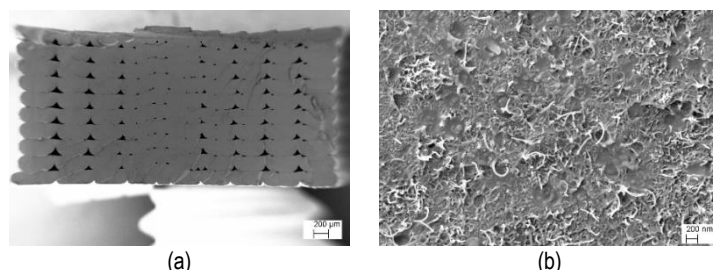
Samples	D _{el} (GPa ⁻¹)	D _{ve,3600s} (GPa ⁻¹)	D _{tot,3600s} (GPa ⁻¹)	D _e (GPa ⁻¹)	k (GPa ⁻¹ s ⁻ⁿ)	n	R ²
F-E	0.482	0.369	0.851	0.488	0.012	0.419	0.9924
F-CNT-1-E	0.471	0.362	0.833	0.460	0.020	0.364	0.9889
F-CNT-2-E	0.450	0.261	0.710	0.447	0.016	0.345	0.9912
F-CNT-4-E	0.436	0.225	0.660	0.436	0.014	0.342	0.9920
F-CNT-6-E	0.405	0.246	0.652	0.393	0.020	0.319	0.9844
F-CNT-8-E	0.380	0.246	0.626	0.374	0.016	0.347	0.9925

5.4 Fused deposition modelling with ABS-carbon nanotubes nanocomposites

On the basis of the work presented in the previous sections, neat ABS (F) and 6 wt% of CNT filaments were selected to feed a high-temperature FDM 3D-printer to specify the effects of CNT on the properties 3D-printed components along various build orientations: horizontal concentric (HC), horizontal 45°/-45° infill (H45) and perpendicular concentric (PC).

5.4.1 Morphological analyses

In Figure 5.4-1 (a–f), the cross-sections of FDM nanocomposite specimens at low and high magnifications are visualized. Moreover, for FDM specimens the presence of voids (about 3 and 1 vol % as observed from Figure 5a, c respectively) is documented. Also, uniform dispersion of nanofillers can be observed in Figure 5.4-1 (b, d, f) for all FDM specimens at different build orientations. By using the ImageJ software, the diameter of nanotubes was estimated to be about 33 ± 3 nm for all specimens (average of ten measurements).



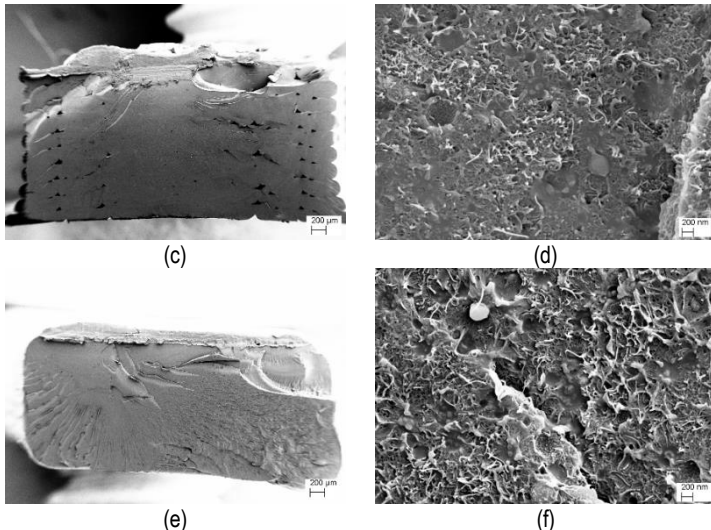
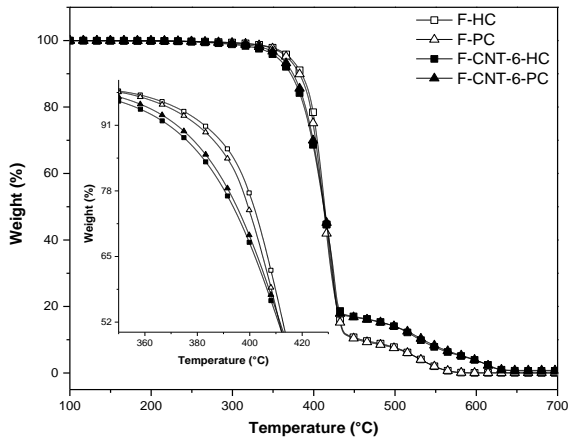


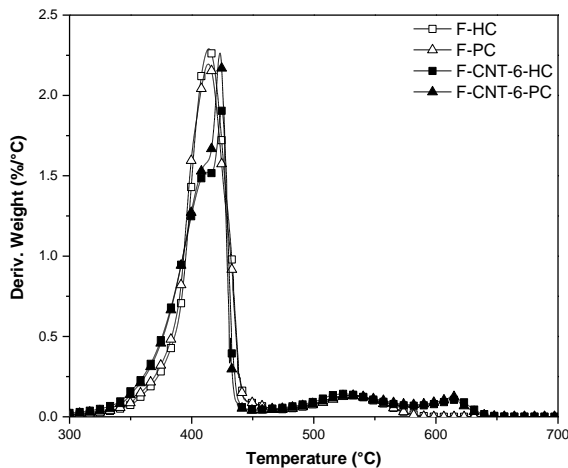
Figure 5.4-1. SEM micrographs of 3D-printed dumbbell specimens printed from carbon nanotubes nanocomposites, F-CNT-6-HC (a, b), F-CNT-6-H45 (c, d) and F-CNT-6-PC (e, f).

5.4.2 Thermal degradation behaviour

TGA thermograms reported in Figure 5.4-2 (a-b) prove that 3D-printed specimens prepared at different built orientations (HC and PC) exhibited a behaviour similar to that observed for neat ABS filaments. However, as reported in Table 5.3-3, 3D-printed nanocomposite samples, i.e. F-CNT-6-HC and F-CNT-6-PC, showed a slightly lower T_{onset} than the corresponding neat ABS samples. The residue at 475°C and 575°C was considered to evaluate the composition of CNT. In particular, the relative residue obtained after subtraction of ABS contribute fit quite well with the 6 wt% of CNT.



(a)



(b)

Figure 5.4-2. TGA curves of neat and 6 wt% nanofilled ABS 3D printed samples (HC and PC) under air atmosphere: (a) Residual mass as a function of temperature; (b) Derivative of the mass loss.

Table 5.4-1. TGA data of pure ABS and its nanocomposites in an air atmosphere.

Samples	T _{onset} (°C)	T _{max1} (°C)	T _{max2} (°C)	T _{CNT} (°C)	Residue at (wt%)			Relative residue at (wt%)	
					475°C	575°C	700°C	475°C	575°C
F-HC	391.9	414.0	531.8	-	9.2	0.2	0.0	0.0	0.0
F-PC	391.0	415.2	535.6	-	8.9	0.2	0.0	0.0	0.0
F-CNT-6-HC	382.3	424.5	525.3	618.0	15.8	5.4	0.6	6.6	5.2
F-CNT-6-PC	388.0	423.1	529.0	613.6	15.6	5.7	0.8	6.7	5.5

5.4.3 Differential scanning calorimetry

All DSC thermograms of neat ABS matrix and of CTN filled composites are reported in Figure 5.4-3 and were used for the determination of the glass transition temperature T_g (see Table 5.4-2). The glass transition temperature of 3D-printed neat ABS (F-HC and F-PC) is slightly higher than that of neat ABS filament at the first heating run but similar in the second heating run. Moreover, the presence of nanotubes does not have any significant effect on glass transition temperature of nanocomposites in all the three steps of the cycle (first heating-cooling second heating).

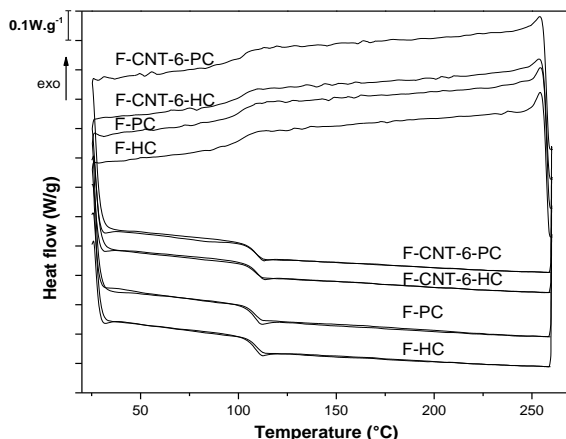


Figure 5.4-3. DSC thermogram of neat ABS and its ABS/CNT nanocomposites of 3D-printed samples in the heating-cooling-heating cycle.

Table 5.4-2. Glass transition temperatures of styrene–acrylonitrile phase (T_g) for ABS and relative nanocomposite of FDM samples from DSC.

Samples	T_g (°C)		
	First heating	Cooling	Second heating
F-HC	109.0	101.9	108.1
F-PC	108.1	101.1	108.3
F-CNT-6-HC	108.5	102.4	109.7
F-CNT-6-PC	108.5	102.9	108.7

5.4.4 Mechanical behaviour

5.4.4.1 Quasi-static tensile test

Stress-strain curves of 3D-printed specimens are shown in Figure 5.4-4 and resulting mechanical parameters are summarized in Table 5.4-3. Tensile modulus of H45 sample is comparable to that of HC sample probably because of good contact between bead extruded microfilaments and a lower fraction of voids in H45, as documented by SEM images (Figure 5.4-1a and c). Similarly enough, the lower yield strength of H45 with respect to that of HC is most probably due to internal orientations of deposited filaments as shown in Figure 5.4-1(a and c). H45 or HC samples are expected to behave almost as isotropic or transversally isotropic materials. On the other hand, ABS-PC samples manifest a brittle behaviour due to the weakness of interlayer bonding and the same behaviour is even clearer for F-CNT-6-PC samples because interlayer bonding could be significantly reduced by the higher viscosity in the molten state. Correspondingly, the ductility factor is zero, due to the absence of any toughening mechanism in the fracture process. In addition, the presence of CNTs resulted in an enhancement of both tensile modulus and yield stress for all FDM samples. The elastic modulus of ABS/CNT nanocomposites continuously increased up to 22%, 18% and 5% above that of unfilled ABS at the orientation of HC, H45 and PC, respectively. The highest yield stress can be observed in F-CNT-6-HC sample owing to deposited filaments parallel to the applied load and the reinforcing effect of carbon nanotubes. As a side effect, the elongation at break of FDM composites samples was significantly reduced proportionally to the CNT content.

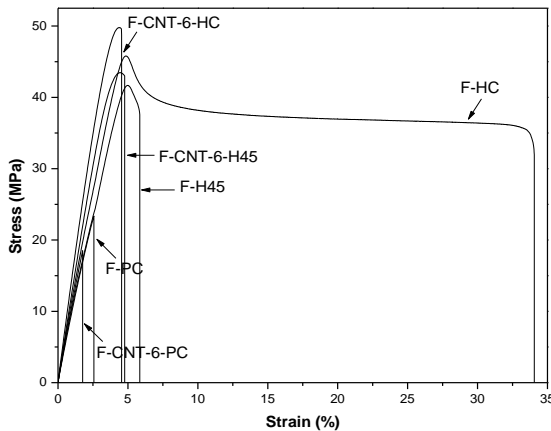


Figure 5.4-4. Tensile stress-strain curve of ABS and ABS-CNT of 3D-printed samples.

Table 5.4-3. Quasi-static tensile properties of ABS and its nanocomposite of FDM samples.

Samples	E (MPa)	σ_y (MPa)	σ_b (MPa)	ε_b (%)	TEB* (MJ/m ³)	Ductility factor** P/TEB
F-HC	2235±170	45.7± 0.5	31.9±1.7	30.0± 10.4	10.7±3.76	0.866±0.077
F-H45	2308±112	41.1±0.9	37.9±1.6	5.3±0.5	1.30±0.16	0.204±0.120
F-PC	2077±44	-	22.0±4.4	2.4±0.7	0.30±0.10	0
F-CNT-6-HC	2735±158	49.6±0.6	49.2±0.6	4.5±0.2	1.35±0.10	0.048±0.044
F-CNT-6-H45	2739±268	43.2±0.3	42.6±0.4	4.6±0.3	1.19±0.11	0.054±0.056
F-CNT-6-PC	2181±51	-	18.7±1.5	1.9±0.1	0.18±0.03	0

*Total energy to break. **Ratio between the propagation energy (P) from the yield to break point, with respect to TEB.

5.4.4.2 Fracture mechanism

Figure 5.4-5 presents the fractured surface of ABS and CNT-6 3D-printed specimens broken in liquid nitrogen. For both HC and H45 samples, it is easy to observe along the thickness in Z direction 10 flattened parallel deposited bead microfilaments with a dimension of about 420 microns in width and 210 microns in height for F-HC (and about 410 micron and 210 micron for F-CNT-6-HC).

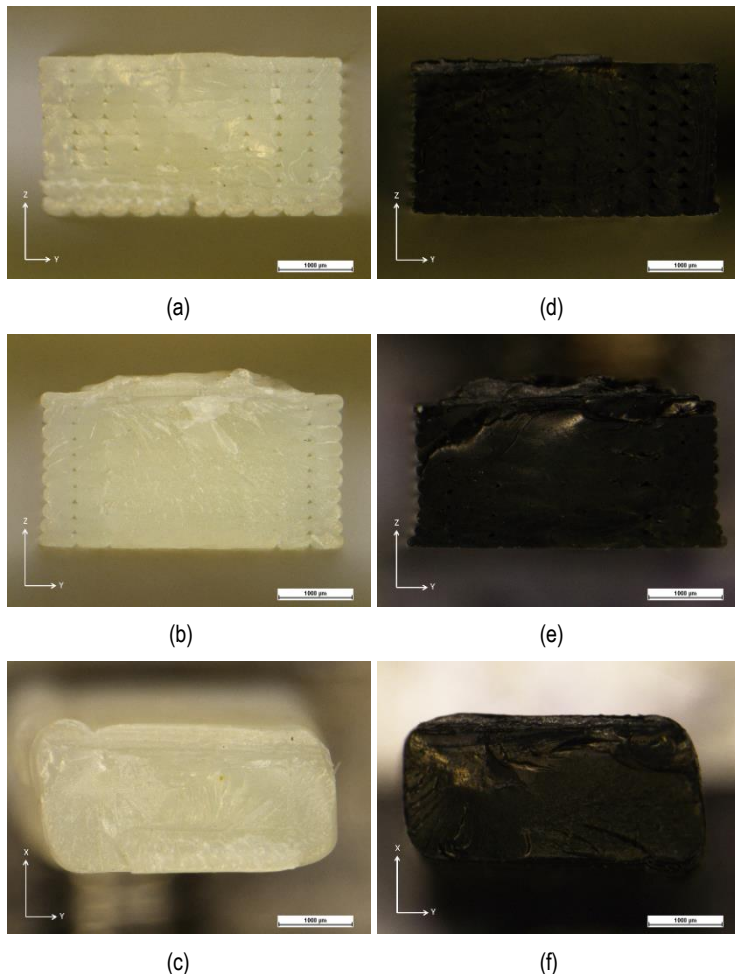


Figure 5.4-5. Frozen fracture of cross-section of 3D-printed dumbbells: (a) F-HC, (b) F-H45, (c) F-PC, (d) F-CNT-6-HC, (e) F-CNT-6-H45 and (f) F-CNT-6-PC.

At the same time, along with the sample width in the Y direction, HC evidenced 10 deposited microfilaments, whereas only 4 deposited parallel microfilaments could be observed in the external contours of H45 samples (2 on the right and 2 on the left). The inner microfilaments oriented at $+45^\circ/-45^\circ$ could not be easily distinguished and an almost homogeneous zone appeared. For this reason, the similar stiffness of HC and H45 can be attributed to the combined effect of both the larger number of voids and orientation of microfilaments. On the other hand, for F-PC and F-CNT-6-PC no

traces of voids and of deposited microfilaments were observed in the cryo-fractured surface. These results have been attributed to the higher temperature of interlayer overlapping that is dependent on two factors: (i) the lower deposition rate (16 mm/s of PC sample with respect to 40 mm/s of other samples) and consequently the lower viscosity of deposited microfilament; and (ii) the lower time of deposition of the layer in PC samples with respect to HC samples (23 s vs. 46 s, respectively) and hence the higher temperature of the last deposited layer in PC sample (surface of deposition).

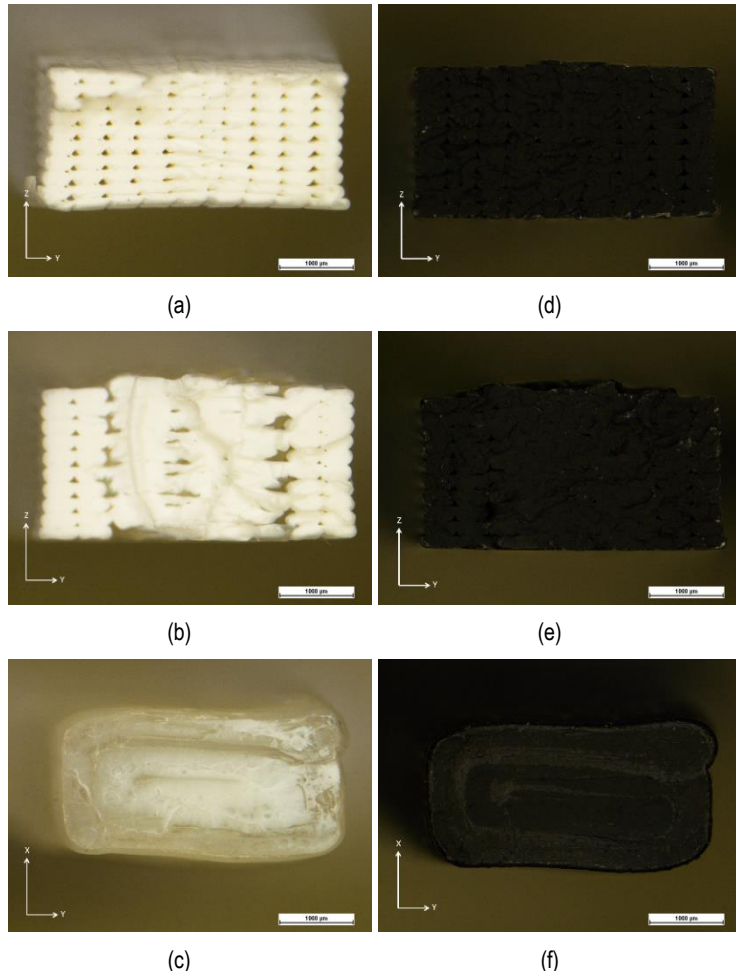


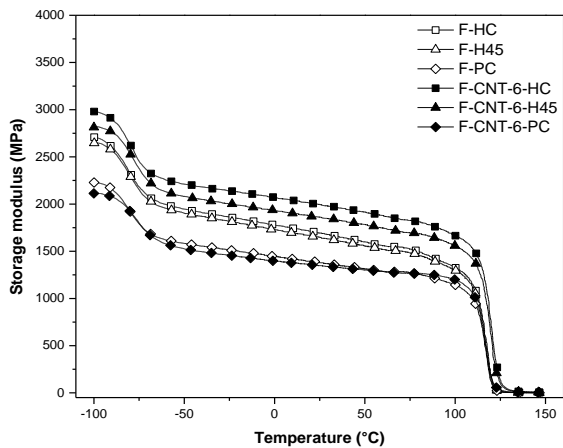
Figure 5.4-6. Tensile fracture of cross-section of 3D-printed dumbbells: (a) F-HC, (b) F-H45, (c) F-PC, (d) F-CNT-6-HC, (e) F-CNT-6-H45 and (f) F-CNT-6-PC.

Difference is the case of a fractured cross-section of 3D-printed samples derived from the tensile test, as shown in Figure 5.4-6. The clear shape and size of the triangular voids between the deposited microfilaments (see Figure 5.4-6a) were observed due to the plastic deformation under tensile load. Moreover, some traces of microfilaments were partially evidenced in VC sample of both neat ABS and its nanocomposites, as shown in Figure 5.4-6 (c, f), which suggests a weak adhesion of the inter-layer bonding between microfilaments.

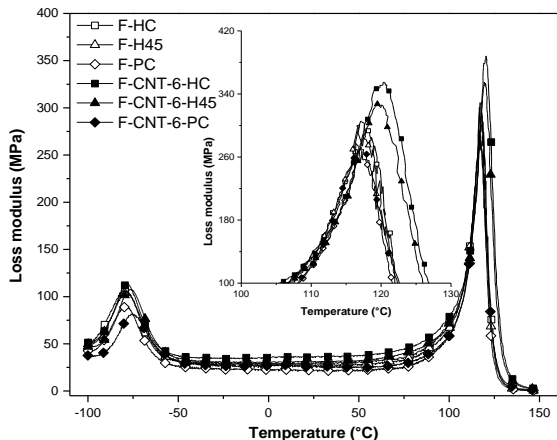
5.4.5 Dynamic mechanical response and coefficient of thermal expansion

As expected, the storage modulus of 3D-printed specimens at build parallel and $\pm 45^\circ$ orientations (HC and H45) is higher than that measured on samples with the PC orientation. The behaviour observed for HC and H45 samples is related to the direction of the deposited filaments preferentially aligned and isotropic materials inclined at $\pm 45^\circ$ along the tensile applied load respectively, while the deposited layers in PC specimens are mostly oriented transversally to the tensile force. In general, the 3D-printed samples show storage modulus lower than original filaments due to the presence of voids and specific orientation of extruded microfilaments in 3D-printed samples (HC and PC).

The data summarized in Table 5.4-4, clearly show that the storage modulus of HC or H45 at 30°C is enhanced by about 15% or 12% due to the addition of carbon nanotubes. The observed effect is even more pronounced at higher temperatures: at 130°C the storage modulus of F-CNT-6-HC or F-CNT-6-H45 is 5 times higher than that of neat ABS-HC and ABS-H45. On the other hand, CNT do not exhibit any stiffening effect on storage modulus along PC orientation in the temperature range - 50 to 30°C, while a three-fold increase in the storage modulus can be observed at 130°C. The presence of carbon nanotubes also increases the glass temperature of F-CNT-6-HC and F-CNT-6-H45 by about 3°C, which is identical with previously reported an increase in T_g for nanocomposite filaments (see Table 5.4-5).



(a)



(b)

Figure 5.4-7. Dynamic mechanical thermograms a) and c) storage modulus (E') and b) loss modulus (E'') of neat ABS and nanocomposite samples as measured on 3D-printed specimens along different orientation (HC, H45, PC).

Table 5.4-4. Storage modulus and stiffness loss from DMTA analysis of neat ABS and its nanocomposites as measured on filaments and FDM samples.

Samples	Storage modulus					Stiffness loss* at T_g	
	-100°C (MPa)	-50°C (MPa)	30°C (MPa)	90°C (MPa)	130°C (MPa)	SL T_{g1}	SL T_{g2}
F-HC	2709	1948	1678	1415	5.4	0.454	0.840
F-H45	2646	1904	1631	1384	4.7	0.455	0.846
F-PC	2229	1583	1367	1207	3.9	0.473	0.880
F-CNT-6-HC	2980	2211	1977	1749	32.6	0.389	0.868
F-CNT-6-H45	2813	2080	1845	1632	25.9	0.397	0.871
F-CNT-6-PC	2114	1527	1338	1245	11.8	0.439	0.922

*Stiffness loss calculated following the Eq. (5.3-7).

Table 5.4-5. Damping peaks and loss modulus from DMTA analysis of neat ABS and its nanocomposites as measured on filaments and FDM samples.

Samples	Loss modulus				Damping peaks	
	B peak		SAN peak		B-phase T_{g1}	SAN- phase T_{g2}
	E''_{peak} (MPa)	T_{peak} (°C)	E''_{peak} (MPa)	T_{peak} (°C)		
F-HC	107	-79.5	304	117.2	-78.6	124.9
F-H45	105	-78.7	293	116.9	-78.0	124.8
F-PC	89	-79.7	267	117.0	-77.9	124.1
F-CNT-6-HC	114	-78.0	354	120.3	-77.5	127.6
F-CNT-6-H45	108	-77.1	326	120.0	-75.3	127.0
F-CNT-6-PC	81	-75.3	270	117.1	-73.9	123.4

Figure 5.4-8 (a-b) shows the reduction of the main transition of storage modulus (R) and F -factor [79, 185] which are plotted as functions of the CTN fraction. In Figure 11a, the stiffening effect of CNTs in the rubbery phase above T_g of SAN is well documented. In particular, this effect seems to be more pronounced for FDM samples (HC and H45) with respect to filaments F-CNT-6-E, probably owing to the higher orientation and adhesion/dispersion of carbon nanotubes in FDM process.

Moreover, the F -factor represents a relative measure of modulus in the temperature interval of the glass transition, assuming that modulus at glassy state is dominated by the strength of intermolecular forces when polymer chains and nanofillers are packed [79]. Thus, the higher F -factor, the higher the effectiveness of the filler. Figure 5.4-8b presents the increase in the F -factor of filaments with the fraction of CNT and it confirms the relative effectiveness of CNT nanofiller with its fraction in composites in the rubbery phase.

For FDM sample (HC and H45), the reinforcing efficiency is slightly lower than filament at 6 wt % of CNT, maintaining almost the same adhesion level of nanofiller and matrix during FDM process. On the other hand, PC sample shows a different effect

since the properties of these specimens are mainly dependent on the inter-layer matrix adhesion and mostly independent on the compatibility of the polymer chains and nanofiller.

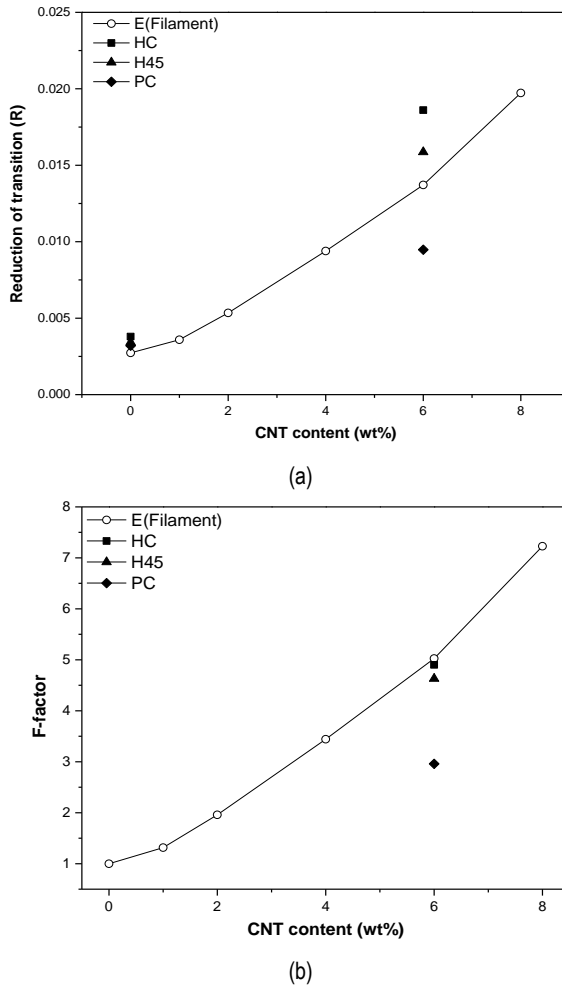


Figure 5.4-8. Reduction of main transition of storage modulus- R (a) and F -factor (b) as function of CNT nanofiller loading measured on filaments and 3D-printed samples (HC, H45 and PC).

Thermal strain of ABS/CNT FDM samples is plotted in Figure 5.4-9, and coefficient of thermal expansion of all samples is reported in Table 5.4-6. In the temperature interval 20/50°C, FDM specimens (HC, H45 and PC) printed from neat ABS, exhibit CLTE values of 85.8, 74.5 and $79.1 \times 10^{-6}/\text{K}$, respectively (see Table 5.4-6). The presence of CNTs accounts for a reduction of the CLTE of FDM specimens by 31% or 27% for HC or H45 but no effect was observed for PC build orientation.

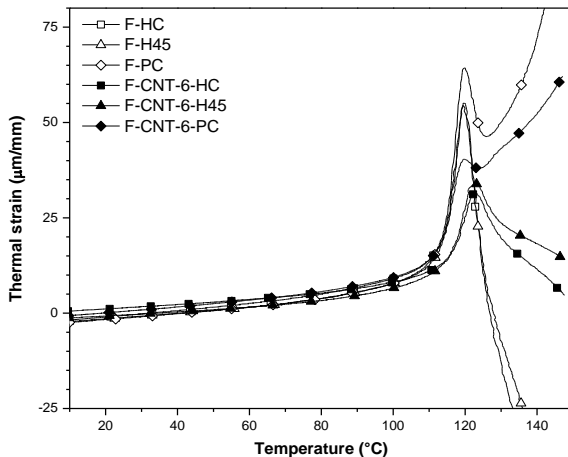


Figure 5.4-9. Thermal strain of neat ABS and nanocomposite samples as measured on 3D-printed samples along different orientations (HC, H45, and PC).

Table 5.4-6. Coefficients of linear thermal expansion (CLTE) and linear thermal deformation (CLTD) of ABS and its nanocomposites as measured on filament and FDM samples.

Sample	CLTE ($\times 10^{-6}/\text{K}$)				CLTD ($\times 10^{-6}/\text{K}$)
	ΔT_1	ΔT_2	ΔT_3	ΔT_4	
F-HC	61.0 ± 0.1	85.8 ± 0.3	156.6 ± 1.2	1040 ± 41	-4860 ± 50
F-CNT-6-HC	40.2 ± 0.1	59.0 ± 0.2	106.7 ± 0.9	479 ± 11	-805 ± 4
F-H45	58.0 ± 0.2	74.5 ± 0.2	146.5 ± 1.1	1210 ± 36	-3620 ± 32
F-CNT-6-H45	41.1 ± 0.1	54.0 ± 0.2	114.3 ± 1.0	587 ± 16	-506 ± 2
F-PC	61.0 ± 0.2	79.1 ± 0.2	147.3 ± 0.9	1330 ± 36	3310 ± 67
F-CNT-6-PC	57.8 ± 0.1	79.4 ± 0.3	139.7 ± 0.8	1010 ± 28	1090 ± 12

Temperature interval: $\Delta T_1 = -50/-20^\circ\text{C}$; $\Delta T_2 = 20/50^\circ\text{C}$; $\Delta T_3 = 70/90^\circ\text{C}$; $\Delta T_4 = 108/113^\circ\text{C}$; $\Delta T_5 = 130/150^\circ\text{C}$.

5.4.6 Creep stability

Figure 5.4-10 shows the creep compliance at 30°C of neat ABS and composites found for FDM samples. Incorporation of CNTs in ABS accounts for a pronounced reduction of both compliance components, as reported in Table 5.4-7. D_{el} is characterized by an almost linear decrease with CNTs fraction, which is in conformity with the inverse trend of tensile modulus (Table 5.4-3 and Table 5.4-4). A similar effect of CNT on both elastic and viscoelastic creep compliance was observed: 6 wt % of the nanofiller in ABS matrix reduced the total compliance of nanocomposite by 16%, 12% and 10% for HC, H45 and PC respectively.

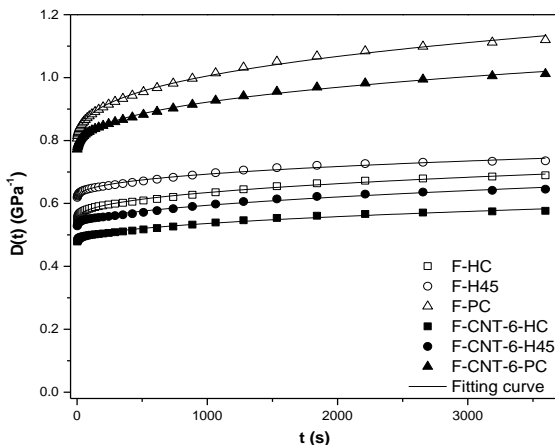


Figure 5.4-10. Creep compliance, $D(t)$ at 30°C, of neat ABS and nanocomposites as measured on 3D-printed samples along different orientations at 3.0 MPa.

The fitting parameters for experimental creep data are summarized in Table 5.4-7. The fitting model was satisfactory, as R^2 around 0.99 was found for all samples value. The addition of CNT reduced the creep compliance of composites; in particular, the values of parameter D_e for 3D-parts are in good agreement with the values of D_{el} .

Table 5.4-7. Creep test of neat ABS and its nanocomposites as measured on filaments and FDM samples.

Samples	D _{el} (GPa ⁻¹)	D _{ve,3600s} (GPa ⁻¹)	D _{tot,3600s} (GPa ⁻¹)	D _e (GPa ⁻¹)	k (GPa ⁻¹ s ⁻ⁿ)	n	R ²
F-HC	0.521	0.169	0.689	0.547	0.005	0.402	0.9951
F-CNT-6-HC	0.454	0.123	0.577	0.479	0.002	0.469	0.9905
F-H45	0.587	0.148	0.735	0.616	0.005	0.392	0.9910
F-CNT-6-H45	0.501	0.145	0.645	0.531	0.002	0.503	0.9917
F-PC	0.756	0.364	1.120	0.783	0.019	0.355	0.9980
F-CNT-6-PC	0.729	0.283	1.012	0.758	0.013	0.366	0.9981

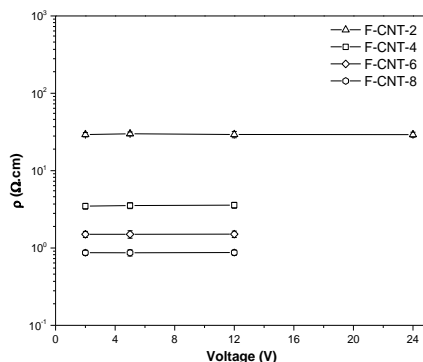
5.5 Electrical properties of ABS-carbon nanotubes nanocomposites

The previous sections have illustrated how CNT affects mechanical properties of prepared composites but most important effects of CNT can be expected in the field of electrical properties. Improvements of conductivity and electrical properties by incorporated CNT in different polymer, such as polyamide [83], polypropylene [84], polylactide [81] and ABS [78, 80, 181] have been documented in literature.

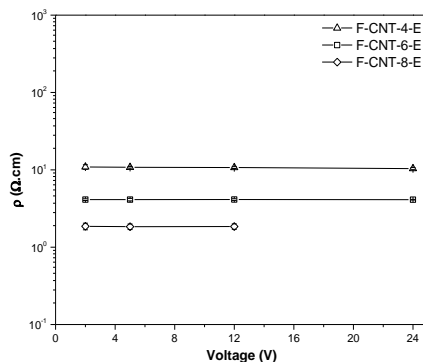
The measurement of electrical resistivity is essential to determine the CNTs content required to achieve an appreciable reduction of resistivity for applications. The electrical volume resistivity was carried out on samples obtained by the compression moulding (CM), on extruded filament (E), on fiber, on 3D-printed samples and filament plates. In particular, applications for the surface temperature under applied voltage were performed on CM, filaments and 3D samples. In the last section, strain monitoring capabilities were also tested for FDM samples with 6 wt% of CNT.

5.5.1 Electrical resistivity

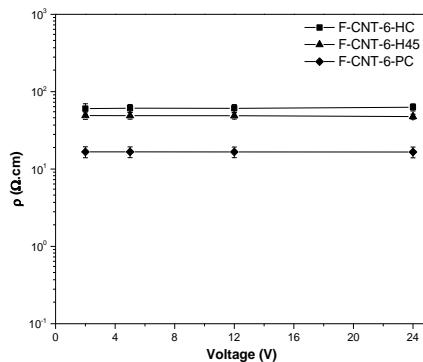
The results of the electrical volume resistivity test on the compression mould (CM), the filament (E) and 3D-printed samples are reported in Figure 5.5-1 (a, b and c), respectively. In Figure 5.5-1a, these results showed that the volume resistivity of the ABS/CNT nanocomposite plates decreased exponentially with the increase of the CNT concentration. Moreover, the electrical resistivity of the loaded samples does not appreciably change with the applied voltage up to 12 V. It can be concluded that these materials behave like ohmic conductors. Due to the Joule's effect the samples with higher than 2 wt% of CNT cannot testing at 24 V. For filament samples, the F-CNT-8-E sample could not be tested at 24 V either due to the Joule's effect.



(a)



(b)



(c)

Figure 5.5-1. Electrical volume resistivity of ABS nanocomposites: compression moulding (a), filaments (b) and 6 wt% CNT filled nanocomposites with different 3D printing (c).

In Figure 5.5-2 the electrical resistivity data measured on compression molding (CM) and filament (E) samples at an applied voltage of 5 V are plotted as a function of CNT content. For CM samples, a significant resistivity drop can be achieved at CNT contents lower than 2 wt%. For example, as the CNT concentration was increased from neat ABS to 2 wt% of CNT, the volume resistivity of the nanocomposites decreased by fifteen orders of magnitude (from $10^{16} \Omega \cdot \text{cm}$ to $2.9 \times 10^1 \Omega \cdot \text{cm}$). This result is quite similar to that reported in the literature for ABS/MWCNT nanocomposites for which an electrical percolation threshold of below 1 wt% is reported [86, 87]. The better results can be obtained with the F-CNT-6 and F-CNT-8 nanocomposites, for which a reduction of about sixteen orders of magnitude is achieved. In addition, the measurements on filaments reveal that the volume resistivity of the nanocomposites significantly decreases with at least 4 wt% of nanofiller whereas at CNT fractions up to 2 wt% the materials still exhibit an insulating behaviour and filaments could not be tested by means of the four probes configuration. The incorporation of CNT decreases the electrical resistivity of filaments to about $11 \Omega \cdot \text{cm}$, $4.1 \Omega \cdot \text{cm}$ and $1.8 \Omega \cdot \text{cm}$ for F-CNT-4-E, F-CNT-6-E, and F-CNT-8-E, respectively.

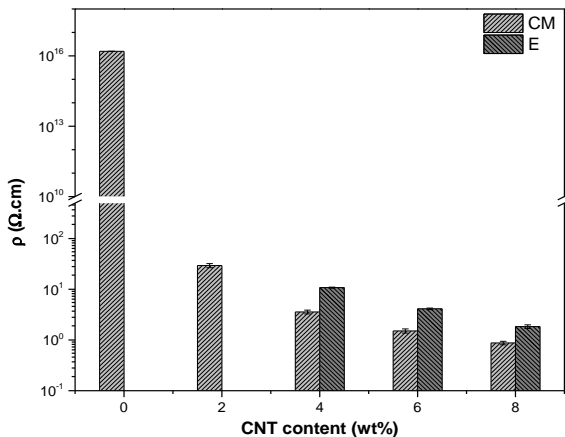


Figure 5.5-2. Electrical volume resistivity of ABS/CNT nanocomposites measured on compression moulding (CM) and filament (E) samples at an applied voltage of 5 V.

The evolution of electrical resistivity in ABS/CNT nanocomposites with weight content of CNT nanofiller in Figure 5.5-2 is due to network formation of CNT as shown in Figure 5.5-3. An analytical model of ABS/CNT nanocomposites is detailed in section 6.5.

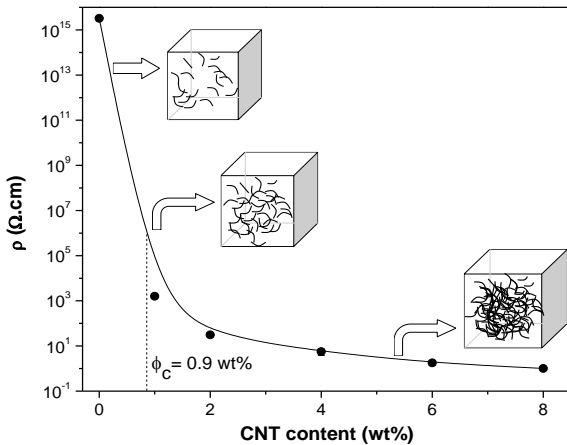


Figure 5.5-3. Evolution of electrical resistivity in ABS nanocomposite plates with a volume concentration (for ϕ_c detail in section 6.5).

The resistivity of 3D-printed samples F-CNT-6-H45 and F-CNT-6-PC shown in Figure 5.5-1c is independent of applied voltages and is higher than the correspondent filament (F-CNT-6-E). This partial reduction of conductivity not only in comparison with single filaments but also with compression molded specimens at the same composition (see Table 5.5-1) could be attributed to the internal features of FDM samples as shown in Figure 5.5-4.

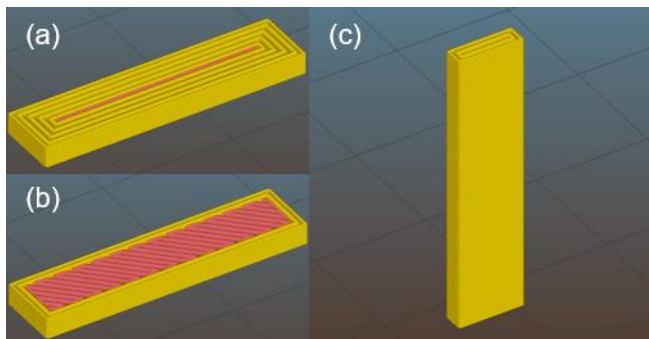


Figure 5.5-4. Internal features of FDM samples: (a) HC, (b) H45 and (c) PC.

Moreover, it should be noted that F-CNT-6-HC shows the highest resistivity, whereas F-CNT-6-PC the lowest. These results could be related to the better contact between deposited fibers beads, resulting in higher conductivity of samples; these findings are in good conformity with the documentation of SEM images (Figure 5.4-1e),

where F-CNT-6-PC specimens exhibit better and extensive contacts between the layer of deposited fibers in the direction of electrical measurements. Another consequence of different in resistivity of FDM samples is the presence of voids, as observed in their fracture surface (see Figure 5.4-1). In fact, the resistivity decreased with the volume of voids as shown in Figure 5.5-5.

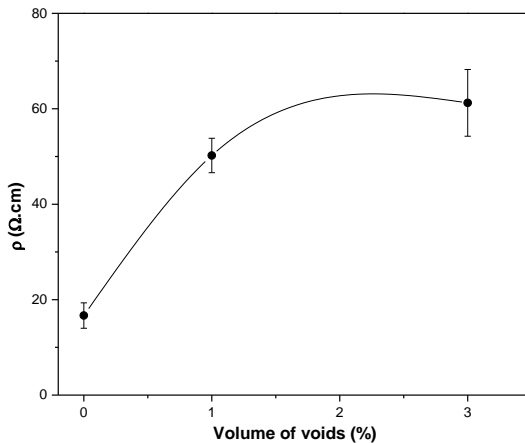


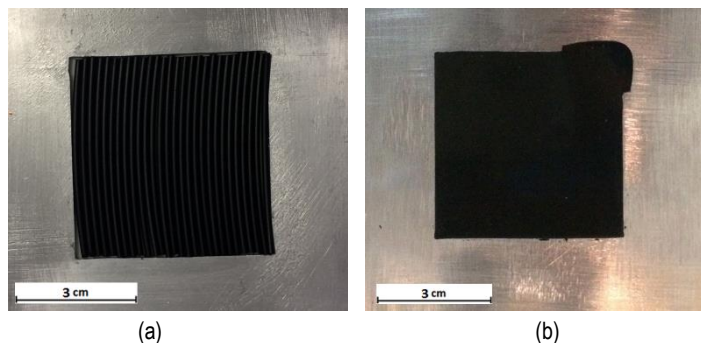
Figure 5.5-5. Electrical resistivity of FDM samples as a volume of voids from Figure 5.4-1.

Similarly, in literature, Zhang et al. reported that the electrical resistivity of 3D-printed components was found lower than the pristine 3D-printing fibers and the results were also confirmed to be highly dependent on the contact resistivity by numerical simulation method [16].

In order to understand the electrical behaviour of composite filaments and to evaluate the effect of CNT orientation in ABS, the most conductive filaments (i.e., F-CNT-6-E and F-CNT-8-E) were compression-molded for the production of homogeneous plates (resistivity results are shown in Figure 5.5-7). It worth noting that the electrical resistivity of CNT8-0, CNT8-45 and CNT8-90 was found to directly depend on the angles of filament orientation in the plate (Figure 5.5-6c). The resistivity of CNT8-0 is similar to that of CNT8 filament owing to the almost identical filaments orientation, whereas CNT8-90 leads to the lower level of filaments alignment with respect to the electrical field. The higher the angle, the higher the resistivity. And the same for specimens CNT6-0, CNT6-45 and CNT6-90, at resistivity even higher. From these findings, the electrical resistivity of filaments could be considered a quasi-isotropic behaviour of materials with partial random oriented CNT.

Table 5.5-1. Electrical volume resistivity of different kinds of ABS-CNT samples at an applied voltage of 5 V.

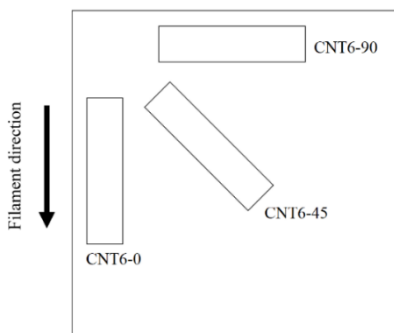
CTN content (wt%)	Plates ($\Omega \cdot \text{cm}$)	Filament $\Phi=1.70 \text{ mm}$ ($\Omega \cdot \text{cm}$)	3D-printed fiber $\Phi=0.50-0.55 \text{ mm}$ ($\Omega \cdot \text{cm}$)	3D samples ($\Omega \cdot \text{cm}$)
2%	29.9 ± 1.7	-	520 ± 95	Not prepared
4%	3.54 ± 0.31	10.8 ± 0.3	8.41 ± 1.26	Not prepared
6%	1.50 ± 0.17	4.12 ± 0.15	2.05 ± 0.09	61.2 ± 7.0 (HC) 49.0 ± 4.8 (H45) 16.8 ± 2.7 (PC)
8%	0.87 ± 0.08	1.84 ± 0.15	1.18 ± 0.04	Not prepared



(a)

(b)

Filament plate



(c)

Figure 5.5-6. Summary of preparation of filament plate with the mould $50 \times 50 \times 1.0 \text{ mm}$ starting with filaments at 6 and 8 wt% of CNT: (a) before compression and (b) after compression. (c) Schematic of samples at the different angles ($0, 45$ and 90°) for measuring electrical resistivity (see Figure 5.5-7).

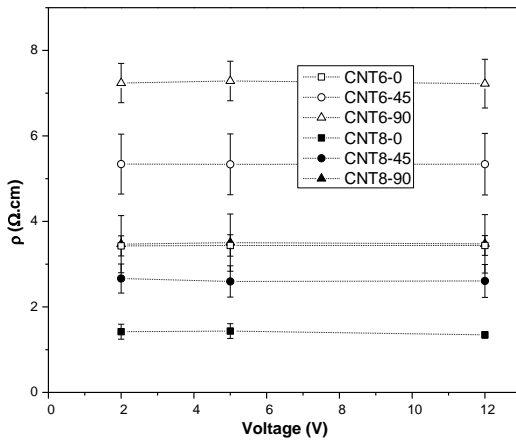


Figure 5.5-7. Electrical volume resistivity of ABS 6 wt% and 8 wt% filled nanocomposites of filament plates at different angles (0, 45 and 90°) as a function of the applied voltage of the applied voltage.

However, after FDM process the conductivity of 3D-printed fibers (see Table 5.5-1) slightly increases, so that is comparable to that of plate samples. The results suggest that the orientation CNT during the extrusion contributes to the reduction of the resistivity of the composites. A similar effect was also observed for the composites with graphene oxide [97] and carbon black [16].

The beneficial effect of CNT could be particularly summarized in the double results to increase the stiffness and to reduce the resistivity of ABS nanocomposites with a normalized content of nanofiller, by considering a coefficient Q calculated according to the following equation:

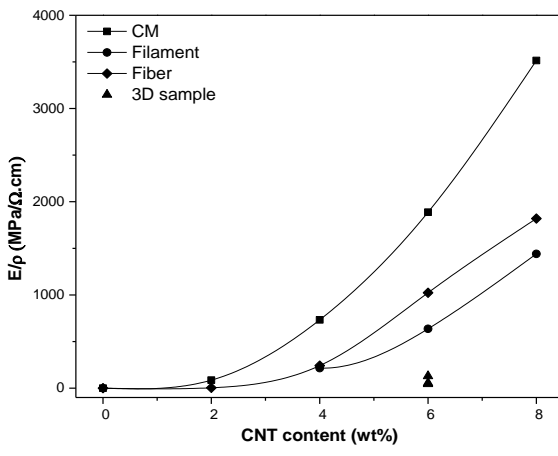
$$Q = \frac{E}{\rho \times w_f} \quad (5.5-1)$$

where E is the elastic modulus

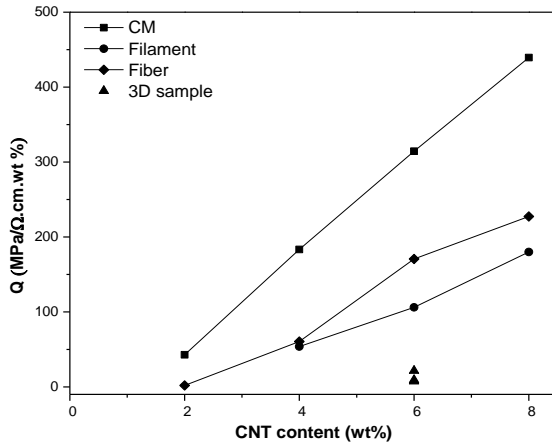
ρ is the volume resistivity

w_f is the CNT content.

Figure 5.5-8 (a-b) depicts this double effect, revealing that compression moulding samples exhibited the best behaviour, while filaments and fibers exhibited a relative good behaviour especially with a CNT of 6-8 wt%. The relative lower values of 3D-printed specimens directly depend on the specific FDM process.



(a)



(b)

Figure 5.5-8. (a) the ratio modulus/resistivity reference at 5 V; (b) the ratio modulus/resistivity and CNT content as a function of CNT % for compression moulding (plates), filament, fiber and 3D samples.

5.5.2 Surface temperature under applied voltage

In this paragraph, the measurements of Joule's heating upon voltage application of the samples with different contents of CNT are presented. These tests were performed by using two different voltages, 12 V and 24 V which are commonly

reached by batteries for automotive applications. We monitored the evolution of the surface temperature as a function of the voltages, the time and the composition of nanocomposite materials.

Representative images of the evolution of the surface temperature taken by an IR thermocamera under an applied voltage of 12 V for the F-CNT-6 and F-CNT-8 nanocomposite plates are reported in Figure 5.5-9. It is immediately evident that the samples can be rapidly heated if a voltage is applied, and a homogeneous temperature profile can be detected even after prolonged time (i.e., 120 s). As it could be expected, the temperature in the central section of the sample is higher than that detectable on the borders, because the heat exchange is favoured in the external zones of the samples. Under an applied voltage of 24 V (see Figure 5.5-10), both F-CNT-6 and F-CNT-8 samples reached a temperature higher than 280°C after 10 s.

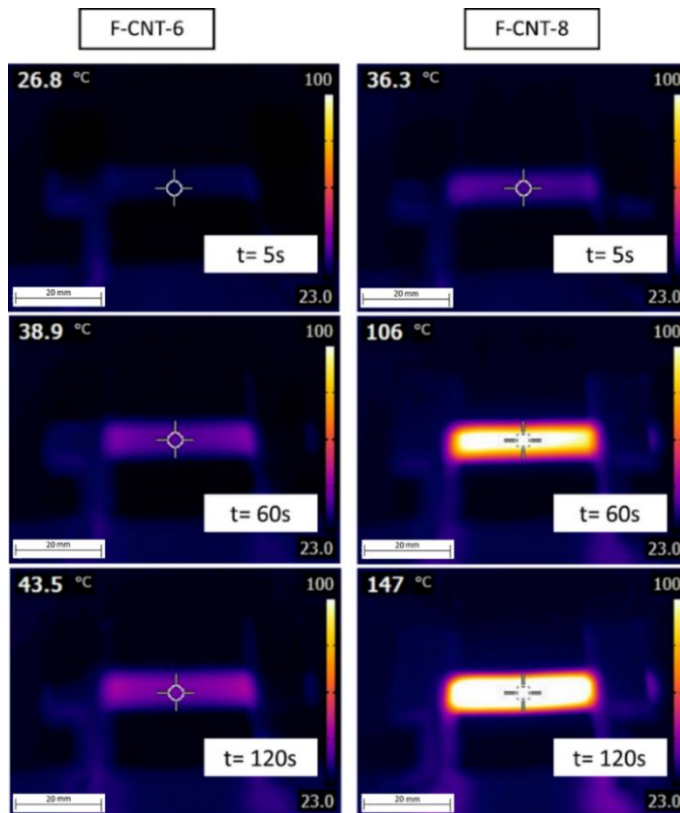


Figure 5.5-9. Infrared thermal imaging of F-CNT-6 (left) and F-CNT-8 (right) nanocomposites samples under an applied voltage of 12 V.

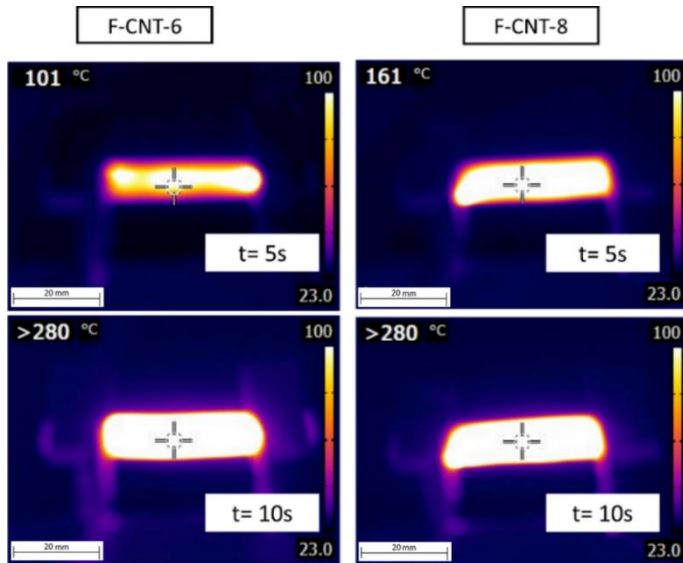
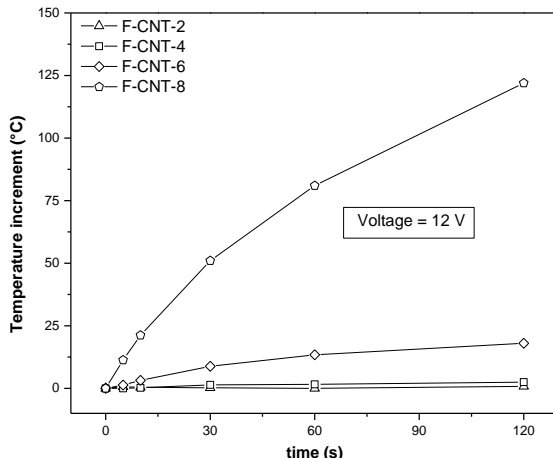
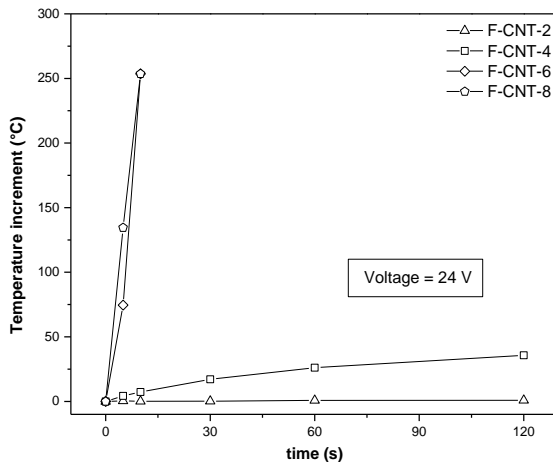


Figure 5.5-10. Infrared thermal imaging of F-CNT-6 (left) and F-CNT-8 (right) nanocomposites samples under an applied voltage of 24 V.

The numerical results of the temperature increment upon an applied voltage of 12 V and 24 V on compression molded samples are shown in Figure 5.5-11(a-b), respectively. The first aspect to underline is that not all the samples can be significantly heated through the voltage application. In fact, only samples with CNT content higher than 4 wt% can increase their surface temperature when a voltage of 12 V is applied. At an applied voltage of 24 V, only F-CNT-2 sample does not significantly increase its surface temperature, while F-CNT-4 sample shows a moderate heating after 120 s. Very effective results can be obtained for all the other samples. For instance, for F-CNT-6 and F-CNT-8 samples it was not possible to reach the end of the test because they thermally decompose with the emission of dense smoke, characteristic of polymers containing aromatic rings.



(a)



(b)

Figure 5.5-11. Increment of surface temperature upon a voltage of 12 V (a) and 24 V (b) for ABS/CNT nanocomposites from compression moulding with different CNT content at room temperature of 23°C.

In Figure 5.5-12, we can see the representative images of the evolution of surface temperature upon voltage application to F-CNT-6-E filament and FDM samples. As shown in Figure 5.5-13(a-b) the increment of the temperature of all samples under both voltages (12 V and 24 V) seems to reach the plateau after 60 seconds. Obviously, the higher the applied voltage, the higher the increase in

temperature. Besides, the resistivity of composite materials of ABS/CNT filaments has a good correlation with their behaviour in Joule's effect measurements. The higher the conductivity, the higher the increase in the surface temperature of samples due to the dissipation of thermal energy. For example, F-CNT-4-E sample does not show any significant increase in temperature, whereas a rather high increase in temperature can be seen for F-CNT-8-E. It is worth noting that, at applied 24 V at 120 s (Figure 5.5-13b), the generated surface temperature of the F-CNT-8-E sample exceeds the glass transition temperature. Following these results in order to avoid thermal degradation of materials during prolonged voltage application, between the various ABS materials studied in this research, the F-CNT-6 samples appeared the most convenient nanocomposite materials for electro-conductive applications.

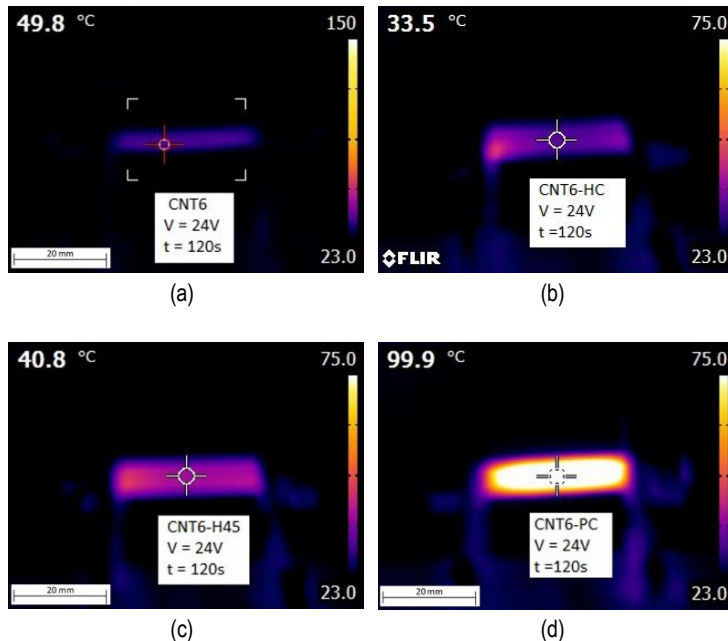


Figure 5.5-12. Results of thermal imaging upon voltage application at 24 V at 120 seconds: F-CNT-6-E (a), F-CNT-6-HC (b), F-CNT-6-H45 (c) and F-CNT-6-PC (d).

The electrical measurements of 3D-printed samples with CNT contents of 6 wt% built with different orientations were performed by using the same two voltages applied values to the filaments (12 V and 24 V). Surface temperature under applied voltage shows good correlation with resistivity measurements. Lower resistivity resulted in a higher increment of temperature, e.g. F-CNT-6-PC reached the highest temperature

of about 100°C after 120 s. However, the local temperature of all FDM samples achieved via the Joule's effect remains below the glass transition temperature of ABS, which allows us to presume good thermal stability of produced nanocomposite materials in electrical applications.

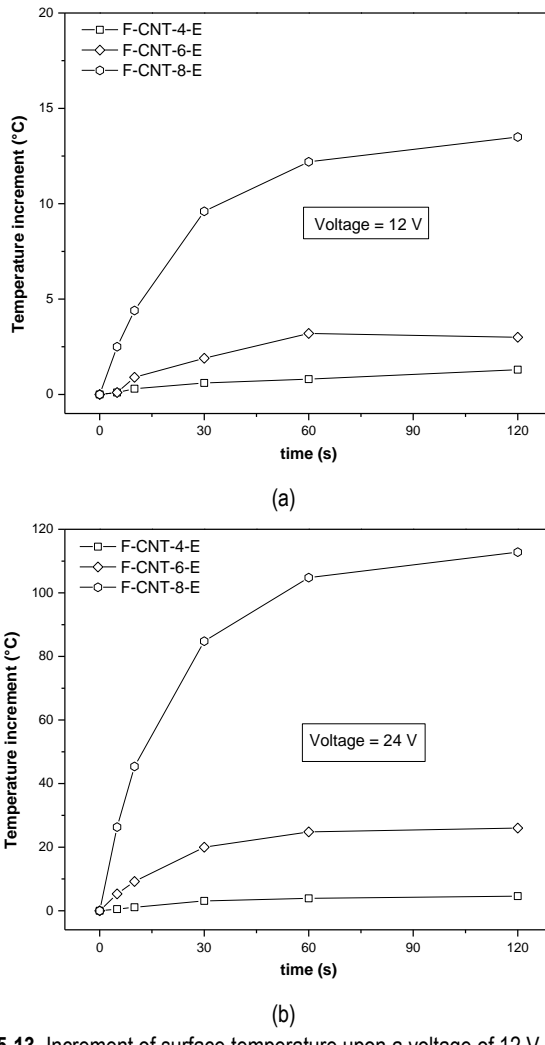
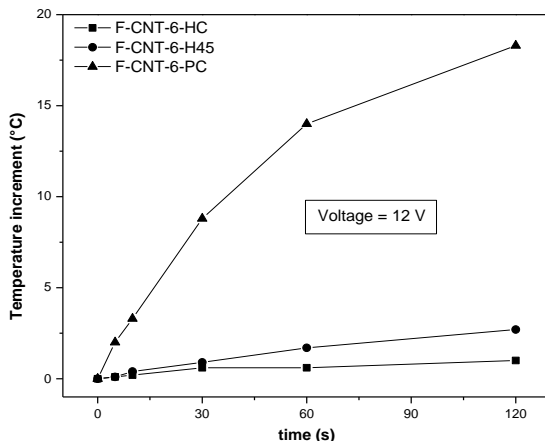
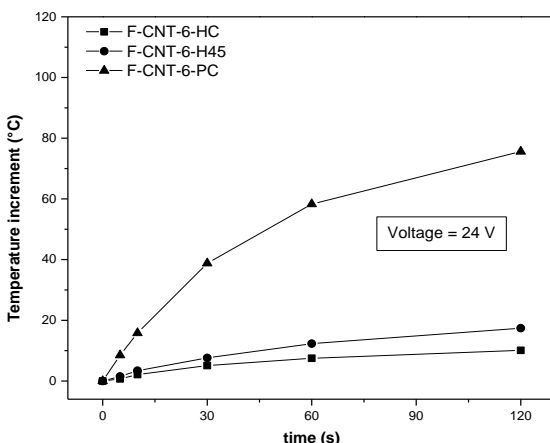


Figure 5.5-13. Increment of surface temperature upon a voltage of 12 V (a) and 24 V (b) for ABS nanocomposites filaments with different CNT loading at room temperature of 23°C.



(a)



(b)

Figure 5.5-14. Increment of surface temperature upon a voltage of 12 V (a) and 24 V (b) for ABS nanocomposites 3D printed samples with 6 wt% CNT content at room temperature of 23°C.

5.5.3 Strain monitoring

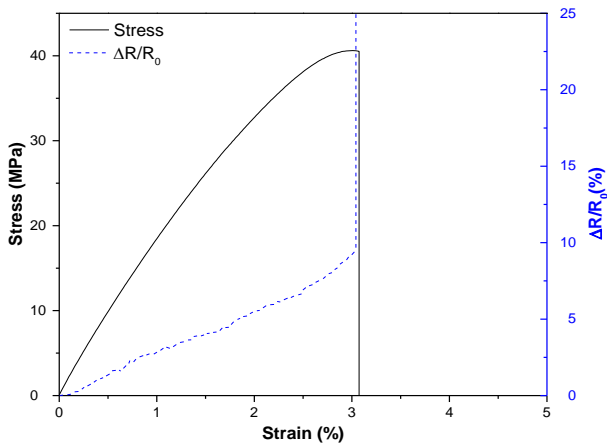
In order to investigate the effect of an applied strain on the conductivity behaviour, the 3D-printed nanocomposite samples (HC and H45) were tested in various mechanical loading modes, and their absolute resistances were monitored simultaneously by two probe contact method.

Table 5.5-2. Initial resistance values (R_0) of the 3D-printed samples before the application of the stain.

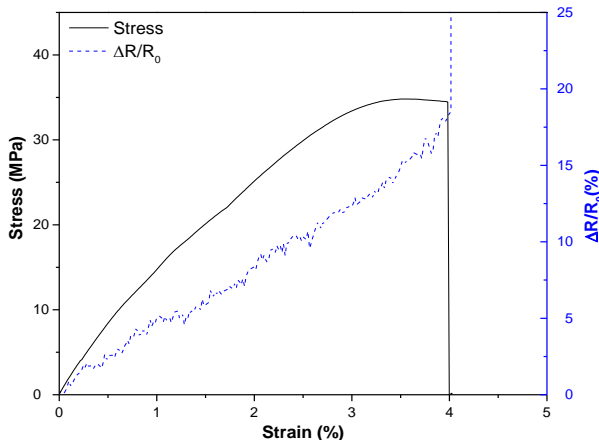
Test	R_0 (Ω)	
	F-CNT-6-HC	F-CNT-6-H45
Tensile fracture	238	431
Ramp strain	527, 188, 278, 202	730, 454, 712, 875
Cyclic strain	407	603
Creep mode	402	669

5.5.3.1 Tensile fracture

Stress-strain behaviour and relative electrical resistance variation ($\Delta R/R_0$) during quasi-static tensile tests on F-CNT-6-HC and F-CNT-6-H45 samples are reported in Figure 5.5-15. A tensile stress applied to FDM nanocomposites causes the electrical change ($\Delta R/R_0$) a positive linear increment until the fracture point for both samples. This behaviour could be explained by the destruction of percolating paths forming the conducting network [186]. Moreover, it is important to note that F-CNT-6-H45 is more sensitive to strain change than F-CNT-6-HC due to the different infill pattern. For example, for strain of 2%, $\Delta R/R_0$ for the sample with F-CNT-6-HC is about 5.3% and for the sample with F-CNT-6-H45 is about 8.4%. Failure of the nanocomposites, corresponding to the breakage of the specimen, was detected as a pronounced drop in the electrical resistance. This demonstrated capability of detecting and locating is advantageous for the damaged component. It is worthwhile to note the gauge factor according to the formula ($K = (\Delta R/R_0)/\epsilon$) at different stain level is reported in Table 5.5-3.



(a)



(b)

Figure 5.5-15. Electrical resistivity change ($\Delta R/R_0$) and stress of 3D-printed F-CNT-6 nanocomposites under applied strain up to fracture: F-CNT-6-HC (a) and F-CNT-6-H45 (b).

Table 5.5-3. Gauge factor of ABS/CNT 3D-printed samples at different infill pattern.

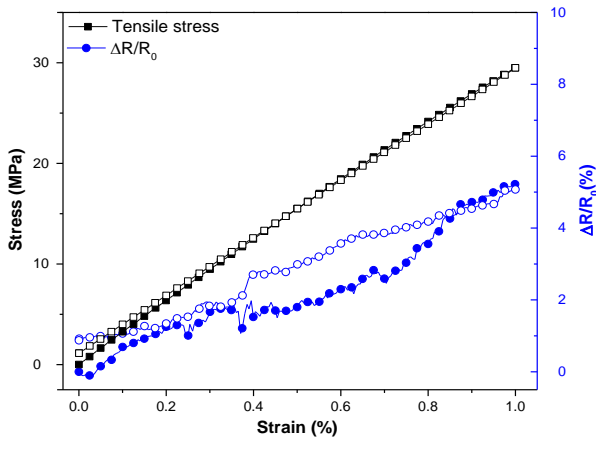
Gauge factor (K)	At 1%	At 2%	At 3%
F-CNT-6-HC	3.2	2.7	2.9
F-CNT-6-H45	4.6	3.7	4.0

5.5.3.2 Ramp strain

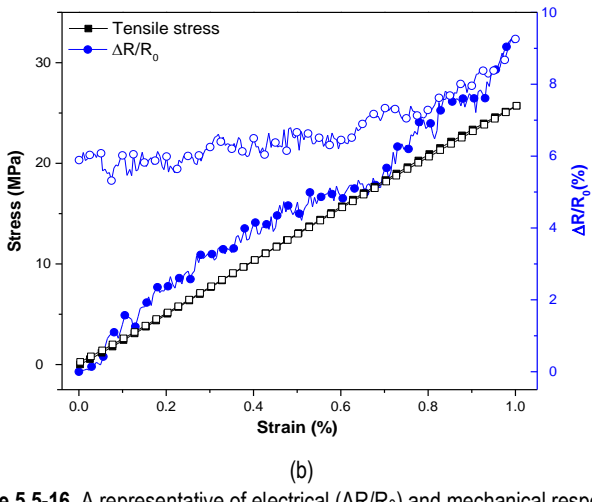
Figure 5.5-16(a-b) describes the relative change of electrical resistance ($\Delta R/R_0$) of 3D-printed samples under ramp strain from electrical extensometer up to 1% and unloading (recovery). The higher the applied stress, the higher the resistance change. The resistance change of HC specimen was almost reversible during unloading while that of H45 a significant loss of conductivity was observed. It is worthwhile to note the gauge factor $K= 4.5$ and $K=9.2$ for F-CNT-6-HC and F-CNT-6-H45 respectively. The results suggest a higher piezo-resistivity for H45 3D-printed parts. In particular, it should be underlined the high sensitivity of the $\Delta R/R_0$ curve at low deformation levels. This result of gauge factor is comparable to works by Georgousis et al. [186], but it is even more significant, compared to several works reported by Oliva-Avile et al. [187], Bautista-Quijano et al. [188] and Moriche et al. [189].

Table 5.5-4. Gauge factor of ABS/CNT 3D-printed samples at different infill pattern.

Sample	Gauge factor (K)
F-CNT-6-HC	4.5 ± 1.3 (n=4)
F-CNT-6-H45	9.2 ± 1.5 (n=4)



(a)



(b)

Figure 5.5-16. A representative of electrical ($\Delta R/R_0$) and mechanical response of 3D-printed ABS/CNT nanocomposites during loading (full symbol) and unloading (open symbol) under tensile test: F-CNT-6-HC (a) and F-CNT-6-H45 (b).

5.5.3.3 Cyclic strain

Once reversibility of the electrical network has been investigated, a low cycle deformation was applied to samples in order evaluate if the piezoresistivity is reversible during a finite number of cycles strain. Figure 5.5-18a and Figure 5.5-20a presents the electrical resistance for F-CNT-6-HC and F-CNT-6-H45 respectively under 50 strain cycles applied in the strain range of $0.1\% < \varepsilon < 0.5\%$. It is evident that in cyclic strain, the electrical resistance for both samples progressively decreases. Results suggested a possible rearrangement, rotations, and reorientation, of 1D nanoparticles forming the electrical network as reported by Bautista-Quijano et al. [188]. It is different from 2D reinforcement such as graphene 2D that nanoparticles are less susceptible to these phenomena as the initial electrical resistance was reached after each cycle [189].

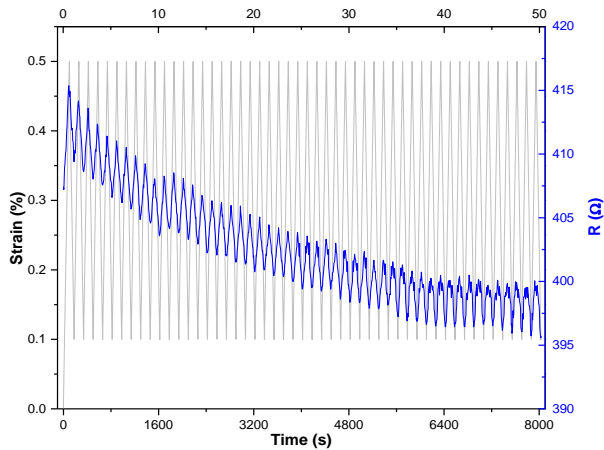
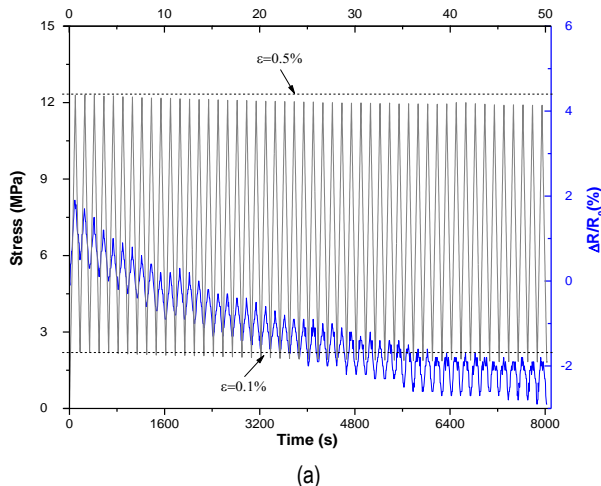
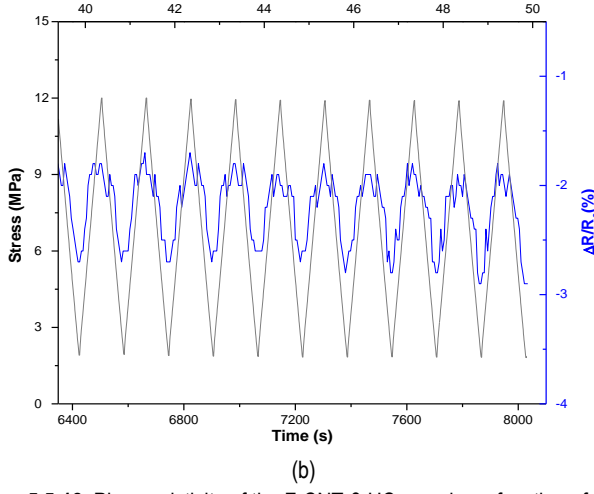


Figure 5.5-17. Piezoresistivity of the F-CNT-6-HC sample : resistance variation during 50 cycles of controlled strain (0.1-0.5%) under tensile loading.



(a)



(b)

Figure 5.5-18. Piezoresistivity of the F-CNT-6-HC sample as function of stress during 50 cycles (a) under tensile loading and detail of the last 10 cycles (b).

Figure 5.5-18b and Figure 5.5-20b present the response of the last 10 cycles in order to evidence the decreasing of electrical resistance change of F-CNT-6-HC and F-CNT-6-H45 samples. Moreover, after the 50 cycles, the amplitude of the electrical signal diminished around 28% and 62% for HC and H45 3D-printed samples respectively.

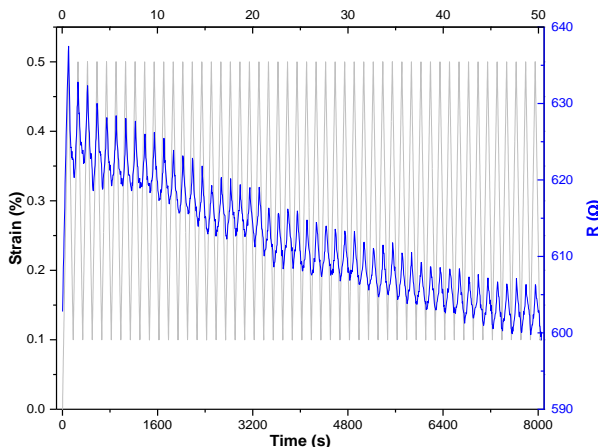


Figure 5.5-19. Piezoresistivity of the F-CNT-6-H45 sample: resistance variation as function of controlled strain (0.1–0.5%) during 50 cycles under tensile loading.

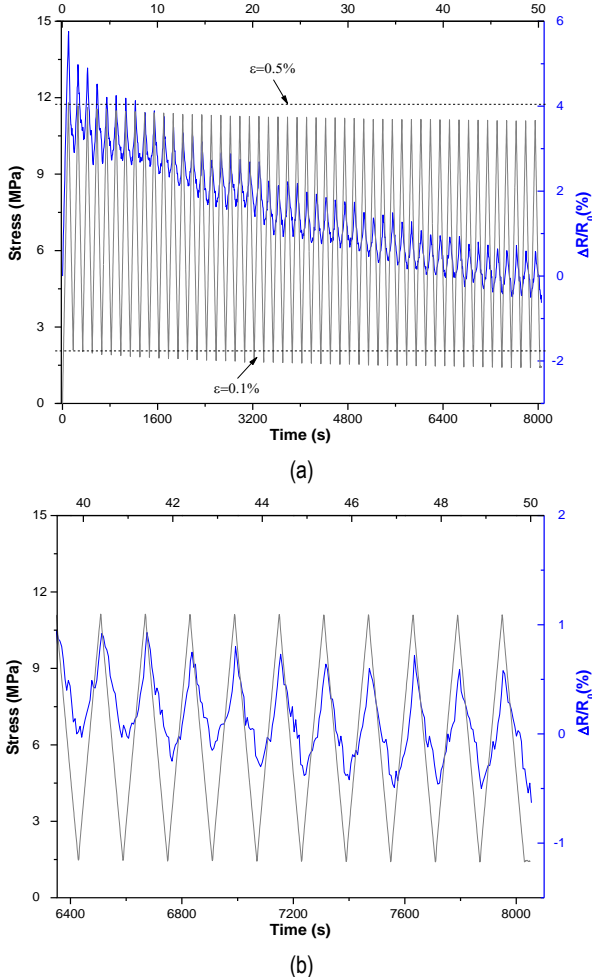


Figure 5.5-20. Piezoresistivity of the F-CNT-6-H45 samples and (a) 50 strain, (b) 50 stress cycles under tensile loading and (c) detail of the last 10 cycles.

In order to understand the gauge factor with respect to cyclic strain, gauge factor (K_i) at each step of cycle were elaborate following the equation:

$$K_i = \frac{((R_{i+1} - R_i) / R_i)}{\varepsilon} \quad (5.5-2)$$

Figure 5.5-21 represents the value of gauge factor during number of cycle, showing that the gauge factor of both HC and H45 samples progressively reduce to a stable value about 2.3-2.7 after 30 cycles. Selected values are reported in Table 5.5-5.

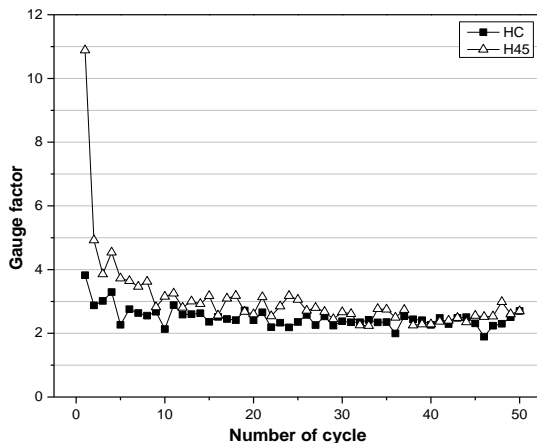


Figure 5.5-21. Gauge factor of the 6 wt% CNT 3D-printed nanocomposite samples along number of cycle strain of HC and H45.

Table 5.5-5. Selected values of gauge factor of ABS/CNT 3D-printed samples.

Cycle	Gauge factor (K)	
	F-CNT-6-HC	F-CNT-6-H45
1 st	3.8	10.9
2 nd	2.9	4.9
---	--	--
40 th	2.3	2.3
45 th	2.3	2.6
50 th	2.7	2.7

Finally it is worth noting in Figure 5.5-18a and Figure 5.5-20a, the effect of stress reduction during 50 cycle of controlled strain deformation. In particular the max-min stress reduced from 12.3/2.2 MPa to 11.9/1.8 MPa in the last cycle for F-CNT-6-HC sample (about 0.4MPa). In the case of F-CNT-6-H45 sample, a higher stress reduction of about 0.70MPa was observed, resulting the max/min stress of 11.8/2.1 MPa and 11.1/1.4 MPa in the first and in the 50th cycle, respectively. This effect could be attributed to viscoelastic effect of stress relaxation and/or thermal heating for a mild Joule's effect.

The images of the samples of F-CNT-6-HC and F-CNT-6-H45 before and after testing are presented in Figure 5.5-22 and Figure 5.5-23, respectively. After 50 cycle under tensile loading, no evidences of damage can be observed in any sample.

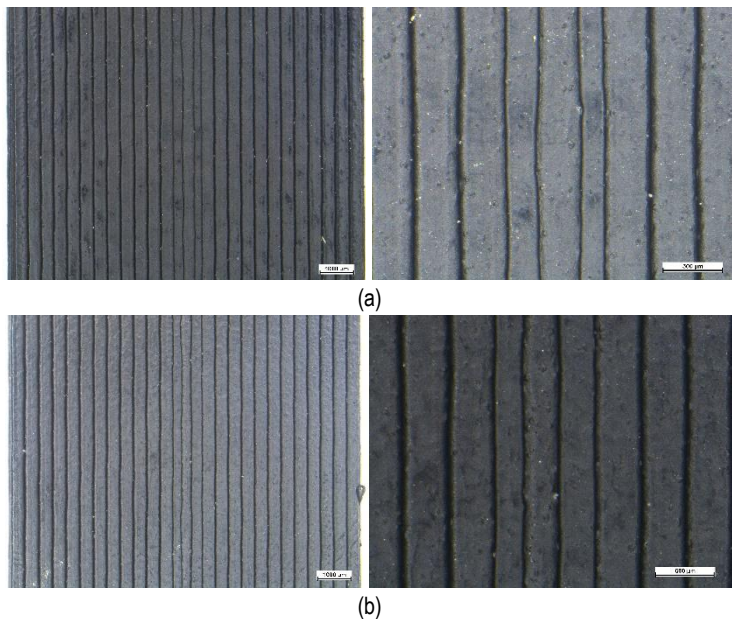
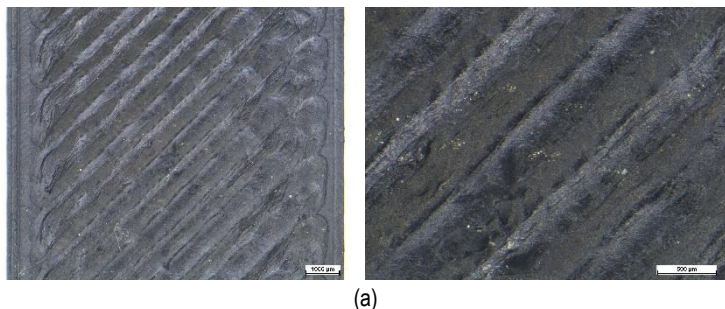
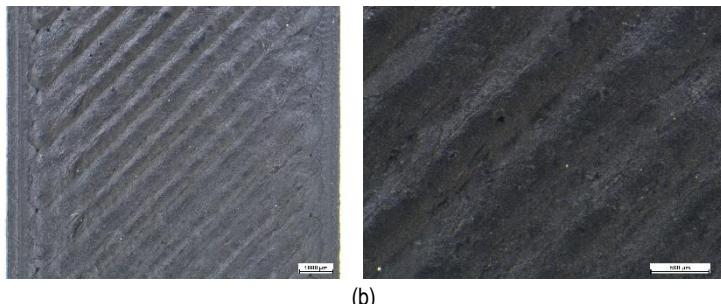


Figure 5.5-22. F-CNT-6-HC sample: (a) before, and (b) after 50 cycles under tensile loading.



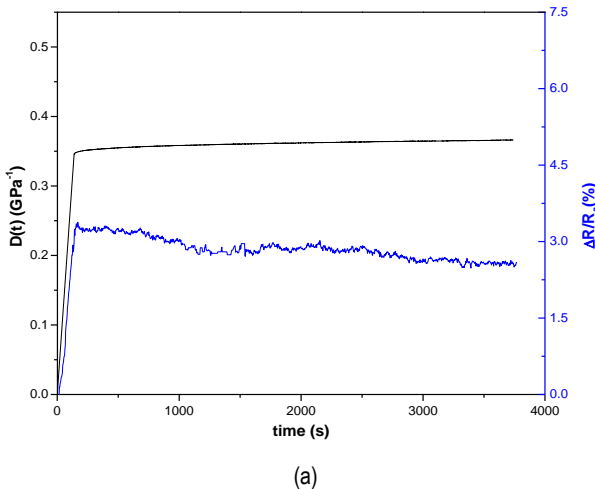


(b)

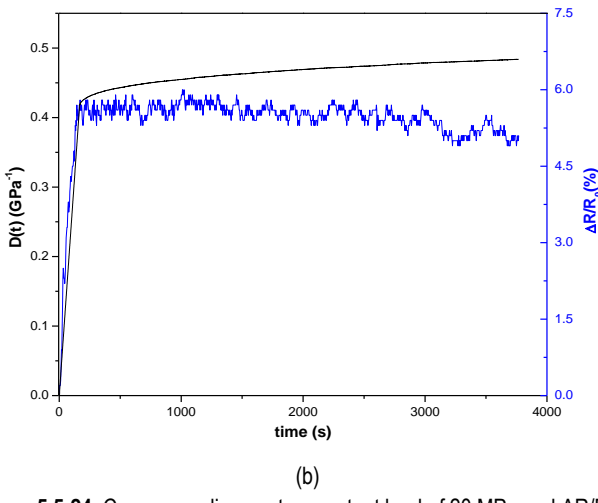
Figure 5.5-23. F-CNT-6-H45 sample: (a) before, and (b) after 50 cycles under tensile loading.

5.5.3.4 Creep mode

The performance of the samples under permanent stress also needs to be characterized. With the purpose of analyzing the samples capability when a permanent load is applied, a creep test was carried out with a stress of 20 MPa at maintenance time of 3600 s. Figure 5.5-24a and b depicts $\Delta R/R_0$ and creep compliance $D(t)$ curve for F-CNT-6-HC and F-CNT-6-H45 specimens, respectively. The initial sudden increase of electrical resistance was induced by load application. It is interesting to note that $\Delta R/R_0$ of both HC and H45 appear to slightly decrease during creep time, probably as a consequence of the orientation and the partial reformation of the conductive network [190].



(a)



(b)

Figure 5.5-24. Creep compliance at a constant load of 20 MPa and $\Delta R/R_0$ for different infill samples: (a) F-CNT-6-HC and (b) F-CNT-6-H45.

5.6 Summary ABS-carbon nanotubes nanocomposites

Carbon nanotubes (in fractions up to 8 wt %) were directly melt compounded with relatively high viscosity ABS (F) matrix by using a completely solvent-free process. Subsequently, by using a twin-screw extruder, composite filaments were appositely extruded for application in 3D printing with fused deposition modelling.

The optimum CNT fraction for fused deposition modelling process was found to be 6 wt %. Thermal, mechanical and electrical properties of neat ABS and ABS/CNT composites have been investigated on produced filaments and 3D-printed parts. CNT has the positive effect on the resistance to long-lasting loads due to the reduction of creep compliance. Besides, the enhancement of both tensile modulus and strength was found for filaments and FDM products, except for vertical 3D built specimens. On the other hand, elongation at break of the composites was reduced in proportion to the CNT fraction. The presence of CNT also promoted the thermal stability of 3D-printed parts due to the reduction in coefficient of thermal expansion.

Electrical conductivity of 3D-printed samples was markedly incremented but a partial loss in conductivity with respect to filament nanocomposite was also observed. Moreover, the resistivity of 3D-printed parts is highly dependent on the build microfilaments orientation, which consequently leads to different surface temperature increment under applied voltages. For FDM-printed parts, the carbon nanotubes in playing the best reinforcement in thermal mechanical behaviour for HC and H45 orientation but less effective in electrical properties.

The strain sensing capabilities of the conducting FDM samples by 6wt% of CNT with different two infill patterns (HC, and H45) were studied. The resistance change and damage in the conductive FDM parts were detectable upon the strain applied. The higher sensitivity of the 3D-part within the H45 pattern in comparison to HC by measurement the gauge factor. The CNT conductive network path in FDM products seems to be reform during the fatigue and creep load.

In short, carbon nanotubes were proven to significantly reduce the flow properties of ABS nanocomposites, but remarkably improved electrical conductivity and mechanical properties.

Chapter VI

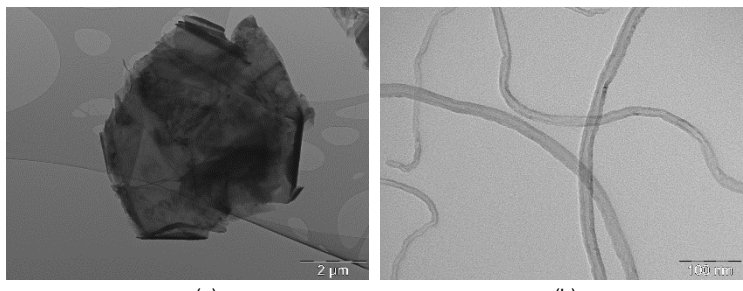
Comparative study of graphene and carbon nanotube filled ABS nanocomposites plates

In literature, studies on graphene (GNP) and carbon nanotubes (CNT) nanocomposites have been massively reported. In particular, the comparative study between this two nanofillers has been detailed in a few scientific reports in the epoxy [191-195] and polyamide [196] with the highest nanofiller content of 5 wt%. Only one report is focused on the comparison between graphene and carbon nanotubes in ABS at concentrations up to 1.2 vol% (~2.5 wt%) reached by solution mixing [197].

This chapter is dedicated to the effects of graphene and carbon nanotube nanofillers in ABS nanocomposites in order to specifically highlight the potentialities of each nanofiller. Although some prior works [191-197] have been dedicated to the comparisons between graphene and CNT nanocomposites with the same matrix, the effect of these two fillers on processability, mechanical and electrical properties of nanocomposites filled at percentage in the range of 2-8 wt% are not reported yet. Therefore, the characterization could provide useful information about both CNT and GNP-M5 nanofiller, which consequently should be properly selected for applications. Noteworthy, ABS without mould lubricant (Sinkral®F322) with relatively low melt flow is the selected matrix for the production of nanocomposites prepared by melt compounding and compression moulding (section 3.2.2) and investigated in this work.

6.1 Morphology

The morphologies of graphene-M5 (GNP-M5) and carbon nanotube (CNT) have been characterized by TEM microscopy, as represented in Figure 6.1-1. Figure 6.1-1a shows the typical thin sheet structure of the GNP. From TEM micrographs, the average diameter of platelets of GNP has been measured to be about 5.5 to 6.8 μm . In addition, it was also observed that some GNP nanoplatelets superimposed on top of each other and wrinkled into an irregular shape. Figure 6.1-1b displays the morphological structure of CNT and clearly documents that these investigated CNT have the outer diameter of tubes about 15-20 nm within wall thickness of about 4-6 nm.

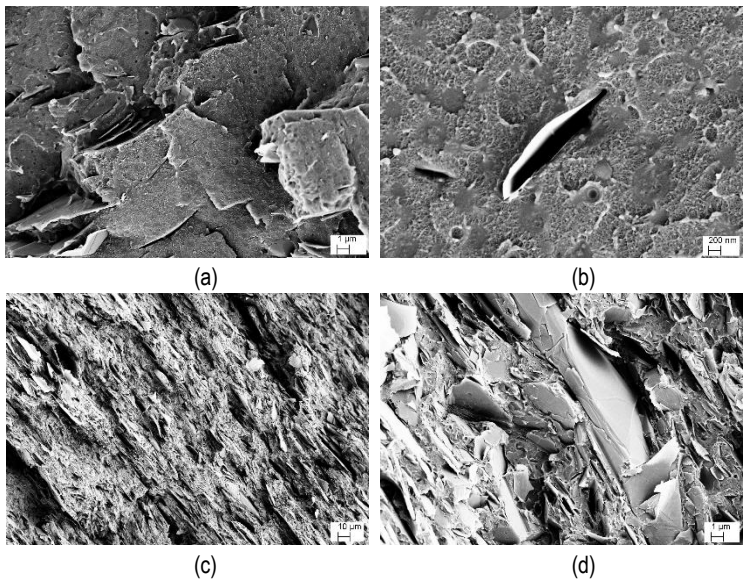


(a)

(b)

Figure 6.1-1. TEM micrographs of the selected carbonaceous nanoparticles: (a) GNP-M5 and (b) CNT.

The SEM images of the fracture surface of ABS/graphene and ABS/CNT samples are represented in Figure 6.1-2(a-d) and Figure 6.1-2(e-f), respectively. A relatively poor adhesion level between graphene and ABS was documented in Figure 6.1-2b. Figure 6.1-2c shows F-M5-30 sample with the highest GNP concentration where graphene flakes appear distributed quite homogeneously within the matrix even though at the highest concentration of 30 wt%. A relative good dispersion was also observed for graphene nanofiller. In addition, carbon nanotubes were clearly observed in the SEM micrographs (Figure 6.1-2e-f), with uniform distribution and excellent dispersion.



(a)

(b)

(c)

(d)

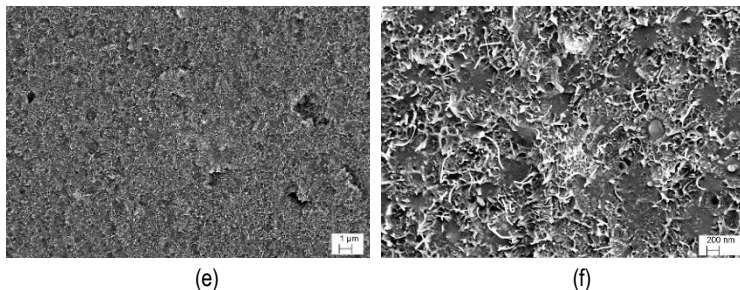


Figure 6.1-2. SEM micrographs of the samples of F-CNT-6 (a, b), F-M5-6 (c, d) and F-M5-30 (e, f).

6.2 Melt flow index

The processability of the nanocomposites materials was investigated by comparing their melt flow index. Figure 6.2-1 shows that the effect of the nanofiller amounts, the types of nanofillers and the temperature on MFI value of nanocomposites. It is worthwhile to note that the MFI value decreased with the nanofiller content. In addition, CNT nanofiller show more reduction in MFI of ABS in comparison to graphene. Moreover, the higher the temperature, the higher the MFI value with respect to filler content.

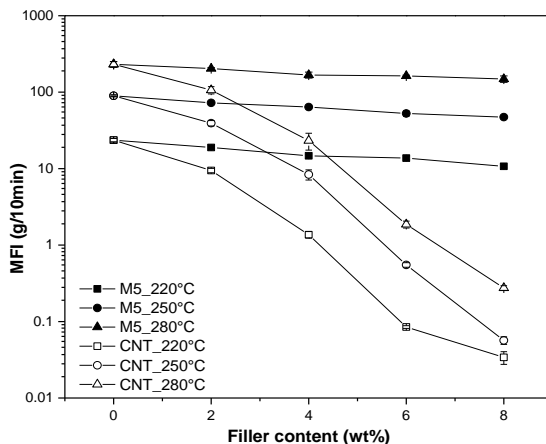


Figure 6.2-1. Melt flow index of ABS/graphene (full symbol) and ABS/CNT(open symbols) nanocomposites at different temperatures and nanofiller content.

Following the results of MFI at different temperature, activation energy (E_{act}) of nanocomposites can be evaluated from the slope of the best fitting straight lines by using Kissinger approach [198]:

$$\log(MFI) = \log(C_0) - \left(\frac{E_{act}}{2.303R} \right) \frac{1}{T} \quad (6.2-1)$$

where C_0 is a pre-exponential factor, T is the selected temperature of melt flow index, and R , the universal gas constant, is 8.314 J / mol. K. The value of intercept C_0 formally represents melt flow at infinite temperature.

As reported in Table 6.2-1, the activation energy of neat ABS was 86.6 kJ/mol, and it increased with the content of both graphene and CNT. However it should be noted that the activation energy of ABS/CTN nanocomposites is higher than that of corresponding graphene nanocomposites, thus indicating the difficulty of these materials to flow. In other words, CNT nanocomposites required more energy for processing. For instance, activation energy values of nanocomposite with 6 wt% of nanofiller was about 100 kJ/mol graphene and $E_{act} = 117$ kJ/mol for CNT.

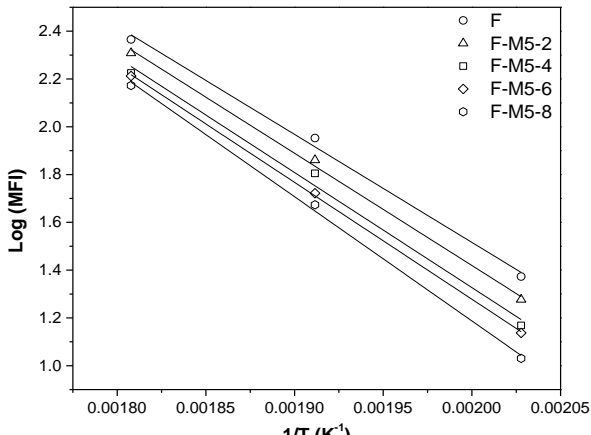
Table 6.2-1. Melt flow index and activation energy for neat ABS and carbon nanotubes and graphene nanocomposites.

Samples	MFI (g/10 mins)			Log(C_0)	E_{act}^a (kJ/mol)
	220°C	250°C	280°C		
F	23.6 ± 1.3	89.7 ± 2.5	232 ± 19	10.6	86.6 ± 5.5
F-M5-2	18.9 ± 1.0	72.5 ± 1.8	203 ± 6	10.8	89.9 ± 3.9
F-M5-4	14.7 ± 1.0	63.9 ± 0.7	172 ± 5	11.0	93.1 ± 7.3
F-M5-6	13.7 ± 0.7	52.7 ± 4.3	163 ± 4	11.1	93.7 ± 1.6
F-M5-8	10.7 ± 0.5	47.1 ± 1.0	149 ± 14	11.6	99.6 ± 3.9
F-M5-12	8.3 ± 0.2	nt ^c	nt ^c	-	nt ^c
F-M5-16	6.3 ± 0.2	nt ^c	nt ^c	-	nt ^c
F-M5-20	5.2 ± 0.4	nt ^c	nt ^c	-	nt ^c
F-M5-30	1.9 ± 0.1	nt ^c	nt ^c	-	nt ^c
F-CNT-2	9.5 ± 0.6	39.3 ± 3.2	107 ± 12	10.7	91.7 ± 6.3
F-CNT-4	1.4 ± 0.1	8.4 ± 1.3	23.3 ± 5.8	11.6	107.6 ± 13.6
F-CNT-6	0.08 ± 0.01	0.55 ± 0.04	1.87 ± 0.19	11.4	117.2 ± 10.3
F-CNT-8	0.03 ± 0.01	0.06 ± 0.01	0.28 ± 0.02	11.4	126.8 ^b

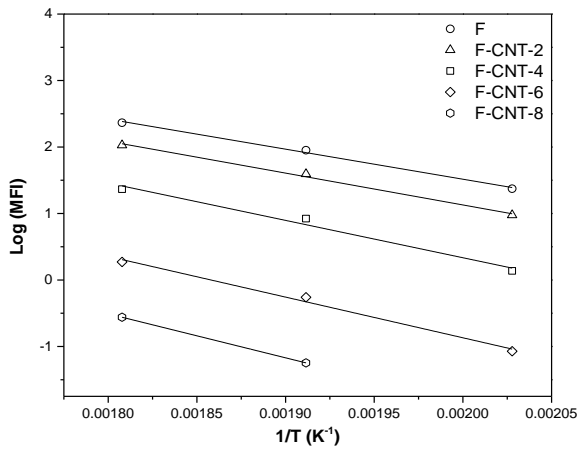
^a E_{act} activation energy was evaluated following Eq. (6.2-1).

^b evaluated in the range temperature of 250°C and 280°C.

^c nt= not tested.



(a)



(b)

Figure 6.2-2. Melt flow index of graphene (a) and carbon nanotubes (b) nanocomposites as a function of temperature.

6.3 Quasi-static tensile test

Tensile testing was carried out to investigate the reinforcement effect of graphene and CNT on ABS nanocomposites. The tensile properties of ABS/M5 and ABS/CNT nanocomposites are summarised in Table 6.3-1. As expected, both ABS/M5 and ABS/CNT show an enhancement of tensile properties compared to the neat ABS.

In Figure 6.3-1a, the elastic modulus of graphene-based nanocomposites is higher than that of carbon nanotubes. For instance, the elastic modulus of composites containing 8 wt% of M5 was increased from 2315 MPa to 3523 MPa (i.e. 52%) and whereas in the case of 8 wt% of CNT a corresponding increase up to 3068 MPa (i.e. 32%) was measured. The elastic modulus of composites was influenced by various factors depending on nanofillers including their stiffness, shape, and orientation. Yielding phenomenon was observed only for nanocomposites up to 4% of nanofiller.

Table 6.3-1. Comparison of the tensile properties of ABS/CNT and ABS/M5 nanocomposites.

Samples	E (MPa)	σ_y (MPa)	σ_b (MPa)	ε_b (%)	TEB(MJ.mm ⁻³)	E_{norm}^a
F	2315 ± 100	41.7 ± 0.4	33.6 ± 0.4	35.9 ± 6.1	11.785 ± 2.007	nd ^b
F-M5-2	2631 ± 133	41.5 ± 1.2	39.9 ± 2.3	4.1 ± 0.2	1.057 ± 0.078	6.8
F-M5-4	2911 ± 109	40.2 ± 1.5	39.3 ± 1.2	3.7 ± 0.2	0.929 ± 0.096	6.4
F-M5-6	3406 ± 86	-	41.5 ± 0.8	3.1 ± 0.1	0.788 ± 0.086	7.9
F-M5-8	3523 ± 209	-	41.4 ± 1.0	3.1 ± 0.3	0.780 ± 0.132	6.5
F-M5-12	4450 ± 224	-	42.4 ± 1.7	2.5 ± 0.3	0.645 ± 0.115	7.7
F-M5-16	5072 ± 270	-	41.6 ± 1.1	2.0 ± 0.1	0.491 ± 0.032	7.4
F-M5-20	5725 ± 308	-	42.9 ± 1.6	1.9 ± 0.1	0.468 ± 0.041	7.4
F-M5-30	7362 ± 569	-	44.3 ± 1.9	1.3 ± 0.1	0.340 ± 0.034	7.3
F-CNT-2	2513 ± 101	43.3 ± 0.4	34.1 ± 1.5	7.5 ± 2.4	2.313 ± 0.832	4.3
F-CNT-4	2622 ± 29	43.5 ± 1.0	40.3 ± 1.8	4.5 ± 0.6	1.253 ± 0.263	3.3
F-CNT-6	2849 ± 70	-	46.6 ± 0.5	3.9 ± 0.2	1.112 ± 0.110	3.8
F-CNT-8	3068 ± 156	-	45.1 ± 2.3	3.2 ± 0.3	0.805 ± 0.117	4.1

^a normalised value of the improvement of the modulus following equation (4.2-1).

^b not defined

On the other hand, the various factors affecting the tensile strength of ABS nanocomposites include the filler/matrix interfacial adhesion, the amount of filler, its properties and geometry and dispersion level in the matrix. In Figure 6.3-1b, the higher strength of ABS/CNT than ABS/M5 nanocomposites is attributed to the easier dispersion of CNT with respect to GNP-M5. Moreover, this behaviour could be associated to the two-dimensional (2D) aspect of graphene that seemed easier to aggregate due to its plane-to-plane contact area. Consequently, graphene, having 2D structure, could to be wrinkled and to be detached from ABS (see Figure 6.1-2) whereas some bending and twisting in the structure of the CNT could prevent the detachment of CNT from ABS matrix. Thus, these factors induced a better interfacial interaction between the CNT and ABS matrix. As a result, the load can efficiently be transferred from the ABS matrix, and therefore the tensile strength could be better improved in CNT nanocomposites. And analogously, the strain at break was observed to be more severely reduced in the case of M5 nanocomposites.

Another interesting result is the very high concentration of graphene that was possible to reach by proper processing conditions. In particular 30 wt% represents the highest content reported in literature for ABS/graphene composites, and these composites have manifested an elastic modulus of about 7362 MPa and a tensile strength of about 44 MPa.

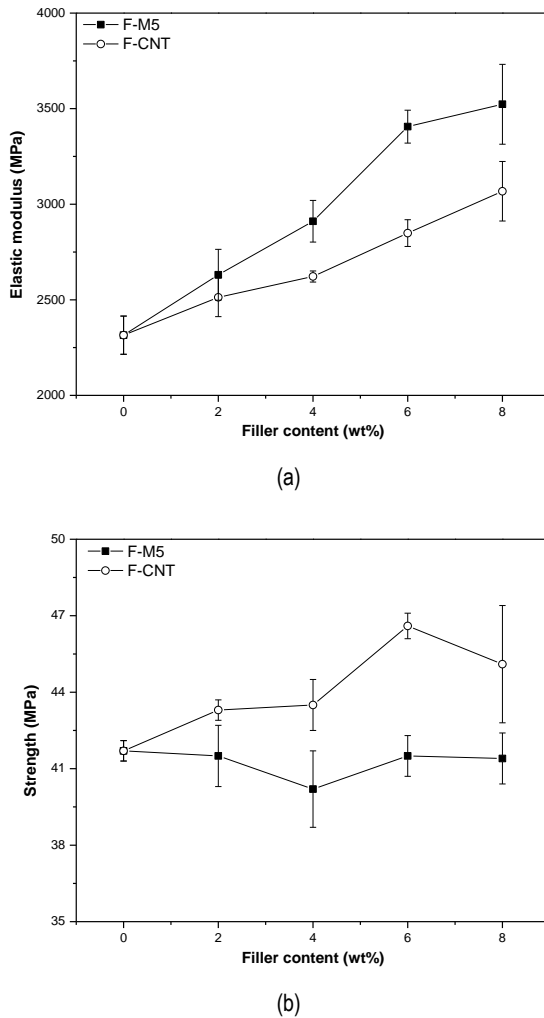


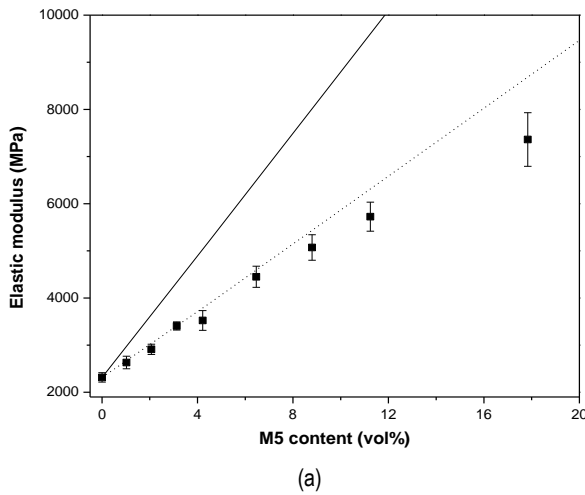
Figure 6.3-1. Comparison of tensile properties of nanocomposites with ABS/M5 and ABS/CNT: (a) elastic modulus and (b) strength.

According to the experimental data, a maximum strength value was obtained for 6% of CNT, whereas a maximum stiffening effect (E_{norm}) was observed for 6% of

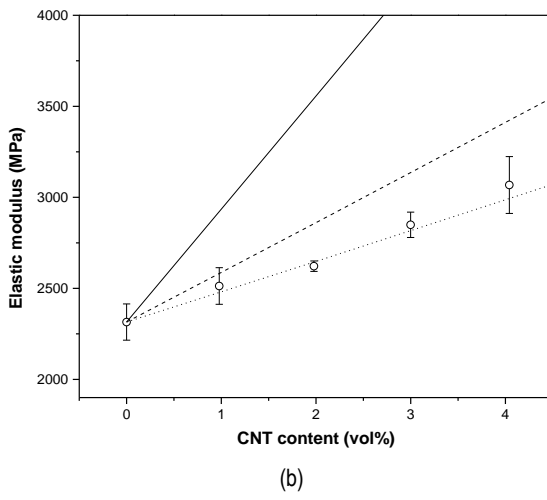
M5, maintaining an acceptable deformation at break (3-4%) for both the compositions, even in absence of yielding.

In the Halpin-Tsai model an experimental modulus for neat ABS of 2315 MPa was considered (Table 6.3-1). The aspect ratios are considered equal to 833 for GNP-M5 ($D_f = 5000$ nm and $t_f = 6$ nm) and 158 for CNT ($L_f = 1500$ nm and $D_f = 9.5$ nm). The elastic modulus of 70 GPa has been assumed for both graphene and carbon nanotubes [159, 160].

The experimental data are well-fitted assuming a 3D randomly orientated nanofiller due to the melt compounding process. However, the elastic modulus of ABS/M5 nanocomposites were lower than the predicted elastic modulus when the content of GNP-M5 is higher than 6.5 vol% (12 wt%), resulting in the loss of the reinforcement efficiency (Figure 6.3-2a).



(a)



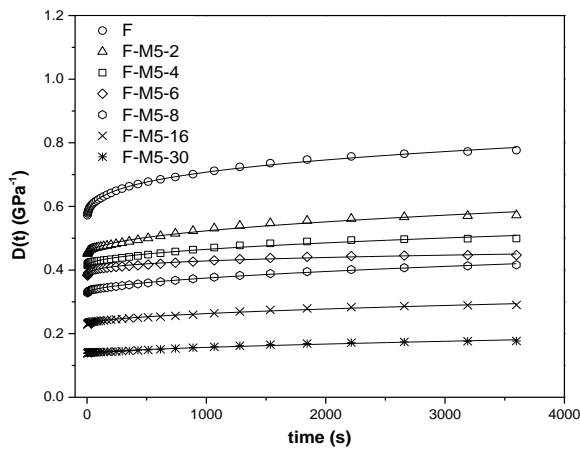
(b)

Figure 6.3-2. Elastic modulus of nanocomposites with ABS/M5 (a) and ABS/CNT (b). Continuous (—) and dash lines (— —) and dot lines (...) represent prediction according to Halpin-Tsai models with parallel, 2D random and 3D random orientation, respectively.

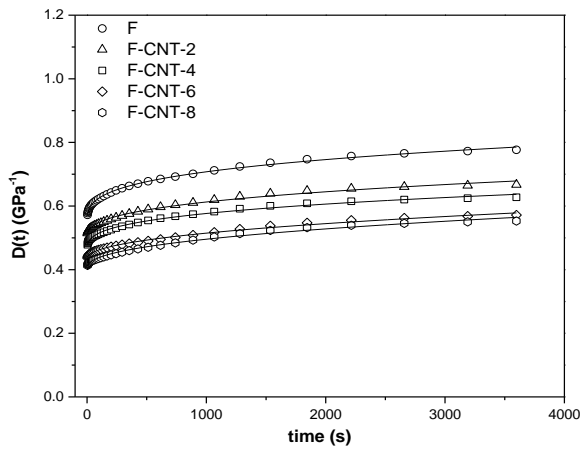
6.4 Creep stability

The isothermal creep compliance of ABS/CNT and ABS/M5 nanocomposites respectively, under a constant load of 3.9 MPa and at 30°C is reported in Figure 6.4-1(a-b). Following the described models of creep evaluation, the elastic (D_e), viscoelastic $D_{ve,3600s}$ and total ($D_t,3600s$) components of the creep compliance after 3600s are have been calculated; the resutls are summarized in Table 6.4-1. As expected, the introduction of graphene and carbon nanotubes nanoparticles results in a significant improvement of the creep stability of the material. In particular, the higher the filler content, the lower the creep compliance (see Figure 6.4-2). The role of nanofillers is to restrict the polymeric chain mobility, thus promoting a better creep stability.

In addition, the creep compliances of nanocomposites at the same content of nanofillers do seem to be significantly reduced by the presence of graphene compared to the carbon nanotube. This reduction largely associated with a reduction of the values of elastic component D_e . ABS/graphene nanocomposites exhibited a higher creep stability with respect to CNT nanocomposites, in direct dependence on their higher stiffness (see elastic modulus in Table 6.3-1).

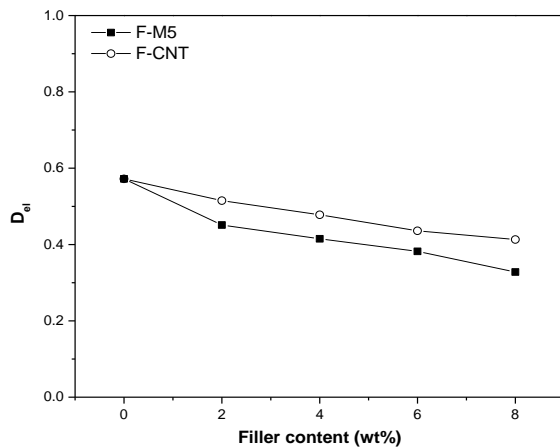


(a)

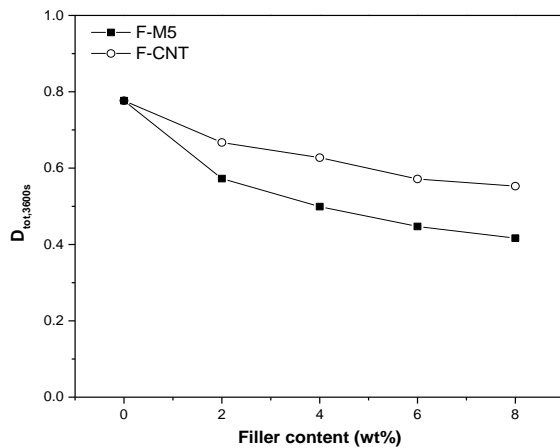


(b)

Figure 6.4-1. Creep compliance of graphene (a) and carbon nanotubes (b) nanocomposites at 30°C at 3.9 MPa.



(a)



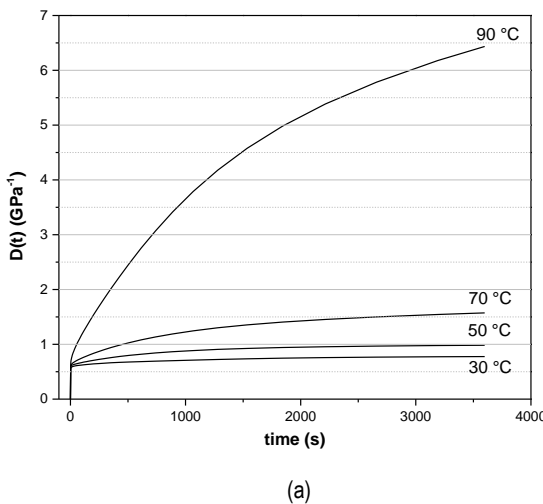
(b)

Figure 6.4-2. Comparison of creep compliance of nanocomposites with ABS/M5 and ABS/CNT: (a) elastic (D_{el}) and (b) total $D(t=3600\text{ s})$.

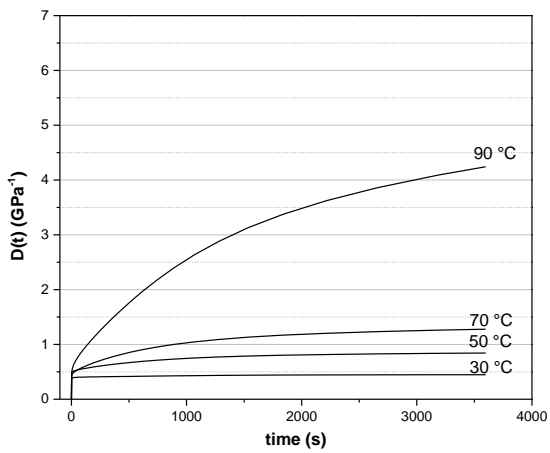
Table 6.4-1. Creep compliance data of ABS-graphene and ABS-CNT nanocomposites according E.q (5.3-8).

Samples	D _{el} (GPa ⁻¹)	D _{ve,3600s} (GPa ⁻¹)	D _{tot,3600s} (GPa ⁻¹)	D _e (GPa ⁻¹)	k (GPa ⁻¹ s ⁻ⁿ)	n	R ²
F	0.572	0.205	0.777	0.5415	0.0210	0.2994	0.9981
F-M5-2	0.451	0.122	0.573	0.4462	0.0034	0.4506	0.9874
F-M5-4	0.415	0.084	0.499	0.4128	0.0020	0.4744	0.9821
F-M5-6	0.382	0.065	0.447	0.3719	0.0099	0.2533	0.9890
F-M5-8	0.328	0.088	0.416	0.3280	0.0012	0.5272	0.9966
F-M5-16	0.214	0.077	0.290	0.2291	0.0010	0.5086	0.9903
F-M5-30	0.138	0.039	0.177	0.1384	0.0002	0.6505	0.9830
F-CNT-2	0.515	0.205	0.777	0.4964	0.0103	0.3512	0.9928
F-CNT-4	0.478	0.152	0.667	0.4588	0.0127	0.3224	0.9947
F-CNT-6	0.436	0.149	0.627	0.4331	0.0037	0.4497	0.9952
F-CNT-8	0.413	0.135	0.572	0.4051	0.0043	0.4402	0.9914

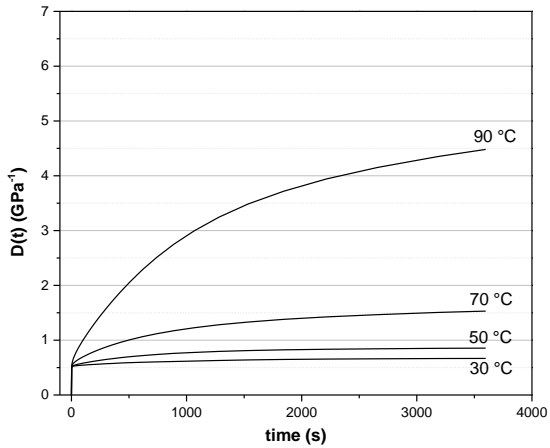
Further information can be obtained by considering the creep compliance curves of Figure 6.4-3, obtained at various temperatures from 30°C to 90°C. It can be noted that the deformation behaviour of the materials is strongly dependent on the temperature. In Figure 6.4-4, the reduction of the creep compliance of F-M5-6 and F-CNT-6 is more pronounced at the highest temperature investigated (90°C).



(a)



(b)



(c)

Figure 6.4-3. Creep compliance of F (a), F-M5-6 (b) and F-CNT-6 (c) nanocomposites under applied load of 3.9 MPa at 30-90°C.

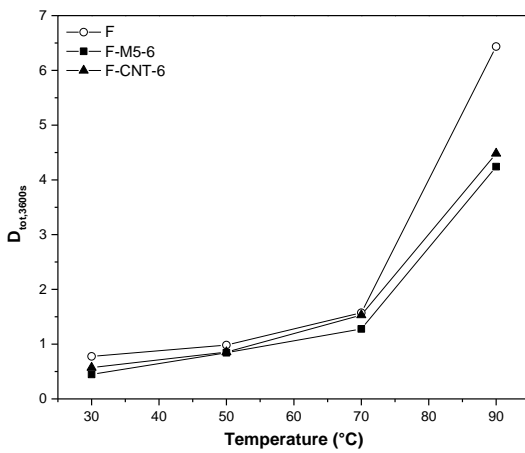


Figure 6.4-4. Creep compliance of F, F-M5-6, and F-CNT-6 nanocomposites at 3.9 MPa at different temperature range.

Table 6.4-2. Creep compliance data of ABS-graphene and ABS-CNT nanocomposites according Eq (5.3-8).

Samples	D _{el} (GPa ⁻¹)	D _{ve,3600s} (GPa ⁻¹)	D _{tot,3600s} (GPa ⁻¹)	D _e (GPa ⁻¹)	k (GPa ⁻¹ s ⁻ⁿ)	n	R ²
T= 50 °C							
F	0.604	0.380	0.984	0.5545	0.0164	0.3538	0.9823
F-M5-6	0.494	0.349	0.843	0.4519	0.0232	0.3553	0.9840
F-CNT-6	0.521	0.334	0.855	0.4711	0.0268	0.3367	0.9793
T= 70 °C							
F	0.617	0.957	1.574	0.5416	0.0342	0.4243	0.9904
F-M5-6	0.442	0.836	1.278	0.3436	0.0522	0.3620	0.9860
F-CNT-6	0.534	0.997	1.532	0.4298	0.0531	0.3788	0.9887
T= 90 °C							
F	0.687	5.747	6.435	0.4931	0.0569	0.5744	0.9943
F-M5-6	0.516	3.726	4.242	0.3745	0.0507	0.5363	0.9939
F-CNT-6	0.561	3.920	4.482	0.3149	0.0894	0.4774	0.9904

Following the results of total creep compliance at different temperatures, activation energy (E_{act}) of the creep process for investigated nanocomposites can be evaluated from the slope of the best fitting straight lines by using Kissinger approach [198]:

$$\log(D_{t,3600s}) = \log(D_0) - \left(\frac{E_{act}}{2.303R} \right) 1/T \quad (6.4-1)$$

where D_0 is a pre-exponential factor, T is the selected temperature for creep experiments, and R, the universal gas constant, is 8.314 J / mol. K. The value of intercept D_0 formally represents melt flow at infinite temperature.

In Table 6.4-3, the activation energy of neat ABS was 15 KJ/mol, and it increased with the content of both graphene and CNT. However, it should be noted that the activation energy of ABS/GNP nanocomposites is higher than that of correspondent ABS/CNT nanocomposites, thus indicating an higher reduction of creep compliance.

Table 6.4-3. The activation energy for the creep process.

Samples	E_{act} (kJ/mol)
F	15.1 ± 3.4
F-M5-6	22.8 ± 1.9
F-CNT-6	21.2 ± 3.0

6.5 Electrical resistivity

The electrical volume resistivity values of CTN and graphene filled ABS compression molded plates are reported in Figure 6.5-1 as a function of the nanofiller fraction. The introduction of the carbon-based nanofiller in the insulating polymeric matrix increases the conductivity of the nanocomposites with different effects in dependence on the type and the content. For example, a resistivity value lower than $10^2 \Omega \cdot \text{cm}$ can be achieved with a CNT content of 1 wt%. The introduction of CNTs confers a good conductivity to the nanocomposite samples, and it is possible to appreciate the lower electrical percolation threshold in CNT nanocomposites with respect to GNP-M5-filled nanocomposites. This threshold value is below 2 wt% for CNT, while GNP-M5 amount between 8 and 12 wt% can be visually estimated. The higher resistivity reduction reached with the introduction of carbon nanotube compared to graphene could be attributed to the better dispersion level and their higher aspect ratio.

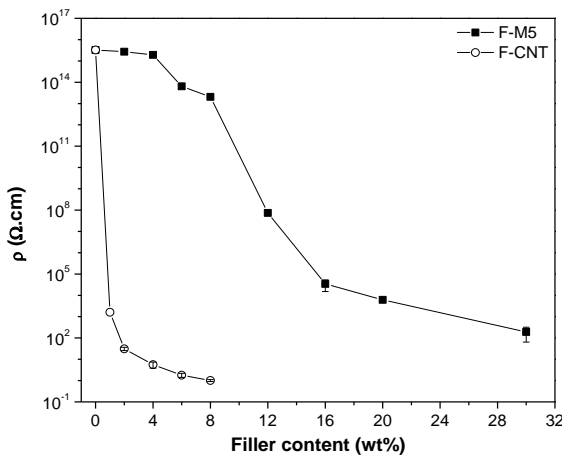


Figure 6.5-1. Electrical volume resistivity of ABS/M5 and ABS/CNT nanocomposites. The applied voltage was 5 V or 100 V for samples having resistivity lower or higher than $10^7 \Omega \cdot \text{cm}$, respectively.

According to the statistical percolation theory, the data of electrical resistivity as functions to volume filler fraction were fitted by power law as:

$$\sigma = \sigma_0 (\phi - \phi_c)^t \quad (6.5-1)$$

This equation can be adapted to electrical resistivity as follows:

$$\log\left(\frac{1}{\rho}\right) = t \log(\phi - \phi_c) + \log\left(\frac{1}{\rho_0}\right) \quad (6.5-2)$$

where ρ = volume resistivity, ρ_0 = scale factor related to the filler intrinsic resistivity, ϕ = filler volume fraction, ϕ_c = percolation threshold, and t = critical exponent. Exponent t value in the range 1.1-1.3 indicates the conduction through 2D network whereas for 3D network the value lies in the range of 1.6-2.0.

The best-fit line in Figure 6.5-2 shows that the percolation critical concentration is 3.8 vol% (~7.3 wt %) for GNP and 0.4 vol% (~0.9 wt %) for CNT, respectively. In addition, the t values were found to be 7.3 and 1.8 for graphene and carbon nanotubes, respectively. The results suggested that the 3D network is formed for both graphene and CNT. In literature, Zhao et al. [199] reported the t values in the range of 2.40-6.92 for graphene-based polymer composites. The t values for CNT were found in general in the range of 1.3-4.0 [200], and around 2.0 is the frequently found in the literature [86].

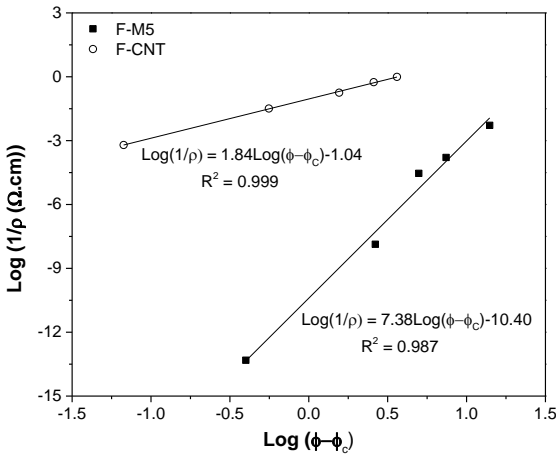


Figure 6.5-2. Percolation theory power law fit of ABS/M5 and ABS/CNT nanocomposites.

The beneficial effect of graphene and CNT represented by the combined result to increase the stiffness, and to reduce melt flow index and the resistivity of ABS nanocomposites. Therefore a merit coefficient P can be calculated according to the equation:

$$P = \frac{E \times MFI}{\rho} \quad (6.5-3)$$

where E is the elastic modulus

MFI is the melt flow index value at 250°C

ρ is volume resistivity.

Figure 6.5-3 shows the combined effect of elastic modulus, melt flow index and resistivity as a function of nanofiller content. The parameter P progressively increases with graphene content, and it reaches to a highest value at 4 wt% of CNT.

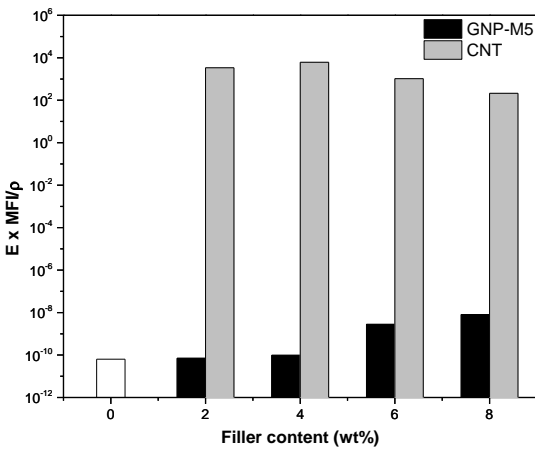


Figure 6.5-3. The combined effect of elastic modulus, melt flow index and resistivity as a function of nanofiller content.

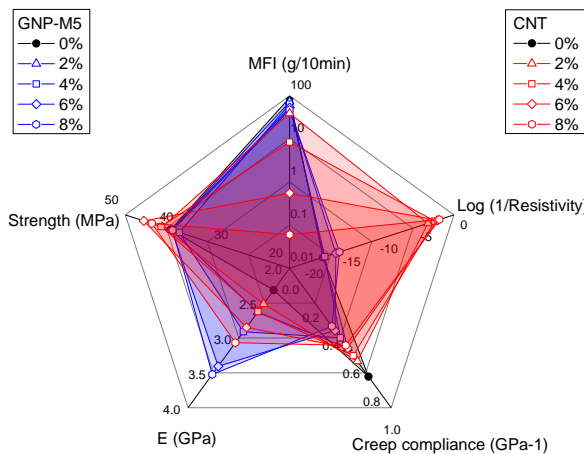


Figure 6.5-4. Comparison of selected properties of ABS/M5 and ABS/CNT nanocomposites as function of nanofiller content (2-8 wt%).

It is possible to observe that graphene and CNT provide some positive influences in different manners as shown in Figure 6.5-4. In the same time, some properties are negatively affected, even if at different levels. Therefore, a combination of these two fillers can be properly selected in order to tune the properties of resulting nanocomposites for the intended application.

Table 6.5-1. Summary of the main properties of ABS matrix and its composites with GNP-M5 and CNT nanofillers. The values at 2 wt% and 8 wt% are reported.

Properties	F	F-M5-2 ➔ F-M5-8	F-CNT-2 ➔ F-CNT-8	M5 Factor	CNT Factor	Effective filler
MFI (g/10min)	89.7	72.5 ➔ 47.1	39.3 ➔ 0.1	0.81 ➔ 0.53	0.44 ➔ 1.1E-03	GNP
E (MPa)	2315	2631 ➔ 3523	2513 ➔ 3068	1.14 ➔ 1.52	39.3 ➔ 0.1	GNP
Strength (MPa)	41.7	41.5 ➔ 41.4	43.3 ➔ 45.1	1.00 ➔ 0.99	1.04 ➔ 1.08	Equivalent
TEB (MJ.mm ⁻³)	11.8	1.057 ➔ 0.780	2.313 ➔ 0.805	0.090 ➔ 0.066	0.196 ➔ 0.068	Equivalent
Strain at break (%)	35.9	4.1 ➔ 3.2	7.5 ➔ 3.1	0.11 ➔ 0.09	0.21 ➔ 0.09	Equivalent
Creep compliance (GPa ⁻¹)	0.777	0.573 ➔ 0.416	0.667 ➔ 0.553	0.74 ➔ 0.54	0.86 ➔ 0.71	GNP
Resistivity (Ω.cm)	3.27E+15	2.72E+15 ➔ 2.07E+13	2.94E+01 ➔ 8.73E-01	1.2E+00 ➔ 1.6E+02	1.1E+14 ➔ 3.7E+15	CNT

The relative factor was calculated by the ratio of the property of composites (P_c) with respect to ABS matrix (P_{ABS}) according to the equation:

$$\text{Relative properties} = P_c / P_{ABS} \quad (6.5-4)$$

where P is GNP or CNT relative properties.

In the case of resistivity was calculated according to the inverse Eq. (6.5-5).

$$\text{Relative properties} = P_{ABS} / P_c \quad (6.5-5)$$

6.6 *Summary of a comparative study of graphene and carbon nanotube nanocomposites compression molded plates*

In order to evaluate the possibility of improvement of carbon based ABS nanocomposites, by using a hybrid composition, a preliminary comparison of graphene and CNT nanofiller, and their effect in ABS nanocomposites are presented. A comparative evaluation is detailed in the followings, in order to the select the most convenient composition for hybrid systems.

According to the experimental results, the incorporation of GNP-M5 and CNT into ABS matrix induced a significant impact on the properties of the ABS nanocomposites. The addition of both nanofillers determined an increase of modulus and strength, and a high reduction of deformation at break. In particular, a significantly higher reduction in MFI value by the addition of CNT compared to GNP-M5 was reported. The ABS/M5 samples showed a slightly higher stiffness and creep stability compared to the ABS/CNT. On the other hand, the tensile strength of ABS/M5 samples were almost constant, whereas the tensile strength of the ABS/CNT was enhanced because of the better dispersion level and the interfacial interactions between CNTs and the ABS matrix compared to graphene. In addition, ABS/CNT showed significant higher electrical properties in comparison to ABS/M5. It follows that CNT and graphene provide a positive influences in different manners. Therefore, a combination of these two fillers is investigated in the following chapter. Following the approach adopted in Chapter V, the nanofiller content of 6 wt% was selected and hybrid nanocomposites were prepared and the results reported in the following Chapter VII.

Chapter VII

ABS-graphene-carbon nanotubes hybrid nanocomposites

This chapter is dedicated to ABS-graphene-carbon nanotube hybrid nanocomposites with the aim to produce suitable filaments through a solvent-free procedure based on melt compounding and extrusion for FDM process. Section 7.1 is about the hybrid ABS-graphene-CNT nanocomposites plates from compression moulding process. Section 7.2 describes the suitable ABS-graphene-CNT filament was employed in FDM process with a comparison of properties on samples obtained by compression moulding, extruded filament and FDM printed parts.

7.1 *ABS-graphene-carbon nanotubes hybrid nanocomposites compression molded plates*

After the comparison of the ABS filled with single carbon nanotube and graphene nanocomposites, nanocomposites with CNT/M5 hybrids for a fixed weight fraction (6 wt%) were investigated. A mixture of CNT and GNP-M5 in ABS were produced through melt compounding in an internal mixer followed by compression moulding (plates). Evaluation on processability, mechanical, electrical and electromagnetic shielding (EMI SE) were carried out.

7.1.1 Compounding and morphology

Table 7.1-1. Designation and formulation of ABS/CNT/M5 hybrid nanocomposites dependence of melt flow index (220°C/10 Kg).

Sample	ABS®F322 (wt%)	CNT (wt%)	GNP-M5 (wt%)	CNT/M5 Relative ratio	MFI (g/10min)
F	100	0	0	Neat	23.6 ± 1.3
F-M5-6	94	0	6	0:100	13.7 ± 0.7
F-M5-5.4-CNT-0.6	94	0.6	5.4	10:90	9.8 ± 0.4
F-M5-4.2-CNT-1.8	94	1.8	4.2	30:70	5.2 ± 0.4
F-M5-3-CNT-3	94	3	3	50:50	1.97 ± 0.17
F-M5-1.8-CNT-4.2	94	4.2	1.8	70:30	0.42 ± 0.01
F-M5-0.6-CNT-5.4	94	5.4	0.6	90:10	0.09 ± 0.01
F-CNT-6	94	6	0	100:0	0.08 ± 0.00

As reported in Table 7.1-1, the investigated formulations are a combination of ABS with two nanofillers GNP-M5 and CNT. The total amount of nanofiller of nanocomposites was fixed at 6 wt% and the relative ratio between CNT/M5 was

varied. Figure 7.1-1 presents the flow properties of hybrid nanocomposites formulation at a fixed total amount of filler (6 wt%) as a function of the different fraction ratio. The MFI values of nanocomposites significantly decreased with the increase of CNT content.

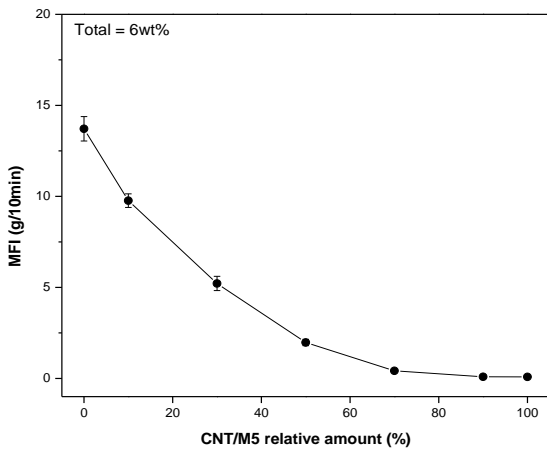
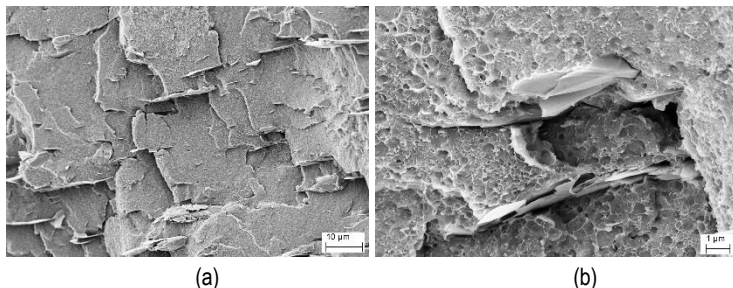
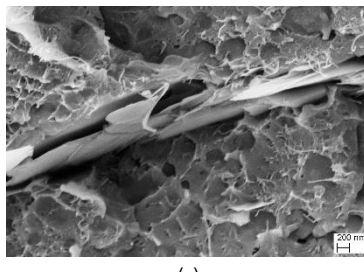


Figure 7.1-1. Melt flow index (220°C/10kg) of ABS/CNT/M5 hybrid nanocomposites.

The effect of compounding on the quality of carbon nanotubes and graphene-M5 dispersion within the ABS matrix was evaluated on the fracture surface of F-M5-3-CNT-3 nanocomposite plate by SEM analysis and results are presented in Figure 7.1-2(a-c). From the SEM figures, it is evidenced that a poor adhesion level between graphene and ABS can be still observed.





(c)

Figure 7.1-2. SEM micrographs of F-M5-3-CNT-3 nanocomposite plates at different magnification of 3,000 \times (a), 20,000 \times (b) and 50,000 \times (c).

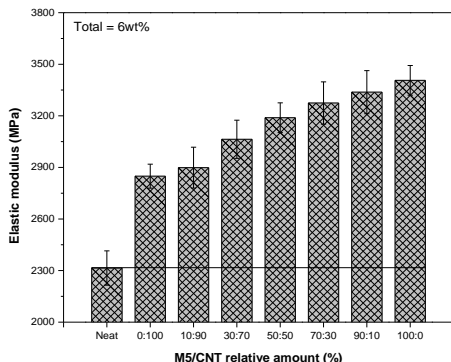
7.1.2 Quasi-static tensile test

The tensile properties of nanocomposites with ABS /M5/CNT hybrids at filler concentration of 6 wt% are summarized in Table 7.1-2. The tensile properties of various mixture ratios of CNT/M5 hybrids were collectively superior to pure ABS. As reported in Figure 7.1-3(a-b), the elastic modulus of nanocomposites linearly increases with the GNP-M5 content. For example, single filler CNT and GNP-M5 nanocomposites exhibited 23% and 47% elastic modulus improvement, respectively, while the hybrid nanocomposites with a ratio 50:50 exhibited 37% improvement. On the other hand, the strength of nanocomposites increases with CNT content, as shown in Figure 7.1-3b. From Figure 7.1-3c, the strain at break of F-CNT-6 is slightly higher than that of F-M5-6 nanocomposites, and the F-CNT-3-M5-3 exhibited the highest strain at break compared the nanocomposites.

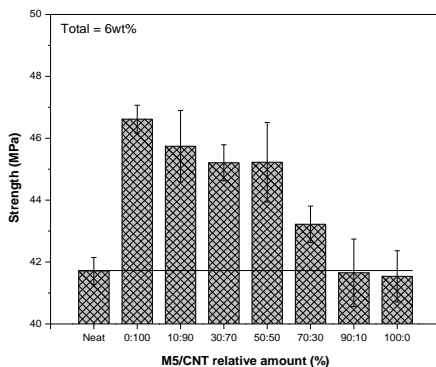
Some works reporting synergistic effect for hybrid carbon nanotubes-graphene nanocomposites at a low concentration of 1 wt% nanofiller can be found in the literature [192, 194, 201]. Nevertheless, our results indicated no synergistic effects until a higher concentration of nanofiller.

Table 7.1-2. Tensile properties of ABS/M5/CNT hybrid nanocomposites.

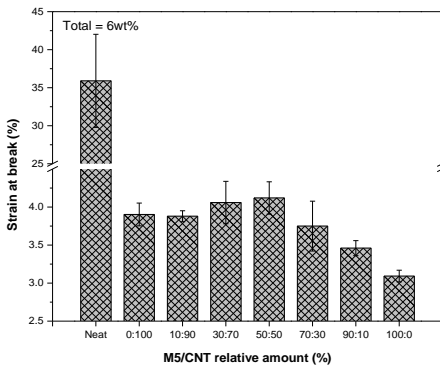
Samples	E (MPa)	σ_y (MPa)	σ_b (MPa)	ϵ_b (%)	TEB (MJ.mm $^{-3}$)
F	2315 ± 100	41.7 ± 0.4	33.6 ± 0.4	35.9 ± 6.1	11.785 ± 2.007
F-CNT-6	2849 ± 70	-	46.4 ± 0.4	3.9 ± 0.2	1.112 ± 0.110
F-M5-0.6-CNT-5.4	2899 ± 119	-	45.7 ± 1.2	3.9 ± 0.1	1.030 ± 0.033
F-M5-1.8-CNT-4.2	3064 ± 111	-	45.2 ± 0.6	4.1 ± 0.3	1.110 ± 0.133
F-M5-3-CNT-3	3189 ± 87	-	45.2 ± 1.3	4.1 ± 0.2	1.156 ± 0.104
F-M5-4.2-CNT-1.8	3275 ± 123	-	43.2 ± 0.6	3.8 ± 0.3	0.995 ± 0.139
F-M5-5.4-CNT-0.6	3338 ± 125	-	41.7 ± 1.1	3.5 ± 0.1	0.868 ± 0.041
F-M5-6	3406 ± 86	-	41.5 ± 0.8	3.1 ± 0.1	0.788 ± 0.086



(a)



(b)



(c)

Figure 7.1-3. Tensile properties of ABS/M5/CNT hybrid nanocomposites: (a) elastic modulus, (b) maximum stress and (c) strain at break.

7.1.3 Electrical resistivity

Four-probe electrical measurements were performed, and the results of bulk resistivity measurements of the samples containing GNP-M5 and CNT nanofillers are reported in Table 7.1-3. From this set of data (see Figure 7.1-4), it is possible to understand that increasing the CNTs relative amount the resistivity decreases with a nonlinear trend, because of the synergistic effect for electrical resistivity due to the presence of both nanofillers. With a total nanofiller amount of 6 wt%, the nanocomposite required at least a CNT/M5 ratio of 30:70 to reach a good conductivity.

Table 7.1-3. Electrical volume resistivity of ABS /M5/CNT hybrid nanocomposites with 6 wt% of nanofillers at an applied voltage of 5 V.

Samples	Electrical resistivity ($\Omega \cdot \text{cm}$)
F-CNT-6	1.51 ± 0.14
F-M5-0.6-CNT-5.4	1.54 ± 0.21
F-M5-1.8-CNT-4.2	1.90 ± 0.13
F-M5-3-CNT-3	4.13 ± 0.69
F-M5-4.2-CNT-1.8	12.7 ± 0.9
F-M5-5.4-CNT-0.6	$1.49\text{E}+07$
F-M5-6	$6.44\text{E}+13$

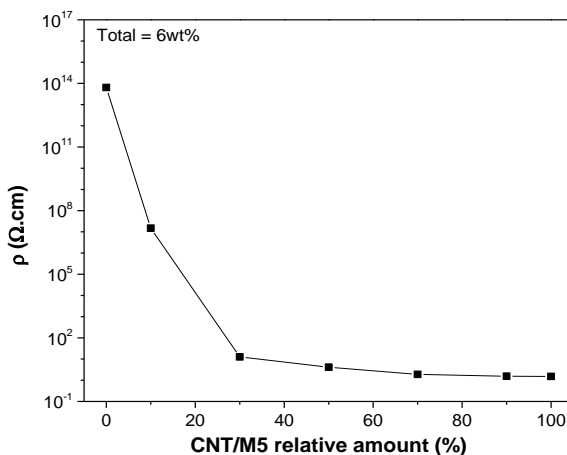


Figure 7.1-4. Electrical volume resistivity of hybrid nanocomposites with total nanofiller of 6 wt% as a function of CNT/M5 relative amount.

7.1.4 Electromagnetic interference shielding effectiveness (EMI SE)

Figure 6.1-2 shows the representative plots of EMI SE expressed in decibel (dB) of the neat ABS and various single GNP-M5, single CNT and hybrid (50:50) compression molded nanocomposites at 6 wt% filler. In the frequency range from 8 to 12.4 GHz, the EMI SE of all samples is almost independent from the frequency. The higher shielding effectiveness was achieved in the following order: F-CNT-6 > F-M5-3-CNT-3 > F-M5-6 > F. Moreover, a good correlation with electrical volume resistivity can be detected.

Materials for EMI shielding purposes are generally targeted to have a minimum of -20 dB of attenuation, at these values of shielding more than 99% of the incident wave is attenuated ensuring that electronic equipment does not generate, or is not affected by, electromagnetic interference [202, 203]. Therefore, it is interesting to note that samples contain 6 wt% of CNT and hybrid (50:50) nanofillers could reach to -46 dB and -31.7 dB, respectively, which meet the EMI SE levels required for commercial applications.

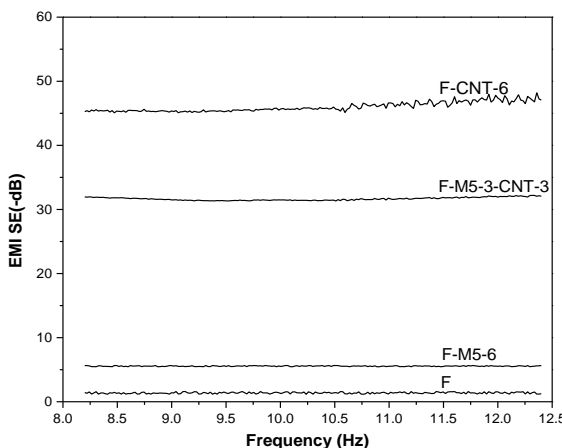


Figure 7.1-5. Representative curves of EMI SE of neat ABS, single and hybrid nanocomposites at 6 wt% from compression moulding.

Due to the almost independence on frequency, the average values of reflection and absorption contributes in the range frequency of 8.2–12.4 GHz were reported and compared in Figure 7.1-6. For the compositions contain carbon nanotubes, contribute of absorption on shielding efficiency is higher than that of reflection, i.e. $SE_A > SE_R$. On the other hand, for ABS/graphene composites the dominant shielding mechanism

is reflection, due to the platelet-shaped GNP-M5 that provide a higher surface area for interaction with the electromagnetic waves.

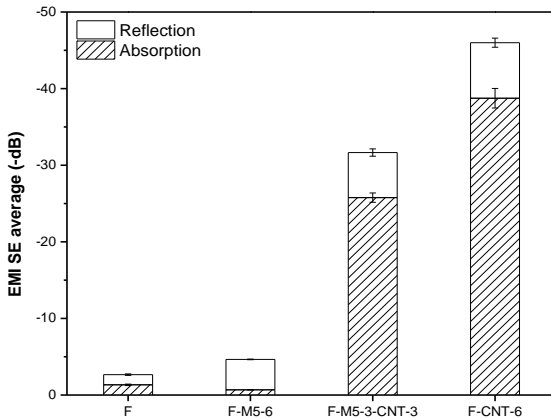


Figure 7.1-6. Influence of absorption and reflection mechanisms on the EMI SE of hybrid nanocomposites from compression moulding.

A summary of main properties of graphene-CNT hybrid nanocomposites at 6 wt% is reported in Table 7.1-4. From Figure 7.1-7, the merit parameter P assumes the highest value at 50:50 and 70:30 of CNT/M5 relative ratio.

Table 7.1-4. The summary of properties graphene-CNT hybrid nanocomposites.

Relative ratio	MFI (g/10min)	ρ ($\Omega \cdot \text{cm}$)	E (MPa)	Strength (MPa)	ϵ_b (%)	TEB (MJ/mm ³)	$E \times MFI/\rho$
Neat	23.61	3.27E+15	2315	41.7	35.9	11.785	1.67E-11
0:100	13.71	1.04E+15	3406	41.5	3.1	0.788	7.25E-10
10:90	9.77	1.49E+07	3338	41.7	3.5	0.868	2.19E-03
30:70	5.22	1.27E+01	3275	43.2	3.8	0.995	1.35E+03
50:50	1.97	4.13E+00	3189	45.2	4.1	1.156	1.52E+03
70:30	0.42	1.90E+00	3064	45.2	4.1	1.110	6.75E+02
90:10	0.09	1.54E+00	2899	45.7	3.9	1.030	1.68E+02
100:0	0.08	1.51E+00	2849	46.6	3.9	1.112	1.60E+02

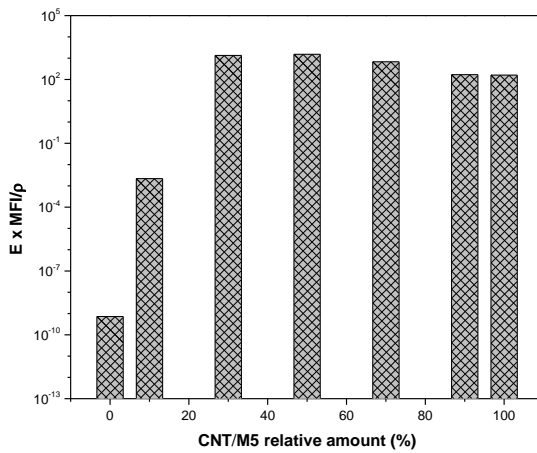


Figure 7.1-7. The combined effect of elastic modulus, melt flow index and resistivity as a function of CNT/M5 relative amount of total 6 wt%.

Figure 7.1-8 shows the processability, resistivity, electromagnetic shielding, and tensile properties of graphene, carbon nanotubes and hybrid nanocomposites at 6 wt% from compression moulding. It is interesting to observe that the 50:50 samples (F-M5-3-CNT-3) is a good compromise between the decrease of processability and the increase of mechanical, electrical resistivity and electromagnetic properties.

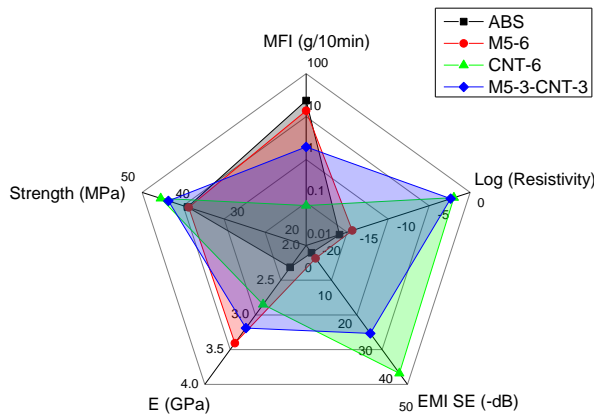


Figure 7.1-8. Processability, resistivity, electromagnetic shielding, tensile properties of graphene, carbon nanotubes and hybrid nanocomposites at 6 wt% from compression moulding.

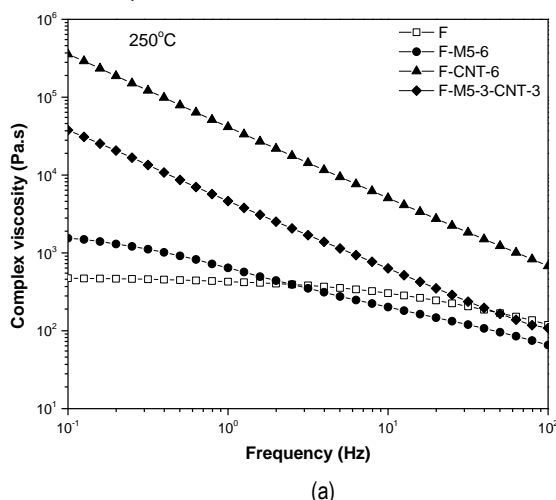
7.2 Fused deposition modelling with ABS-graphene-carbon nanotubes hybrid nanocomposites

By considering the enhancement of properties (mechanical and electrical) and processability, a selected composition is 50:50 of M5/CNT of hybrid nanocomposites was extruded into filaments nanocomposites for FDM. It is worthwhile to note that the materials F-M5-3-CNT-3 (50:50) can be 3D-printed through FDM machine at a nozzle temperature of 250°C.

7.2.1 Rheological behaviour

Rheological investigations provide insights about the filler dispersion in the matrix, network formation and the material's behaviour during the process. The graphs given in Figure 7.2-1 show the complex viscosity of neat ABS and nanocomposites with 6 wt% filler as a function of frequency at 250°C and 280°C. Due to the effect of temperature, the complex viscosity of all samples decreased. It is possible to observe that the complex viscosity of ABS increased with the addition of nanofillers. At temperature of 250°C, the viscosity of ABS/graphene is relative higher than neat ABS at low frequencies, but slightly lower at high frequencies. At low frequencies, the viscosity increased by 3 orders of magnitude for ABS/CNT with 6 wt% filler content and by 2 orders of magnitude for hybrid nanocomposites.

On the other hand at higher frequencies the difference between ABS matrix and 6% nanofilled composites is lower, in the range of one order of magnitude. In particular, it is worth noting that at 250°C F-M5-6 exhibited a complex viscosity at 100Hz even lower than pure ABS matrix.



(a)

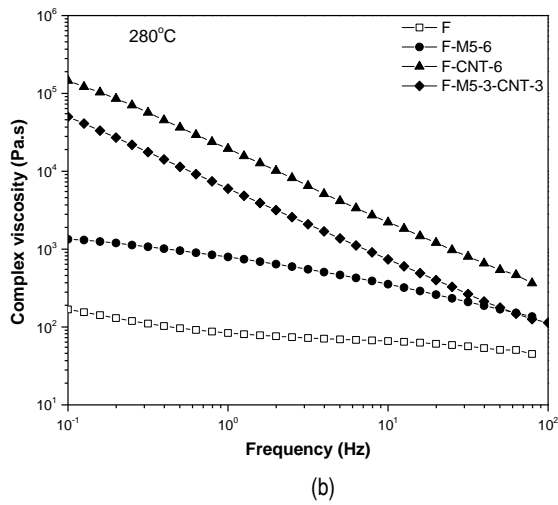
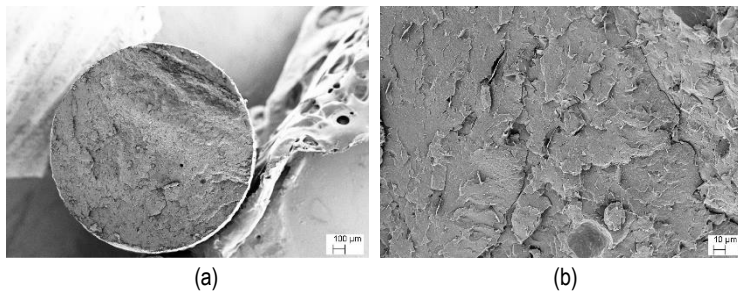


Figure 7.2-1. Complex viscosity as a function of frequency for F-M5-6, F-CNT-6 and F-M5-3-CNT-3 composite plates at (a) 250°C and (b) 280°C.

These findings can be interpreted as an effect of orientation of nanofiller, as previously observed in the ABS composites containing carbon black (1-3 wt%) or CNT (up to 1 wt%) [204]. The higher the frequency, the higher the filler orientation, and the lower the viscosity.

7.2.2 Morphology

The effect of double steps of compounding and extrusion, and the quality of carbon nanotubes and graphene-M5 dispersion into ABS matrix was evaluated of the fracture surface of F-M5-3-CNT-3-E nanocomposite filament by SEM analysis and results are represented Figure 7.2-2(a-d). From Figure 7.2-2a, a small amount of voids can be observed. According to Figure 7.2-2b, the graphene nanoplatelets in the filaments appear to be oriented mostly perpendicular to the fracture plane.



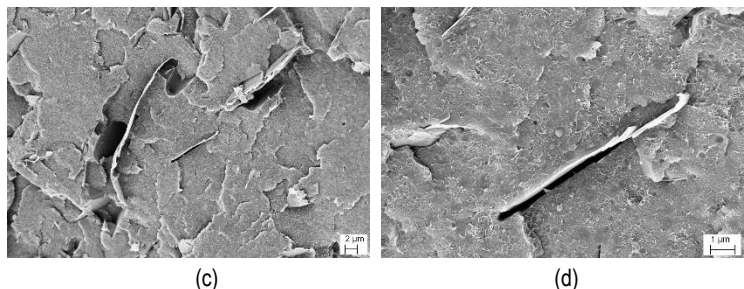


Figure 7.2-2. SEM micrographs of F-M5-3-CNT-3-E nanocomposite filament at different magnification of 100 \times (a), 1,000 \times (b), 5,000 \times (c) and 20,000 \times (d).

Similarly to the filaments, in Figure 7.2-3c, the graphene nanoplatelets for F-M5-3-CNT-3-HC parts appear to be oriented mostly perpendicular to the fracture plane and therefore most likely along the loading direction of dumbbell specimens. It can be therefore inferred that, during extrusion and FDM process, the graphene nanoplatelets are forced to align along the layer plane.

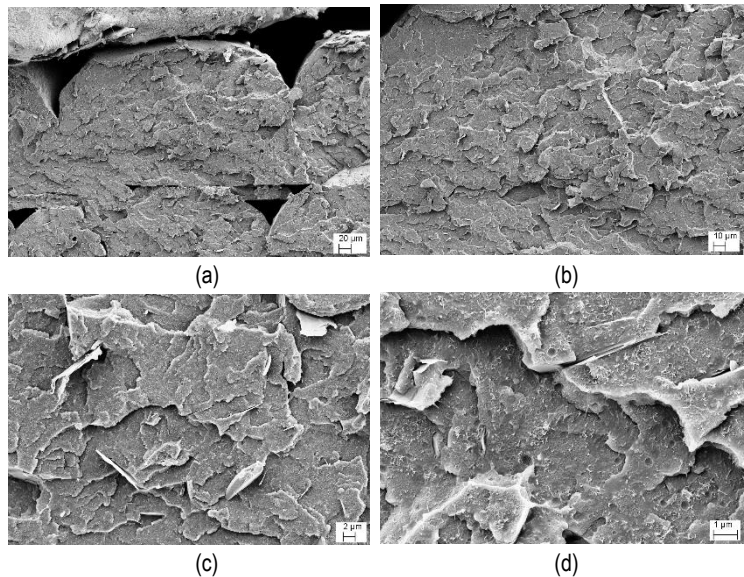


Figure 7.2-3. SEM micrographs of 3D-printed dumbbell specimens printed from F-M5-3-CNT-3-HC at different magnification of 100 \times (a), 1,000 \times (b), 5,000 \times (c) and 20,000 \times (d).

7.2.3 Quasi-static tensile test

The tensile mechanical properties including elastic modulus (E), yield stress and fracture stress and strain are summarized in Table 7.2-1. The ductility of filament nanocomposites progressively reduces with the nanofiller amount as compared to neat ABS. In addition, it is worthwhile to note that the elastic modulus of the 50:50 hybrid nanocomposites was higher than that of single CNT nanocomposites. The elastic modulus of ABS/CNT/M5 nanocomposites continuously increases up to 26% over unfilled ABS. On the other hand, the strength and strain at break of hybrid composite filament were slightly lower than pure CNT nanocomposites, and the sample was fracture before yield point.

The numerical values of tensile properties of FDM samples are also reported in Table 7.2-1. The tensile properties of 3D-printed (HC and H45) samples showed a tendency similar to compression moulded plates and filaments. From Table 7.2-1, the elastic modulus of hybrid nanocomposites of HC and H45 samples were further increased compared pure CNT nanocomposites, whereas, strength and strain at break slightly reduced for this hybrid composition (50:50) as compared to single CNT nanocomposites.

On the other hand, strength and strain at break values of 50:50 hybrid at PC build orientation were significantly reduced as compared to neat ABS, and the samples F-M5-3-CNT-3-PC behave as a brittle material, due to the weakness of bond properties at the cross-sections.

Table 7.2-1. Quasi-static tensile properties of ABS and its nanocomposite of filaments (E) and FDM samples (HC, H45, and PC).

FDM orientation	Materials	E (MPa)	σ_y (MPa)	σ_b (MPa)	ϵ_b (%)
Filaments	F	2207 ± 65	42.8 ± 1.9	35.0 ± 0.4	25.6 ± 15.8
	F-CNT-6	2625 ± 55	47.1 ± 0.5	44.6 ± 1.0	3.2 ± 0.5
	F-M5-3-CNT-3	2787 ± 78	-	40.0 ± 0.4	2.0 ± 0.1
HC	F	2235 ± 170	45.7 ± 0.5	31.9 ± 1.7	30.0 ± 10.4
	F-CNT-6	2735 ± 158	49.6 ± 0.6	49.2 ± 0.6	4.5 ± 0.2
	F-M5-3-CNT-3	3228 ± 235	46.4 ± 0.5	41.8 ± 0.9	6.0 ± 0.2
H45	F	2308 ± 112	41.1 ± 0.9	37.9 ± 1.6	5.3 ± 0.5
	F-CNT-6	2739 ± 268	43.2 ± 0.3	42.6 ± 0.4	4.6 ± 0.3
	F-M5-3-CNT-3	3191 ± 132	-	39.3 ± 0.7	3.8 ± 0.1
PC	F	2077 ± 44	-	22.0 ± 4.4	2.4 ± 0.7
	F-CNT-6	2181 ± 51	-	18.7 ± 1.5	1.9 ± 0.1
	F-M5-3-CNT-3	1825 ± 178	-	10.1 ± 0.7	1.4 ± 0.1

7.2.4 Electrical resistivity

Figure 7.2-4a shows electrical volume resistivity of the hybrid composition for the filament (E) and 3D-printed samples as a function of the applied voltage. Moreover, the electrical resistivity of the loaded samples does not appreciably change with the applied voltage up to 24 V. It can be concluded that these materials behave like ohmic conductors. The electrical resistivity of hybrid nanocomposite filament is about $8.45 \Omega\text{.cm}$, while the resistivity of FDM samples is about $4.2 \times 10^5 \Omega\text{.cm}$, $1.5 \times 10^5 \Omega\text{.cm}$, and $1.1 \times 10^4 \Omega\text{.cm}$ for HC, H45, and PC respectively.

The resistivity of single CNT and 50:50 of CNT/M5 at 6 wt% with different processing techniques is plotted in Figure 7.2-4b. The electrical resistivity of both F-CNT-6 and F-M5-3-CNT-3 nanocomposites increases in the order compression moulding (CM) < the filament (E) < FDM samples (HC, H45, and PC) respectively.

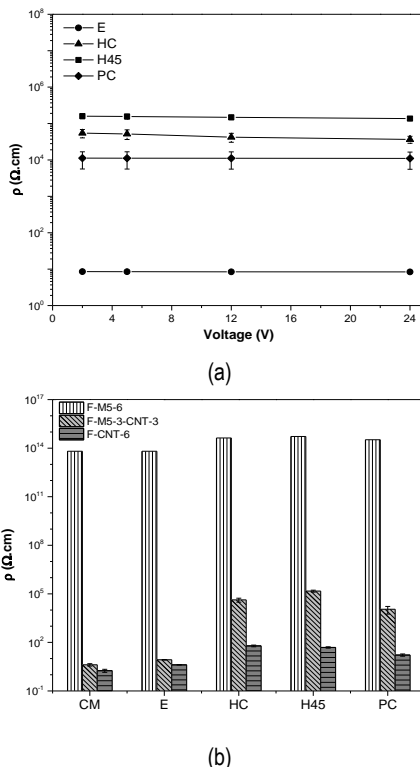
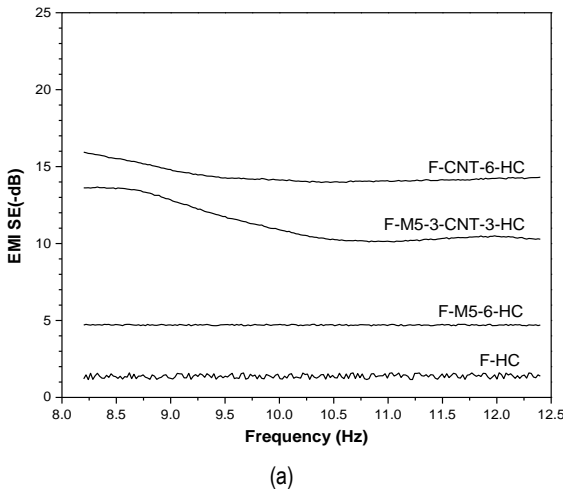


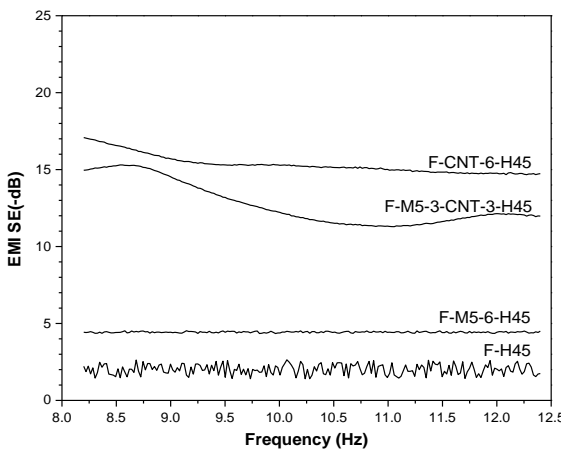
Figure 7.2-4. Electrical volume resistivity: a) F-M5-3-CNT-3 hybrid nanocomposites as a function applied voltage and b) F-M5-6, F-CNT-6 and F-M5-3-CNT-3 at different processing: compression moulding (CM), the filament (E), FDM samples (HC, H45, and PC).

7.2.5 Electromagnetic interference shielding effectiveness (EMI SE)

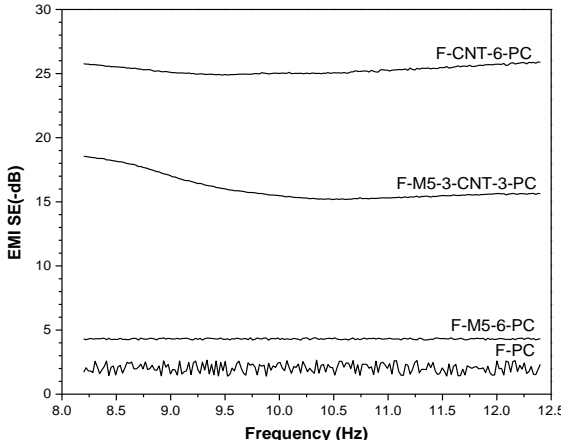
Figure 7.2.5(a-c) shows the representative plots of EMI SE of neat ABS and various single GNP-M5, single CNT and hybrid (50:50) nanocomposites at 6 wt% from FDM at different build orientation in the frequency range from 8 to 12.4 GHz. The nanocomposites with CNT showed a slight influence of the shielding effectiveness on the frequency in the X-band.

Accordingly, EMI SE responses were found to be a function of both, the type of filler as well as build orientation of the specimens. For the polymer composites formulations, the higher shielding effectiveness was achieved in the order of F-CNT-6 > F-M5-3-CNT-3 > F-M5-6 > F independently from the build orientation of the specimens. These results show the same tendency as electrical volume resistivity. For as the effect of the build orientation is concerned, it is observed that the specimens prepared along the PC build orientation better attenuated the electromagnetic radiation. For instance, the total EMI SE of CNT-based composite built along PC was around -25.3 dB whereas the same composite built along HC and H45 showed an attenuation of -14.4 and -15.3 dB, respectively. Similar differences are observed for hybrid composites, -16.1, -11.3 and -12.7 dB for PC, HC and H45 respectively. The ABS/graphene showed lower values of attenuation, near -4.5 dB independent on the growing direction.





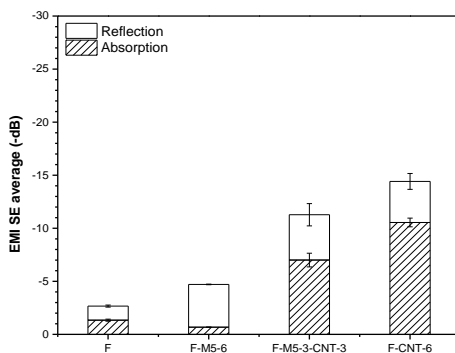
(b)



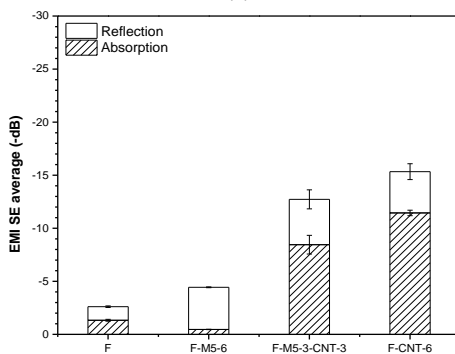
(c)

Figure 7.2-5. Representative curves of EMI SE of hybrid nanocomposites from compression moulding and FDM process: (a) HC, (b) H45 and (c) PC.

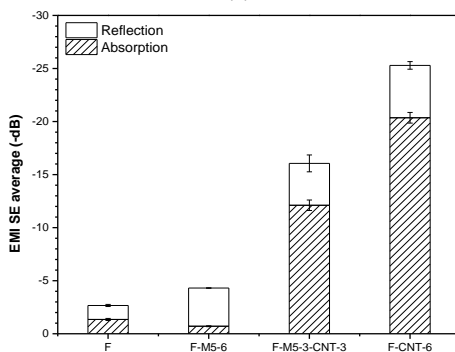
The average values of reflection and absorption contributes in the frequency range of 8.2–12.4 GHz were reported and compared in Figure 7.2-6. For the FDM samples contain carbon nanotubes independent on the build orientation, the shielding absorption contributes higher than that of reflection one, $SE_A > SE_R$. In particular, the dominant shielding mechanism for ABS/graphene composites is the reflection, due to the platelet-shaped GNP-M5 regardless the build orientation.



(a)



(b)



(c)

Figure 7.2-6. Influence of absorption and reflection mechanisms on the EMI SE of hybrid nanocomposites from FDM process: (a) HC, (b) H45 and (c) PC.

The relationship between the decrease of resistivity and the effect of magnetic shield is shown in Figure 7.2-7 that correlates the better performance induced by the addition of GNP-M5, CNT and their mixture with reduced resistivity and the corresponding higher EMI SE. The samples from compression moulding showed the results better than those from 3D printed samples.

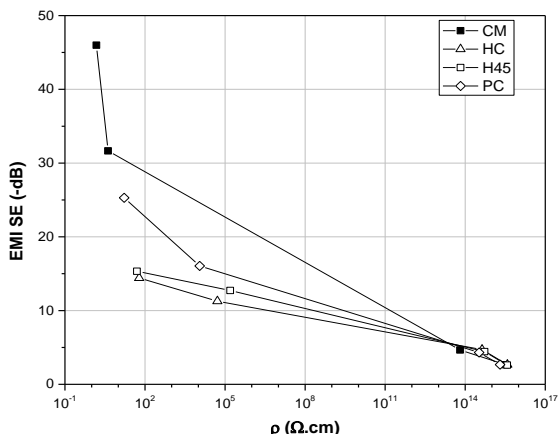


Figure 7.2-7. Electromagnetic shield vs resistivity of neat ABS, ABS-M5, ABS-CNT and hybrid nanocomposite at 6 wt%.

A final comparison of properties of some ABS nanocomposites presented in this study and correspondant engineering polymers containing a similar type of carbon nanoparticles such as ABS/PC, PLA or polyamides is presented in Table 7.2-2. The comparative values could be useful for ranking the various nanocomposites in dependance on the required applications.

Table 7.2-2. Comparison of selected properties of ABS nanocomposites studied in this research with respect to other carbon-based engineering polymers.

Matrix	Type of nanofiller	Process technique	Nanofiller content	Modulus	Strength	Conductivity (S/cm)	EMI SE (-dB)	Ref
ABS	-	-	0	2315 MPa	41.7 MPa	1.6×10^{-16}	2.7	In this study
ABS	GNP	Melt mixing	6 wt%	+47 %	-1 %	1.6×10^{-14}	4.7	In this study
ABS	CNT	Melt mixing	6 wt%	+23 %	+11 %	6.6×10^{-1}	46.0	In this study
ABS	GNP/CNT	Melt mixing	6 wt%	+37 %	+8 %	2.4×10^{-1}	31.7	In this study
PLA	r-GO	Melt mixing	6 wt%	+36 %	+74 %	4.7×10^0	-	[97]
ABS	CB	Melt mixing	15 wt%	-	-	3.4×10^{-4}	-	[16]
ABS	GO	Solution mixing	5.6 wt%	-	-	1.1×10^{-5}	-	[104]
PBT	GNP	Solution mixing	8.4 vol%	-	-	4.0×10^{-2}	-	[102]
ABS/PC	GNP	Melt mixing	3 wt%	+30 %	+15 %	-	-	[70]
ABS	Graphite	Melt mixing	40 vol%	+96 %	-19 %	-	-	[63]
ABS	C18-graphene	Solution mixing	1 wt%	+18 %	+38 %	-	-	[64]
ABS	graphite	Melt mixing	15 wt%	-	-	1.6×10^{-1}	60	[65]
ABS	GNP nanosheet	Solution mixing	0.13 vol%	-	-	1.0×10^{-3}	-	[66]
ABS	GNP nanosheet	Solution mixing	2 wt%	+48 %	+41 %	-	-	[68]
ABS	Graphite	Melt mixing	4.9 vol%	-	-	2.0×10^{-1}	-	[69]
Polyamide	Graphene	Melt mixing	5 wt%	-	-	2.0×10^{-2}	-	[196]
ABS	CNT	Solution mixing	6.1 vol%	-	-	1.0×10^0	-	[86]
PHAs	f-MWCNT	Melt mixing	1 wt%	+33 %	+102 %	1.0×10^{-7}	-	[103]
Polyamide	CNT	Melt mixing	5 wt%	-	-	1.4×10^{-1}	-	[196]
PBT	CNT	Solution mixing	3.5 vol%	-	-	2.5×10^{-1}	-	[102]
ABS	CNT	Solid mixing	5 wt%	-	-	2.0×10^{-3}	38.0	[205]

Chapter VIII

General conclusions and Future perspectives

Graphene nanoplatelets (GNP) and carbon nanotubes (CNT) nanofillers were successfully melt compounded in acrylonitrile–butadiene–styrene (ABS) matrix by using a completely solvent-free process and then extruded into filaments for FDM. Standard composition in the range of 2-8 wt% were selected to produce ABS nanocomposites. The materials properties were monitored along the processing routes including compression moulding, filaments and FDM parts.

The final materials through all processing routes, were deeply characterized by means of thermo-mechanical, electrical and electromagnetic analysis.

Some general conclusion have been led in the following:

- Both nanofillers could be easily compounded in ABS matrix with or without internal lubricant.
- Up to 30 wt% of GNP was dispersed in ABS matrix, whereas a maximum of 8 wt% of CNT was achieved.
- Composition of 4-6 wt% were properly selected for 3D printing.
- It is worth to underline that the improvement of normalised modulus observed for GNP-M5/ABS composite is the highest ever reported in the open scientific literature on carbon-based fillers (except the case of carbon fiber and reduced graphene-oxide ABS composites).
- The nanofillers reduce the flow behaviour, and the effect in particularly severe for carbon nanotubes.
- The presence of graphene and carbon nanotubes have no significant influence on the glass transition temperature either on thermal decomposition of ABS.
- Excellent dispersion of CNT and relative good for graphene in ABS matrix were observed in SEM analysis.
- In all the case, both GNP-M5 and CNT nanofillers significant increased the stiffness of ABS matrix. For example, the improvement about 30% for ABS filled with 4 wt% of GNP-M5 and about 20% for 6 wt% of CNT with respect to neat ABS were obtained.
- The strength of nanocomposites slightly reduced by addition of GNP-M5, while significantly increased by adding CNT. In both cases, a significant reduction of the strain at break of nanocomposites were noted.
- DMTA tests confirmed the stiffening effect of nanoparticles as higher storage modulus for all compositions with nanoparticles. Both GNP-M5 and CNT are also proven to reduce the coefficient of thermal dilation of 3D printed parts, and they also improve their thermal stability.

- The creep compliance significantly reduced by addition of the GNP-M5 and CNT nanofiller, determining an improvement of nanocomposites stability under long-lasting loads.
- The electrical conductive filaments and FDM parts were achieved after addition of CNT. However, their conductivity was reduced after 3D printing processing.
- GNP-CNT hybrid nanocomposites showed a good compromise between processability and enhancement of properties (mainly mechanical and electrical properties).
- Electromagnetic interference shielding effectiveness of ABS filled CNT 6 wt%, and hybrid 3 wt% GNP-M5 and 3 wt% of CNT obtained from compression molding, meet the requirement for application for compression moulding. EMI SE value slightly decreased in the case of FDM parts.

Following the considerations of the promising results obtained from carbon-based nanocomposites, hybrid compositions of carbon nanotube and carbon black incorporated in ABS were also produced for FDM application. Detail are described in collateral research activities (see Chapter IX) with specific attention to mechanical properties and EMI SE improvement.

For future works, the surface treatments of nanofillers or the effect of a compatibilizer can be considered to improve the quality of nanoparticles/ABS interface and their influence on processing through additive manufacturing. In FDM process, the effect of some other parameters (e.g. layer height, infill density, nozzle temperature, the temperature of printing environment, printing speed) on the mechanical properties including fracture toughness, impact or compression resistance still remains to be studied. Moreover, future research could be devoted to the investigation of other properties for the various composition such as ageing resistance, barrier properties (permeability to gases, fire reaction), stability of microstructure and effect of reprocessing.

Finally, it should be underlined that conductive parts of carbonaceous ABS nanocomposites obtained via FDM may be open new interesting perspectives for some industrial applications including strain sensor, electromagnetic shielding casing, etc. At this purpose, a proper selection of hybrid composition based on carbon nanotubes, carbon black, and graphene could be derived from synergistic effects and a good compromise between the processability and the final properties of materials.

Chapter IX

Collateral research activities

9.1 Fused deposition modelling with carbon nanotubes-carbon black hybrid nanocomposites

Part of this chapter has been published in:

D. P. Schmitz, L. G. Ecco, S. Dul, E. C. L. Pereira, B. G. Soares, G. M. O. Barra, A. Pegoretti
“Electromagnetic Interference Shielding Effectiveness of ABS carbon-based Polymer Composites Manufactured via Fused Deposition Modelling”
Materials Today Communication, 2018. 15(1): p. 70-80.

This work reports the preparation of electrically conductive and efficient EMI shielding ABS-carbonaceous based nanocomposites specimens via FDM. Initially, an investigation on the rheological behaviour of the ABS composites is made for the selection of the formulations to be processed via FDM. The feedstock filaments for FDM were prepared at a fixed filler weight fraction of 3 wt% and 5 wt% consisting of carbon nanotube (CNT), carbon black (CB) as well as hybrid formulation (both CNT and CB). In order to verify the effect of the printing pattern of FDM, the solid components were built along three different growing directions and the electromagnetic interference shielding effectiveness of the specimens was assessed in the X-band frequency range.

9.1.1 Materials and sample preparations

9.1.1.1 Materials

The polymeric matrix used in this work was the copolymer acrylonitrile–butadiene–styrene (ABS), under the trade name of Cyclocac™ Resin MG47 supplied in pellets form by Sabic, Brazil. The carbonaceous filler used in the preparation of the polymer nanocomposites were: Multi-walled carbon nanotubes (CNT), trade name Nanocyl™ NC7000 provided by Nanocyl S.A, Belgium; Carbon black (CB) trade name PRINTEX XE 2-B, purchased from Orion Engineered Carbon, US. The nanocomposites were prepared, as detailed in Table 9.1-1.

For sample designation, the unfilled matrix was denoted as ABS, while the coding of the nanocomposites indicated the matrix, the filler type, and the filler weight amount, as well. For instance, a sample filled with 1.5 wt% of CNT and 1.5 wt% of CB is coded as CB1.5-CNT1.5.

Table 9.1-1. Nanocomposites formulations used in the preparation of FDM specimens.

Samples	Filler	Composite formulation (wt %)
ABS	--	ABS (100)
CB3	CNT	ABS (97) / CNT (3)
CNT3	Carbon black	ABS (97) / CB (3)
CB1.5-CNT1.5	CNT+Carbon black	ABS (97) / CNT (1.5) / CB (1.5)
CB2.5-CNT2.5	CNT+Carbon black	ABS (95) / CNT (2.5) / CB (2.5)

9.1.1.2 Composites preparation and FDM manufacturing

- Compouding

Before processing the ABS pellets and the carbonaceous fillers were vacuum dried overnight at 60°C. Neat ABS, as well as ABS/ nanocomposites, were prepared using an internal mixer (Thermo Scientific HaakeTM, PolylabTM Rheomix) with mixing chamber capacity of 75 g and counter-rotating rotors. The temperature in the mixing chamber was 230°C, the rotors speed set at 60 rpm for a mixing time of 15 min. To properly feed the extruder, the resulting materials were reduced to millimeter-sized particles using a low-speed granulator (Piovan, model: RN 166).

- Filament preparation

Before filament extrusion, the granulated materials were vacuum dried overnight at 60°C. Neat ABS and the nanocomposites filaments were prepared using a Thermo Haake PTW16 intermeshing corotating twin-screw extruder (screw diameter = 16 mm; L/D ratio = 25; rod die diameter 1.80 mm). The processing temperature of feeding zone (Zone 1) to rod die (Zone 5) increased from 150, 210, 215, 215 and 220°C, respectively. The screw rotation speed was fixed at 10 rpm, and the collection rate was regulated in order to obtain a final diameter of the extruded filaments of 1.75 ± 0.10 mm. Two parameters of the process, the pressure at the die and torque were constantly recorded during the production of the filaments.

- Preparation of the specimens via FDM for EMI SE

Before FDM manufacturing the extruded filaments were vacuum dried overnight at 60°C. The specimens were produced using a Sharebot Next Generation machine (Sharebot NG, Nibionno, Italy). The manufacturing process was controlled and designed using the open source software Slic3r. The following printing parameters were selected and maintained constant for all the composites formulations: object infill 100%; deposition rate of 40 mm/s; nozzle diameter 0.4 mm; layer height 0.20 mm; nozzle temperature 250°C; printing platform temperature 110°C. The layer height and

the object infill are the diameter of the deposited filament and the percentage of infill of the space inside the solid layers and the perimeters, respectively.

For EMI SE analysis, the specimens were designed into a square shape with a side of 45 mm and a thickness of 2 mm, and they were built-up along three different growing directions named perpendicular concentric (PC), horizontal alternate (H45) and horizontal concentric (HC), as shown in the schematic representation given in Figure 9.1-1. The dimensions have been specifically defined on the basis of the EMI SE tests specifications.

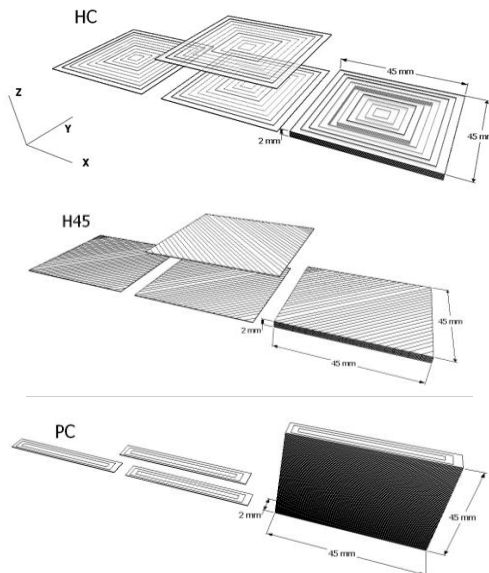


Figure 9.1-1. Schematic representation of the specimens built along the three build orientation. For each build orientation from the left to the right: first deposited layer, representation of the second layer and, the resulting solid component with proper dimensions.

9.1.2 Density measurements

Table 9.1-2 reports the densities of the carbonaceous fillers as well as the densities of neat ABS and the nanocomposites. The density of neat ABS filament was found near 1.034 g/cm³. Due to the addition of each type of filler, the densities of nanocomposites were increased to 1.048-1.051 g/cm³. The specific gravity of neat ABS, informed by the supplier, was considered as theoretical density of ABS and inputted into to estimate the theoretical density of the composites. The density values

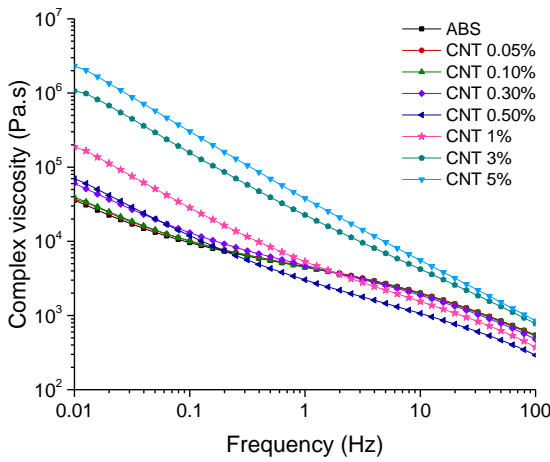
of the additives, measured via helium pycnometry, were inserted to calculate the volume fraction of each fillers in the composites. The detail of voids (V_v) determination are reported in Density measurements (Section 3.3.1.1).

Table 9.1-2. Density of the carbonaceous fillers, polymer nanocomposites volume fraction, density and voids fraction.

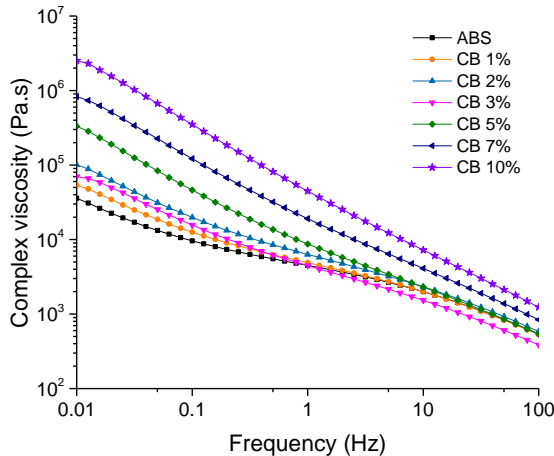
Filler	Density- H_e pycnometry (g/cm ³)	Composites	Vol (%)	Experimental density (g/cm ³)	Theoretical density (g/cm ³)	V_v (%)
CNT	2.287 ± 0.099	ABS	-	1.034 ± 0.001	1.040	-
		CNT3	1.383	1.049 ± 0.003	1.057	0.77
CB	2.389 ± 0.066	CB3	1.325	1.048 ± 0.003	1.058	0.92
		CB1.5-CNT1.5	1.354	1.051 ± 0.002	1.057	0.61
		CB2.5-CNT2.5	2.283	1.056 ± 0.001	1.069	1.22

9.1.3 Rheological behaviour

Rheological investigations provide insights about the filler dispersion in the matrix, network formation and the material's behaviour during process. Binary composites of ABS/CNT and ABS/CB were studied to better understand which formulations is the more promising to be employed for FDM application. The graphs given in Figure 9.1-2 show the complex viscosity of ABS/CNT and ABS/CB as a function of frequency at 230°C, for different amounts of filler content. It is possible to observe that the complex viscosity of ABS is already relatively high and increase with the addition of filler. At low frequencies the viscosity increased by 2 orders of magnitude for ABS/CNT with 5 wt% filler content and for ABS/CB with 10 wt% filler content. The complex viscosity curves of ABS/CNT manifest a transition between 0.3 and 0.5 wt% which indicates rheological percolation. For ABS/CB this transition is visible between 3 and 5 wt%.



(a)



(b)

Figure 9.1-2. Complex viscosity as a function of frequency for ABS/CNT (a) and ABS/CB (b) composites with various filler contents.

Because viscosity, for both CNT- and CB-based composites, increases highly between 3 and 5 wt% a specific formulation of 3 wt% of filler was chosen to continue the study and fabricate the FDM samples. Formulations at this weight fraction of fillers were considered the most appropriated for avoiding clogging the printing nozzle. Additionally, to choose a hybrid formulation, the same study was made. As it can be seen in Figure 9.1-3, the complex viscosity showed by hybrid composites with different

CNT/CB fractions, with fixed total amount of filler (3 wt%), increases with the increase of CNT. According to these results, a single formulation of ABS/CNT.CB with total amount of 3 wt% and a filler fraction of 50:50 has been selected to insure an appropriate viscosity.

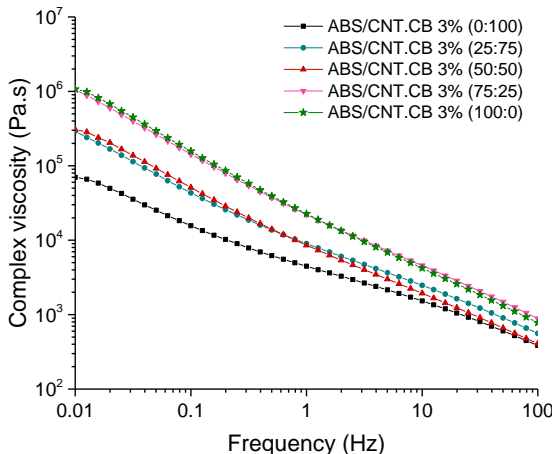


Figure 9.1-3. Complex viscosity as a function of frequency of hybrid ABS with 3 wt% total filler amount at different fractions.

9.1.4 Microstructure of the specimens obtained via FDM

In Figure 9.1-4 both the photos of the FDM specimens as well as the micrographs of their fracture surfaces analyzed via optical microscopy are reported. The axes inserted into the images are in accordance to the 3D axis representation presented in Figure 9.1-1. The photographs exhibit the FDM specimens of neat ABS and ABS/CNT for each growing direction.

The micrographs evidence the boundaries between the deposited filaments during the construction of the specimens. Since PC specimens were built perpendicularly to the collecting platform, in Figure 9.1-4(b) the deposited filaments are forming the layer-upon-layer structure whereas for H45 and HC (Figure 9.1-4(e) and Figure 9.1-4(h), respectively) they were representative of the outermost surface.

Figure 9.1-4(c) shows the top view at the left corner for PC specimen showing the presence of a central gap of 0.2 mm width (arrow inserted in the image) in the construction direction over the YX plane. The layer-upon-layer of H45 and HC are evidenced in the top view images of these specimens give in Figure 9.1-4(f) and Figure 9.1-4(i), respectively.

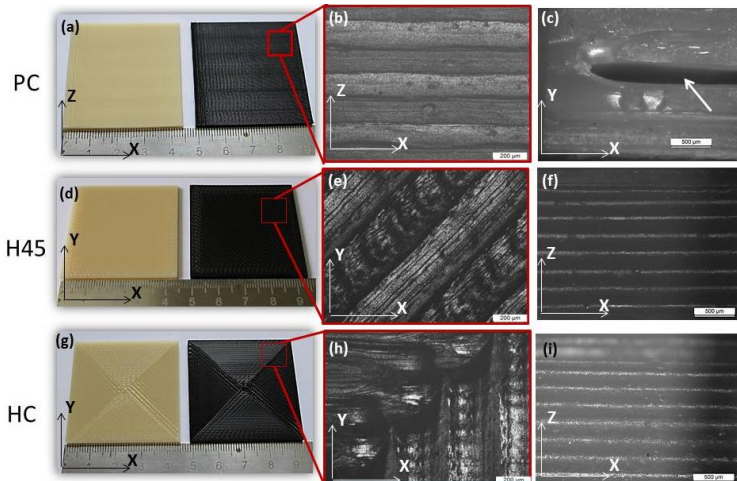


Figure 9.1-4. Photographs of the FDM components: PC (a), H45 (d) and HC (g). Optical microscopy at 100x magnification, PC (b), H45 (e) and HC (h). Optical microscopy at 50x magnification top view of PC (c), H45 (f) and HC (i).

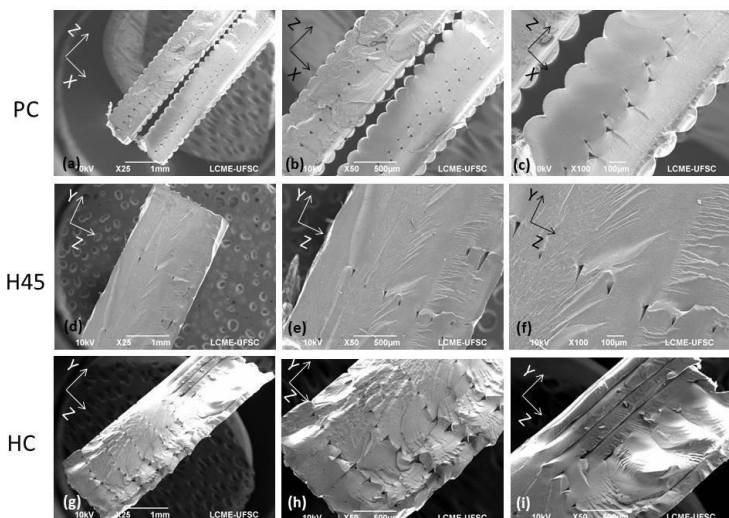


Figure 9.1-5. SEM images of cross-section for respective growing directions: PC (a-c), HC (d-f) and H45 (g-h).

The images displayed in Figure 9.1-5 are the cross-sections of the FDM specimens analyzed via SEM. For all the growing directions a reduction of the filament cross-section attributed to the cooling of the specimens and a possible orientation during FDM process can be observed. Similar shape modifications while processing via FDM have been already reported

In addition, for PC specimens it is possible to see the central gap in the ZX plane and micro voids in the intersections of the filaments of respective layers. For H45 and HC, the images also revealed the presence of micro-voids between the filaments. In particular for H45 in the direction of the filaments (Figure 9.1-5(f)) the boundary formed by the deposited layers can be seen while for HC specimens the layers appear to be well compacted (Figure 9.1-5(g) to Figure 9.1-5(i)).

9.1.5 Electrical conductivity – DC regime

The electrical conductivity values of the extruded filaments as function of filler type are compared in Figure 9.1-6. The electrical conductivity values of the nanocomposites were effectively modified in comparison to neat ABS due to the addition of carbonaceous fillers at the weight fraction 3 wt%. The higher values were obtained for the composites with CNT followed by the hybrid systems and by the CB filled systems.

In particular, the electrical conductivity was significantly increased from about 10^{-15} S.cm $^{-1}$ of neat ABS up to 10^{-2} S.cm $^{-1}$ of ABS/CNT composites. ABS/CB composites showed the lowest electrical conductivity, around 10^{-7} S.cm $^{-1}$. This differences can be attributed to CNT's higher aspect ratio, which facilitates the creation of a continuous conductive network within the ABS matrix. Moreover, CNTs are intrinsically more conductive than CB. When both CNT and CB were added to form the hybrid composites, the electrical conductive was found to be in the order of 10^{-3} S.cm $^{-1}$. Therefore, CNT and CB together formed an efficient conductive network using half of the weight fraction of carbon nanotube.

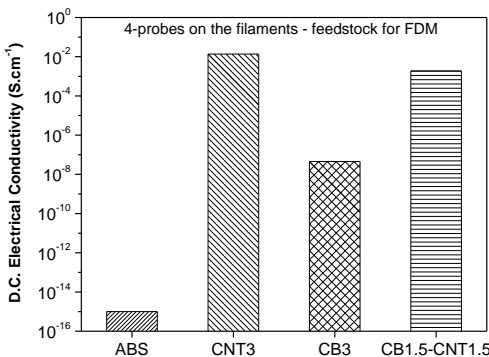


Figure 9.1-6. D.C. electrical conductivity of the extruded filaments with 3 wt% of nanofillers.

Figure 9.1-7 shows the volume electrical conductivity of the specimens for each composite formulation as function of the growing direction during FDM processing. Highlighting that the volume conductivity of FDM specimens was measured placing the terminals onto the opposites faces according to the 3D axis representation given in Figure 9.1-1: for PC plan YX; for HC and H45 plan ZX. According to Figure 9.1-7, the volume conductivity of the specimens prepared via FDM was found to be dependent on their growing direction. Those built along PC direction manifest the highest volume conductivity values, nearly two orders of magnitude higher than HC and H45 growing directions independent on the composite formulation. For instance, in the case of ABS/CNT, the specimen built along PC direction had the volume conductivity measured near $10^{-6} \text{ S} \cdot \text{cm}^{-1}$ whereas those specimens built along HC or H45 showed volume conductivity near $10^{-8} \text{ S} \cdot \text{cm}^{-1}$. Similar for CB1.5-CNT1.5, the volume conductivity was found in the order of 10^{-7} for PC and $10^{-9} \text{ S} \cdot \text{cm}^{-1}$ for HC and H45 growing directions.

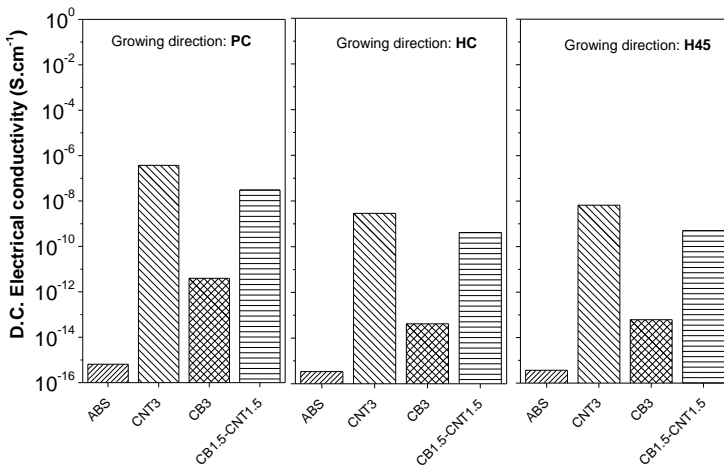


Figure 9.1-7. D.C. volume conductivity of ABS carbon-based solid components produced via FDM in three different layer-by-layer growing directions: perpendicular (left graph), horizontal concentric (center graph) and horizontal alternate (right graph).

The electrical conductivity of FDM specimens were approximately 5 to 6 orders of magnitude lower compared to the respective filament. It is assumed that the extruded filaments are homogeneous, do not present macro defects, and the fillers are adequately distributed and dispersed along the polymer matrix in a way that an efficient conductive network had been formed during extrusion. Therefore, the drop on the electrical conductivity is attributed to the change in printing patterns of the specimens manufactured via FDM and to the fact that a fully compaction is not reached. In particular, the specimens built along PC direction have a more efficient conductive structure than HC and H45 specimens. The volume electrical conductivity of PC was approximately two orders of magnitude higher independent on the composite formulation, despite the fact that PC are approximately 0.40 grams lighter and presented macro voids or holes along the body of the specimens. During the electrical conductivity tests, the electrical charges were offered less resistance as they were moved along the direction of the filaments, note that PC specimens present a continuous pathway, (see Figure 9.1-4(c)). For H45 and HC instead, the electrical charges move throughout the specimens crossing the interfaces between the layers, lowering the volume conductivity of these specimens.

Table 9.1-3. Electrical conductivity (σ) of extruded filaments and the specimens obtained via FDM with 3 wt% of nanofillers.

Composite formulation	σ of filament ($S.cm^{-1}$)	σ on FDM components ($S.cm^{-1}$)		
		PC	HC	H45
ABS	10^{-16}	10^{-16}	10^{-16}	10^{-16}
CNT3	10^{-2}	10^{-7}	10^{-9}	10^{-9}
CB3	10^{-8}	10^{-14}	10^{-14}	10^{-14}
CB1.5-CNT1.5	10^{-3}	10^{-8}	10^{-10}	10^{-10}

9.1.6 Electromagnetic interference shielding effectiveness (EMI SE)

The stack plot given in Figure 9.1-8 shows the total EMI SE for ABS composites specimens prepared via FDM as function of their growing direction, recalling that the incident wave reached the respective faces of FDM specimens: for PC plan YX; for HC and H45 plan ZX, according to Figure 9.1-1.

Accordingly, EMI SE responses were found to be function of both the filler type as well as the growing direction of the specimens. Looking at the polymer composites formulations, the higher shielding effectiveness was achieved in the order following order: CNT3 > CB1.5-CNT1.5 > CB3 > neat ABS independent on the growing direction of the specimens.

Considering the printing patterns, it can be observed that the specimens prepared along the PC direction better attenuated the electromagnetic radiation. For instance, the total EMI SE of carbon nanotube based composite built along PC was around -16 dB whereas the same composite built along HC and H45 showed an attenuation of -10 and -11 dB, respectively. Similar differences are observed for CB1.5-CNT1.5, -12, -8 and -8 dB for PC, HC and H45 respectively. The CB3 showed lower values of attenuation, near -4 dB independent on the growing direction.

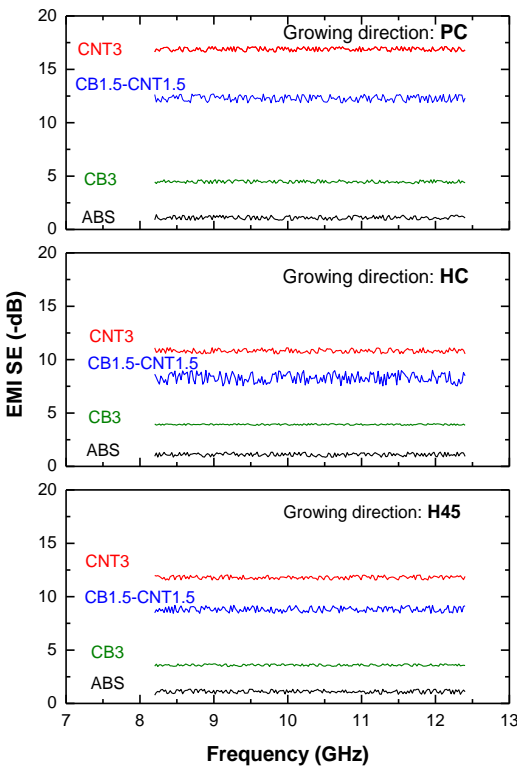
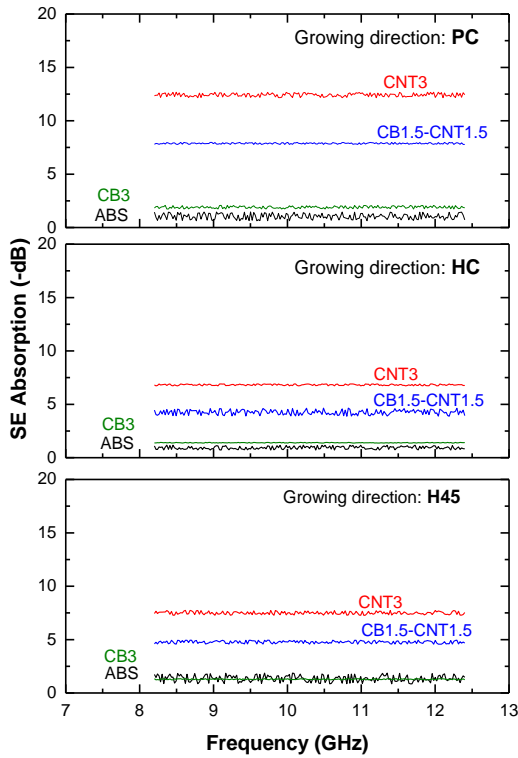


Figure 9.1-8. Total electromagnetic interference shielding effectiveness of ABS carbon-based composites of 3 wt% of nanofillers in three different layer-by-layer growing directions: perpendicular (upper graph), horizontal concentric (middle graph) and horizontal alternate (bottom graph).

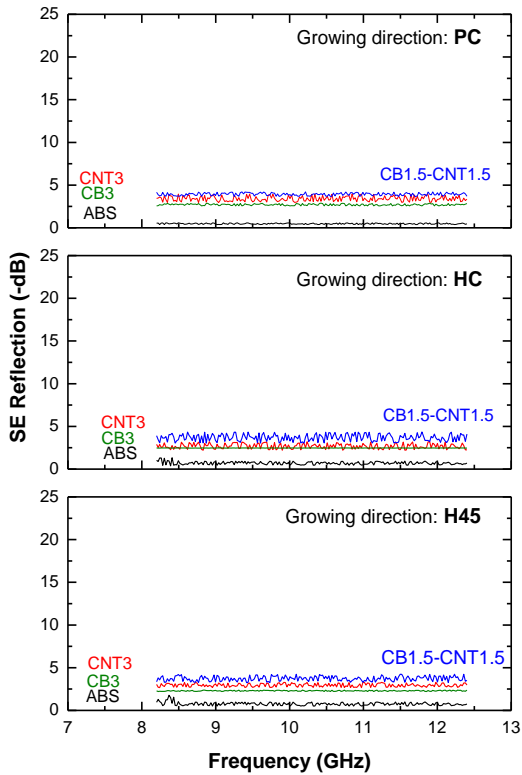
The shielding effectiveness is achieved by attenuating the power of the incident wave passing through the specimens wherein two main mechanisms are operating: the reflection or the absorption of the incident wave [93]. The two stack plots given in Figure 9.1-9 make a distinction between both the shielding effectiveness by absorption (SE_A) and shielding effectiveness by reflection (SE_R). It is possible to appreciate that absorption is the commanding mechanism of shielding when the incident wave propagates through the specimens.

The mechanisms of attenuation are function of both the dielectric and the magnetic properties of the material to which the component is made of. Carbon-based composites are attributed changes at the electrical properties, i.e. dielectric constant,

compared to neat matrix due to the addition of these fillers [206-208] and, therefore, the commanding attenuation by means of absorption is justified by the use of carbon based fillers during the formulation of the ABS composites.



(a)



(b)

Figure 9.1-9. Shielding by absorption (a) and by reflection portion (b) of ABS carbon-based composites of 3 wt% of nanofillers in three different layer-by-layer growing directions: perpendicular (upper graph), horizontal concentric (middle graph) and horizontal alternate (bottom graph).

The outcomes of experimental measurements obtained in this work are displayed in Table 9.1-3. For obtaining 3D components manufactured via FDM having high EMI SE responses, the first step is preparing the extruded feedstock filament with electrical conductivity as higher as possible therefore, a proper selection of the filler and dispersion method are essential. In this work, the hybridization of CNT/CB reduced by half the weight fraction of carbon nanotubes and the extruded filaments of composites CNT3 and CB1.5-CNT1.5 showed similar electrical conductivity values. Nevertheless, once the 3D components are manufactured the volume conductivity of the specimens seems to be a physical property that would indicate on EMI SE performances. The printing patterns should be designed in a way that the FDM

manufactured component offers as low electrical resistance as possible to the movement of charges, i.e. higher volume electrical conductivity. In this work the PC specimens, have shown the highest volume electrical conductivity, despite the presence of a lacuna, micro voids and reduced weight compared to the other growing directions. As a consequence, the PC components have shown the highest EMI SE responses.

Materials for EMI shielding purposes are normally targeted to have a minimum of -20 dB of attenuation, at these values of shielding more than 99% of the incident wave is attenuated ensuring that electronic equipment does not generate, or is not affected by, electromagnetic interference [202, 203]. The values of attenuation obtained in this work were lower than the minimum of attenuation that ensures safety. It is expected that formulations with higher weight fraction of either CNT or a hybrid combination of CNT/CB could effortlessly go higher than -20 dB. For that, it would be necessary to overcome the limitation of processing high viscous composites formulations via FDM. Advanced machines that could work at higher deposition temperatures, lower deposition rate and lower layer height could be a possible solution. On the other hand, it has been verified that components made of carbon-based ABS polymer composites manufactured via FDM can have their EMI SE optimized if appropriately designed and shaped.

Table 9.1-4. Total EMI SE, shielding effectiveness by reflection (SE_R) and shielding effectiveness by absorption (SE_A) at the frequency range of 8 to 12 GHz of neat ABS and carbon-based nanocomposites.

Composite formulation	EMI SE (-dB)			SE Absorption (-dB)			SE Reflection (-dB)		
	PC	HC	H45	PC	HC	H45	PC	HC	H45
ABS	1	1	1	< 1	< 1	< 1	< 1	< 1	< 1
CNT3	16	10	11	12	7	7	4	3	4
CB3	4	4	3	2	1	1	2	2	2
CNT1.5-CB1.5	12	8	8	8	4	4	4	3	4

9.1.7 Quasi-static tensile test

The stress-strain curves of ABS and nanocomposites filaments are shown in Figure 9.1-10. The effect of CNT and CB on the elastic modulus (E), strength (σ_{max}), and strain at break (ϵ_b) of neat ABS and ABS nanocomposite extruded filaments and 3D-printed dumbbells with different orientations are summarized in Table 9.1-5 and Table 9.1-6, respectively. In general, it can be noted how the presence of CNT and CB promotes a significant increase of the elastic modulus of the ABS matrix and the strength.

In Table 9.1-5, improvement of elastic modulus about 6-10% was obtained for single and hybrid CB, and CNT and the highest improvement is about 12% for 5 wt% of hybrid CB and CNT. The higher strength of nanofilled ABS filament in comparison to neat ABS. The strength of composites containing the amount 3 wt% is increased from 45.1 MPa to 47.5 MPa (i.e. 5%), to 49.8 MPa (i.e. 10%) and to 49.6 MPa (i.e. 10%) for CB, CNT and CB+CNT nanofillers respectively. At the highest content of 5 wt% the strength reach to 50.6 MPa.

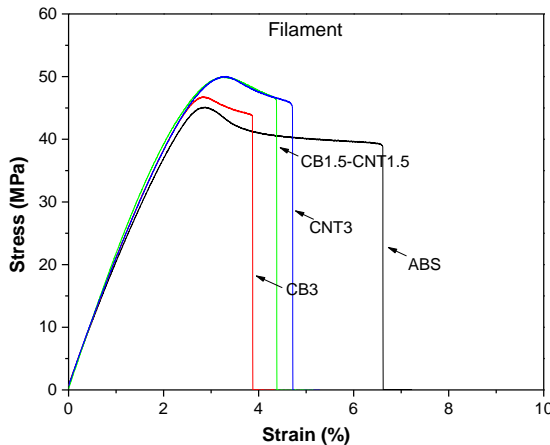


Figure 9.1-10. Stress-strain curve of ABS and nanocomposites filaments.

Table 9.1-5. Quasi-static tensile properties of ABS and its nanocomposite of filaments.

Samples	E (MPa)	σ_{\max} (MPa)	ϵ_b (%)
ABS	2093 ± 30	45.1 ± 0.1	5.1 ± 2.0
CB3	2220 ± 53	47.5 ± 0.5	3.8 ± 0.4
CNT3	2319 ± 87	49.8 ± 0.6	4.3 ± 0.4
CB1.5-CNT1.5	2226 ± 40	49.6 ± 0.5	4.6 ± 0.8
CB2.5-CNT2.5	2338 ± 69	50.6 ± 0.4	4.1 ± 0.5

The stress-strain curves of 3-D printed dumbbell specimens for each growing direction (HC, H45, and PC) are shown in Figure 9.1-11, Figure 9.1-12 and Figure 9.1-13, respectively. Results of mechanical tests of 3D-printed samples are summarized in Table 6.2-1. The tensile modulus of H45 sample is comparable to that of HC sample probably because of good contact between bead extruded fibers and a lower fraction of voids in H45. Similarly enough, the lower yield strength of H45 with respect to that of HC is most probably due to internal orientations of deposited

filaments, whereas PC samples exhibited the poor mechanical properties due to the weakness of interlayer bonding.

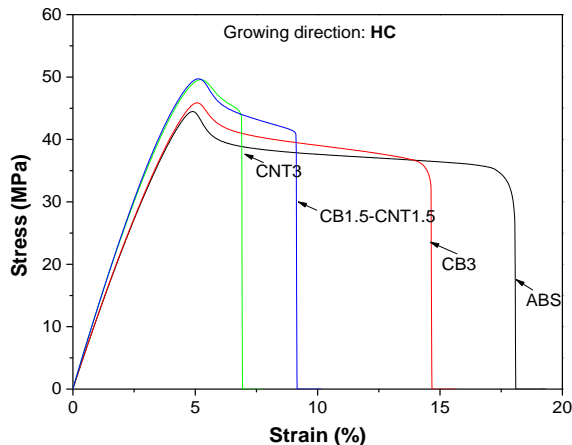


Figure 9.1-11. Stress-strain curve of 3D-printed ABS and nanocomposites. Growing direction: HC.

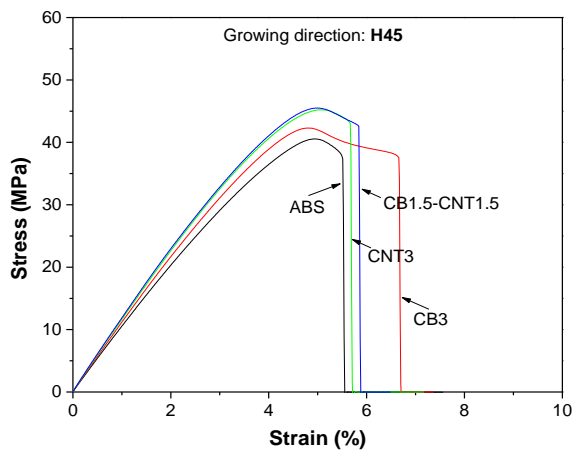


Figure 9.1-12. Stress-strain curve of 3D-printed ABS and nanocomposites. Growing direction: H45.

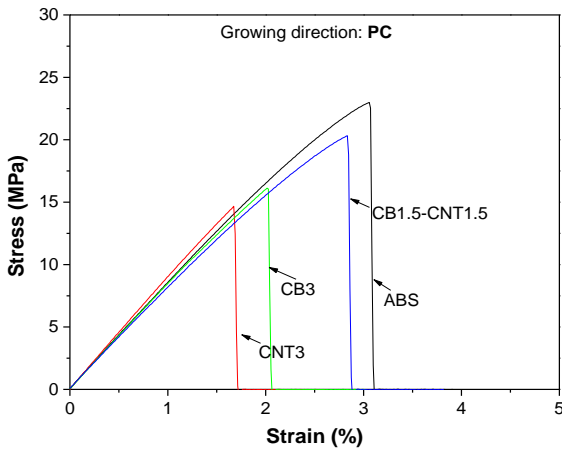


Figure 9.1-13. Stress-strain curve of 3D-printed ABS and nanocomposites. Growing direction: PC.

Table 9.1-6. Quasi-static tensile properties of ABS and its nanocomposite of 3D samples.

FDM orientation	Materials	E (MPa)	σ_{\max} (MPa)	ϵ_b (%)
HC	ABS	2113 ± 112	44.1 ± 0.4	16.8 ± 4.0
	CB3	2158 ± 240	45.8 ± 0.2	14.6 ± 1.0
	CNT3	2472 ± 153	50.5 ± 1.6	8.0 ± 1.0
	CB1.5-CNT1.5	2295 ± 238	49.5 ± 0.6	9.1 ± 0.1
	CB2.5-CNT2.5	2552 ± 213	51.7 ± 0.3	7.5 ± 1.5
H45	ABS	2196 ± 147	40.3 ± 0.2	5.3 ± 0.2
	CB3	2481 ± 174	41.9 ± 0.3	6.6 ± 0.3
	CNT3	2594 ± 153	45.2 ± 0.4	5.7 ± 0.3
	CB1.5-CNT1.5	2565 ± 119	44.3 ± 1.3	5.9 ± 0.9
	CB2.5-CNT2.5	2632 ± 138	45.8 ± 0.1	5.7 ± 0.2
PC	ABS	1734 ± 64	22.3 ± 1.2	3.0 ± 0.2
	CB3	1736 ± 141	15.7 ± 2.6	1.8 ± 0.3
	CNT3	1782 ± 178	16.6 ± 1.6	2.1 ± 0.1
	CB1.5-CNT1.5	1621 ± 134	20.3 ± 0.2	2.7 ± 0.3
	CB2.5-CNT2.5	1742 ± 116	13.5 ± 0.4	1.7 ± 0.1

The elastic modulus and strength of ABS/CNT nanocomposites increase over unfilled ABS at the orientation of HC and H45. The highest strength can be observed in CB2.5-CNT2.5. As a side effect, the elongation at break of FDM composites samples was significantly reduced, especially for HC build orientation. On the other hand, the sample in PC build orientation, only slight improvement in elastic modulus

was obtained, but serve reduction in strength. For instance, the strength of ABS-CB-2.5-CNT-2.5 at PC build orientation was only 13.5 MPa because the interlayer bonding could be significantly reduced by the higher viscosity in a molten state.

9.1.8 Summary ABS-carbon nanotubes-carbon black hybrid nanocomposites

Multi-walled carbon nanotubes, carbon black and a 50:50 hybrid formulation were dispersed into ABS matrix at a fixed concentration of 3 wt%. Extruded filaments of resulting polymer composites were prepared and used as feedstock for fused deposition modelling. The fused deposition modelling components were manufactured along three different printing orientations. The electrical conductivity, electromagnetic interference shielding efficiency and mechanical properties of resulting 3D printed components were assessed.

The incorporation of carbonaceous filler in the ABS matrix resulted in an increase in complex viscosity. A fixed filler concentration of 3 wt% has been selected for the preparation of the feedstock filaments for additive manufacturing of the specimens. At the weight fraction of 3%, the most appropriate correlation between the electrical conductivity and the viscosity of the composites had been observed.

Extruded filaments of the ABS loaded with 3 wt% of multi-walled carbon nanotubes, carbon black and 50:50 hybrid composition have shown higher electrical conductivity values as well as improved mechanical properties such as elastic modulus and strength when compared to neat ABS. The volume electrical conductivity, the electromagnetic interference shielding efficiency and the mechanical properties of 3D printed specimens are intensely dependent on the printing patterns.

References

- [1] K.V. Wong and A. Hernandez, *A review of additive manufacturing*, ISRN Mechanical Engineering, **2012**. 2012(1): p. 1-10.
- [2] I. Durgun and R. Ertan, *Experimental investigation of FDM process for improvement of mechanical properties and production cost*, Rapid Prototyping Journal, **2014**. 20(3): p. 228-235.
- [3] O. Ivanova, C. Williams, and T. Campbell, *Additive manufacturing (AM) and nanotechnology: promises and challenges*, Rapid Prototyping Journal, **2013**. 19(5): p. 353-364.
- [4] D. Dimitrov, K. Schreve, and N.d. Beer, *Advances in three dimensional printing – state of the art and future perspectives*, Rapid Prototyping Journal, **2006**. 12(3): p. 136-147.
- [5] P. Krawczak, *Additive manufacturing of plastic and polymer composite parts: Promises and challenges of 3D-printing*, Express Polymer Letters, **2015**. 9(11): p. 959-959.
- [6] H. Nevin and H. Mehrdad, *Deposition direction-dependent failure criteria for fused deposition modeling polycarbonate*, Rapid Prototyping Journal, **2014**. 20(3): p. 221-227.
- [7] D.W. Hutmacher, T. Schantz, I. Zein, K.W. Ng, S.H. Teoh, and K.C. Tan, *Mechanical properties and cell cultural response of polycaprolactone scaffolds designed and fabricated via fused deposition modeling*, Journal of Biomedical Materials Research, **2001**. 55(2): p. 203-216.
- [8] H.S. Ramanath, C.K. Chua, K.F. Leong, and K.D. Shah, *Melt flow behaviour of poly-ε-caprolactone in fused deposition modelling*, Journal of Materials Science: Materials in Medicine, **2008**. 19(7): p. 2541-2550.
- [9] J.-H. Shim, J.-Y. Won, S.-J. Sung, D.-H. Lim, W.-S. Yun, Y.-C. Jeon, et al., *Comparative efficacies of a 3D-printed PCL/PLGA/β-TCP membrane and a titanium membrane for guided bone regeneration in beagle dogs*, Polymers, **2015**. 7(10): p. 2061-2077.
- [10] L.J. Love, V. Kunc, O. Rios, C.E. Duty, A.M. Elliott, B.K. Post, et al., *The importance of carbon fiber to polymer additive manufacturing*, Journal of Materials Research, **2014**. 29(17): p. 1893-1898.
- [11] H.L. Tekinalp, V. Kunc, G.M. Velez-Garcia, C.E. Duty, L.J. Love, A.K. Naskar, et al., *Highly oriented carbon fiber-polymer composites via additive manufacturing*, Composites Science and Technology, **2014**. 105(0): p. 144-150.
- [12] A. Torrado Perez, D. Roberson, and R. Wicker, *Fracture Surface Analysis of 3D-Printed Tensile Specimens of Novel ABS-Based Materials*, Journal of Failure Analysis and Prevention, **2014**. 14(3): p. 343-353.
- [13] T.A. Campbell and O.S. Ivanova, *3D printing of multifunctional nanocomposites*, Nano Today, **2013**. 8(2): p. 119-120.
- [14] G. Postiglione, G. Natale, G. Griffini, M. Levi, and S. Turri, *UV-assisted three-dimensional printing of polymer nanocomposites based on inorganic fillers*, Polymer Composites, **2017**. 38(8): p. 1662-1670.

- [15] S.J. Leigh, R.J. Bradley, C.P. Pursell, D.R. Billson, and D.A. Hutchins, *A Simple, low-cost conductive composite material for 3D printing of electronic sensors*, PLOS ONE, **2012**. 7(11): p. 49365-49370.
- [16] J. Zhang, B. Yang, F. Fu, F. You, X. Dong, and M. Dai, *Resistivity and its anisotropy characterization of 3D-printed acrylonitrile butadiene styrene Copolymer (ABS)/carbon black (CB) composites*, Applied Sciences, **2017**. 7(1): p. 20-31.
- [17] W. Zhong, F. Li, Z. Zhang, L. Song, and Z. Li, *Short fiber reinforced composites for fused deposition modeling*, Materials Science and Engineering: A, **2001**. 301(2): p. 125-130.
- [18] M.L. Shofner, K. Lozano, F.J. Rodriguez-Macias, and E.V. Barrera, *Nanofiber-reinforced polymers prepared by fused deposition modeling*, Journal of Applied Polymer Science, **2003**. 89(11): p. 3081-3090.
- [19] F. Rouhollah Dermanaki, D. Hamid, B. Vincent Le, A.G. Loick, K. My Ali El, L. Martin, et al., *Direct-write fabrication of freestanding nanocomposite strain sensors*, Nanotechnology, **2012**. 23(8): p. 085502-085510.
- [20] R.D. Farahani, H. Dalir, V. Le Borgne, L.A. Gautier, M.A. El Khakani, M. Lévesque, et al., *Reinforcing epoxy nanocomposites with functionalized carbon nanotubes via biotin-streptavidin interactions*, Composites Science and Technology, **2012**. 72(12): p. 1387-1395.
- [21] S.-z. Guo, X. Yang, M.-C. Heuzey, and D. Therriault, *3D printing of a multifunctional nanocomposite helical liquid sensor*, Nanoscale, **2015**. 7(15): p. 6451-6456.
- [22] G. Postiglione, G. Natale, G. Griffini, M. Levi, and S. Turri, *Conductive 3D microstructures by direct 3D printing of polymer/carbon nanotube nanocomposites via liquid deposition modeling*, Composites Part A: Applied Science and Manufacturing, **2015**. 76(1): p. 110-114.
- [23] B.G. Compton and J.A. Lewis, *3D-printing of lightweight cellular composites*, Advanced Materials, **2014**. 26(34): p. 5930-5935.
- [24] I. Gibson, D. Rosen, and B. Stucker, *Additive Manufacturing Technologies: 3D Printing, Rapid Prototyping, and Direct Digital Manufacturing*, **2014**: Springer New York.
- [25] R. Dermanaki Farahani and M. Dubé, *Printing polymer nanocomposites and composites in three dimensions*, Advanced Engineering Materials, **2017**. p. 1700539-1700547.
- [26] <https://www.manufacturingguide.com/en/fused-deposition-modeling-fdm>.
- [27] B. Kamaljit Singh, S. Rupinder, and S. Harwinder, *Development of rapid tooling using fused deposition modeling: a review*, Rapid Prototyping Journal, **2016**. 22(2): p. 281-299.
- [28] C.H. Rauwendaal, *Polymer extrusion*, in *British Polymer Journal*. **1986**. Munchen: Hanser Publishers. p. 20-25.
- [29] G.A. Kruder, *Extrusion*, in *Encyclopedia of Polymer Science and Technology*. **1985**. New York: John Wiley & Sons, Inc. p. 571-631.
- [30] G. Liao, Z. Li, Y. Cheng, D. Xu, D. Zhu, S. Jiang, et al., *Properties of oriented carbon fiber/polyamide 12 composite parts fabricated by fused deposition modeling*, Materials & Design, **2018**. 139(1): p. 283-292.
- [31] Z. Rymansaib, P. Iravani, E. Emslie, M. Medvidović-Kosanović, M. Sak-Bosnar, R. Verdejo, et al., *All-polystyrene 3D-printed electrochemical device*

- with embedded carbon nanofiber-graphite-polystyrene composite conductor*, *Electroanalysis*, **2016**. 28(7): p. 1517-1523.
- [32] W. Wu, P. Geng, G. Li, D. Zhao, H. Zhang, and J. Zhao, *Influence of layer thickness and raster angle on the mechanical properties of 3D-printed PEEK and a comparative mechanical study between PEEK and ABS*, *Materials*, **2015**. 8(9): p. 5271-5283.
- [33] C. Yang, X. Tian, D. Li, Y. Cao, F. Zhao, and C. Shi, *Influence of thermal processing conditions in 3D printing on the crystallinity and mechanical properties of PEEK material*, *Journal of Materials Processing Technology*, **2017**. 248(1): p. 1-7.
- [34] M.S. Hossain, D. Espalin, J. Ramos, M. Perez, and R. Wicker, *Improved mechanical properties of fused deposition modeling-manufactured parts through build parameter modifications*, *Journal of Manufacturing Science and Engineering-Transactions of the Asme*, **2014**. 136(6): p. 12.
- [35] R.J. Crawford, *General Properties of Plastics*, in *Plastics Engineering (Third Edition)*. **1998**. Oxford: Butterworth-Heinemann. p. 1-40.
- [36] J.A. Brydson, *The Historical Development of Plastics Materials*, in *Plastics Materials (Seventh Edition)*. **1999**. Oxford: Butterworth-Heinemann. p. 1-18.
- [37] E.A. Campo, *Industrial polymers*, in *Industrial Polymers*. **2007**: Carl Hanser Verlag GmbH & Co. KG. p. I-XIII.
- [38] B. Ben Difallah, M. Kharrat, M. Dammak, and G. Monteil, *Mechanical and tribological response of ABS polymer matrix filled with graphite powder*, *Materials & Design*, **2012**. 34(1): p. 782-787.
- [39] F. Wang, Y. Zhang, B.B. Zhang, R.Y. Hong, M.R. Kumar, and C.R. Xie, *Enhanced electrical conductivity and mechanical properties of ABS/EPDM composites filled with graphene*, *Composites Part B: Engineering*, **2015**. 83(1): p. 66-74.
- [40] O. Mohamed, S. Masood, and J. Bhowmik, *Optimization of fused deposition modeling process parameters: a review of current research and future prospects*, *Advances in Manufacturing*, **2015**. 3(1): p. 42-53.
- [41] <https://www.simplify3d.com/support/print-quality-troubleshooting/>.
- [42] A. Duguay, J. Nader, A. Kiziltas, D. Gardner, and H. Dagher, *Exfoliated graphite nanoplatelet-filled impact modified polypropylene nanocomposites: influence of particle diameter, filler loading, and coupling agent on the mechanical properties*, *Applied Nanoscience*, **2014**. 4(3): p. 279-291.
- [43] M. Hedayati, M. Salehi, R. Bagheri, M. Panjepour, and A. Maghzian, *Ball milling preparation and characterization of poly (ether ether ketone)/surface modified silica nanocomposite*, *Powder Technology*, **2011**. 207(1): p. 296-303.
- [44] R.K. Gupta, E. Kennel, and K.-J. Kim, *Polymer nanocomposites handbook*, **2009**: CRC press.
- [45] J. Ma, Q.S. Meng, I. Zaman, S.M. Zhu, A. Michelmore, N. Kawashima, et al., *Development of polymer composites using modified, high-structural integrity graphene platelets*, *Composites Science and Technology*, **2014**. 91(p. 82-90.
- [46] P.A. Askeland, Fukushima, H., Do, I., Kalaitzidou, K., & Drzal, L. T, *Exfoliated graphite nanoplatelets [2] surface treatment*, *NSTI Nanotechnology Conference and Trade Show- NSTI Nanotech 2006 Technical Proceedings*, **2006**. 1 (p. 76-78.

- [47] F. Hussain, M. Hojjati, M. Okamoto, and R.E. Gorga, *Review article: Polymer-matrix Nanocomposites, Processing, Manufacturing, and Application: An Overview*, Journal of Composite Materials, **2006**. 40(17): p. 1511-1575.
- [48] E. Yildirir, N. Miskolczi, J.A. Onwudili, K.E. Németh, P.T. Williams, and J. Sója, *Evaluating the mechanical properties of reinforced LDPE composites made with carbon fibres recovered via solvothermal processing*, Composites Part B: Engineering, **2015**. 78(p. 393-400).
- [49] M. Pumera, *Graphene-based nanomaterials and their electrochemistry*, Chemical Society Reviews, **2010**. 39(11): p. 4146-4157.
- [50] B. Li and W.H. Zhong, *Review on polymer/graphite nanoplatelet nanocomposites*, Journal of Materials Science, **2011**. 46(17): p. 5595-5614.
- [51] R. Sengupta, M. Bhattacharya, S. Bandyopadhyay, and A.K. Bhowmick, *A review on the mechanical and electrical properties of graphite and modified graphite reinforced polymer composites*, Progress in Polymer Science, **2011**. 36(5): p. 638-670.
- [52] XG Sciences (2017) *xGnP® Graphene Nanoplatelets Product Data from <http://xgsciences.com/products/graphene-nanoplatelets/>* consulted on June 20th, 2018.
- [53] X. Jiang and L.T. Drzal, *Multifunctional high density polyethylene nanocomposites produced by incorporation of exfoliated graphite nanoplatelets 1: Morphology and mechanical properties*, Polymer Composites, **2010**. 31(6): p. 1091-1098.
- [54] K. Kalaitzidou, H. Fukushima, and L.T. Drzal, *Multifunctional polypropylene composites produced by incorporation of exfoliated graphite nanoplatelets*, Carbon, **2007**. 45(7): p. 1446-1452.
- [55] M. Mehrali, S.T. Latibari, M. Mehrali, T.M. Indra Mahlia, H.S. Cornelis Metselaar, M.S. Naghavi, et al., *Preparation and characterization of palmitic acid/graphene nanoplatelets composite with remarkable thermal conductivity as a novel shape-stabilized phase change material*, Applied Thermal Engineering, **2013**. 61(2): p. 633-640.
- [56] M. Kim, S.-H. Hwang, B.-J. Kim, J.-B. Baek, H.S. Shin, H.W. Park, et al., *Modeling, processing, and characterization of exfoliated graphite nanoplatelet-nylon 6 composite fibers*, Composites Part B: Engineering, **2014**. 66(1): p. 511-517.
- [57] D. Pedrazzoli and A. Pegoretti, *Expanded graphite nanoplatelets as coupling agents in glass fiber reinforced polypropylene composites*, Composites Part A: Applied Science and Manufacturing, **2014**. 66(1): p. 25-34.
- [58] T.D. Thanh, L. Kaprálková, J. Hromádková, and I. Kelnar, *Effect of graphite nanoplatelets on the structure and properties of PA6-elastomer nanocomposites*, European Polymer Journal, **2014**. 50(1): p. 39-45.
- [59] D.R. Klimek-McDonald, J.A. King, I. Miskioglu, E.J. Pineda, and G.M. Odegard, *Determination and Modeling of Mechanical Properties for Graphene Nanoplatelet/Epoxy Composites*, Polymer Composites, **2016**. in press (
- [60] H.M. Chong, S.J. Hinder, and A.C. Taylor, *Graphene nanoplatelet-modified epoxy: effect of aspect ratio and surface functionality on mechanical properties and toughening mechanisms*, Journal of Materials Science, **2016**. 51(19): p. 8764-8790.

- [61] S. Basu, M. Singh, B.K. Satapathy, and M. Fahim, *Dielectric, electrical, and rheological characterization of graphene-filled polystyrene nanocomposites*, Polymer Composites, **2013**. 34(12): p. 2082-2093.
- [62] X. Pang, X. Shi, X. Kang, M. Duan, and M. Weng, *Preparation of borate-modified expandable graphite and its flame retardancy on acrylonitrile-butadiene-styrene resin*, Polymer Composites, **2016**. 37(9): p. 2673-2683.
- [63] A.K. Pandey, R. Kumar, V.S. Kachhavah, and K.K. Kar, *Mechanical and thermal behaviours of graphite flake-reinforced acrylonitrile-butadiene-styrene composites and their correlation with entanglement density, adhesion, reinforcement and C factor*, RSC Advances, **2016**. 6(56): p. 50559-50571.
- [64] C. Heo, H.-G. Moon, C.S. Yoon, and J.-H. Chang, *ABS nanocomposite films based on functionalized-graphene sheets*, Journal of Applied Polymer Science, **2012**. 124(6): p. 4663-4670.
- [65] V.K. Sachdev, K. Patel, S. Bhattacharya, and R.P. Tandon, *Electromagnetic interference shielding of graphite/acrylonitrile butadiene styrene composites*, Journal of Applied Polymer Science, **2011**. 120(2): p. 1100-1105.
- [66] C. Gao, S. Zhang, F. Wang, B. Wen, C. Han, Y. Ding, et al., *Graphene networks with low percolation threshold in ABS nanocomposites: selective localization and electrical and rheological properties*, ACS Applied Materials & Interfaces, **2014**. 6(15): p. 12252-12260.
- [67] F.M. Uhl, Q. Yao, and C.A. Wilkie, *Formation of nanocomposites of styrene and its copolymers using graphite as the nanomaterial*, Polymers for Advanced Technologies, **2005**. 16(7): p. 533-540.
- [68] N. Hong, J. Zhan, X. Wang, A.A. Stec, T. Richard Hull, H. Ge, et al., *Enhanced mechanical, thermal and flame retardant properties by combining graphene nanosheets and metal hydroxide nanorods for Acrylonitrile-Butadiene-Styrene copolymer composite*, Composites Part A: Applied Science and Manufacturing, **2014**. 64(0): p. 203-210.
- [69] H.S. Dahiya, N. Kishore, and R.M. Mehra, *Effect of percolation on electrical and dielectric properties of acrylonitrile butadiene styrene/graphite composite*, Journal of Applied Polymer Science, **2007**. 106(3): p. 2101-2110.
- [70] R.H. Pour, A. Hassan, M. Soheilmoghadam, and H.C. Bidsorkhi, *Mechanical, thermal, and morphological properties of graphene reinforced polycarbonate/acrylonitrile butadiene styrene nanocomposites*, Polymer Composites, **2016**. 37(6): p. 1633-1640.
- [71] R.T.K. Baker, M.A. Barber, P.S. Harris, F.S. Feates, and R.J. Waite, *Nucleation and growth of carbon deposits from the nickel catalyzed decomposition of acetylene*, Journal of Catalysis, **1972**. 26(1): p. 51-62.
- [72] S. Iijima, *Helical microtubules of graphitic carbon*, Nature, **1991**. 354(1): p. 56.
- [73] R. Vidu, M. Rahman, M. Mahmoudi, M. Enachescu, T.D. Poteca, and I. Opris, *Nanostructures: a platform for brain repair and augmentation*, Frontiers in Systems Neuroscience, **2014**. 8(1): p. 91.
- [74] A. Aqel, K.M.M.A. El-Nour, R.A.A. Ammar, and A. Al-Warthan, *Carbon nanotubes, science and technology part (I) structure, synthesis and characterisation*, Arabian Journal of Chemistry, **2012**. 5(1): p. 1-23.

- [75] A. Eatemadi, H. Daraee, H. Karimkhanloo, M. Kouhi, N. Zarghami, A. Akbarzadeh, et al., *Carbon nanotubes: properties, synthesis, purification, and medical applications*, *Nanoscale Research Letters*, **2014**. 9(1): p. 393.
- [76] X.-L. Xie, Y.-W. Mai, and X.-P. Zhou, *Dispersion and alignment of carbon nanotubes in polymer matrix: A review*, *Materials Science and Engineering: R: Reports*, **2005**. 49(4): p. 89-112.
- [77] M.S.P. Shaffer and J.K.W. Sandler, *Carbon nanotube/nanofibre polymer composites*, in *Processing and Properties of Nanocomposites*. **2012**: WORLD SCIENTIFIC. p. 1-59.
- [78] J. Jyoti, S. Basu, B.P. Singh, and S.R. Dhakate, *Superior mechanical and electrical properties of multiwall carbon nanotube reinforced acrylonitrile butadiene styrene high performance composites*, *Composites Part B: Engineering*, **2015**. 83(1): p. 58-65.
- [79] J. Jyoti, B.P. Singh, A.K. Arya, and S.R. Dhakate, *Dynamic mechanical properties of multiwall carbon nanotube reinforced ABS composites and their correlation with entanglement density, adhesion, reinforcement and C factor*, *RSC Advances*, **2016**. 6(5): p. 3997-4006.
- [80] M.H. Al-Saleh, B.A. Al-Saidi, and R.M. Al-Zoubi, *Experimental and theoretical analysis of the mechanical and thermal properties of carbon nanotube/acrylonitrile-styrene-butadiene nanocomposites*, *Polymer*, **2016**. 89(1): p. 12-17.
- [81] L. Wang, J. Qiu, E. Sakai, and X. Wei, *The relationship between microstructure and mechanical properties of carbon nanotubes/polylactic acid nanocomposites prepared by twin-screw extrusion*, *Composites Part A: Applied Science and Manufacturing*, **2016**. 89(1): p. 18-25.
- [82] A. Dorigato, V. Moretti, S. Dul, S.H. Unterberger, and A. Pegoretti, *Electrically conductive nanocomposites for fused deposition modelling*, *Synthetic Metals*, **2017**. 226(p. 7-14.
- [83] B. Krause, P. Pötschke, and L. Häußler, *Influence of small scale melt mixing conditions on electrical resistivity of carbon nanotube-polyamide composites*, *Composites Science and Technology*, **2009**. 69(10): p. 1505-1515.
- [84] M.T. Müller, B. Krause, B. Kretzschmar, and P. Pötschke, *Influence of feeding conditions in twin-screw extrusion of PP/MWCNT composites on electrical and mechanical properties*, *Composites Science and Technology*, **2011**. 71(13): p. 1535-1542.
- [85] V. Choudhary and A. Gupta, *Polymer/carbon nanotube nanocomposites*, in *Carbon nanotubes - polymer nanocomposites*. **2011**. Rijeka: InTech. p. 65-108.
- [86] M.H. Al-Saleh, H.K. Al-Anid, and Y.A. Hussain, *CNT/ABS nanocomposites by solution processing: Proper dispersion and selective localization for low percolation threshold*, *Composites Part A: Applied Science and Manufacturing*, **2013**. 46(1): p. 53-59.
- [87] B.K. Singh, P. Kar, N.K. Shrivastava, S. Banerjee, and B.B. Khatua, *Electrical and mechanical properties of acrylonitrile-butadiene-styrene/multiwall carbon nanotube nanocomposites prepared by melt-blending*, *Journal of Applied Polymer Science*, **2012**. 124(4): p. 3165-3174.

- [88] G. Kaur, R. Adhikari, P. Cass, M. Bown, and P. Gunatillake, *Electrically conductive polymers and composites for biomedical applications*, RSC Advances, **2015**. 5(47): p. 37553-37567.
- [89] M.H. Al-Saleh and U. Sundararaj, *Electromagnetic interference shielding mechanisms of CNT/polymer composites*, Carbon, **2009**. 47(7): p. 1738-1746.
- [90] Y. Yang, M.C. Gupta, K.L. Dudley, and R.W. Lawrence, *Novel Carbon Nanotube-Polystyrene Foam Composites for Electromagnetic Interference Shielding*, Nano Letters, **2005**. 5(11): p. 2131-2134.
- [91] Z. Liu, G. Bai, Y. Huang, Y. Ma, F. Du, F. Li, et al., *Reflection and absorption contributions to the electromagnetic interference shielding of single-walled carbon nanotube/polyurethane composites*, Carbon, **2007**. 45(4): p. 821-827.
- [92] H.M. Kim, K. Kim, C.Y. Lee, J. Joo, S.J. Cho, H.S. Yoon, et al., *Electrical conductivity and electromagnetic interference shielding of multiwalled carbon nanotube composites containing Fe catalyst*, Applied Physics Letters, **2004**. 84(4): p. 589-591.
- [93] J.-M. Thomassin, C. Jérôme, T. Padoen, C. Bailly, I. Huynen, and C. Detrembleur, *Polymer/carbon based composites as electromagnetic interference (EMI) shielding materials*, Materials Science and Engineering: R: Reports, **2013**. 74(7): p. 211-232.
- [94] U. Kalsoom, P.N. Nesterenko, and B. Paull, *Recent developments in 3D printable composite materials*, RSC Advances, **2016**. 6(65): p. 60355-60371.
- [95] J.T. Muth, D.M. Vogt, R.L. Truby, Y. Mengüç, D.B. Kolesky, R.J. Wood, et al., *Embedded 3D printing of strain sensors within highly stretchable elastomers*, Advanced Materials, **2014**. 26(36): p. 6307-6312.
- [96] K. Chizari, M. Arjmand, Z. Liu, U. Sundararaj, and D. Therriault, *Three-dimensional printing of highly conductive polymer nanocomposites for EMI shielding applications*, Materials Today Communications, **2017**. 11(1): p. 112-118.
- [97] D. Zhang, B. Chi, B. Li, Z. Gao, Y. Du, J. Guo, et al., *Fabrication of highly conductive graphene flexible circuits by 3D printing*, Synthetic Metals, **2016**. 217(1): p. 79-86.
- [98] K. Sun, T.-S. Wei, B.Y. Ahn, J.Y. Seo, S.J. Dillon, and J.A. Lewis, *3D printing of interdigitated Li-Ion microbattery architectures*, Advanced Materials, **2013**. 25(33): p. 4539-4543.
- [99] P. Parandoush and D. Lin, *A review on additive manufacturing of polymer-fiber composites*, Composite Structures, **2017**. in press
- [100] R.D. Farahani, M. Dubé, and D. Therriault, *Three-dimensional printing of multifunctional nanocomposites: manufacturing techniques and applications*, Advanced Materials, **2016**. 28(28): p. 5794-5821.
- [101] F. Ning, W. Cong, Y. Hu, and H. Wang, *Additive manufacturing of carbon fiber-reinforced plastic composites using fused deposition modeling: Effects of process parameters on tensile properties*, Journal of Composite Materials, **2017**. 51(4): p. 451-462.
- [102] K. Gnanasekaran, T. Heijmans, S. van Bennekom, H. Woldhuis, S. Wijnia, G. de With, et al., *3D printing of CNT- and graphene-based conductive polymer nanocomposites by fused deposition modeling*, Applied Materials Today, **2017**. 9(1): p. 21-28.

- [103] C.S. Wu and H.T. Liao, *Interface design of environmentally friendly carbon nanotube-filled polyester composites: Fabrication, characterisation, functionality and application*, Express Polymer Letters, **2017**. 11(3): p. 187-198.
- [104] X. Wei, D. Li, W. Jiang, Z. Gu, X. Wang, Z. Zhang, et al., *3D printable graphene composite*, Scientific Reports, **2015**. 5(1): p. 11181.
- [105] R. Singh, G. Sandhu, R. Penna, and I. Farina, *Investigations for Thermal and Electrical Conductivity of ABS-Graphene Blended Prototypes*, Materials, **2017**. 10(8): p. 881.
- [106] M. Nikzad, S.H. Masood, and I. Sbarski, *Thermo-mechanical properties of a highly filled polymeric composites for Fused Deposition Modeling*, Materials & Design, **2011**. 32(6): p. 3448-3456.
- [107] F. Ning, W. Cong, J. Qiu, J. Wei, and S. Wang, *Additive manufacturing of carbon fiber reinforced thermoplastic composites using fused deposition modeling*, Composites Part B: Engineering, **2015**. 80(1): p. 369-378.
- [108] N. Li, Y. Li, and S. Liu, *Rapid prototyping of continuous carbon fiber reinforced polylactic acid composites by 3D printing*, Journal of Materials Processing Technology, **2016**. 238(1): p. 218-225.
- [109] H.S. Patanwala, D. Hong, S.R. Vora, B. Bognet, and A.W.K. Ma, *The microstructure and mechanical properties of 3D printed carbon nanotube-polylactic acid composites*, Polymer Composites, **2017**. in press
- [110] S. Meng, H. He, Y. Jia, P. Yu, B. Huang, and J. Chen, *Effect of nanoparticles on the mechanical properties of acrylonitrile–butadiene–styrene specimens fabricated by fused deposition modeling*, Journal of Applied Polymer Science, **2017**. 134(7): p. 44470-44478.
- [111] Q. Zhang, F. Zhang, S.P. Medarametla, H. Li, C. Zhou, and D. Lin, *3D printing of graphene aerogels*, Small, **2016**. 12(13): p. 1702-1708.
- [112] S. Dul, L. Fambri, and A. Pegoretti, *Fused deposition modelling with ABS-graphene nanocomposites*, Composites Part A: Applied Science and Manufacturing, **2016**. 85(1): p. 181-191.
- [113] R.O. Ebewele, *Polymer science and technology*, **1996**: CRC Press LLC.
- [114] Versalis S.p.A SINKRAL®ABS Product Data from http://www.materialdatacenter.com/ms/en/Sinkral/Versalis+S%252Ep%252E_A/1895 consulted on June 20th, 2018.
- [115] Nanocyl®NC7000™ (2016) Multiwall Carbon Nanotubes Product Data from <http://www.nanocyl.com/wp-content/uploads/2016/07/DM-TI-02-TDS-NC7000-V08.pdfXG> consulted on June 20th, 2018.
- [116] J. Liang, Y. Huang, L. Zhang, Y. Wang, Y. Ma, T. Guo, et al., *Molecular-Level Dispersion of Graphene into Poly(vinyl alcohol) and Effective Reinforcement of their Nanocomposites*, Advanced Functional Materials, **2009**. 19(14): p. 2297-2302.
- [117] J.C.H. Afdal and J.L. Kardos, *The Halpin-Tsai equations: A review*, Polymer Engineering & Science, **1976**. 16(5): p. 344-352.
- [118] K. Kalaitzidou, H. Fukushima, and L.T. Drzal, *A new compounding method for exfoliated graphite–polypropylene nanocomposites with enhanced flexural properties and lower percolation threshold*, Composites Science and Technology, **2007**. 67(10): p. 2045-2051.

- [119] J.A. King, D.R. Klimek, I. Miskioglu, and G.M. Odegard, *Mechanical properties of graphene nanoplatelet/epoxy composites*, Journal of Composite Materials, **2015**. 49(6): p. 659-668.
- [120] J.C. Halpin and T.W. Tsai, *Effects of environmental factors on composite materials*, U.S. Air Force Materials Laboratory Rept, **1967**. AFML-TR-67(1): p. 423-483.
- [121] J.C. Halpin, *Stiffness and expansion estimates for oriented short fiber composites*, Journal of Composite Materials, **1969**. 3(4): p. 732-734.
- [122] M.A. Van Es, "Polymer-clay nanocomposites: the importance of particle dimensions," PhD Thesis, Faculty of Applied Sciences, Delft University of Technology, **2001**.
- [123] T.D. Fornes and D.R. Paul, *Modeling properties of nylon 6/clay nanocomposites using composite theories*, Polymer, **2003**. 44(17): p. 4993-5013.
- [124] T.K. Gupta, B.P. Singh, S. Teotia, V. Katyal, S.R. Dhakate, and R.B. Mathur, *Designing of multiwalled carbon nanotubes reinforced polyurethane composites as electromagnetic interference shielding materials*, Journal of Polymer Research, **2013**. 20(6): p. 169.
- [125] M.H. Al-Saleh, W.H. Saadeh, and U. Sundararaj, *EMI shielding effectiveness of carbon based nanostructured polymeric materials: A comparative study*, Carbon, **2013**. 60(1): p. 146-156.
- [126] F. Wang, L.T. Drzal, Y. Qin, and Z. Huang, *Mechanical properties and thermal conductivity of graphene nanoplatelet/epoxy composites*, Journal of Materials Science, **2015**. 50(3): p. 1082-1093.
- [127] S. Biniak, G. Szymański, J. Siedlewski, and A. Świtkowski, *The characterization of activated carbons with oxygen and nitrogen surface groups*, Carbon, **1997**. 35(12): p. 1799-1810.
- [128] B. Quan, S.-H. Yu, D.Y. Chung, A. Jin, J.H. Park, Y.-E. Sung, et al., *Single source precursor-based solvothermal synthesis of heteroatom-doped graphene and its energy storage and conversion applications*, **2014**. 4(1): p. 5639-5644.
- [129] A. Boldizar and K. Möller, *Degradation of ABS during repeated processing and accelerated ageing*, Polymer Degradation and Stability, **2003**. 81(2): p. 359-366.
- [130] L.L. Blyler, *The influence of additives on the flow behavior of ABS*, Polymer Engineering & Science, **1974**. 14(11): p. 806-809.
- [131] H. Blom, R. Yeh, R. Wojnarowski, and M. Ling, *Detection of degradation of ABS materials via DSC*, Journal of Thermal Analysis and Calorimetry, **2006**. 83(1): p. 113-115.
- [132] P. Singh and A.K. Ghosh, *Torsional, tensile and structural properties of acrylonitrile-butadiene-styrene clay nanocomposites*, Materials & Design, **2014**. 55(1): p. 137-145.
- [133] P. Rytlewski, K. Moraczewski, and M. Żenkiewicz, *Effects of coffee on the stability of accelerated aged poly(acrylonitrile-butadiene-styrene)*, Journal of Applied Polymer Science, **2014**. 131(4): p. 39887-39894.
- [134] T.F. Reed, H.E. Bair, and R.G. Vadimsky, *The Causes of pitting and haze on molded ABS plastic surfaces*, in *Recent Advances in Polymer Blends, Grafts, and Blocks*. **1974**. Boston, MA: Springer US. p. 359-373.

- [135] H.E. Bair, D.J. Boyle, and B. Twombly, *Evaluation of four ABS resins by thermal analysis*, Journal of thermal analysis, **1996**. 46(3): p. 955-963.
- [136] P. Noorunnisa Khanam, M.A. AlMaadeed, M. Ouederni, E. Harkin-Jones, B. Mayoral, A. Hamilton, et al., *Melt processing and properties of linear low density polyethylene-graphene nanoplatelet composites*, Vacuum, **2016**. 130(1): p. 63-71.
- [137] H. Kim and C.W. Macosko, *Processing-property relationships of polycarbonate/graphene composites*, Polymer, **2009**. 50(15): p. 3797-3809.
- [138] X. Wang, L. Song, H. Yang, H. Lu, and Y. Hu, *Synergistic effect of graphene on antidripping and fire resistance of intumescence flame retardant poly(butylene succinate) composites*, Industrial & Engineering Chemistry Research, **2011**. 50(9): p. 5376-5383.
- [139] H. Oxfall, G. Ariu, T. Gkourmpis, R.W. Rychwalski, and M. Rigdahl, *Effect of carbon black on electrical and rheological properties of graphite nanoplatelets/poly(ethylene-butyl acrylate) composites*, Express Polymer Letters, **2015**. 9(1): p. 66-76.
- [140] J.R. Potts, D.R. Dreyer, C.W. Bielawski, and R.S. Ruoff, *Graphene-based polymer nanocomposites*, Polymer, **2011**. 52(1): p. 5-25.
- [141] E. Kuzdzal, B. Cichy, and S. Dulik, *Morphological properties of fillers for polymeric materials; the influence on rheological properties of compositions with unsaturated polyester resin*, CHEMIK, **2016**. 70(1): p. 185–192.
- [142] M. El Achaby, F.-E. Arrakhiz, S. Vaudreuil, A. el Kacem Qaiss, M. Bousmina, and O. Fassi-Fehri, *Mechanical, thermal, and rheological properties of graphene-based polypropylene nanocomposites prepared by melt mixing*, Polymer Composites, **2012**. 33(5): p. 733-744.
- [143] H.E. Bair, *Thermal analysis of additives in polymers*, Turi E. Ed, in *Thermal Characterization of Polymeric Materials*. **1981**: Academic Press. p. 845-909.
- [144] C. Merlini, A. Pegoretti, P.C. Vargas, T.F. da Cunha, S.D.A.S. Ramôa, B.G. Soares, et al., *Electromagnetic interference shielding effectiveness of composites based on polyurethane derived from castor oil and nanostructured carbon fillers*, Polymer Composites, **2017**. in press
- [145] S. Kuester, C. Merlini, G.M.O. Barra, J.C. Ferreira, A. Lucas, A.C. de Souza, et al., *Processing and characterization of conductive composites based on poly(styrene-b-ethylene-ran-butylene-b-styrene) (SEBS) and carbon additives: A comparative study of expanded graphite and carbon black*, Composites Part B: Engineering, **2016**. 84(1): p. 236-247.
- [146] D.-X. Yan, H. Pang, B. Li, R. Vajtai, L. Xu, P.-G. Ren, et al., *Structured reduced graphene oxide/polymer composites for ultra-efficient electromagnetic interference shielding*, Advanced Functional Materials, **2015**. 25(4): p. 559-566.
- [147] C. Merlini, G.M.O. Barra, M.D.P.P. da Cunha, S.D.A.S. Ramôa, B.G. Soares, and A. Pegoretti, *Electrically conductive composites of polyurethane derived from castor oil with polypyrrole-coated peach palm fibers*, Polymer Composites, **2017**. 38(10): p. 2146-2155.
- [148] J.A. King, W.A. Pisani, D.R. Klimek-McDonald, W.F. Perger, and G.M. Odegard, *Shielding effectiveness of carbon-filled polycarbonate composites*, Journal of Applied Polymer Science, **2015**. 132(43): p. 42719-42719.

- [149] L. T. Drzal, (2013) <http://xgsciences.com/wp-content/uploads/2013/04/Drzal-Presentation.pdf> consulted on June 20th, 2018.
- [150] J.A. King, M.D. Via, F.A. Morrison, K.R. Wiese, E.A. Beach, M.J. Cieslinski, et al., *Characterization of exfoliated graphite nanoplatelets/polycarbonate composites: electrical and thermal conductivity, and tensile, flexural, and rheological properties*, Journal of Composite Materials, **2012**. 46(9): p. 1029-1039.
- [151] D. Jiang and D.E. Smith, *Anisotropic mechanical properties of oriented carbon fiber filled polymer composites produced with fused filament fabrication*, Additive Manufacturing, **2017**. 18(1): p. 84-94.
- [152] J. Li and Y.F. Zhang, *The tensile properties of short carbon fiber reinforced ABS and ABS/PA6 composites*, Journal of Reinforced Plastics and Composites, **2010**. 29(11): p. 1727-1733.
- [153] V. Panwar and K. Pal, *An optimal reduction technique for rGO/ABS composites having high-end dynamic properties based on Cole-Cole plot, degree of entanglement and C-factor*, Composites Part B: Engineering, **2017**. 114(1): p. 46-57.
- [154] J.-W. Lee, J.-C. Lee, J. Pandey, S.-H. Ahn, and Y.J. Kang, *Mechanical properties and sound insulation effect of ABS/carbon-black composites*, Journal of Composite Materials, **2010**. 44(14): p. 1701-1716.
- [155] S. Vikas, G. Meenakshi, and J. Prashant, *Preparation, characterization and study of mechanical properties of graphene/ABS nano-composites*, Indian Journal of Science and Technology, **2017**. 10(17): p. 1-5.
- [156] C. Lee, X. Wei, J.W. Kysar, and J. Hone, *Measurement of the elastic properties and intrinsic strength of monolayer graphene*, Science, **2008**. 321(5887): p. 385-388.
- [157] C. Gómez-Navarro, M. Burghard, and K. Kern, *Elastic Properties of Chemically Derived Single Graphene Sheets*, Nano Letters, **2008**. 8(7): p. 2045-2049.
- [158] B. Mayoral, E. Harkin-Jones, P.N. Khanam, M.A. AlMaadeed, M. Ouederni, A.R. Hamilton, et al., *Melt processing and characterisation of polyamide 6/graphene nanoplatelet composites*, RSC Advances, **2015**. 5(65): p. 52395-52409.
- [159] K. Mehdi, P. Raghuram V., B. Md A., and K. Kalaitzidou, *Effect of interphase modulus and nanofiller agglomeration on the tensile modulus of graphite nanoplatelets and carbon nanotube reinforced polypropylene nanocomposites*, Carbon Letter, **2010**. 11(1): p. 325-331.
- [160] D. Pedrazzoli and A. Pegoretti, *Hybridization of short glass fiber polypropylene composites with nanosilica and graphite nanoplatelets*, Journal of Reinforced Plastics and Composites, **2014**. 33(18): p. 1682-1695.
- [161] ASTM Standard D123 - 15b Standard Terminology Relating to Textiles.
- [162] A. Tsouknidas, M. Pantazopoulos, I. Katsoulis, D. Fasnakis, S. Maropoulos, and N. Michailidis, *Impact absorption capacity of 3D-printed components fabricated by fused deposition modelling*, Materials & Design, **2016**. 102(1): p. 41-44.
- [163] M. Fernandez-Vicente, W. Calle, S. Ferrandiz, and A. Conejero, *Effect of Infill Parameters on Tensile Mechanical Behavior in Desktop 3D Printing*, 3D Printing and Additive Manufacturing, **2016**. 3(3): p. 183-192.

- [164] *Tensile strength of partially filled FFF printed parts: experimental results*, Rapid Prototyping Journal, **2017**. 23(1): p. 122-128.
- [165] L. Fambri, S. Bragagna, and C. Migliaresi, *Biodegradable Fibers of Poly-L, DL-lactide 70/30 Produced by Melt Spinning*, Macromolecular Symposia, **2006**. 234(1): p. 20-25.
- [166] S. Q., R. G.M., B. C.T., and G. P., *Effect of processing conditions on the bonding quality of FDM polymer filaments*, Rapid Prototyping Journal, **2008**. 14(2): p. 72-80.
- [167] S.H. Ahn, M. Montero, D. Odell, S. Roundy, and P.K. Wright, *Anisotropic material properties of fused deposition modeling ABS*, Rapid Prototyping Journal, **2002**. 8(4): p. 248-257.
- [168] B. Valentan, D. Pogacar, T. Brajih, T.Z. Hartner, A. Pilipovic, and I. Drstvensek, *Development of a 3D printer for thermoplastic modelling*, Materiali in Tehnologije, **2012**. 46(6): p. 589-594.
- [169] H. Jami, S.H. Masood, and W.Q. Song, *Dynamic response of FDM made ABS parts in different part orientations*, Advanced Materials Research, **2013**. 748(1): p. 291-294.
- [170] T. Riccò, A. Pavan, and F. Danusso, *Dynamic transition of grafted polybutadiene in ABS resins*, Polymer, **1975**. 16(9): p. 685-689.
- [171] J. Más, A. Vidaurre, J.M. Meseguer, F. Romero, M.M. Pradas, J.L.G. Ribelles, et al., *Dynamic mechanical properties of polycarbonate and acrylonitrile-butadiene-styrene copolymer blends*, Journal of Applied Polymer Science, **2002**. 83(7): p. 1507-1516.
- [172] M.P. Sepe, *Dynamic mechanical analysis for plastics engineering*, **1998**. Norwich, New York: Plastics Design Library.
- [173] B.E. Tiganis, L.S. Burn, P. Davis, and A.J. Hill, *Thermal degradation of acrylonitrile-butadiene-styrene (ABS) blends*, Polymer Degradation and Stability, **2002**. 76(3): p. 425-434.
- [174] A. Arivazhagan and S.H. Masood, *Dynamic mechanical properties of ABS material processed by Fused Deposition Modelling*, International Journal of Engineering Research and Applications, **2012**. 2(3): p. 2009-2014.
- [175] R. Crawford, *Plastics Engineering*, **1998**. 3rd ed. Oxford: Butterworth-Heinemann.
- [176] J. Kolařík and A. Pegoretti, *Proposal of the Boltzmann-like superposition principle for nonlinear tensile creep of thermoplastics*, Polymer Testing, **2008**. 27(5): p. 596-606.
- [177] A. Dorigato, A. Pegoretti, and J. Kolařík, *Nonlinear tensile creep of linear low density polyethylene/fumed silica nanocomposites: Time-strain superposition and creep prediction*, Polymer Composites, **2010**. 31(11): p. 1947-1955.
- [178] A. Pegoretti, *Creep and fatigue behavior of polymer nanocomposites*, in *Nano- and Micromechanics of Polymer Blends and Composites*. **2009**: Carl Hanser Verlag GmbH & Co. KG. p. 301-339.
- [179] G. Williams and D.C. Watts, *Non-symmetrical dielectric relaxation behaviour arising from a simple empirical decay function*, Transactions of the Faraday Society, **1970**. 66(1): p. 80-85.
- [180] W.N. Findley, *26-Year creep and recovery of poly(vinyl chloride) and polyethylene*, Polymer Engineering & Science, **1987**. 27(8): p. 582-585.

- [181] A. Dorigato, V. Moretti, S. Dul, S.H. Unterberger, and A. Pegoretti, *Electrically conductive nanocomposites for fused deposition modelling*, Synthetic Metals, **2017**. 226(1): p. 7-14.
- [182] S. Yang, J. Rafael Castilleja, E.V. Barrera, and K. Lozano, *Thermal analysis of an acrylonitrile–butadiene–styrene/SWNT composite*, Polymer Degradation and Stability, **2004**. 83(3): p. 383-388.
- [183] M.L. Shofner, F.J. Rodriguez-Macias, R. Vaidyanathan, and E.V. Barrera, *Single wall nanotube and vapor grown carbon fiber reinforced polymers processed by extrusion freeform fabrication*, Composites Part a-Applied Science and Manufacturing, **2003**. 34(12): p. 1207-1217.
- [184] S. Dul, H. Mahmood, L. Fambri, and A. Pegoretti, *Graphene-ABS nanocomposites for fused deposition modelling*, in *ECCM 2017 - Proceeding of the 17th European Conference on Composite Materials*. **2016**. Munich.
- [185] L.A. Pothan, Z. Oommen, and S. Thomas, *Dynamic mechanical analysis of banana fiber reinforced polyester composites*, Composites Science and Technology, **2003**. 63(2): p. 283-293.
- [186] G. Georgousis, C. Pandis, A. Kalamiotis, P. Georgioupolos, A. Kyritsis, E. Kontou, et al., *Strain sensing in polymer/carbon nanotube composites by electrical resistance measurement*, Composites Part B: Engineering, **2015**. 68(1): p. 162-169.
- [187] A.I. Oliva-Avilés, F. Avilés, and V. Sosa, *Electrical and piezoresistive properties of multi-walled carbon nanotube/polymer composite films aligned by an electric field*, Carbon, **2011**. 49(9): p. 2989-2997.
- [188] J.R. Bautista-Quijano, F. Avilés, J.O. Aguilar, and A. Tapia, *Strain sensing capabilities of a piezoresistive MWCNT-polysulfone film*, Sensors and Actuators A: Physical, **2010**. 159(2): p. 135-140.
- [189] R. Moriche, M. Sánchez, S.G. Prolongo, A. Jiménez-Suárez, and A. Ureña, *Reversible phenomena and failure localization in self-monitoring GNP/epoxy nanocomposites*, Composite Structures, **2016**. 136(1): p. 101-105.
- [190] D. Pedrazzoli, A. Dorigato, and A. Pegoretti, *Monitoring the mechanical behavior under ramp and creep conditions of electrically conductive polymer composites*, Composites Part A: Applied Science and Manufacturing, **2012**. 43(8): p. 1285-1292.
- [191] M.R. Zakaria, M.H. Abdul Kudus, H. Md. Akil, and M.Z. Mohd Thirmizir, *Comparative study of graphene nanoparticle and multiwall carbon nanotube filled epoxy nanocomposites based on mechanical, thermal and dielectric properties*, Composites Part B: Engineering, **2017**. 119(1): p. 57-66.
- [192] S.-Y. Yang, W.-N. Lin, Y.-L. Huang, H.-W. Tien, J.-Y. Wang, C.-C.M. Ma, et al., *Synergistic effects of graphene platelets and carbon nanotubes on the mechanical and thermal properties of epoxy composites*, Carbon, **2011**. 49(3): p. 793-803.
- [193] C. Kostagiannakopoulou, X. Tsilimigkra, G. Sotiriadis, and V. Kostopoulos, *Synergy effect of carbon nano-fillers on the fracture toughness of structural composites*, Composites Part B: Engineering, **2017**. 129(1): p. 18-25.
- [194] P.-N. Wang, T.-H. Hsieh, C.-L. Chiang, and M.-Y. Shen, *Synergistic effects of mechanical properties on graphene nanoplatelet and multiwalled carbon nanotube hybrids reinforced epoxy/carbon fiber composites*, Journal of Nanomaterials, **2015**. 2015(1): p. 9.

- [195] J. Li, P.-S. Wong, and J.-K. Kim, *Hybrid nanocomposites containing carbon nanotubes and graphite nanoplatelets*, Materials Science and Engineering: A, **2008**. 483-484(1): p. 660-663.
- [196] S. Chatterjee, F.A. Nüesch, and B.T.T. Chu, *Comparing carbon nanotubes and graphene nanoplatelets as reinforcements in polyamide 12 composites*, Nanotechnology, **2011**. 22(27): p. 275714.
- [197] Q. Waheed, A.N. Khan, and R. Jan, *Investigating the reinforcement effect of few layer graphene and multi-walled carbon nanotubes in acrylonitrile-butadiene-styrene*, Polymer, **2016**. 97(1): p. 496-503.
- [198] J.P. Elder, *The general applicability of the Kissinger equation in thermal analysis*, Journal of thermal analysis, **1985**. 30(3): p. 657-669.
- [199] W. Li, A. Dichiara, and J. Bai, *Carbon nanotube-graphene nanoplatelet hybrids as high-performance multifunctional reinforcements in epoxy composites*, Composites Science and Technology, **2013**. 74(1): p. 221-227.
- [200] W. Bauhofer and J.Z. Kovacs, *A review and analysis of electrical percolation in carbon nanotube polymer composites*, Composites Science and Technology, **2009**. 69(10): p. 1486-1498.
- [201] D. Yuan, D. Pedrazzoli, and I. Manas-Zloczower, *Synergistic effects in thermoplastic polyurethanes incorporating hybrid carbon nanofillers*, International Polymer Processing, **2016**. 31(5): p. 554-561.
- [202] S.D.A.S. Ramôa, G.M.O. Barra, C. Merlini, W.H. Schreiner, S. Livi, and B.G. Soares, *Production of montmorillonite/polypyrrole nanocomposites through in situ oxidative polymerization of pyrrole: Effect of anionic and cationic surfactants on structure and properties*, Applied Clay Science, **2015**. 104(1): p. 160-167.
- [203] B.G. Soares, M.E. Leyva, G.M.O. Barra, and D. Khastgir, *Dielectric behavior of polyaniline synthesized by different techniques*, European Polymer Journal, **2006**. 42(3): p. 676-686.
- [204] D.P. Schmitz, L.G. Ecco, S. Dul, E.C.L. Pereira, B.G. Soares, G.M.O. Barra, et al., *Electromagnetic interference shielding effectiveness of ABS carbon-based composites manufactured via fused deposition modelling*, Materials Today Communications, **2018**. 15(1): p. 70-80.
- [205] V.K. Sachdev, S.K. Sharma, M. Tomar, V. Gupta, and R.P. Tandon, *EMI shielding of MWCNT/ABS nanocomposites in contrast to graphite/ABS composites and MWCNT/PS nanocomposites*, RSC Advances, **2016**. 6(51): p. 45049-45058.
- [206] S. Kashi, R.K. Gupta, T. Baum, N. Kao, and S.N. Bhattacharya, *Morphology, electromagnetic properties and electromagnetic interference shielding performance of poly lactide/graphene nanoplatelet nanocomposites*, Materials & Design, **2016**. 95(1): p. 119-126.
- [207] Y. Li, B. Shen, D. Yi, L. Zhang, W. Zhai, X. Wei, et al., *The influence of gradient and sandwich configurations on the electromagnetic interference shielding performance of multilayered thermoplastic polyurethane/graphene composite foams*, Composites Science and Technology, **2017**. 138(1): p. 209-216.
- [208] S.E. Zakiyan, H. Azizi, and I. Ghasemi, *Influence of chain mobility on rheological, dielectric and electromagnetic interference shielding properties of poly methyl-methacrylate composites filled with graphene*

and carbon nanotube, Composites Science and Technology, **2017**. 142(1): p. 10-19.

Publications on peer reviewed journals

- S. Dul, L. Fambri, A. Pegoretti, *Fused deposition modelling with ABS-graphene nanocomposites*. Composites Part A - Applied Science and Manufacturing, **2016**. 85: p. 181-191.
- A. Dorigato, V. Moretti, S. Dul, S.H. Unterberger, A. Pegoretti, *Electrically conductive nanocomposites for fused deposition modelling*. Synthetic Metals, **2017**. 226: p. 7-14.
- S. Dul, L. Fambri, C. Merlini, G.M.O. Barra, M. Bersani, L. Vanzetti, A. Pegoretti, *Effect of graphene nanoplatelets structure on the properties of acrylonitrile-butadiene-styrene-composites*. Polymers Composites, **2017**. In press.
- S. Dul, L. Fambri, A. Pegoretti, *Filaments production and fused deposition modelling of ABS/carbon nanotubes composites*. Nanomaterials, **2018**. 8(1): p. 49-73.
- D. P. Schmitz, L. G. Ecco, S. Dul, E. C. L. Pereira, B. G. Soares, G. M. O. Barra, A. Pegoretti, *Electromagnetic Interference Shielding Effectiveness of ABS carbon-based Polymer Composites Manufactured via Fused Deposition Modelling*. Materials Today Communication, **2018**. 15(1): p. 70-80.
- L. G. Ecco, S. Dul, D. P. Schmitz, B. G. Soares, G. M. O. Barra, L. Fambri, A. Pegoretti, *Rapid fabrication of an efficient electromagnetic interference shielding ABS polymer-composite via fused deposition modeling*. Composites Part A - Applied Science and Manufacturing, **2018**. Under review.
- S. Dul, L. Fambri, A. Pegoretti, *Effect of the filler in ABS nanocomposites - Comparison of graphene and carbon nanotubes*. Nanomaterials, **2018**. In submission.
- S. Dul, L. Fambri, A. Pegoretti, *Strain monitoring of carbon nanotubes nanocomposites by fused deposition modelling*. In preparation.
- S. Dul, L. G. Ecco, L. Fambri, A. Pegoretti, *ABS/carbon nanotubes/graphene hybrid nanocomposites for fused deposition modelling*. In preparation.

Participation to congresses, schools and workshops

- S. Dul, H. Mahmood, L. Fambri, A. Pegoretti, *Graphene-ABS nanocomposites for fused deposition modelling*. In European Conference on Composite Materials (ECCM 2017), June 26-30th, **2016**, Munich (Germany).
- S. Dul, L. Fambri, A. Pegoretti, *Carbon nanotubes-ABS nanocomposites for fused deposition modelling*. In Milan Polymer Days conference (MIPOL2017), February 15-16th, **2017**, Milan (Italy).

- S. Dul, L. Fambri, A. Pegoretti, *Strain monitoring of carbon nanotubes nanocomposites by fused deposition modelling*. In Europolymer conference 2017 (EUPOC-2017), May 21-25th, 2017, Gargnano (Italy).
- Summer school on “Fatigue and damage mechanics of composite materials”, July 13-17th, 2015, Vicenza (Italy).
- Summer school on “Materials for industry”, September 18-22th, 2017, Brescia (Italy).

Other activities

Journal reviewing

- Materials & Design (IF = 4.364)

Student tutoring

- Research advisor of a graduate student (Valerio Moretti) in Materials Science and Engineering (University of Trento, 2014-2015) regarding thesis of “Electrical conductive nanocomposite materials for fused deposition modelling”.

Collaboration research

- Research collaborator to a visiting researcher (Dr. Luiz Gustavo Ecco) in Department of Mechanical Engineering Universidade Federal de Santa Catarina, September 2017 regarding the “Rapid fabrication of an efficient electromagnetic interference shielding ABS polymer-composite via fused deposition modeling”.
- Research collaborator to a visiting doctoral student (Débora Schmitz) in Department of Mechanical Engineering Universidade Federal de Santa Catarina, January-April, 2018 regarding the “Electromagnetic interference shielding effectiveness of ABS carbon-based polymer composites manufactured via fused deposition modelling”.

Acknowledgements

I gratefully thank AREAS+ EU Project of Erasmus Mundus Action 2 Programme for scholarship support. I am also grateful to my tutors Prof. Alessandro Pegoretti and Prof. Luca Fambri (Department of Industrial Engineering – University of Trento, Italy), who followed me throughout this period. Their assistance and guidance during my PhD study were so valuable and appreciate. Special acknowledgements are also due to the technician Alfredo Casagranda and Claudia Gavazza working at the Polymers and Composites Laboratory for their fruitful support on some experimental activities and laboratory matters.

I would like to gratefully thank also Prof. Barra Guilherme, Prof. Claudia Merlini, Dr. Luiz Gustavo Ecco, and Débora Schmitz (Department of Mechanical Engineering, Federal University of Santa Catarina, Brazil) for help with electromagnetic interference shielding analysis. I would gratefully thank Massimo Bersani and Vanzetti Lia Emanuelia (Centre for Materials and Microsystems, Fondazione Bruno Kessler, Trento, Italy) for XPS analysis. I wish to thank Dr. Seraphin Unterberger (Unit for Material Technology, University of Innsbruck, Austria) for helping to carry out thermal conductivity test.

I wish to thank Versalis S.p.A. (Mantova, Italy) for donating ABS pellet polymer for this work. I am also thankful to Sharebot S.r.l. (Nibionno, LC, Italy) for providing the prototype of the HT Next Generation desktop 3D-printer.

My sincere thanks to all colleagues whom I have known for shared everyday work and friendship: Annalisa Cataldi, Haroon Mahmood, Daniele Rigotti, Giulia Fredi, Andrea Dorigato, Denis Lorenzi and so many others.

Finally, I gratefully thank my beloved family and friends for their loving support through all of these years. My friend Giulio Molon were really fundamental for his kind support through my time in Italy. A very special thank goes to my mother, my father and brothers for their encouragement.

Trento, 22nd June 2018